UNIVERSITEIT VAN PRETORIA
UNIVERSITY OF PRETORIA
YUNIBESITHI YA PRETORIA

BASE METAL LOSSES TO FURNACE SLAG DURING PROCESSING OF PLATINUM-BEARING CONCENTRATES

by

Lesley Andrews

1 July 2008

Submitted in partial fulfillment of the requirements for the degree MSc (Applied Science) Metallurgy in the Faculty of Engineering, Built Environment and Information Technology, University of Pretoria, Pretoria.

UNIVERSITEIT VAN PRETORIA
UNIVERSITY OF PRETORIA
YUNIBESITHI YA PRETORIA

BASE METAL LOSSES TO FURNACE SLAG DURING PROCESSING OF PLATINUM-BEARING CONCENTRATES

by

Lesley Andrews

1 July 2008

Submitted in partial fulfillment of the requirements for the degree MSc (Applied Science) Metallurgy in the Faculty of Engineering, Built Environment and Information Technology, University of Pretoria, Pretoria.

ABSTRACT

The base metal distribution in, and losses to, Anglo Platinum six-in-line and slag cleaning furnace slags were characterised to coincide with various process changes at Waterval Smelter from 1999 to 2007. The base metals are presumed to be reliable indicators of PGE losses and are easier to detect and measure than these elements are. In addition, base metal and sulphur levels are used to monitor and control many smelter processes, including slag cleaning and converting.

Some losses to slag are recoverable but others are not – these have been quantified during this study. Slag composition and smelting temperatures have varied substantially, and optimisation of the slag cleaning furnace – a first for the South African platinum industry – has produced a wide variation in oxidation conditions. Most of the base metal losses in the slag cleaning furnace are mechanically entrained matte particles, the largest of which should be recovered. These have been examined to establish any relationship between composition, size, and depth within the furnace so that recommendations can be made to limit these types of losses.

In the six-in-line furnaces, over half of base metal losses to slag are as dissolved phases, which are not recoverable. Levels of dissolved metals have been measured and related to furnace operating conditions and slag composition. The prediction of such base metal losses is not easy, because the slag compositions are so complex. One aspect of the project has been to compare the measured distribution of the base metals with those calculated using the FactSage equilibrium model, to identify problem areas, and to recommend actions which could improve the predictions of this and similar modelling programs for base metal dissolution in slag.

New electron microbeam techniques have been developed to quantify base metal distribution in slag, and novel combinations of these techniques with analytical chemistry and Mössbauer Spectroscopy have been pioneered.

UNIVERSITEIT VAN PRETORIA
UNIVERSITY OF PRETORIA
YUNIBESITHI YA PRETORIA

ACKNOWLEDGEMENTS

As the author of this dissertation, I am grateful to Anglo Platinum and to Anglo Research for sponsorship of the project, and for permission to write it up, and especially to Dr Robert Schouwstra who encouraged my venture into the field of pyrometallurgy. Many people have been involved with sample preparation and analysis, most especially the staff of the Mineralogical Research and Analytical Departments at Anglo Research. The kind assistance of Professor Fraans Waanders of North West University with Mössbauer Spectroscopy is acknowledged, as is the help of Dr Johan Nell (of Hatch) in sample-taking and general discussion.

Personnel from Anglo Platinum Head Office and all three smelters have assisted with the project. Special mention should be made of Rodney Hundermark, Kevin van der Merwe and Keith Hines for their patience with continual questioning about smelter processes, and of Dr Lloyd Nelson for general encouragement. Warren Armstrong, Alpheus Moshokwa, and many others have kindly helped me to take samples, frequently under fairly trying conditions.

The staff of the Metallurgical Engineering Department of the University of Pretoria have been most supportive, especially Professor Chris Pistorius, my supervisor, whose enthusiasm is infectious, and Mrs Sarah Havenga who has always been at hand to facilitate meetings, and sort out any administration problems.

Last but not least, I really appreciate the support of my husband and two sons (one of whom upset my project schedule by getting married a year ago!). Sharing a home computer with two graphic designers and an automobile consultant requires much diplomacy, and I have to acknowledge that my dissertation was usually prioritised!

Thanks to All.

Lesley

CONTENTS

Page

1 INTRODUCTION **1**

2 AIM OF THIS STUDY **2**

3 PREVIOUS WORK **3**

3.1 Introduction 3

3.2 Base metal dissolution in slag 4

3.2.1 Species involved 5

3.2.2 Physical and compositional factors affecting base metal dissolution in slag 9

3.2.2.1 The effect of pO_2 on base metal dissolution in slag 10

3.2.2.2 The effect of temperature on base metal dissolution in slag 10

3.2.2.3 The effect of slag composition on base metal dissolution in 10

3.2.2.4 The effect of matte composition on base metal dissolution in slag 11

3.2.2.5 The effect of iron sulphide in the feed and/or matte 12

3.2.3 Activities and activity coefficients 13

3.2.4 Distribution and partition coefficients, and factors affecting these 14

3.3 Mechanical entrainment of matte in slag 19

3.3.1 Origin of entrained matte in slag 20

3.3.2 Settling of entrained matte in a furnace 20

3.3.3 Matte flotation in slag 22

3.3.4 Coalescence of entrained matte phases 27

3.3.5 Matte behaviour in industrial furnaces and converters 27

3.3.6 Effect of electric and magnetic fields 38

3.4 Processes used in base metal recovery (slag cleaning) 39

4 SMELTER PROCESSES **41**

4.1 History 41

4.2 Process overview 41

4.3 Electric furnace smelting 43

4.4 Converting 44

4.5 Slag cleaning (pyrometallurgical) 47

4.6 Process flow and mass balances 48

5 SAMPLING 55

5.1 Electric furnace (six-in-line) sampling 55

5.1.1 Sampling overview 55

5.1.2 Sampling methodology (six-in-lines) 55

5.2 Slag cleaning furnace sampling 56

5.2.1 Sampling overview 56

5.2.2 Sampling methodology (SCF) 56

6 ANALYTICAL TECHNIQUES 57

6.1 Overview 57

6.2 Chemical analysis 57

6.3 X-ray powder diffraction (XRD) 58

6.4 Section preparation 58

6.5 Scanning electron microscopy 59

6.6 Automated scanning electron microscopy 60

6.7 Electron microprobe analysis 61

6.8 Mössbauer Spectroscopy 64

6.9 FactSage modelling 65

7 RESULTS 67

7.1 Electric furnaces (six-in-line) 67

7.1.1 Furnace feed 67

7.1.1.1 Flash drier product 67

7.1.1.2 Reverts 68

7.1.1.3 Recycles 70

7.1.1.4 Union furnace matte and Pierce Smith converter slag 71

7.1.2 Furnace matte 72

7.1.3 Furnace slag 73

7.1.3.1 Glass phase 75

7.1.3.2 Spinel phases 76

7.1.3.3 Entrained matte and sulphide phases 78

7.1.4 Sounding bar results 81

7.2 Slag cleaning furnace (SCF) 85

7.2.1 Early work 85

7.2.2 SCF feed (September 2005) 86

7.2.2.1 Silica flux 86

7.2.2.2 Flash drier product 86

7.2.2.3 Granulated converter slag 87

7.2.3 SCF matte 89

7.2.4 SCF slag 90

7.2.4.1 glass and spinel phases 92

7.2.4.2 entrained matte 93

7.3 Mossbauer spectroscopy results 94

7.3.1 Six-in-line furnaces 94

7.3.2 Slag cleaning furnace. 94

7.4 FactSage modeling of slag-matte equilibrium 95

7.4.1 Six-in-line furnaces – slag in equilibrium with bulk matte 95

7.4.2 Slag cleaning furnace – slag in equilibrium with bulk matte 96

7.4.3 Base metal dissolution types in slag 97

8 DISCUSSION 100

8.1 Distribution of base metals in smelter feed and products 100

8.2 Dissolved base metals 101

8.3 Entrained matte in slag 108

8.4 Fe^{3+}/Fe^{2+} measurement for slag pO_2 calculation, and other Mössbauer information 121

8.5 Calculation of the equilibrium base metal dissolution in the slag 122

8.5.1 Reactions and equilibrium constants 122

8.5.2 Activities and activity coefficients in slag and matte 123

8.5.3 Oxygen activities (pO_2) 125

8.5.4 Calculated base metal distribution 125

8.6 Slag-matte equilibria in the furnaces 128

8.7 Origin of entrained matte in slag 130

8.8 Process optimisation 132

8.8.1 Six-in-line furnaces 132

8.8.2 Slag cleaning furnace 132

8.9 Modelling of dissolved base metal levels 133

9 CONCLUSIONS 134

10 RECOMMENDATIONS 135

11 REFERENCES 136

APPENDIX A (TABLES) A1

APPENDIX B (FIGURES) B1

APPENDIX C (STATISTICS) C1

1 INTRODUCTION

More than eighty per cent of worldwide platinum group element (PGE) reserves are found in South Africa (NELL, 2004). The base metals (nickel, copper and cobalt) are also recovered as part of the platinum-producing processes operated in the Rustenburg area, north west of Pretoria. The metals are mined from the Bushveld Complex mainly as sulphide minerals contained in the platinum ores – the Merensky Reef, the Platreef and the UG-2 chromitite reef.

In 2006, South Africa was the tenth largest nickel producer in the world, with a mine production of 2.9% of the global output (the D.M.E., 2007). Although not the core concern of platinum producers, the base metals earn considerable income in their own right. Total refined production from Anglo Platinum operations in 2007 amounted to 192000 tonnes nickel (at 10.7 US$/lb), and 101000 tonnes copper (at 2.9 US$/lb). The contribution from nickel exceeded 10 % of total sales revenue (Anglo Platinum 2007 Annual Report).

After mining, the base metals pass through the concentrating, smelting and converting process route and are finally recovered from the nickel-copper converter matte by electrowinning at the Rustenburg Base Metals Refinery (HOFIREK & HALTON, 1990).

A number of challenges have faced platinum producers during recent years, requiring process development from mining to refining (CRAMER, 2001), which also affects base metal production. Mining constraints have led to an increased production of UG-2 ore, which is more refractory to smelting and contains less than one tenth of the copper and nickel found in the Merensky Reef (JONES, 1999). In addition, traditional converting practices at the smelters gave rise to relatively high sulphur emissions (primarily as SO_2), and revised government air pollution specifications led to the commissioning of new smelting and converting processes.

The process changes introduced at Anglo Platinum smelters to meet these challenges have included the construction of (and conversion to) higher power density furnaces, the replacement of Peirce Smith converters by Ausmelt converters, and the introduction of a slag cleaning furnace to treat converter slag. The time span for the above changes was 1998 to 2006, although a certain degree of process optimisation is still in progress.

The history of smelter operations and details of the processes involved will be dealt with in Chapter 4.

2 AIM OF THIS STUDY

The aim of this research project was to monitor the base metal distribution in, and losses to, Anglo Platinum six-in-line and slag cleaning furnace slags over the process changes described in the Introduction, and also to examine feed materials such as ore concentrate and converter slag to establish base metal distribution and variation.

New electron microbeam techniques (electron microprobe trace analysis, and computer-controlled scanning electron microscopy) had to be developed and combined with analytical chemistry and Mössbauer Spectroscopy results to characterise the base metal distribution in slag.

During the course of the project, the application of modelling software to predict base metal dissolution in slag was also investigated.

Information acquired during the project is to be used to assist process optimisation at the smelters.

3 PREVIOUS WORK

3.1 INTRODUCTION

There is abundant literature dealing with base metal losses to slag, embracing the fields of copper and nickel smelting and converting, as well as cobalt recovery. In the papers reviewed, pO_2 in slag ranged from 10^{-12} to 10^{-5} atm, slag temperatures from 1200 to 1600 °C, and slag iron content from <10 to >50 %.

The first part of this review deals with base metal distribution in the furnace, dissolution in slag, factors affecting this, the chemical species involved, and the thermodynamics behind partitioning. The metallurgical and geochemical aspects of sulphide/silicate distribution are also reviewed. The second part of the review covers the behaviour of mechanically entrained matte, its origin in slag, settling, transport, and recovery during pyrometallurgical slag cleaning. Finally, the current status of slag cleaning methods is examined, and the application of such methods in the Southern African smelting industry is reviewed briefly. The authors referenced in the review are listed alphabetically from pages 128 – 137.

Two extensive reviews were produced in 1981-2 covering the chemistry of nickel and copper smelting slags and pyrometallurgical slag treatment (FLOYD & MACKEY, 1981, MACKEY, 1982), and these are referred to throughout the review. Most of the information on nickel and copper is still current, though more is now known about cobalt distribution and recovery.

The base metals are more stable as sulphide, rather than oxide, species and therefore partition preferentially into the sulphide matte in the six-in-line and slag cleaning furnaces investigated in this study. A first indication of the relative stabilities of sulphide (matte) and oxide (slag) species can be obtained by considering a Yazawa-style diagram (YAZAWA, 1979) – such a diagram maps the combinations of oxygen activity (p_{O_2}) and sulphur activity (p_{S_2}) which stabilise a pure metal, its pure oxide, or its pure sulphide. Because pure species are considered, the diagram only gives an approximate indication. A calculated Yazawa diagram for a temperature of 1500°C is shown in Figure 1. The calculations were performed using FactSage modelling software (this is described later under Analytical Techniques) and pure liquid species were considered in plotting the diagram. The FactSage database does not contain information for pure liquid Co_3S_2, however, so the free energy of this species was found from the FactSage matte solution model ("FTmisc-MATT"). Lines of constant partial pressure of SO_2 are shown on the diagram. The rectangle in broken lines indicates the uncertainty range of conditions in the Anglo Platinum six-in-line electric furnaces, based on 2005 data. As discussed later in this dissertation, the p_{S_2} is expected to be between 0.008 atm and 0.66 atm, and the p_{O_2} between 10^{-7} atm and 10^{-5} atm (combinations of the higher oxygen pressures and higher sulphur pressures are not feasible, since these lead to SO_2 pressures which are well above 1 atm. The rectangle, however, is a rough indication of the possible range of conditions).

The diagram indicates that conditions in the electrical furnace are in the stability regions of the sulphides of copper, nickel and cobalt. This means that these elements are largely expected to report to the matte – as is indeed the case. In contrast, the furnace conditions span the stability regions of iron oxide and iron sulphide – in line with the observed substantial concentrations of iron in both the slag (oxide) and matte (sulphide) phases.

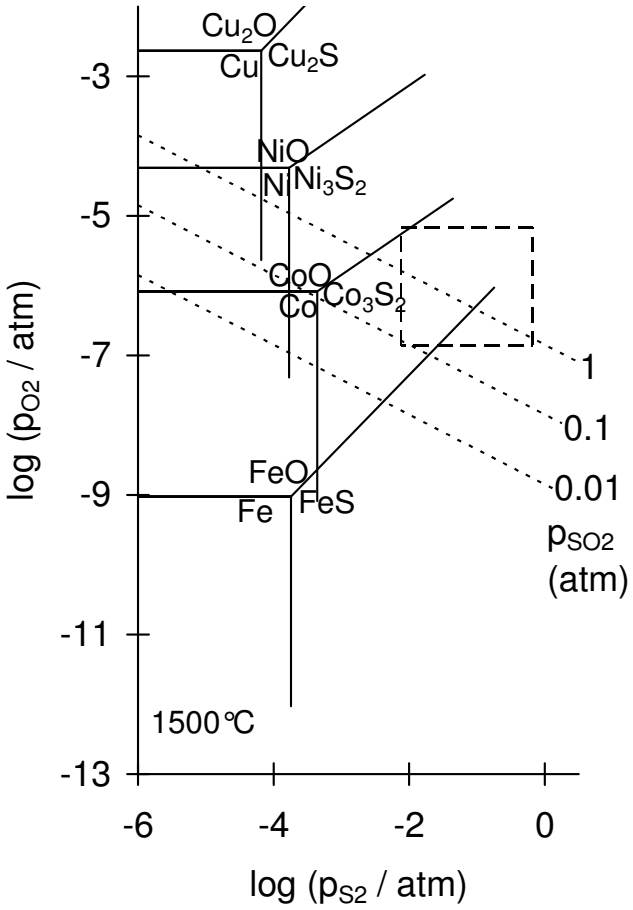

Figure 1: Yazawa diagram for liquid species at 1500℃. Calculated using data from FactSage.

Losses of base metals to slag during smelting are caused both by matte entrainment and chemical dissolution (oxidic and sulphidic). For example, MARUYAMA and co-workers (2003) produced the diagram shown in Figure 2 relating chemical copper losses of these kinds to matte grade, after a study of copper losses during flash smelting.

3.2 BASE METAL DISSOLUTION IN SLAG

Base metals may be present in solid solution, or chemically bound, in slag. These are described as *dissolved* base metals, and in the slags of this study can account for more than 50 % of the total base metal content.

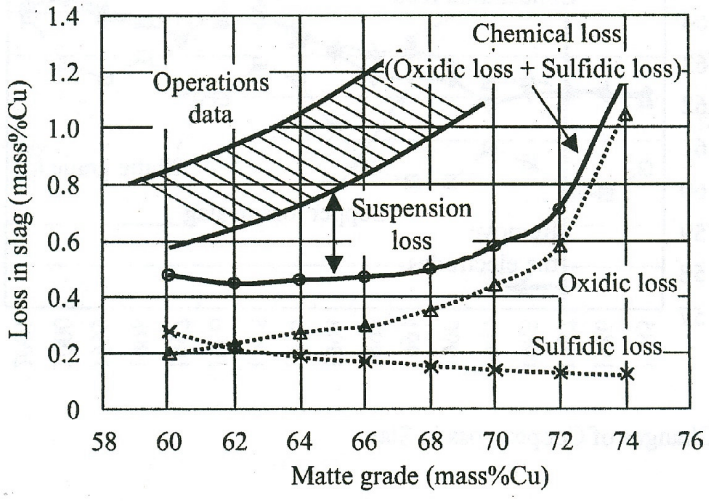

Figure 2: Diagram showing the different typed of copper losses to slag incurred during flash smelting (after Maruyama et al., 2003).

3.2.1 Species involved

Base metal dissolution in the slag types of this study is now known to be predominantly oxidic. Earlier work on copper smelting slags put much more emphasis on sulphidic dissolution (YAZAWA *et al.,* 1983, SHIMPO *et al.,* 1986, NAGAMORI, 1974) but this has been questioned more recently by GASKELL and co-workers (1990), and SRIDHAR and co-workers (1997), as will be described in this section.

The concept of oxidic and sulphidic dissolution of copper in slag was developed by Sehnalek and Imris, and independently by Nagamori (MACKAY, 1982). The total dissolved copper in the slag was thought to be the sum of the oxidic and sulphidic dissolutions.

Five different types of dissolution were described in fayalitic slags (NAGAMORI & MACKEY, 1978, MACKEY, 1982). These, and the elements involved were oxidic (Pb, Zn, Ni, Co, Sn, Cu, In), sulphidic (Cu, Pb, Ni, Co), monoatomic (Bi, Sb, As, Se, Te, Au, Ag), molecular (S, Se, Te) and halidic (Au, Ag, Pt, Cu).

NAGAMORI (1974), NAGAMORI & MACKEY (1978) and TAKEDA (2003) provide data and equations which allow the calculation of oxidic dissolution of copper and nickel in slag. The 'ionic concept of slag' was observed, where molecular species are chosen as $FeO_{1.5}$ rather than Fe_2O_3, $CuO_{0.5}$ not Cu_2O, $AlO_{1.5}$ not Al_2O_3, *etc*. This is in contrast to earlier investigators who assumed that copper in electric furnace slag dissolves as Cu_2O (BARNETT & JEFFES, 1977). The predominant nickel oxide species present in slag is NiO (BARNETT & JEFFES, 1977, SAHOO & REDDY, 1984, HENAO, *et al.,* 2002).

The reactions which take place during oxidic base metal dissolution in slag are –

$$Ni(l) + 0.5O_2(g) = NiO(l)$$ [(l) = liquid state and (g) = gaseous state]

and

$$Co(l) + 0.5O_2(g) = CoO(l)$$ (SAHOO and REDDY, 1984, HOLZHEID *et al.*, 1997)

and

$$Cu(l) + 0.25O_2(g) = CuO_{0.5}(l)$$ (TAKEDA, 2003)

So, for Ni (and Co) –

$$K_1 = a_{NiO} / a_{Ni} \cdot p_{O2}^{0.5}$$

where K_1 is the equilibrium constant

a_{NiO} is the activity of NiO in the slag

a_{Ni} is the activity of Ni in the matte or metal

and pO_2 is the partial pressure of oxygen.

and for Cu –

$$K_2 = a_{CuO(0.5)} / a_{Cu} \cdot p_{O2}^{0.25}$$

where K_2 is another equilibrium constant

$a_{CuO(0.5)}$ is the activity of $CuO_{0.5}$ in the slag

a_{Cu} is the activity of Cu in the matte or metal

and pO_2 is the partial pressure of oxygen.

K_1 and K_2 can be calculated using ΔG^0 and temperature, or obtained from data tables, and, since

activity (a) = activity coefficient (γ) x mole fraction (M),

This allows the activity coefficients for dissolution/oxidation to be calculated, and hence the base metal dissolution.

Calculation of base metal partitioning for matte-slag equilibrium –

$$Ni(l)_m + FeO(l)_s = Fe(l)_m + NiO(l)_s \quad [m = matte, s = slag]$$

and

$$Co(l)_m + FeO(l)_s = Fe(l)_m + CoO(l)_s$$

(AMMANN *et al.*, 1979, JONES & PARKER, 2001) and, presumably, for copper –

$$Cu(l)_m + 0.5FeO(l)_s = 0.5Fe(l)_m + CuO_{0.5}$$

So, for Ni (and Co) –

$$K_3 = (a_{Fe})_m(a_{NiO})_s / (a_{Ni})_m(a_{FeO})_s$$

where K_3 is the equilibrium constant

$(a_{Fe})_m$ is the activity of Fe in the matte

$(a_{NiO})_s$ is the activity of NiO in the slag

$(a_{Ni})_m$ is the activity of Ni in the matte

$(a_{FeO})_s$ is the activity of FeO in the slag

and for Cu –

$$K_4 = (a_{Fe})_m^{0.5}(a_{CuO(0.5)})_s / (a_{Cu})_m(a_{FeO})_s^{0.5}$$

where K_4 is another equilibrium constant

$a_{CuO(0.5)}$ is the activity of $CuO_{0.5}$ in the slag

a_{Cu} is the activity of Cu in the matte or metal

and pO_2 is the partial pressure of oxygen.

Again, the equilibrium constants (K_3 and K_4) can be calculated from standard data tables.

Sulphidic species in slag were initially thought to be Ni_3S_2 and Cu_2S (BARNETT & JEFFES, 1977), but were later identified as $CuS_{0.5}$ and $NiS_{0.67}$ (FONT *et al.,* 1998b, 1999). (When alloy is in equilibrium with slag some nickel is present as Ni (SAHOO & REDDY, 1984)).

Laboratory experiments were run to measure sulphidic dissolution as part of an investigation of copper dissolution in fayalitic slags (NAGAMORI, 1974). Three types of sulphidic copper dissolution in slag were then postulated, depending on whether the species present were Cu_2S, $CuS_{0.5}$ or Cu. MACKEY (1982) commented that splitting the sulphidic and oxidic dissolutions into different types is not really important – it was aimed at application in operating copper smelters.

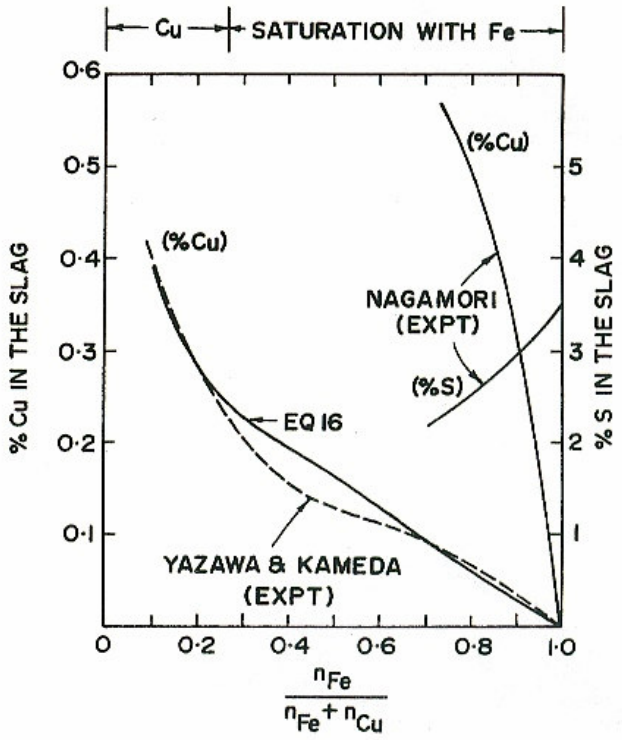

Figure 3: The solubilities of copper and sulphur in slags (after Gaskell et al., 1990). The data plotted was taken from Nagamori (1974), and from Yazawa and Kameda (1954).

The findings of Nagamori, Mackey, and earlier authors have been questioned by GASKELL and co-workers (1990) who state that "Nagamori's mathematical models for sulphidic dissolution have no basis in thermodynamics". These authors also point out that copper dissolution as a sulphide is disproved by the results, which show the copper content of the slag to increase and the sulphur content of the slag to decrease (Figure 3).

Data from forty-two copper smelting plants, including reverberatory, blast and flash furnaces, were compiled by SRIDHAR and co-workers (1997). The authors found that there is no need to invoke sulphidic copper dissolution to explain the copper losses to industrial slag – these can be adequately described by the oxygen potential and the entrained sulphide content of the slag. Their conclusions that dissolution is predominantly oxidic are reinforced by the FactSage calculations on the slags of this study described below.

While the Yazawa diagram (Figure 1) gives a first indication of whether specific elements can be expected to partition to the matte or slag phases in Anglo Platinum furnace slags, it gives no information on the form in which elements report to the slag phase. That is, no information is given on whether the base metals dissolved in the slag are best described as oxidic or sulphidic species.

An indication of the prevalence of oxidic and sulphidic species in such slags is given by the FactSage equilibrium calculation, the basis of which was described by PELTON and co-workers (1993) – only a brief summary is given here. Sulphur is assumed to enter the slag as sulphide ions; the sulphide capacity of the slag depends on the concentration of basic oxides (including alkali earth oxides such as MgO and CaO, and also transition metal oxides such as FeO, NiO, CoO and $CuO_{0.5}$) in the slag. The sulphide capacity of a multicomponent slag is found from the weighed average of the logarithm of the sulphide capacity, for all the basic oxides. The amount of sulphur dissolved in the slag depends on the sulphide capacity and on the partial pressures of S_2 and O_2 – the ratio of the concentration of sulphidic species to basic oxidic species in the slag is then proportional to the ratio $(p_{S_2}/p_{O_2})^{0.5}$. In the FactSage implementation of this model, it is assumed that the ratio X_{MS}/X_{MO} is the same for all basic oxides, where X_{MS} is the mole fraction of the sulphidic species MS in the slag, and X_{MO} is the mole fraction of the oxidic species MO (of the same cation M^{n+}) in the slag.

As an example of this calculation for a typical electric furnace slag, Figure 4 shows the ratio X_{MS}/X_{MO} for a slag with the base composition (mass percentages) 21.3% MgO, 13.1% FeO, 50.5% SiO_2, 9.1% CaO and 5.4% Al_2O_3 (this corresponds to the 2005 average Waterval furnace slag composition, as used elsewhere in this dissertation), for 1500°C. Amounts of 0.1% of each of NiO, CoO and Cu_2O were also added to the slag for the purpose of the calculation. Equilibrium with gas atmospheres with various ratios of $(p_{S_2}/p_{O_2})^{0.5}$ was calculated with FactSage, up to a maximum of $(p_{S_2}/p_{O_2})^{0.5} = 2200$, which corresponds to the lower right hand corner of the rectangle of possible process conditions, in the Yazawa diagram (Figure 1). As Figure 4 indicates, the reported ratio of sulphidic to oxidic species is the same for all of the cations (only Ni^{2+}, Cu^{+} and Co^{2+} are shown, but it will be the same for Fe^{2+}, Mg^{2+}, and Ca^{2+}) – as expected from the basic assumptions of the FactSage calculation. This does not imply that the relative associations of specific cations with sulphide anions and oxygen anions in the slag are identical, but rather that this model does not distinguish this. It is clear, however, that the prevalence of sulphidic species is small, being less than 1% of the oxidic species even at the highest sulphur content of the slag. The implication is that, when dissolution of the base metals in slag of this kind is to be predicted, information on the activity coefficients of the base metal oxides (not sulphides) is required.

The dominance of oxidic base metals in the slag samples of this study as modelled by FactSage was confirmed by experimental data.

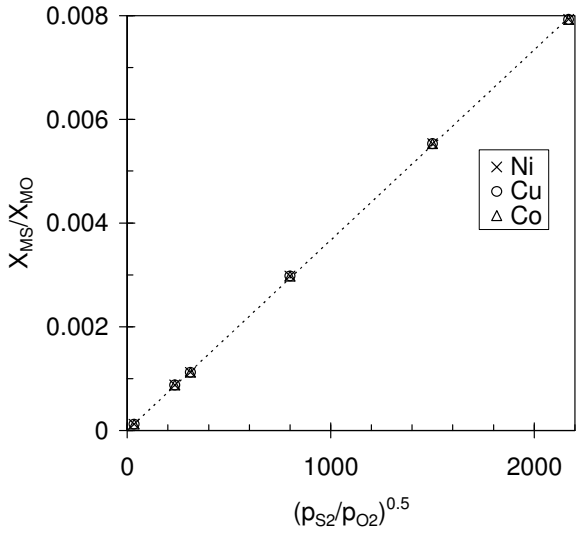

Figure 4: Calculated ratio of sulphidic to oxidic species of basic cations, as expected for the entire range of six-in-line electric furnace conditions (for a temperature of 1500°C).

It should be mentioned that not everyone is convinced that oxidic (or sulphidic) dissolution of base metals in slag occurs, or that the molecular species model is correct. DAVEY & WILLIS (1985) claim that these ideas are in conflict with the ionic nature of slag, and that it is impossible for oxide and sulphide copper to be distinguished if copper is present in ionic form. Dissolution over the slag/matte or metal interface is controlled by the activity of metals in matte and slag, composition, and oxygen potential of the slag, as well as the temperature. The base metals are present in slag as Ni^{2+} and Cu^{+} (RAJAMANI & NALDRETT, 1978, BARNETT, 1979), and these cross the matte/slag interface when M forms M^{+} or M^{2+} in the slag. According to ERIC and coworkers (1994), however, chemical (or electrochemical) losses to slag involve the dissolution of base metals in slag as Ni^{2+} and Cu^{2+}.

It is now generally accepted that slags are composed of charged ions – liquid silicates are polyionic melts with the silicate ions forming an array with cations and oxygen anions (O^{2-}) (MILLS, 1995). In most copper smelting slags, cations are dilute and widely dispersed. Theory requires that molecular species should be expressed as FeO, $FeO_{1.5}$, NiO, $CuO_{0.5}$, etc, – species such as Fe_2O_3 or Cu_2O can only be considered when they are a principal constituent of the slag (>30-50%). Although the base metals are known to be ionic in character in slags, the activity of ions cannot be determined experimentally (MACKEY, 1982). Thus slag basicity is expressed using molecular species, and activities and activity coefficients are described for oxides, sulphides or metals.

3.2.2 Physical and compositional factors affecting base metal dissolution in slag

The dissolution of base metals in slag is controlled by a number of physical and compositional factors. Although there is sometimes consensus among authors about the effects of such factors, there are often differences in opinion. These arise because many smelting systems are complex, and loss control factors that are important, for example, in copper converting, may not always be so relevant in pyrometallurgical slag cleaning of nickel. This is the reason that modelling programs such as FactSage are frequently used to predict the losses that will apply to a specified process.

The major factors affecting base metal dissolution in slag are described below, and are summarised in Table 1 on Page 12.

3.2.2.1 The effect of pO_2 on base metal dissolution in slag

Most authors agree that increasing the oxygen partial pressure (pO_2) in the slag of a slag-matte system increases the dissolution of the base metals (RUDDLE *et al.,* 1966, WANG *et al.,* 1974, BARNETT, 1979, FLOYD & MACKEY, 1981, SAHOO & REDDY, 1984, PAGADOR *et al.,* 1996, 1999, SIMEONOV *et al.,* 1996, CHOI & CHO 1997, LI & TSUKIHASHI, 2001.

It is also reported (WANG *et al.,* 1974), in line with the relationships described on Page 5, that nickel and cobalt dissolution in slag increases linearly with the square root of the oxygen partial pressure ($pO_2^{0.5}$), and that, at low pO_2, nickel solubility in slag is lower than that of copper (PAGADOR *et al.,* 1999). This trend is reversed at higher values of pO_2.

It appears that, when flash smelting or highly oxidising conditions are present, the effect of oxygen enrichment on dissolution in slag may be negligible (TAN & NEUSCHUTZ, 2001). High pO_2 in a converter slag will increase the amount of magnetite (Fe_3O_4) that forms. This should increase the levels of base metals partitioning into the slag, but this may be partially due to entrapment of sulphide or matte phases.

3.2.2.2 The effect of temperature on base metal dissolution in slag

Although some authors write that increasing the temperature reduces base metal solubility in slag (WANG *et al.,* 1974, BARNETT, 1979, PAGADOR *et al.,* 1996, SIMEONOV *et al.,* 1996, CHOI & CHO 1997, LI & TSUKIHASHI, 2001), others claim that it has the reverse effect (NAGAMORI & MACKEY, 1978, PAGADOR *et al.,* 1999, TAN & NEUSCHUTZ, 2001). The latter case may apply only to high-grade systems.

The amount of magnetite that forms decreases with increasing temperature in flash smelting slags (TAN & NEUSCHUTZ, 2001), and therefore base metal losses to slag will decrease, but here the authors probably refer to entrained matte.

The solubility of cobalt in silicate melts shows little temperature dependence in the 1300 °C to 1600 °C range, but nickel solubilities increase significantly with increasing temperature and also increasing pressure (HOLZHEID *et al.,* 1997).

3.2.2.3 The effect of slag composition on base metal dissolution in slag

Again, authors differ in this area. Increasing the basicity, by adding MgO or CaO to the slag, increases the base metal dissolution (ERIC *et al.,* 1994, CHOI & CHO, 1997) and MgO is more effective at increasing solubility than CaO (ERIC *et al.,* 1994). In copper smelting and converting, however, this is not the case, and adding CaO and MgO does not affect copper dissolution in the slag (RUDDLE, 1966, SIMEONOV *et al.,* 1996) or even reduces dissolution (NAGAMORI, 1974, MACKEY, 1982, SHIMPO *et al.,* 1986, PAGADOR *et al.,* 1996, 1999, KIM & SOHN, 1998, TAKEDA 1997, 2000, CHEN *et al.,* 2004).

The amount of cobalt dissolving in silicate slag decreases with increasing CaO addition (FONTANA *et al.,* 1989, CHEN *et al.,* 2004).

Adding silica to the slag decreases base metal dissolution (BARNETT, 1979, ERIC *et al.,* 1994, TAKEDA, 2000, TSEMEKHMAN *et al.,* 2003). Alumina addition also has this effect (NAGAMORI, 1974, MACKEY, 1982, SHIMPO *et al.,* 1986, KIM & SOHN, 1998). RUDDLE (1966), however, reports that alumina had no obvious effect on base metal solubility.

As mentioned earlier, sulphur can attract nickel, cobalt and particularly copper into the slag because these elements form stable sulphides (MACKEY, 1982).

The sulphur exchange between the slag and gas phases can be represented by –

$$1/2S_2 + (O^{2-})_{slag} = 1/2O_2 + (S^{2-})_{slag}$$ (GAYE & LEHMANN, 1995).

The sulphide capacity of a slag can be expressed as –

$$C_s = S \text{ mass } \% \times (pO_2/pS_2)^{0.5}$$

Sulphur, particularly in smelter slags, is predominantly present as sulphide (REDDY, 2003, DU TOIT *et al.,* 2005). According to GAYE & LEHMANN (1995) sulphur is present as sulphide in slag with $pO_2 < 10^{-6}$ atm.

The sulphide capacity, and therefore base metal dissolution, is affected by the levels of slag SiO_2 and CaO. (REDDY, 2003). MACKEY (1982) claims that adding CaO, MgO or Al_2O_3 will decrease sulphur solubility. Sulphide capacity of PGM smelting slags increases with increasing iron oxide content at a given temperature (DU TOIT *et al.,* 2005).

The effect of adding a reducing agent, such as carbon, to slag is to lower the oxygen potential and reduce the metal solubility in slag (BARNETT & JEFFES, 1977). When carbon is added to a furnace, reducing conditions are imposed, and base metal dissolution in slag decreases (JONES *et al*., 1996). This does not happen in Anglo Platinum matte smelting (six-in-line furnaces), because carbon is not added, but it is observed in the slag cleaning furnace.

Finally, the presence of phosphorus in slag encourages base metals to partition into silicate (HIRSCHMAN & GHIORSO, 1994).

3.2.2.4 The effect of matte composition on base metal dissolution in slag

Most authors describe an increase in nickel and copper dissolution in slag with an increase of those metals in the matte (MACKEY, 1982, SAHOO & REDDY, 1984, FONT 1998b, 1999, TAN & NEUSCHUTZ, 2001, TSEMEKHMAN *et al.,* 2003).

The solubility of nickel in slag increases with decreasing sulphur in the matte (HENAO *et al.,* 2002), and increasing the amount of iron in the matte decreases base metals in the slag (NAGAMORI 1974, JONES *et al*., 1996, FONT, 1998, 1999, TAN & NEUSCHUTZ, 2001, TSEMEKHMAN *et al.,* 2003). According to SIMEONOV and co-workers (1996), this occurs via increasing sulphur in the slag. In Mid-Oceanic Ridge basalts (PEACH, *et al.,* 1980), nickel, copper and cobalt in sulphide phases decrease with increasing FeS in sulphide (*i.e.* Ni, Cu and Co in silicate melt would decrease with increasing iron in matte).

HENAO and co-workers (2002) did not observe any increases in sulphur dissolution due to iron in the matte. In some cases, such as in high grade copper matte, there is no obvious dependence of copper dissolution on matte iron levels (TSEMEKHMAN *et al.,* 2003).

In nickel smelting, increasing nickel in matte increases partitioning of copper and cobalt into fayalitic slag (FONT *et al.,* 1998).

3.2.2.5 The effect of iron sulphide in the feed and/or matte

The reduction of base metals in slag by FeS present in feed concentrate or in matte is known as resulphidisation. For copper, this proceeds according to the equation –

$$Cu_2O + FeS = Cu_2S + FeO \quad \text{(BISWAS \& DAVENPORT, 1994).}$$

Iron sulphide is often added to slag treated in a slag cleaning furnace in place of coke to reduce copper into a low-grade matte (THEMELIS & KELLOGG, 1983), but the reduction of nickel oxide from slag requires stronger reducing conditions, as it is thermodynamically less favourable. It seems likely that the reducing effect of iron sulphide in the treatment of slags in this study is secondary to that of coke, but this will be discussed further in Chapter 8.

Table 1: Summary of the effect of physical and compositional parameters on base metal (BM) dissolution in slag.

Factor	*Effect on slag*	*Reference*
Increasing slag pO_2	Increases BM dissolution	Ruddle *et al.* (1966), Wang *et al.* (1974) Barnett (1979), Floyd & Mackey (1981) Sahoo & Reddy (1984), Pagador *et al.* (1996, 1999) Simeonov *et al.* (1996), Choi & Cho (1997) Li & Tsukihashi (2001)
Increasing slag temperature	Decreases BM dissolution	Wang *et al.* (1974), Barnett (1979) Pagador *et al.* (1996), Simeonov *et al.* (1996) Choi & Cho (1997), Li & Tsukihashi (2001)
Increasing slag temperature	Increases BM dissolution	Nagamori & Mackey (1978), Pagador *et al.* (1999) Tan & Neuschutz (2001)
Increasing MgO and CaO (Increasing slag basicity)	Increases BM dissolution	Eric *et al.* (1994), Choi & Cho (1997) Fontana *et al.* (1989)
Increasing MgO and CaO (Increasing slag basicity)	Decreases or does not affect BM dissolution	Ruddle *et al.* (1966), Simeonov *et al.* (1996) Nagamori (1974), Mackey (1982), Shimpo *et al.* (1986) Fontana *et al.* (1989), Pagador *et al.* (1996, 1999) Kim & Sohn (1998), Takeda (1997, 2000), Chen *et al.* (2004)
Increasing SiO_2 (Decreasing slag basicity)	Decreases BM dissolution	Barnett (1979), Eric *et al.* (1994), Takeda (2000) Tsemekhman *et al.* (2003)
Increasing Al_2O_3 (Decreasing slag basicity)	Increases BM dissolution	Sahoo & Reddy (2004)
Increasing Al_2O_3 (Decreasing slag basicity)	Decreases or does not affect BM dissolution	Ruddle *et al.* (1966), Nagamori (1974), Mackey (1982) Shimpo *et al.* (1986), Kim & Sohn (1998)
Increasing sulphur in slag	Increases BM dissolution	Mackey (1982), Davey & Willis (1985)
Increasing carbon in slag	Decreases BM dissolution	Barnett & Jeffes (1977), Jones (1996)
Increasing P in slag	Increases BM dissolution	Hirschman & Ghiorso (1994)
Increasing Na and K in slag	"Affects BM dissolution"	Rajamani & Naldrett (1978)
Increasing BM in matte	Increases BM dissolution	Mackey (1982), Sahoo & Reddy (2004), Font (1998, 1999) Tan & Neuschutz (2001), Tsemekhman *et al.* (2003)
Increasing iron in matte	Decreases or does not affect BM dissolution	Nagamori (1974b), Peach *et al.* (1980), Jones (1996) Font (1998b, 1999), Tan & Neuschutz (2001), Henao *et al.* (2002) Tsekhman *et al.* (2003)
Decreasing sulphur in matte	Increases BM dissolution	Henao *et al.* (2002)

3.2.3 Activities and activity coefficients

The activity (a) of an element in the phase of interest is defined as –

a = activity coefficient (γ) x mole fraction (M) of the element in that phase

Activity coefficients are often independent of pO_2 and temperature within the confines of the smelting reactions.

Factors affecting base metal activities in slag include the activity in the coexisting matte, the composition and therefore activities of other elements in the slag and matte, and the pO_2 and temperature of the system. These are described below, and tabulated in Table 2 on Page 14.

If the activity of the metal in the matte or metal increases, then the amount of that metal in the slag also increases (WANG *et al.,* 1974, BARNETT, 1979).

The relationships between the amount of base metals in slag and the oxide activities have also been documented (RUDDLE et al., 1966, ALTMAN & KELLOGG, 1972, NAGAMORI, 1974, WANG et al., 1974). Experiments varying pO_2 at fixed temperatures show that the amount of nickel and cobalt which dissolves in the slag increases with an increase of the activity of that metal. In the case of copper, the copper content of the slag varies linearly with $a_{CuO(0.5)}$. Similar relationships for the amount of metal in slag vs. $a_{CuO(0.5)}$ are described for various fayalitic slag types by MACKEY (1982). These are also linear.

The presence of Al_2O_3 in slag in equilibrium with alloy increases the solubility of nickel in slag (SAHOO & REDDY, 1984). The activity coefficient of NiO in a silicate melt is "likely to be" a function of Na, K, Al and possibly Ca. (WHITTAKER, 1967).

KATYAL & JEFFES (1989) calculated and tabulated the activity coefficients of CoO and $CuO_{0.5}$ in dilute solution in various silicate and ferrite slags as determined in the laboratory – between Cu-Co alloy and slag. These were found to depend on the slag composition, especially the Fe/Si ratio, the CaO content and the Fe^{3+}/Fe^{2+} ratio (this ratio is an indication of the pO_2).

FONTANA and co-workers (1989) described copper solubility under flash furnace converting conditions. The activity of copper oxide ($a_{CuO(0.5)}$) was found to increase with CaO addition to a maximum, but then remained constant or decreased slightly. The activity coefficient of NiO in slag is independent of pO_2 as is the distribution coefficient of nickel (SAHOO & REDDY, 1984) but this is defined as a "proportionality constant" –

A_{Ni} = % Ni^{2+} in slag/a_{Ni} in metal

In MgO-saturated Fe-Mg silicate slags, the activity coefficients of NiO and CoO increase with increase of these species in the slag (LI & TSUKIHASHI, 2001). The cobalt solubity in slag in contact with Co-Au-Fe alloys increased with both increased pO_2 and increased cobalt activity, and the activity coefficient of CoO is constant and independent of CoO content *up to 10%* in silica-saturated iron silicate slag (GRIMSEY & LUI, 1995).

TEAGUE and co-workers (2001) ran a thermodynamic study on cobalt-containing calcium ferrite and iron silicate slags (but silica was only maximum 4% in these slags). Results showed that the partial substitution of CaO by SiO_2 increased the activities of CoO and Fe_2O_3. In addition, measured activities of CoO and FeO showed positive deviation from ideal, and that of Fe_2O_3 negative deviation. CHEN and co-workers (2004) reviewed the thermodynamic modelling of CoO in iron silicate-based slags and calcium ferrite-based slags.

These authors emphasized that numerous studies have used alloy-slag-gas equilibrium experiments to measure the cobalt activity coefficient, but it is difficult to find appropriate container material that will not detract from the experiment. Dissolution of cobalt is lower in calcium ferrite slag than in iron silicate slag, which explains the recent interest in calcium ferrite slag development. The effect is confined to converting, and high (base metal) grade mattes, however, and not really practical for lower grade smelting. This is due to phase separation problems and the silica content of the smelting feed which inhibits calcium ferrite fusion at smelting temperatures (FONT *et al.,* 2000).

When experimental cobalt activities and distributions are compared to those predicted by MPE (the CSIRO's Multi-Phase Equilibrium modelling programme), there appears to be good agreement in the 'low CoO concentration region' for calcium ferrite, flash smelting and converting slags (CHEN *et al.,* 2004).

HOLZHEID and co-workers (1997) described the activities of NiO, CoO and FeO in silicate melts. These are independent of oxygen fugacity and of temperature (within a 1300 °C to 1600 °C range). Earlier reports on temperature-dependent NiO activity coefficients arose from assuming the solid standard state for NiO in the melt. Using the liquid standard state causes the temperature dependence to disappear. Activity coefficients are not affected by variation of FeO in the melt (from 0 to 12 %) and of MgO (from 4 to 30%) apart from a small increase in γ_{CoO} and γ_{FeO} at MgO contents above 20 %.

COLSON and co-workers (2005) investigated the activities of NiO, FeO and O^{2-} in silicate melts. The activities of NiO and FeO were measured in a variety of CaO-MgO-Al_2O_3 silicate melts using electrochemical methods. The activity of the oxide ion is reported for one composition.

The activity coefficients calculated by the various authors are shown in Table 2.

Table 2: Activity coefficients in the literature. Copper coefficients in blue are reported as $CuO_{0.5}$.

Reference		*Activity coefficients*				
	Reference State	NiO	Cu_2O	CoO	FeO	Slag type
Ruddle *et al.,* 1966	?		0.3-4.2			Iron silicate slag 35-45% SiO_2
Nagamori, 1974	?	0.55-3.04				Cu converting slag
Altman *et al.,* 1976	?		3.6			Reverberatory slag
Sahoo & Reddy, 1984	?	1.59				Al_2O_3 -saturated Fe silicate slag
Fontana *et al.,* 1989	?		6.0-22.0		0.25-0.70	Iron silicate slag
Katyal & Jeffes, 1989	liquid		1.70-8.74	0.62-2.33	0.43-1.87	25-41% SiO_2
Katyal & Jeffes, 1989	liquid		1.72-2.77	0.96-1.22	0.57-0.93	calcium ferrite
Grimsey & Lui, 1995	solid			0.91+/-0.09		Silica saturated 36-42% SiO_2
Lui & Grimsey, 1997	solid			1.7-0.021(wt% SiO_2)		Silica unsaturated
Holzeid *et al.,* 1997	liquid	2.70+/-0.52		1.51+/-0.28	1.70+/-0.22	SiO_2 49-51%
Teague *et al.,* 2001	solid ?			2.0-2.6	1.2-1.4	Ca-Fe silicate, 0-4% SiO_2
Li & Tsukihashi, 2001	solid	1.5-4.4			1.0-4.0	Mg-saturated Fe silicate slags
Colson *et al.*, 2005	liquid	1.59-4.96			0.42-1.02	SiO_2 46-56%

3.2.4 Distribution and partition coefficients, and factors affecting these

In the literature reviewed –

The distribution coefficient (L) = mass % in matte / mass % in slag,

but occasionally these are expressed as the inverse, as is the case with the experimental data in this thesis.

In certain geological references, the distribution coefficient is designated by D or K_D.

The Nernst partition coefficient (also D or K_D) = mass fraction in sulphide / mass fraction in glass or silicate or melt.

Most distribution coefficient references in the literature are related to the metallurgy of flash furnace operation, whereas partition coefficients are preferred in geological and mineralogical references.

$L_{m/s}$ of cobalt and iron in the INCO flash furnace falls with increase of matte grade (SOLAR *et al.* 1978, quoted in MACKEY, 1982). $L_{m/s}$, however, seems unaffected between 25 and 45 % Cu+Ni in the matte. $L_{m/s}$ decreases with increase in matte grade for nickel and cobalt during nickel smelting in an Outokumpu flash furnace (HÄRKKI & JUUSELA, 1974, quoted by MACKEY, 1982). TASKINEN and co-workers (2001), however, examined oxygen pressure effects in the Outokumpu flash smelting furnaces and showed that the distribution coefficients for iron, nickel and cobalt increase with increase of iron in matte. Where distribution or partitioning is only considered between matte/sulphide and silicate melts, the relationships are the same as those in Table 1 (Base metal dissolution in slag).

Information on the effect of magnetite on nickel, cobalt and copper partitioning between matte and slag is also provided by MACKEY (1982). Increasing magnetite in slag increases the distribution of nickel, copper and cobalt, probably because increasing magnetite levels are a sign of higher slag pO_2.

The distribution or partitioning of nickel between silicate and sulphide melts and crystallising phases (predominantly olivine) is dealt with in a number of geological references, as outlined below.

The relationships of nickel and copper in the silicate and sulphide melt described by RAJAMANI & NALDRETT (1978) are analogous to base metal dissolution in slag and matte as mentioned earlier. In essence, the geological and metallurgical relationships are exactly the same, but expressed differently.

As far as sulphide-silicate melts partitioning is concerned, HOLZHEID & PALME (1996) describe the influence of FeO on the solubilities of cobalt and nickel in silicate melts as a background for metal/silicate partitioning between the Earth's core and mantle. (Such studies provide "important constraints for models of accretion and core formation of the earth and various other differentiated bodies"). The low Co:Ni fractionation in the earth's mantle is strange, considering the large differences in metal/silicate partition coefficients.

"Large and intricate" variations in metal-silicate partition coefficients (D) are observed for many elements – including nickel and cobalt (JANA & WALKER, 1997). MACLEAN and SIMAZAKI (1976) investigated the partitioning of Co, Ni, Cu and Zn between sulfide and silicate liquids. Partitioning coefficients were determined for Fe (1.2), Co (7), Ni (150), Cu (50) and Zn (0.5) in iron sulphide/iron silicate liquids at 1150 °C and 1 bar (≅ 1 atm), i.e., partitioning between sulphide and silicate to be in the order Ni>Cu>Co>Fe>Zn. This is the same order as that found between silicate melts and crystals.

The two current methods of modelling partition coefficients assume that partitioning is "crystal controlled" or "melt controlled". Since both work reasonably well, the implication is that there are significant correlations between element behaviour in both environments (COLSON *et al.,* 2005). The two models are the octahedral site preference energy (OSPE) of an element, and the crystal field stabilisation energy (CFSE) of the bonds it

can form, in solid and melt phases. Both theories apply mainly to transition element behaviour, and are therefore of relevance to this study.

The transition metals enter both octahedral (Oh) and tetrahedral (Th) sites in silicate melts, and the proportion of available Th sites increases with increasing alkalis (sodium and potassium) and silica (RAJAMANI & NALDRETT, 1978). Ni^{2+} has the maximum OSPE and shows a strong preference for Oh sites in silicates and liquids. Little is known about the structure of sulphide liquids, however, although they are thought to contain some oxygen when in equilibrium with silicate melts (in natural systems). In monosulphide solid solution (mss – "crystalline sulphide"), cations are surrounded by six sulphur atoms in the form of a trigonal prism, so this kind of coordination could also dominate in sulphide liquid (with predominant iron). Whereas the site infilling of mineral octahedral and liquid tetrahedral sites is governed by the stabilization energy difference between such sites, the effect in sulphide/silicate liquid partitioning is that of the higher stabilization energy of Metal-S π bonds as compared to Metal-O ionic bonds (MACLEAN and SIMAZAKI, 1976).

Nickel would prefer sulphide liquid the most when there are few Oh sites in the silicate melt (low basicity). High spin Co^{2+} and Fe^{3+} form only two π bonds with sulphur as distinct from nickel which forms three (RAJAMANI & NALDRETT, 1978). These species also have lower Oh site preferences, so they are less sulphophile than Ni^{2+}. Cu^{+} has zero Oh preference but it does become increasingly sulphophile with increasing basicity of silicate melt. This agrees with the views of the majority of authors on the effects of increasing basicity on base metal dissolution in slag.

The partitioning of elements between silicate melt and crystallizing olivine is dealt with quite extensively in the literature (DRAKE & HOLLOWAY, 1981, BEATTIE, 1994, HAKLI & WRIGHT, 1967, LEEMAN & LINDSTROM, 1978, MYSEN, 1979, 1982, HIRSCHMANN & GHIORSO, 1994). Although relevant to slow cooling or slag casting studies, such literature is not of primary importance to this study, except perhaps in the case of residual olivine equilibria in the slag bath, as recorded in the sounding bar samples. Some aspects of this field are discussed briefly below, as they provide insight into the effect of ionic radius on the partition coefficient.

Olivines are "structurally simple" (BEATTIE, 1994), and are ideal for the study of factors controlling the partition coefficients of the elements. Experiments were run at temperatures and oxygen fugacity corresponding to rock forming processes. The melt composition was quite variable, but predominantly Mg-Fe-Al-Ca-silicates corresponding to various rock types. For all these conditions, the partition coefficients did not vary enormously, and partition coefficients for elements of a given valency varied smoothly with ionic radius, although separate trends existed for 2^{+} and 3^{+} valencies. The partition coefficients for orthopyroxene-, clinopyroxene-, plagioclase-, biotite- and hornblende-melt pairs are also monotonic functions of ionic radius. This suggests that mineral/melt partitioning occurs by substitution into crystallographic sites and that partitioning of trivalent cations is charge balanced by a coupled Al for Si substitution. Ni^{2+} substitutes for Mg^{2+} and Ca^{2+} on melt sites (and probably with other divalent cations). It mixes less with Al^{3+} (COLSON *et al.,* 2005).

The difference between the NiO and CoO activity coefficients in silicate liquids is responsible for the preferred Ni partitioning into olivine (HOLZHEID et al., 1997). Distribution coefficients were calculated for olivine-melt pairs, and these are slightly temperature-dependent. The partitioning effect is not due to the preferred acceptance of nickel into the olivine structure, but the stronger rejection of nickel as compared to cobalt from the melt. Olivine fractionation depletes magma in nickel and enriches it in copper (MACLEAN and SIMAZAKI, 1976).

Although much information is available on sulphide-silicate melt, silicate mineral-melt and silicate glass-melt, literature on oxide-silicate melt is difficult to find. This would be of relevance to six-in-line and particularly slag cleaning furnace slags as spinel is frequently crystalline at smelting temperatures. TEAGUE and co-workers (2001) mention the preferential partitioning of cobalt into magnetite, where the concentration of cobalt was found to be two to three times that in the melt. This also seems to be the case in the six-in-line spinel phases of this study, but in the SCF the effect is less obvious. It is possible to model the distribution of cations into tetrahedral and octahedral sites in spinel using FactSage (DECTEROV *et al.,* 2004).

A reasonable amount of study has gone into silicate melt/glass partitioning, especially since lunar geoscience was established (many of the rocks on the Moon are glassy, as distinct to those on Earth, where glass is confined to a few volcanic deposits).

KEPPLER (1992) measured the crystal field spectra and studied the geochemistry of transition metal ions in silicate melts and glasses. The crystal field spectra of various cations, including Fe^{2+}, Ni^{2+}, Co^{2+} and Cu^{2+}, were measured after doping these elements into diopside-albite melts. The melts were quenched to room temperature and examined. Sites in the quenched glass holding the Fe^{2+}, Ni^{2+}, and Cu^{2+} cations were strongly distorted from ideal octahedral geometry – Co^{2+} occupied a distorted tetrahedron – because of its small ionic radius and low Oh site preference. The fact that Co^{2+} occupies Th sites does not imply that it is a network former. Co^{2+} complexes to non-bridging oxygen atoms in the melt.

Crystal/melt partitioning behaviour is due to the difference between the CFSE in the melt and in the crystal. "Earlier theories" assumed transition metal partitioning behaviour was controlled by octahedral site preference energies, but this disagrees with spectroscopic evidence. The more polymerised the melt, the more likely are transition metal ions to partition preferentially into crystalline phases, and if two immiscible melts are in equilibrium, the less polymerised melt will contain the higher concentrations of these elements. The structure of a silicate glass corresponds to the structure of the liquid at the glass transformation temperature - here 800 to 1100 °C (this depends on composition and quench rate). Although nickel speciation changes had been reported previously in potassium borate melts (LIN & ANGEL, 1984, quoted in KEPPLER, 1992), in silicate melts of "natural composition" nickel speciation seems to be independent of temperature. The data for iron and nickel suggest that glasses are a good model for their behaviour in melts – obviously this has implications for any study of granulated slag.

CFSE cannot quantitatively explain the high γ_{NiO} in melts compared to that of CoO and FeO (HOLZHEID *et al.,* 1997). This may be due to the high degree of preference of nickel for crystal octahedral sites, rather than for the tetrahedral sites present in high temperature melts. In the solid oxide, nickel is present in octahedral coordination, and even in quenched glasses most of the divalent cations (apart from cobalt) are in

octahedral/distorted octahedral/5-fold coordination. In high temperature silicate liquids, nickel attains tetrahedral coordination. Additional contributions to the non-ideality of nickel partitioning may also come from the clustering tendency of nickel in silicate melts, picked up by high temperature X-ray studies. FARGES & BROWN (1996) used XAFS spectroscopy to establish the coordination environment of nickel in NiO, γ-Ni_2SiO_4 and Ni-bearing sodium disilicate glass and melt. Nickel coordination in sodium disilicate glasses and melts is mainly five-coordinated in the glass, and four-coordinated in the melt. Apparently this resembles observations of iron, magnesium and zinc in similar systems. NiO nucleation was recorded in the sodium disilicate glass, and it is suggested that nickel-rich domains form in the glass. Nickel is not randomly distributed within the glassy network (in contrast to network formers and modifiers) but is located in some nickel-rich domains of the glass.

BROWN and co-workers (1995) carried out X-ray scattering and spectroscopy studies on glass and melts. Four- and five-coordinated Ni(II) was found in a range of compositions of silicate glass using optical and EXAFS spectroscopies, and five-coordinated Ni ($^{[5]}$Ni) dominated in most, especially the sodic ones (GALOISY and CALAS, 1991, 1992, 1993, quoted in FARGES *et al.*, 1995). A mixture of 50:50 $^{[4]}$Ni and $^{[6]}$Ni would also result in an average coordination of 5, but this would be detected by XANES, and it is not. In silicate melts, however, four-coordinated Ni ($^{[4]}$Ni) was the dominant species. Ni(II) is dominantly four-coordinated in olivine composition melt, but dominantly tetrahedral and pentahedral in more silica-rich glasses. That the environments of nickel in high temperature liquids and quenched glasses may be different has a number of implications in the context of activities and element partitioning, and directly contradicts KEPPLER (1992). This may also affect the interpretation of the Mössbauer spectroscopy results in this study.

A summary of the suggested base metal coordination types is given in Table 3 (Page 19).

Lastly, mention should be made of the effects of *diffusion* in silicate melts (CHAKRABORTY, 1995). The chemical mixing of two liquids can only take place by diffusion – it limits the rate of chemical transformation on a local scale, and dominates transport processes when convection is suppressed. Melts with similar viscosity often (but not always) behave similarly with regard to diffusion. Depolymerized and polymerized melts behave differently in this respect, hence there are differences in diffusion behaviour between granitic and basaltic melts. This suggests that matte and entrained matte would take longer to equilibrate with high silica slag – because of high viscosity and poor convection. Diffusion coefficients vary with temperature, and would dictate transport in high viscosity melts, and in capillaries - thin films of melt around grains. Chemical diffusion between entrained matte droplets and slag in the samples of this study must have taken place for equilibrium to be attained.

Table 3: Base metal coordination.

Phase	*Type*	*Coordination*	*Geometry**	*Reference*
Sulphide melt	"Iron bearing"	Ni 6	Tp	Rajamani & Naldrett (1978)
Silicate melt		Ni 6>>4	Oh>>Th	Rajamani & Naldrett (1978)
		Ni 4	Th	Holzheid *et al.* (1997)
	Na disilicate glass	Ni 4	Th	Farges & Brown (1996)
		Ni 4>5	Th and ?Ph	Brown *et al.* (1995)
	Olivine composition	Ni 4	Th	Galoisy & Callas (1991–93)
Silicate glass		Ni 6	Distorted Oh	Keppler (1992)
		Cu 6	Distorted Oh	Keppler (1992)
		Co 4	Distorted Th	Keppler (1992)
		Ni 6 or 5	Distorted Oh, or Ph	Holzheid *et al.* (1997)
		Cu 6 or 5	Distorted Oh, or Ph	Holzheid *et al.* (1997)
	Na disilicate glass	Ni 5	Ph	Farges & Brown (1996)
	Sodic glass	Ni 5>4	Ph and Th	Galoisy & Callas (1991–93)
	"Silica rich glass"	Ni 4 and 5	Th and Ph	Galoisy & Callas (1991–93)
Silicate crystal		Ni 6>>4	Ni Oh>>Th	Rajamani & Naldrett (1978)
Oxide		Ni 6	Ni Oh	Holzheid *et al.* (1997)

*Geometry – Oh = octahedral, Th = tetrahedral, Tp = trigonal prism, Ph = pentahedral.

3.3 MECHANICAL ENTRAINMENT OF MATTE IN SLAG

The relative importance of losses due to entrained and dissolved base metals was already alluded to in Section 3.2, and shown for copper in Figure 2 (MARUYAMA *et al*. 2003).

Virtually all high grade copper smelting processes require slag treatment to recover losses, as base metal loss can be of roughly equal importance to dissolution (THEMELIS & KELLOG, 1983). Entrained matte can be responsible for 25 to 75 % of total copper losses to slag (MINTO & DAVENPORT, 1973). As pointed out by SRIDHAR and co-workers (1997), however, there is a large amount of literature dealing with chemical losses to slag, which gives rise to a large spread of data. This is because the amount of physically entrained matte is not usually measured, and cannot always be accurately calculated.

GBOR and co-workers (2000) examined base metal distribution in Canadian nickel and copper smelting slags. In all of them the form of cobalt was primarily as oxide, but up to 20% of nickel and copper were in entrained sulphides.

As far as the platinum smelting industry is concerned, variable proportions of entrained to dissolved base metals were recorded in Polokwane furnace slag over time (NELSON *et al.,* 2005). This is demonstrated by a correlation of base metal to sulphur contents in slag from bulk chemistry results. The greatest data group is in the dissolved base metal area (0.1–0.4 % sulphur) which indicates that these slags are usually relatively clean (low in entrained matte). The case for Waterval furnace slag is similar, although the earlier slag samples, produced in 1999, show a higher entrained base metal component than those produced in 2005.

It should be emphasized once again that literature on actual measurement of (rather than calculation of) entrained matte in any base metal containing slags is difficult to come across, and that the methods described are not always mineralogical – for example, Matousek refers to a method used by the International Nickel Company of Canada which involves chlorine-alcohol extraction to distinguish suspended sulphide levels from dissolved oxides (in MINTO & DAVENPORT, 1973).

3.3.1 Origin of entrained matte in slag

Physically entrapped matte droplets in furnace slag arise from –

1. Sulphide phases in the feed (ore concentrate)
2. Matte phases in returned converter slag
3. Fine dispersions of matte precipitated from the slag in regions of the furnace where large temperature gradients exist
4. Matte particles carried into slag by gas bubbles rising through the slag/matte interface.

(BARNETT & JEFFES, 1977, MINTO & DAVENPORT, 1972, BARNETT, 1979, IP & TOGURI 1992).The phases described in (1) may arise from "undigested furnace feed" (SNELGROVE & TAYLOR 1980).

LIOW and co-workers (2003) identify two important mechanisms for physical matte entrainment during flash smelting – the physical dispersion of matte in slag by mixing, and the rise of the lower matte level during tapping due to the shear stress between the slag and the matte, which draws matte upwards to the slag tap hole. Physical dispersion of matte in slag can occur through turbulence, gas injection (which floats matte up into slag), pouring of slag or matte into each other, and mixing of the slag/matte interface due to 'slopping'. During tapping, interfacial mixing is minimal because interfacial shear is small – most entrained matte comes about by the incorporation of the matte layer. For this reason furnace operation at Anglo Platinum does not allow slag tapping to less than 20 cm slag depth over the matte level.

MACKEY (1982) suggests that the method of concentrate injection may influence copper levels in reveberatory slags, and IP & TOGURI (2000) claim that particle size analysis shows that fine particles entrained into slag have equal, if not greater, value when compared to other size groups.

Entrained matte in the slag can be attached to magnetite or spinel particles – high magnetite content increases matte entrainment as does higher slag viscosity (ALTMAN *et al.,* 1976, IP & TOGURI, 1992, 2000, IMRIS, 2003). In fact, the presence of solid magnetite (from converter slag return) and/or chromium-bearing spinel (from high chromium feeds) can aggravate matte entrainment in slag considerably. This occurs both by flotation of matte attached to magnetite/spinel over the matte-slag boundary, and by the "capture" of settling matte phases by spinel layers in the lower slag bath.

The amount of entrained matte in slag is influenced by settling, flotation and coalescence opportunities, and these are described below.

3.3.2 Settling of entrained matte in a furnace

The settling of matte in a furnace is influenced by slag and matte properties (*e.g.,* composition, viscosity, density, interfacial tension) as well as stirring, the size of matte droplets and the depth of slag (FLOYD & MACKEY, 1981, FAGERLUND & JALKANEN, 1999). The settling rate of matte droplets is very much size dependent – fine matte can require very long settling times under quiescent bath conditions. Laboratory experiments confirm that the smallest droplets (<2µm) do not settle. The removal of the matte from the slag is complex and includes several simultaneous steps such as chemical reactions, mass transfer between droplet surface and slag, dissolving mechanisms, diffusivity, thermodynamic properties, and so on.

Small matte droplets in the slag may settle, according to POGGI and co-workers (1969) or may be trapped as 'rafts' of droplets floating on the top surface of the slag due to surface tension, or as droplets suspended below small gas bubbles, or as fine droplets which settle extremely slowly.

For coalescence and settling of matte droplets to occur in a furnace, there must be sufficient matte fall. In South African platinum melting, a matte fall of at least 15 % is required to assure good collection and recovery of PGMs (NELL, 2004). Matte levels in the slag cleaning furnace are boosted by the addition of ore concentrate, as the sulphur content of converter slag is insufficient.

Experimental work leading to the mathematical description of matte droplet settling is now described.

MARU and co-workers (1971) wrote about the behaviour of a rigid sphere falling through a liquid-liquid interface. A model was developed to predict the critical radius below which a sphere would not be able to pass through the interface. The behaviour of the column or tail of liquid pulled through the interface after the sphere was described, and photographed. The volume of the phase carried through was directly proportional to the sphere diameter and inversely proportional to the surface tension and viscosity of the liquid. In addition, break-up of the column occurred at a distance from the interface inversely proportional to the surface tension.

The behaviour of a settling droplet of matte in slag, however, is better described by a liquid-liquid model. According to FAGERLUND & JALKANEN (1999), the rate of settling (V_s) for a spherical matte droplet is predicted by –

Gravity = buoyancy + Stokes Law

$4/3\pi r^3.\rho_m.g = 4/3\pi r^3.\rho_s.g + 6\pi.\mu.r.V_s$

or $V_s = (2g.r^2.\Delta\rho)/9\mu$

Where g = gravitational constant (m/s^2)

r = droplet radius (m)

$\Delta\rho = \rho_{matte} - \rho_{slag}$ (density)

μ = viscosity of slag (Pa.s)

It should be noted, however, that larger matte drops, especially, would not actually be spherical. A drop of copper in slag obeys Stoke's Law only when the Reynolds Number of the drop is much less than unity – equivalent to a diameter of <0.5 mm.

The equation above is modified by NELSON and co-workers (2005) to include the Hadamard-Rybczynski formula which compensates for the recirculation that develops within the falling drop, but assumes laminar flow in the slag.

The derivation of the Hadamard-Rybczynski expression (as given in CLIFT *et al.,* 1978) applies to a rigid or fluid spherical particle, moving relative to a fluid of infinite extent, with a steady velocity. Interestingly, the theory predicts that the terminal velocity of a fluid sphere can be as much as 50 % higher than that of a rigid sphere of the same size and density. The expression can be written as –

$$U_T = 2.g.r^2.\Delta\rho/\mu(1+k/2+3k)$$

Where U_T = terminal velocity

μ = slag viscosity

k = viscosity ratio μ_p/μ (μ_p = droplet viscosity)

and, as $\mu >> \mu_p$, $U_T = g.r^2.\ \Delta\rho/3\mu$

This is 1.5 times the settling rate of a solid sphere with the same diameter.

3.3.3 Matte flotation in slag

Entrained matte droplets can be floated into or within the slag bath by attachment to gas bubbles. The gases involved are predominantly sulphur dioxide (SO_2) and carbon monoxide (CO).

It is likely that SO_2 flotation of matte into slag plays a major role in flash smelting or converting, but a only minor role in the type of smelting considered in this study. This gas is produced in the matte, by air or oxygen ingress during tapping. Where converter slag is returned to the furnaces, or where it forms part of the feed, as in the slag cleaning furnace, SO_2 can arise from the reaction of magnetite (Fe_3O_4) with the matte (IMRIS, 2003) –

$$3Fe_3O_{4(s)} + [FeS]_{matte} = 10(FeO)_{slag} + SO_{2(g)}$$

Flotation in melting and slag cleaning furnaces also occurs within the slag where gas rising in the slag attaches to falling sulphide particles from the concentrate. According to NELSON and co-workers (2005), CO is the major gas floating matte into slag, rather than SO_2. The CO is emitted from the carbon electrode tip, or by the reaction of coke in the slag cleaning furnace.

Early work on matte flotation in slag involved simulation and examination of matte particles floating on the slag surface (POGGI *et al.,* 1969, MARU *et al.,* 1971). Later work (FAGERLUND & JALKANEN, 2000, KAPTAY, 2001) included modelling the size and behaviour of liquid matte droplets at the slag/gas interface. This deals with matte flotation on the upper slag surface, and is unlikely to be of major importance in the six-in-line and slag cleaning furnaces studied here, as these are run with total or partial black top (feed cover). The subject has been well-studied because it is one of the easiest ways to measure the interfacial energies of immiscible liquids.

Metal or matte is carried across the matte/slag interface as a coating on rising bubbles (POGGI *et al.,* 1969). If the slag is of low viscosity, the bubbles shatter and inject matte into the slag. If it is of high viscosity, the matte is carried up in the bubble wake. Large bubbles break cleanly through the matte surface and the metal peels off in the slag. Smaller bubbles remain at the slag/matte interface as matte-coated domes which will only shatter if gas is injected from other bubbles.

The flotation behaviour of matte in slag depends on interfacial tension (matte-slag) and surface tension (slag-gas, matte-gas) according to MINTO & DAVENPORT (1972). Interactions between rising gas bubbles and matte droplets (as in Figure 5) were modelled. A droplet can form a film around the bubble or attach to the bubble or ignore the bubble. It all depends on the interfacial tension.

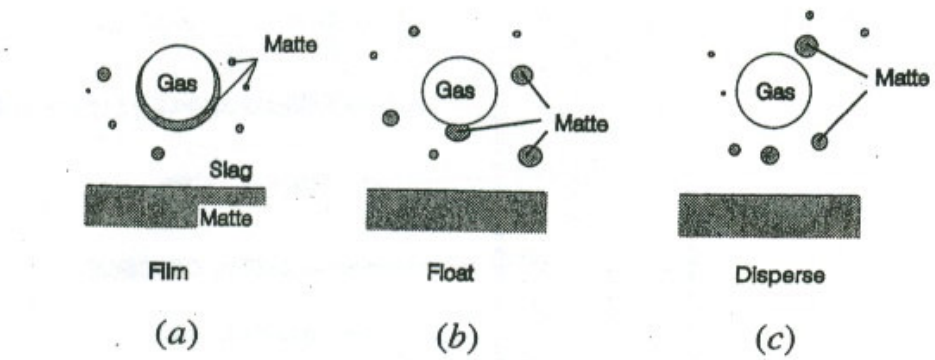

Figure 5: Interactions between a gas bubble and liquid droplets in a continuous phase; (a) droplet forms a film on the gas bubble, (b) droplet attaches to gas bubble upon contact, and (c) no attachment of droplet to bubble through contact. Minto & Davenport (1972) as shown in Ip & Toguri (1992).

Filming of droplets on gas bubbles (case (a)) will occur if the filming coefficient is greater than zero. The filming coefficient is defined as

$$\Phi = \gamma_{s/g} - \gamma_{m/g} - \gamma_{m/s}$$

where $\gamma_{s/g}$ = slag surface tension, $\gamma_{m/g}$ = matte surface tension and $\gamma_{m/s}$ = matte-slag interfacial tension. Flotation (case (b)) will occur if the flotation coefficient is greater than zero –

$$\Delta = \gamma_{s/g} - \gamma_{m/g} + \gamma_{m/s}$$

Case (c) (dispersion) will take place only if the flotation coefficient is less than zero.

Important deductions were as follows –

- Droplet flotation is favoured in *all* matte-slag systems
- Silica saturation inhibits film stability and reduces matte transport into slag
- Replacement of FeO by CaO in slag makes a film more stable, so increases matte transport into slag
- FeS in matte increases film stability
- Higher copper content of the matte leads to dispersion rather than flotation of matte droplets in slag, and Cu_2S in matte (*i.e.* high grade matte in copper smelting) decreases film stability
- The interfacial tension for copper metal is much higher than for Cu_2S – sulphur drastically reduces the interfacial tension of the system.
- Higher smelting temperature reduces film stability

IP & TOGURI (1992, 1993) investigated the surface and interfacial tension of the Cu-Fe-S, Ni-Fe-S, Ni-Cu-S and fayalite slag system and their effect on mechanical entrainment, refractory infiltration and electrocapillary motion of matte droplets in slag (the latter is important in DC electric furnaces). The authors used an X-ray radiographic technique, combined with the sessile drop method, for surface and interfacial tension measurement.

They concluded that –

- Interfacial tension between Ni-Fe-S matte and fayalite slag increases with increasing matte grade (nickel grade), therefore flotation would be favoured
- Sulphur has the greatest influence on the surface tension of Ni-Fe matte
- The iron content of the system has negligible impact on the surface tension of the matte at a constant Ni:S ratio
- The presence of MgO and Al_2O_3 in the slag does not affect the interfacial tension value.
- Interfacial tension between Ni-Fe-S mattes and fayalite slag show similar behaviour to surface tension data.
- The surface tension of Ni_3S_2 decreases linearly with increasing temperature, while FeS and Cu_2S show negligible temperature dependency. In all cases the surface tension is a linear function of temperature.
- In both the Cu-Fe and the Ni-Fe matte/slag systems, the interfacial tension decreases non-linearly with addition of FeS to the matte, and in all cases interfacial tension increases with increasing nickel or copper matte grade (Figures 6 and 7).

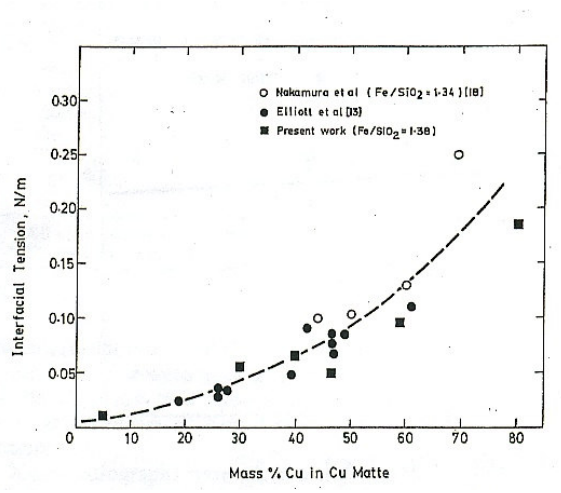

Figure 6: Interfacial tension of the matte-slag system at 1473 K (Ip & Toguri, 1992).

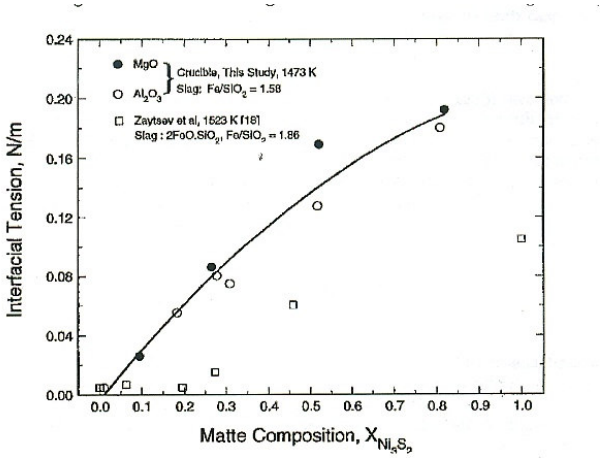

Figure 7: Interfacial tension between Ni-Fe matte and fayalite slag at 1473 K (Ip & Toguri, 1993).

An increase in either nickel or copper grade will slightly increase the flotation behaviour of entrained matte, and it is impossible to avoid entrainment loss due to bubble attachment in nickel and copper matte processing. Filming of matte on gas bubbles will only occur at lower matte grades – <7.5 mol % Ni_3S_2 and <32 % Cu.

IP & TOGURI (1992) and NELSON and co-workers (2005) also reproduce the equations derived to plot a ternary interfacial energy diagram, first developed by CONOCHIE & ROBERTSON (1979). The approach differs from that of MINTO & DAVENPORT (1972), and is based on the balance of surface and interfacial tension forces acting on a droplet resting on a fluid-fluid interface such as the one shown in Figure 8.

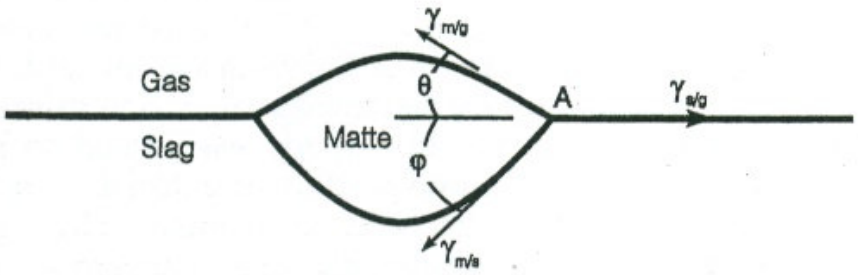

Figure 8: A diagram illustrating the droplet configuration used in Conochie and Robertson's formulation.

From such consideration, the following equations were obtained:

$$\gamma_{s/g} = \gamma_{m/g} \cos \theta + \gamma_{m/s} \cos \varphi$$

So

$$1 - X - Y = Y \cos \theta + X \cos \varphi$$

$$\gamma_{m/g} \sin \theta = \gamma_{m/s} \sin \varphi$$

And

$$Y \sin \theta = X \sin \varphi$$

When

$$X = \gamma_{m/s} / \Sigma\gamma$$

$$Y = \gamma_{m/g} / \Sigma\gamma$$

$$Z = \gamma_{s/g} / \Sigma\gamma$$

Where

$$\Sigma\gamma = \gamma_{s/g} + \gamma_{m/g} + \gamma_{m/s}$$

and

$$X + Y + Z = 1$$

Values for X, Y and Z may be plotted on a ternary diagram as shown in the example in Figure 9.

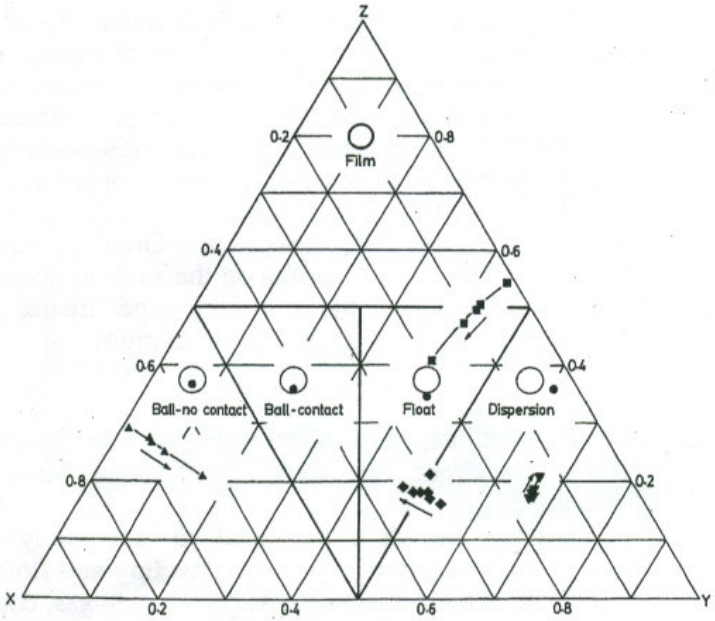

Figure 9: The ternary interfacial energy diagram of Conochie & Robertson (1979) reproduced by Ip & Toguri (1992) for the matte-slag-gas, copper-slag-gas and copper-slag-matte system at 1473K (1200 C). The direction of arrows indicates increasing matte grade or oxygen pressure. The different symbols represent the matte-slag-gas (■), copper-slag-gas (♦), copper-matte-gas (▼) and copper-slag-matte (▲) systems.

NELSON and co-workers (2005) reproduce the ternary diagram (Figure 10) for entrained matte sources in Anglo Platinum's Polokwane PGM furnace (six-in-line) slag. The demarcated area on the right side of the diagram is that of the Polokwane system.

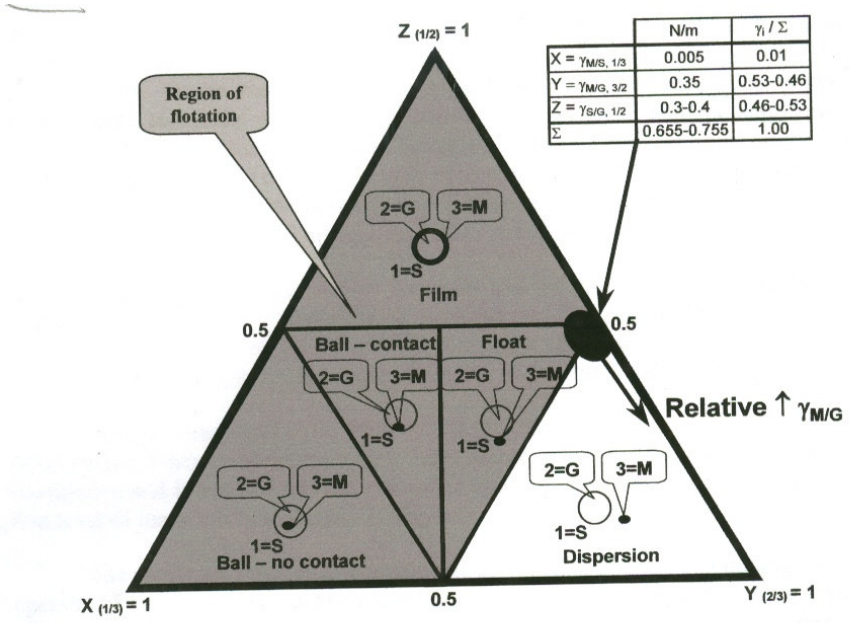

Figure 10: Ternary interfacial energy diagram for a discrete matte phase (3=M) in contact with gas bubbles (2=G) and a continuous slag phase (S=1) (adapted from Conochie and Robertson (1980) by Nelson et al., 2005).

The value calculated for X in the diagram shown in Figure 10 above, however, is much lower than it would be if calculated using the interfacial tensions measured by IP & TOGURI (1992, 1993). If these values are estimated for the Waterval six-in-line and SCF slag of this study, the interfacial tensions would approximate 0.08 N/m and over 0.1 N/m respectively, which would move the expected behaviour of entrained matte droplets into the flotation area.

3.3.4 Coalescence of entrained matte phases

The tiniest matte droplets in a slag will never settle unless they coalesce to form more massive drops. The chance of coalescence can be increased by stirring, or, in DC furnaces, by electromagnetic fields. In the PGE smelting six-in-line furnace, stirring is mainly buoyancy-driven, and this will depend on the temperature and the electrode immersion in the slag (ERIC, 2004), but electromagnetic field effects may be a factor at higher power densities. The ability of drops to coalesce in these furnaces is also increased at low slag viscosity, but this is limited by slag conductivity requirements.

Coalescence efficiency of entrained matte in slag is related to both settling and flotation behaviour. Gas bubbles rising through the slag can enhance drop growth through drop-to-drop coalescence (SHAHROKHI & SHAW, 2000), and the time required for drops to coalesce is largely the time needed for film drainage – when the film ruptures, coalescence is instantaneous. In the case of gravity-induced coalescence, the probability of coalescence decreases with decrease in drop size and in drop-to-drop size ratio. Collision frequency for neutrally-buoyant drops decreases as the kinematic viscosity (= viscosity/slag density) of the slag increases (SAFFMAN & TURNER, 1956).

Other effects hindering coalescence are too low a concentration of droplets (especially in the upper slag bath) – so there must be sufficient matte fall. Although some authors favour agitation as increasing the chance of coalescence (AMMANN *et al.,* 1979), others claim agitation alone reduces chances, but agitation with bubble formation can indeed promote coalescence (SHAHROKHI & SHAW, 2000). These authors also suggest that fine droplet recovery can be increased by the use of bubble injection.

3.3.5 Matte behaviour in industrial furnaces and converters

BARNETT & JEFFES (1977) proved that 60% of entrained matte could be settled under quiescent conditions to clean nickel out of electric furnace slag at INCO. In the case of reverberatory slags (YAZAWA, 1977, quoted by MACKEY, 1982) there is little decrease of entrained copper in slag after one to two hours settling. Viscosity must be as low as practical for reasonable operating conditions, and the velocity of slag particles rising in the matte is faster than the settling of matte in slag. IP & TOGURI (1992) suggest that the loss of copper to slag during converting – both by dissolution and gas flotation – can be reduced by lowering the oxygen pressure, but changing the slag composition only seems to have a minor effect.

The terminal velocity of matte droplets in slag will also play a part, and this will depend mainly on droplet size at a fixed slag viscosity. When the diameter of the matte particle is constant, the main factor influencing settling rate is the slag viscosity (YAZAWA, 1977, 1981 quoted by MACKEY, 1982, and IMRIS, 2003). The

relationship between particle diameter and settling time in reveberatory slags is plotted in Figure 11. The effect of grade is presumably due to the effect this has on the density of the matte droplets concerned.

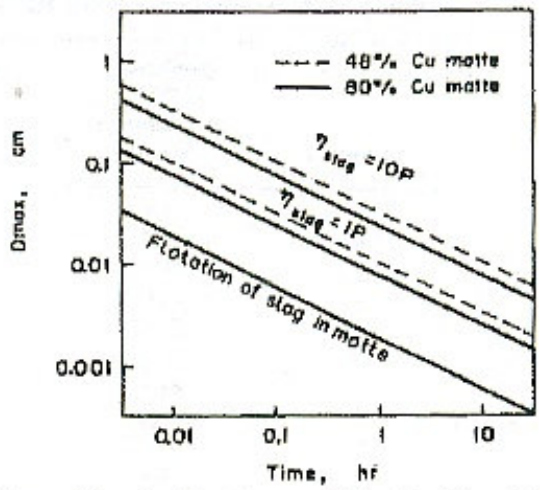

Figure 11: The effect of droplet diameter on settling time through a slag layer 300 mm thick. (Yazawa (1977) quoted in Mackey, 1982). The lowest line in the plot represents "the velocity of slag particles rising in matte". 1P = 0.1 Pa.s.

The settling rate of copper matte in fayalite slag depends on slag composition, where increasing silica (higher viscosity) decreases the settling rate in all 'oxidation degrees' of matte. Separation and settling rates of low grade copper matte in slag are lower than high grade copper matte (FAGERLUND & JALKANEN, 1999).

According to FAGERLUND & JALKANEN (2000), matte droplet flotation by SO_2 at the matte-slag interface occurs independently of the copper content of the matte (grade independent). Under conditions prevailing in an industrial flash furnace, flotation phenomena will enhance coagulation followed by settling of matte droplets through the slag, rather than accelerate matte emulsification.

MARUYAMA and co-workers (2003) used HSC chemistry simulation (an Outokumpu modelling program) to predict losses to slag during flash smelting. Their results (shown earlier in Figure 2), underestimated copper losses to slag. Chemical or dissolved copper were not actually *measured*, only the suspension loss (entrained matte). A sampling rod was used, a similar technique to that of HEJJA & ERIC (1996). The micrographs show relatively coarse slag texture, so it is unlikely that the matte droplets are of the true size. The effect of the thickness of slag layer on losses was also investigated. The thicker the layer the longer matte droplets take to settle, so there is more loss. Losses to slag from top and lower slag layers were checked by sampling slag (for chemical analysis) before and after matte tapping. The settling rate was inferred by measuring mass *vs.* depth, and Stokes Law was employed. In addition, matte particle size *vs.* settling time was estimated (Figure 12).

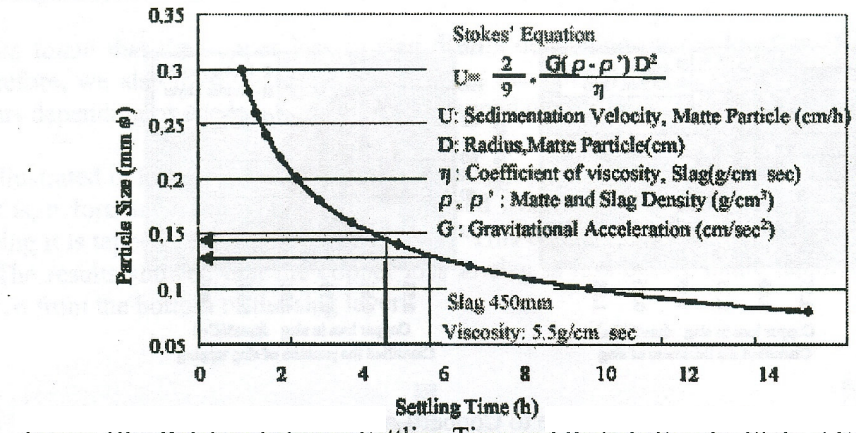

Figure 12: Relationship between settling time and particle size in copper flash smelting (after Maruyama et al., 2003).

It was concluded that copper loss to slag is affected by slag depth, viscosity, and slag tapping location.

IP & TOGURI (2000) analysed slags from copper-nickel smelters and copper converters (but only four samples in total), three samples contained copper and nickel matte droplets, the other sample mainly copper. Microscope photos were taken and the matte droplet size from the photos processed using 'a standard quantitative metallography technique'. All entrained matte particles were assumed to be spherical. Six hundred matte droplets were measured for each of the three nickel-copper samples; in the copper sample over eleven thousand were measured. Many matte droplets were attached to bubbles or trapped by magnetite.

Fine entrained matte droplets were found to settle too slowly, so recovery must be achieved through means other than gravitational settling. In addition, only a small fraction of drop-to-drop collisions resulted in coalescence.

The conclusions were that –

- Large entrained matte droplets can easily be settled while the very fine micron-sized droplets will inevitably be trapped in the slag phase,
- The computer simulated settling study showed that changing the slag viscosity and density difference between slag and matte only has a limited impact on the separation of the matte from the slag when very small droplets are involved (*e.g.* 2 µm), but can boost matte/slag separation significantly for larger drops,
- Methods that can maximise drop coalescence will yield more efficient matte-slag separation.

The effects of slag-matte density differences and slag viscosity on the settling velocity of the matte droplets were tabulated – this data is plotted in Figures 13 and 14 below. These were calculated using Stoke's Law only.

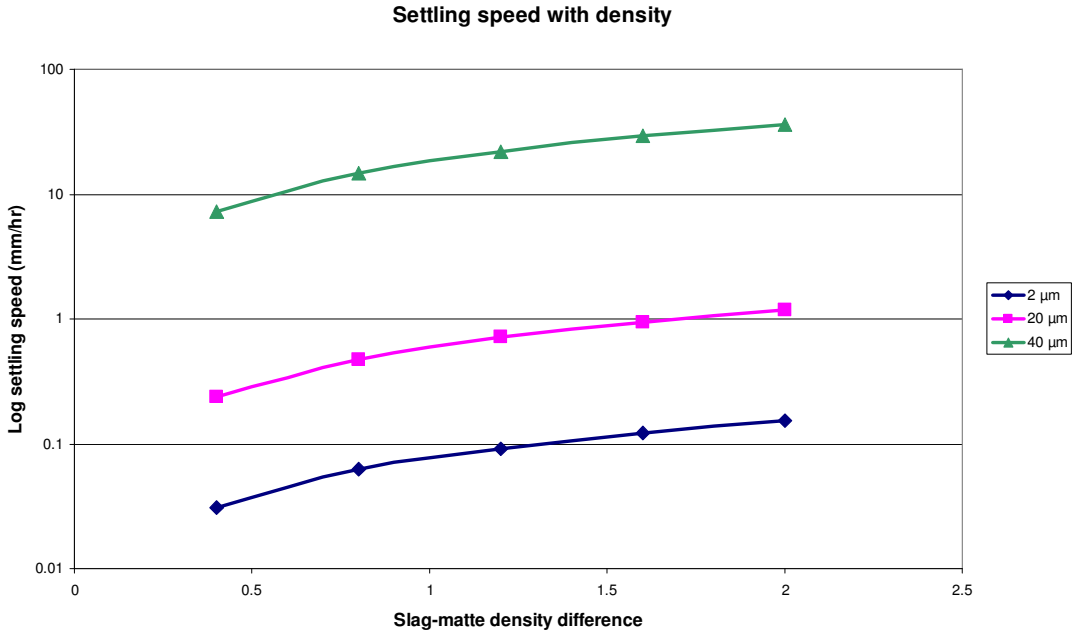

Figure 13: The effect of slag-matte density difference on the settling velocity of matte droplets of 2, 20 and 40 µm diameter. Plotted from the data given in Table II in Ip & Toguri (2000). The slag-matte density was measured in g/cm^3, and a slag viscosity of 0.102 Pa.s was used for the calculation. At this viscosity, the settling times in the slag cleaning furnace in this study would be approximately 40 mm/hour for a 40 µm droplet, just over 1 mm/hour for a 20 µm droplet and 0.15 mm/hour for a 2 µm droplet.

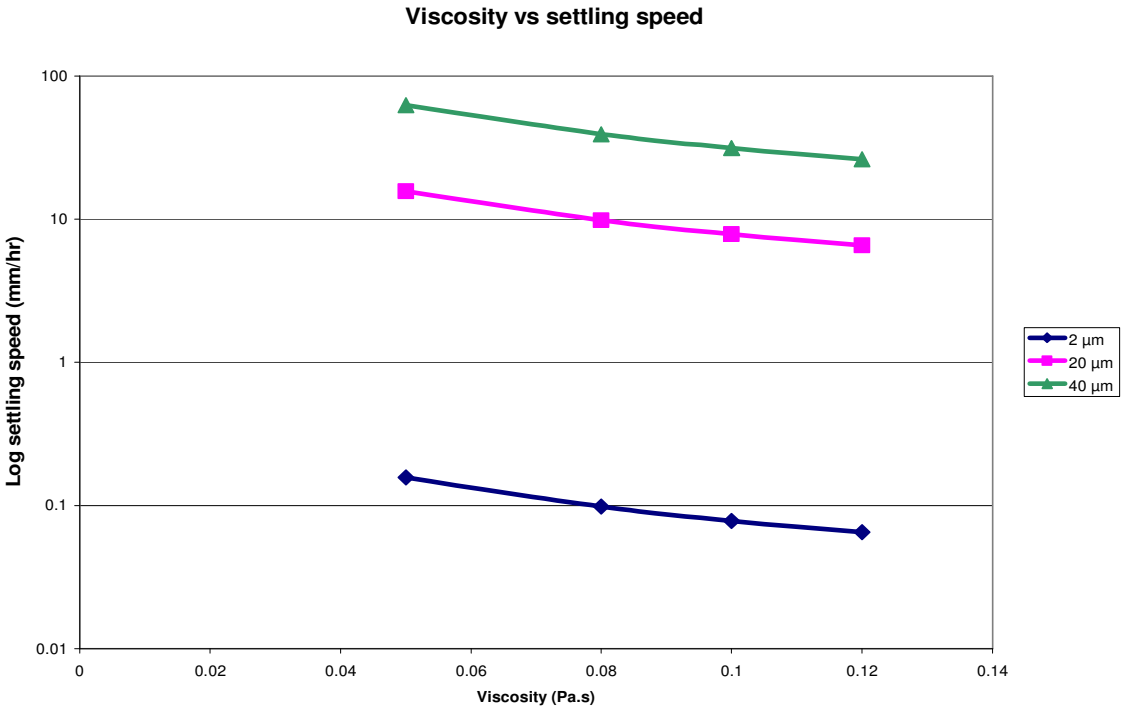

Figure 14: The effect of slag viscosity on settling velocity of matte droplets of 2, 20 and 40 µm diameter. Plotted from data given in Table III in Ip & Toguri (2000). A slag-matte density difference of 1.0 g/cm^3 was used for this calculation.

The slag viscosities and slag-matte density differences in the Figures above may be compared with those of the samples used in this study, which are shown in Table 4.

Table 4: The slag viscosities and slag-matte density differences of the Anglo Platinum furnace products of this study. Viscosity was calculated from slag composition and tapping temperatures, using the MPE modelling program available at the smelters. The relative densities (RD) of matte and slag samples taken in 2005 were measured on a pycnometer.

Furnace	*Date*	*Slag viscosity (Pa.s)*	*Slag-matte ΔRD (g/cm^3)*
Six-in-lines	1999	0.20 – 0.35	≈1?
Six-in-lines	2004	0.30 – 0.50	≈1
Six-in-lines	2005	0.30 – 0.35	1.0
Slag Cleaning Furnace	2005	0.10	2.2

An estimate may be made of the settling times in the slag cleaning furnace, of which the slag viscosity and slag-matte density difference are close to those shown in Figure 13. Although the slag-matte density difference of the six-in-line furnace slags is within the field of those plotted in Figure 13, the viscosity is much higher. Settling speeds were calculated using Stokes Law and the Hadamard-Rybczynski expression, and these are shown in Table 5.

Table 5: Settling speeds (terminal velocity) in mm/hr for various entrained matte droplet diameters in Anglo Platinum slag. Viscosities were taken as 0.3 Pa.s for the six-in-line slag and 0.1 Pa.s for SCF slag, and the density differences were taken as 1.0 and 2.2 respectively.

Furnace	*Stokes Law*			*Hadamard-Rybczynski expression*		
	1 mm	100 µm	10 µm	1 mm	100 µm	10 µm
Six-in-lines	6540	65	0.6	9810	98	1
SCF	43160	432	4	64750	647	6

If the Stokes Law results in Table 5 are compared with those of other workers, agreement with YAZAWA (1977) is good, and with IP & TOGURI (2000) reasonable, but the results do not agree well with those of MARUYAMA *et al.* (2003), even if the highest six-in-line viscosity (0.5 Pa.s) is used in the calculation.

ERIC & HEJJA (1995) deal with settling of entrained matte in six-in-line PGE-smelting furnaces, similar to those examined in this study. Here again the settling rate is affected by droplet size, slag viscosity, and relative density – in turn determined by slag composition. The viscosities of South African plant slags were found to vary as shown in Figure 15 below.

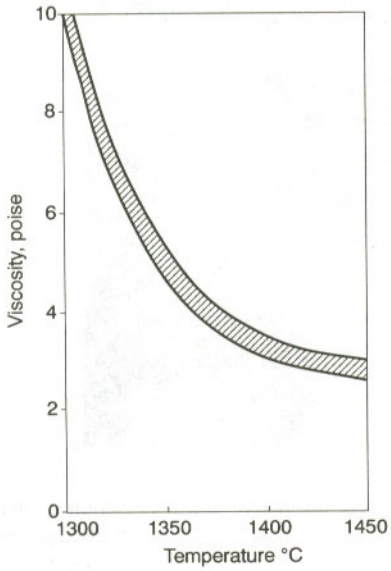

Figure 15: Viscosity range of plant slags encountered in Cu-Ni matte smelting in South Africa (Hejja & Eric, 1996). Note that 1 poise = 0.1 Pa.s.

Later (ERIC, 2004) a wider viscosity range was described for PGM smelting slags, which can vary from 0.15 to 0.4 Pa.s at 1400 °C. Under these conditions matte droplets would have to be larger than 15 µm to settle to the base of the melt.

In fact is difficult to make predictions of this kind because slag viscosity varies not only with temperature, but also with slag composition (ERIC & HEJJA, 1995). The effect of slag composition on the temperature gradient of slag viscosity is shown in Figure 16. Although rather high in slag CaO levels as compared to the slags in this study, the plots show that the most marked effect is due to slag FeO content.

An increase in the Fe/SiO_2 ratio reduces viscosity in iron-saturated and Mg-Ca-Fe silicate slags (DUCRET & RANKIN, 2000). This can be seen in the reduced viscosity of Anglo Platinum SCF slag as compared to the six-in-line furnace slag.

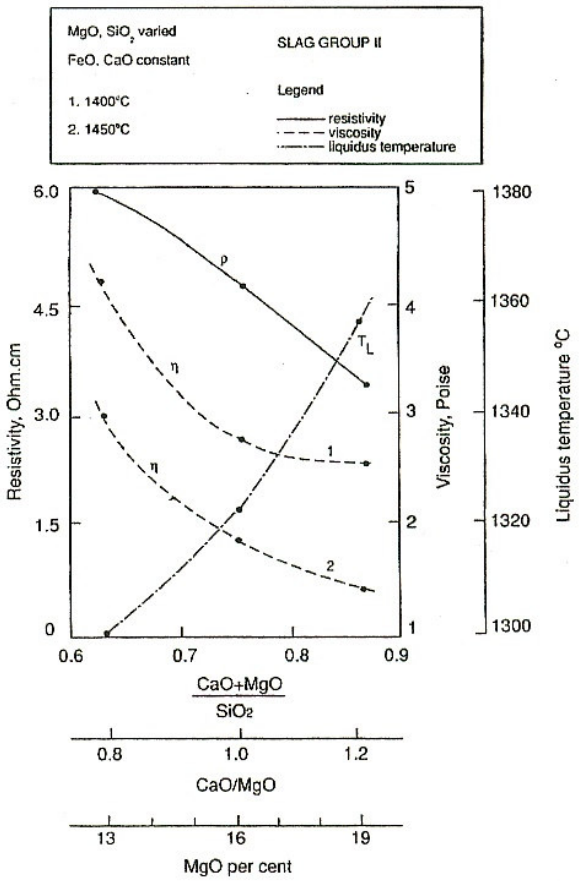

Figure 16: The effect of basicity, CsO/MgO ratio and MgO % on resistivity, viscosity and liquidus temperature of slags (after Eric, 2004).

Considering the slag flow characteristics in the six-in-line furnace, Stokes Law can be used for settling particles as a first approximation, and a particle sphericity (a measure of roundness) of 0.5 to 0.7 assumed (ERIC & HEJJA, 1995). In a furnace of this type, slag flow can be regarded as channel flow (ERIC, 2004). The velocity is mainly in the laminar flow range due to the large volume of melt involved and evenly distributed feed along the entire length of the furnace. Modifications such as those brought about by the electrodes and by periodic converter slag returns, do not substantially alter the laminar flow pattern. The laminar flow region corresponds to $10^4<R_A<10^9$ (R_A is the Rayleigh number).

The variation of matte droplet size with depth in the six-in-line slag bath was investigated (ERIC & HEJJA, 1995, HEJJA & ERIC, 1996). The experimental work involved sampling one of the 'then Lonrho's six-in-line furnaces' with an air-cooled sounding bar (*pers. comm.,* R.H. Eric*, 29 July 2005)*. This was done through the matte end sounding port, and resulting samples were examined microscopically to provide size distributions with depth. The results are accompanied by photomicrographs that reveal considerable crystallinity in the samples involved. This suggests the measured droplet size would not have been exactly the same as that of the droplets in the molten slag. Sounding bar samples taken in the study described in this thesis also displayed a degree of slow cooling, but to a lesser extent, possibly due to the speed of the sample collection.The weight distribution was found to be inversely proportional to the number of particles, and

increased with increasing size range. In other words, particles up to 200 µm may represent only 10 % of total entrained matte weight. Only particles >15 µm in size were considered (ERIC & HEJJA, 1995).

URQUHART and co-workers (1976) also took samples using a sounding bar. The entire length of the six-in-line furnace at Waterval Smelter was sampled. Subsequent examination showed that the entrained matte content of the slag was highest near the slag-matte interface (due to increased slag viscosity and lower slag temperature), and that the slag composition was very homogenous in composition over its vertical height, as has been confirmed in the present study. The variation of matte droplet composition with height in the furnace was not investigated.

According to ERIC & HEJJA (1995, 1996) coalescence of matte droplets in both upper and lower parts of a six-in-line slag bath occurs due to temperature differences, as well as the buoyancy and electromagnetic effects which are the main driving forces in slag movement. Maximum droplet growth takes place when the residence time of the slag in the region just below the liquidus temp is at the optimum for growth. Matte settling is also discussed in conjunction with furnace geometry and electrode stirring action. In the rectangular furnace the effect of electromagnetic forces is minimal, but it may play a more important role in circular furnaces (see later).

The slag residence time in six-in-lines furnaces similar to those used in this study are in the order of 36.5 hours (ERIC, 2004) and 31 hours (URQUHART *et al.,* 1976). It is likely that the present day residence time (after various furnace upgrades) could be as low as 24 hours. The slag depth, though variable, is approximately 1.4 m.

From a matte loss point of view, it is only the material balance in the last settling zone of a six-in-line furnace that matters (the slag end electrode). The furnace can be considered as a series of reactors, however, in order to provide a full-furnace picture (ERIC & HEJJA, 1995) – Figure 17.

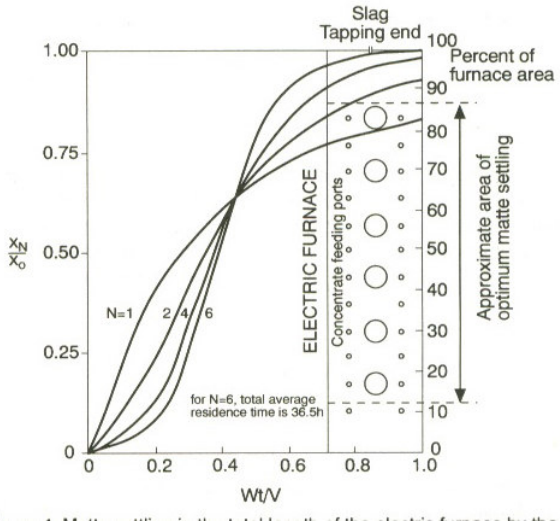

Figure 17: Matte settling in the total length of the electric furnace by the analogy of output from an N tank system of total volume (Hejja & Eric, 1996). X_N/X_0 = settled volume/total volume of matte prills of a given size fraction. Wt/V = ratio of settled matte/total introduced matte.

The height of slag above the tap hole was plotted against metal loss due to matte entrainment for the six-in-line furnaces (ERIC & HEJJA, 1995). The calculations encompassed slag flow viscosities, terminal velocities of matte particles, matte prill size distribution, settler dimensions and tap hole positions and gave birth to Figure 18 below.

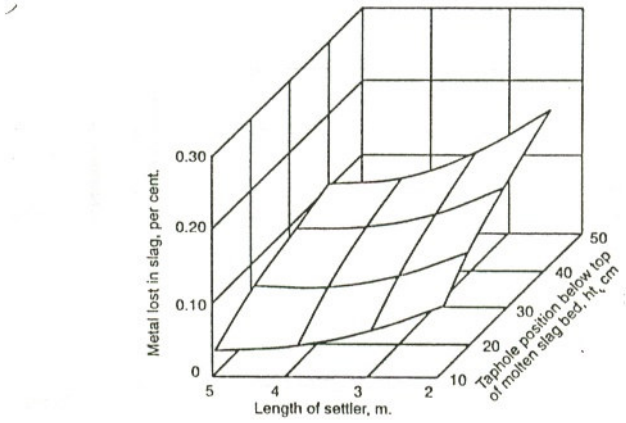

Figure 18: Three dimensional representation of the relationship between distance available for settling of matte particles, taphole position and metal loss due to particle carry-over in slag. (After Eric & Hejja, 1995).

The distance from last electrode to the slag tap hole is 5 m in the six-in-line furnaces. The settling distance is defined (by URQUHART *et al.,* 1976) as the distance from the reaction zone around the electrodes to the slag tap hole. The reaction zone can be predicted from heat transfer considerations, assuming that the temperature variation over the depth of electrode penetration is small. In 1976, this zone was 5.8 m in diameter, but the furnaces were only rated at 19.5 MVA. It is likely that the zone is of similar dimensions today, but reaction rates within it may differ. This means that in 1976, and also at the present time, the settling distance approximates 2.7 m in the six-in-line furnaces. Interestingly, the settling distance when calculated for a circular furnace of the same power rating is slightly lower at 2.4 m.

In practice, the slag temperature profile, and therefore the diameter of the reaction zone varies with depth in the six-in-line furnaces, as suggested in the Ritz profile in Figure 19 (ERIC, 2004). The observed slag velocity in the Anglo Platinum six-in-line furnaces is also too high to reconcile the radial heat distribution as used in the model proposed by Urquhart (ERIC & HEJJA, 1995).

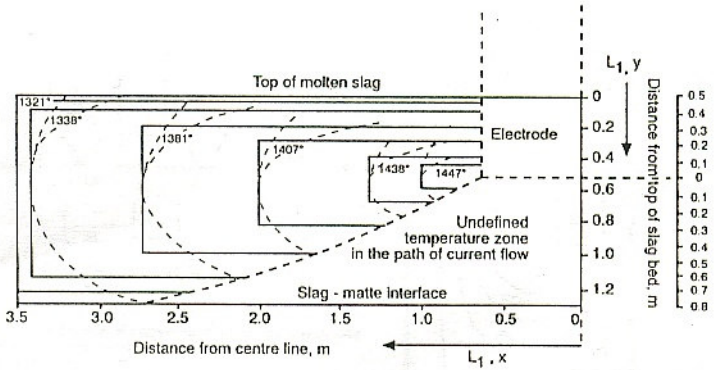

Figure 19: First order Ritz profile of two-dimensional heat distribution in the molten bed of slag (Eric, 2004). The low slag temperatures suggest that this profile was modelled prior to 2000.

If the reaction zone effect is ignored, and the observed slag velocity of 200 mm/s between the electrode and the wall of the six-in-line Anglo Platinum furnaces (ERIC & HEJJA, 1995) still holds true for the higher power rating, then the residence time for slag and non-settled entrained matte phases between the last electrode and the slag tap hole will be in the order of 25 seconds.

Circular furnace symmetries are turbulent and less conducive to matte settling. Depending on the characteristics of the slag used, slag-matte separation can be optimised, but usually it is easier to do so in a rectangular than a circular furnace (ERIC & HEJJA, 1995). Because the three-electrode furnace is turbulent, the trajectories of settling matte droplets are substantially altered due to the reduced distance between the electrodes and the furnace wall (ERIC, 2004). There is a much higher degree of intermixing among matte droplets of different sizes, and this can cause increases in matte loss to tapped slag. Electromagnetic effects may play a more important role in circular AC furnaces; this is certainly so in circular DC furnaces. The position of the tap holes around the furnace can also affect losses – those close to the electrodes would be less quiescent that those between the electrodes. The position of the slag tap holes in the Anglo Platinum SCF could be moved to increase the electrode-tap hole distance by 10-20 %, but constraints are imposed by cooler geometry and slag granulation layout.

XIA and co-workers (2004a) undertook a computational fluid dynamics (CFD) study of the 3D magneto-hydrodynamic flow in an industrial scale circular nickel slag cleaning furnace with three electrodes, using idealized (cylindrical) and actual (conical) electrode shapes. Previously only cylindrical models had been reported. In addition to modelling the flow, they calculated the nickel droplet trajectories and settling behaviour in the slag. Predictions were made and then validated on an operating furnace.
Recently, more attention has been paid to magnetohydrodynamic (MHD) mechanisms in the study of flow and heat transfer in electric furnaces. In a furnace of this type, complex slag flow and heat transfer occur due to the interaction of electromagnetic and buoyancy forces. In the furnace modelled, slag flow was turbulent (Rayleigh no. estimated at 2.7×10^{11}), and the furnace wall was assumed to be insulated (*i.e.* not cooled).
Flow and heat transfer results are reported - temperature, electric potential and heat generation rate contours modelled around the electrodes, then nickel droplet flow simulated. The trajectory of an individual dispersed particle is calculated by integrating the force balance on that particle. Forces taken into account were pressure gradient in the fluid, Stokes steady state viscous drag, inertia and buoyancy due to gravity. Added in was fluid dynamics to deal with turbulent particle dispersion. A collision model was employed to simulate particle-wall interaction with the restitution coefficient set at 1.0 for droplet diameter <900 µm and 0.5 to 0.8 for diameter >1000 µm. The restitution coefficient is the ratio of the incident droplet velocity to its reflected velocity; the furnace wall is presumably taken to be rigid here.
It is concluded that using a cylindrical electrode model is quite close to the actual for slag flow and heat transfer, but "some difference is observed, especially for metal droplet settling behaviour".

In a related publication, XIA and co-workers (2004b) numerically modelled 3D magneto-hydrodynamic (MHD) flow in slag of an industrial scale furnace. This is a three-electrode slag cleaning furnace used after flash smelting of nickel in Finland.

Slag flow patterns, volume fraction distributions, and droplet trajectory diagrams are described and the settling droplet ratio is plotted against time. Although over 80 % of droplets of 1 mm diameter would settle,

less than 20 % of 100 µm droplets would settle. Most of the droplets will settle into the matte in the central bottom region of the furnace. Fine droplets (<50 µm) will not settle, but the settling ratio increases with size. Coagulation of droplets "may" play an important role in settling, and the residence time for some droplets can be over 5000 seconds. If turbulent drop dispersion is taken into account, this has a significant effect on droplet trajectories and distribution.

Droplet volume fraction distributions are predicted for the turbulent and non-turbulent case (Figures 20 and 21).

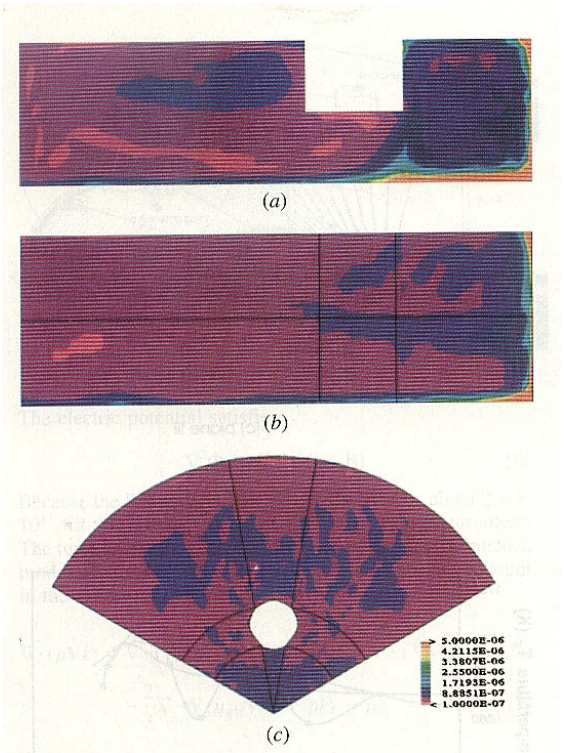

*Figure 20: Predicted droplet volume fraction distributions **with** turbulent particle dispersion taken into account. Initially, 10,524 droplets are uniformly distributed on the free surface and the diameter of the particle is d_p=753 µm: (a) plane I, (b) plane II, and (c) plane III. (Xia et al., 2004b).*

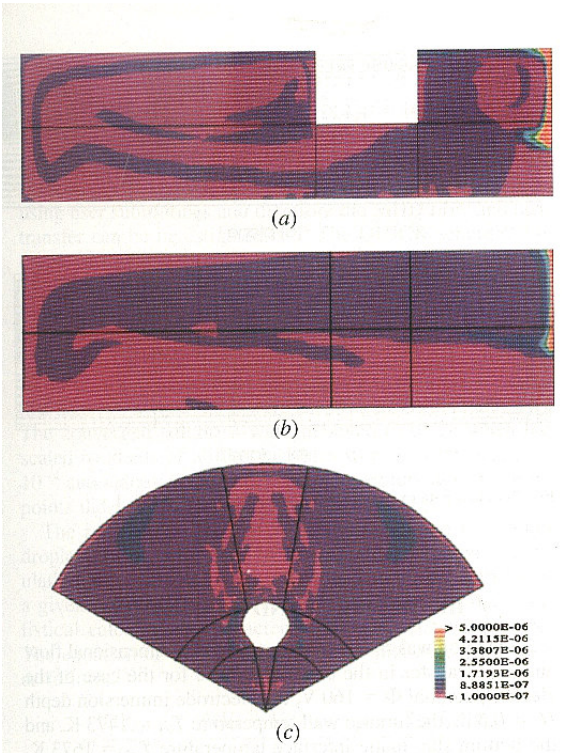

*Figure 21: Predicted droplet volume fraction distributions **without** turbulent particle dispersion taken into account. Initially, 10,524 droplets are uniformly distributed on the free surface and the diameter of the particle is d_p=753 µm: (a) plane I, (b) plane II, and (c) plane III. (Xia et al., 2004b).*

A slag flow diagram was calculated and plotted for the three-electrode furnace (Figure 22). This can be compared with a similar plot reproduced by HEJJA & ERIC (1996) in Figure 23.

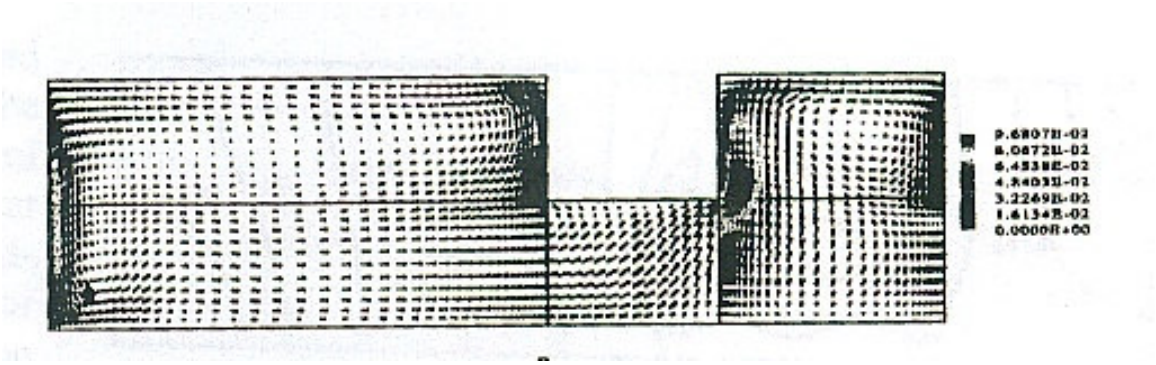

Figure 22: Velocity vector plots (m/s) in the plane passing an electrode (Xia et al., 2004b).

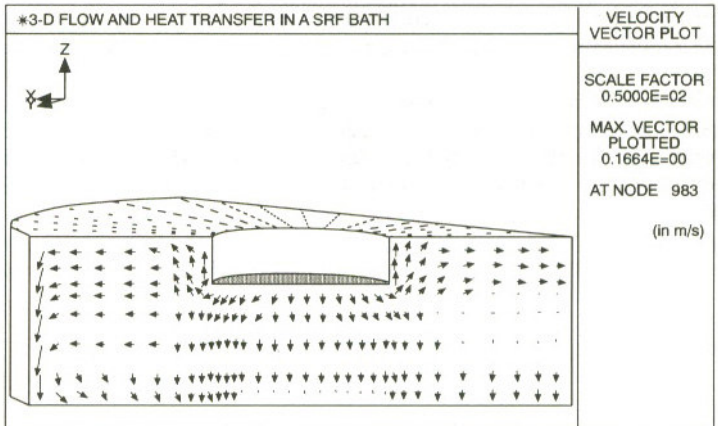

Figure 23: Velocity profiles in a slag resistance furnace bath (3-electrode). Themelis et al., (1991) reproduced in Hejja & Eric (1995).

3.3.6 Effect of electric and magnetic fields

Electrocapillary motion (the movement of a matte droplet in slag due to an electric field) is caused by the interaction between the electric field and the interfacial tension of a matte droplet. The speed and the direction of matte droplet motion are dependent on the composition of *both* matte and slag. Although a certain degree of electrocapillary motion will be experienced by entrained matte droplets in AC smelting and slag cleaning furnaces, the effect is likely to be far less important than it is in DC furnaces. A brief review of the literature in this field follows, for the sake of completeness.

The migratory behaviour of matte droplets in slags when subjected to an external electric field have been examined (CHOO & TOGURI, 1992, ITOH *et al.,*1995, WARCZOK & UTIGARD, 1995, WARCZOK & RIVEROS, 2003). Droplet behaviour in crossed electrical and magnetic fields was also studied (WARCZOK & RIVEROS, 2003, 2007, MONTENEGRO *et al.,* 2003) and applied to recovery in DC electric furnaces.

The interaction between the electric field and surface tension forces that are responsible for motion were analysed with the following results –

- The migration direction was found to depend on both matte and slag composition – depending on the sign of the surface charge (a function of matte and slag composition) the droplet migrates towards the anode or the cathode
- Cu_2S-FeS matte droplets migrated towards the anode and Ni_3S_2-FeS matte droplets towards the cathode, but this may change with slag composition
- Migration rate was independent of droplet size in the 1 – 3 mm range
- Migration rate increased with both applied potential and temperature
- As copper content in the Cu_2S-FeS matte droplets rose above 40%, migration rate increased
- As nickel content in the Ni_3S_2-FeS matte droplets increased, migration rate decreased
- Migration rates were affected by slag composition

And, in addition, the mobility of entrained Cu-Fe matte is strongly affected by the amount of FeO in the slag (IP & TOGURI, 1993).

MONTENEGRO and co-workers (2003) describe magnetic/electric field enhancement of entrained matte recovery using a DC arc furnace to clean copper converter slag. The authors suggest that the reaction rate should be increased by the use of magnetohydrodynamic (MHD) stirring, which would increase coalescence, followed by a period of more quiescent settling.

Results of bench scale experiments show that the use of crossed electric and magnetic fields in the slag cleaning process increases the rate of slag reduction from two to three times as much as in AC slag cleaning. In addition, the MHD slag stirring enhanced mass transfer onto the slag/reductant interface and cathodic reduction of Fe^{3+} and Cu^{+}, thus accelerating slag reduction.

Most authors in this field conclude that DC furnaces are superior for the recovery of entrained matte from slag, as compared to AC electric furnaces, and that superimposing a magnetic field in a DC electric furnace would clean slag even more effectively.

3.4 PROCESSES USED IN BASE METAL RECOVERY (SLAG CLEANING)

Base metals may be recovered from slag using a number of different methods. Although hydrometallurgical treatment or leaching of slag is described in the literature (WHYTE et al., 1977, HEINRICH, 1989) these methods are not used industrially (DEMETRIO *et al.,* 2000). Some authors describe leaching methods to clean flotation tailings from the slag plant (SUBRAMANIAN & THEMELIS, 1972).

The two most common slag cleaning methods are milling followed by flotation, usually of slow-cooled or cast slag, and pyrometallurgical cleaning. Both techniques are used in the copper and nickel smelting industry, but cobalt recovery is predominantly pyrometallurgical, as will be explained later.

The advantages and limitations of flotation, as compared to pyrometallurgy, are discussed for base metal containing slags (BARNETT, 1979, JONES *et al*., 1996, PIRET, 2000).

Environmentally the most chemically stable slags are those that are water quenched/granulated, but this practice is incompatible with milling and flotation because crystallisation must occur (DEMETRIO *et al*., 2000*).* Crystalline phases produced by slow cooling are easier to grind – quenching produces an amorphous slag structure which inhibits fine grinding (SUBRAMANIA & THEMELIS, 1972). The size distribution of entrained matte phases determines the effectiveness of milling and flotation to a large degree. Metal loss into tailings decreases with lower cooling rates, and with fineness of grind. Copper converter slag is nearly twice as hard to grind as copper ore (mainly due to the higher silica content).

In his review of current slag cleaning practices in 1979, BARNETT, a Rustenburg Platinum Mine employee, remarked that slag milling and flotation generally resulted in a greater recovery than pyrometallurgical slag cleaning ("some 7 % greater"). The Slag Plant at Waterval Smelter was operating at that time and recoveries were such that a slag-cleaning furnace was not installed until 2003, to cope with the more highly oxidised slag produced by the ACP converter.

Milling and flotation can only recover entrained matte phases from slag, and not dissolved base metals. Matte phases are not usually floated if they are less than 10 µm in size. The entrained matte phases characteristic of nickel smelting are too fine for flotation recovery (HEINRICH, 1989). The recovery of base metals which are dissolved in the slag silicate and oxide phases requires the reduction of the slag in a furnace with carbon addition, and this is especially true of cobalt (MATOUSEK, 1982, PIRET, 2000).

When electric furnaces are used for slag cleaning, electricity must be cheap (DEMETRIO *et al*., 2000), and this is the case in South Africa (although this may change in the near future). A number of pyrometallurgical techniques, and furnace types, in use in the copper and nickel smelting industries are reviewed in the literature (FLOYD & MACKEY, 1981, MACKEY, 1982). In addition, segregation roasting of slag is described by VIRCIKOVA & MOLNAR (1992). The design and operation of the three-electrode circular electric furnace currently in use at Anglo Platinum is dealt with by JOUBERT and co-workers (2005), and more detail on this furnace is also provided in Section 4. Other methods currently in industrial use include slag cleaning in a tilting horizontal furnace – the El Teniente Process, developed in Chile (MACKAY *et al*., 2000), DC slag cleaning in a one-electrode circular furnace (JONES *et al.,* 2001), DC slag cleaning in a two-stage system – a conventional slag cleaning furnace, and a channel furnace with combined electric and magnetic fields (DEGEL *et al.,* 2006, WARCZOK & RIVEROS, 2007), base metal recovery in a modified Peirce Smith converter at Sudbury (KAIURA, 1989), and an Ausmelt submerged lance reactor for base metal recovery from slags (HUGHES, 2000).

The two designs of slag cleaning furnace in use in Southern African base metal and platinum smelting operations are the three electrode AC electric furnace (as at Waterval Smelter) and the one electrode DC furnace which is emerging as the popular choice for cobalt recovery (JONES, *et al*., 1996, 2001). Both make use of carbon reductant.

4 SMELTER PROCESSES

The history of, and operations at, Anglo Platinum's Waterval Smelter, which is situated in Kroondal, near Rustenburg, have been described in detail in the literature (JONES, 1999, JACOBS, 2006).

4.1 HISTORY

The first platinum smelting operations in the Rustenburg area consisted of a small blast furnace and converting unit, constructed at Klipfontein in 1937, to treat unoxidised ore. The first electric furnaces appeared in 1969 when two Elkem 18 MW furnaces were built on the present Waterval Smelter site. These were upgraded to 34 MW Hatch furnaces between 1994 and 1998. During this time the current flash driers replaced the older rotary driers, and the ceramic filters were introduced to extract dust from furnace off gas.

Figure 24: The converter aisle before the advent of the Anglo Platinum Converting Process (ACP), with the six-in-line furnaces on the right. Matte is being tapped to transfer into one of the Peirce Smith converters. Photograph courtesy of Anglo Platinum (Corporate Communications).

The first four Peirce Smith converters were installed in the early 1970s and in 1976 a contact acid plant was attached to reduce SO_2 emissions. By 2000 six converters were in operation, and a new Ausmelt converter (with attendant acid plant) was commissioned in 2002, with a second converter coming on line in 2006. By then all the Peirce-Smith converters had been decommissioned, and a slag cleaning furnace (installed in 2003) was being used to treat converter slag.

A photograph of the converter aisle as it was when the Smelter celebrated its thirtieth anniversary (in 1999) is shown in Figure 24.

4.2 PROCESS OVERVIEW

The present-day smelter flow sheet is shown in Figure 25.

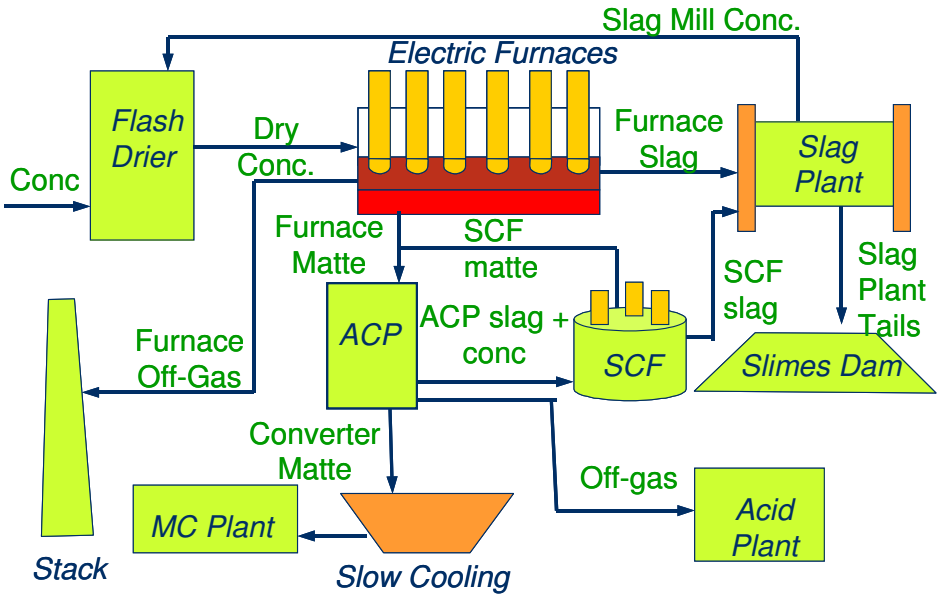

Figure 25: Diagrammatic flow sheet for Waterval Smelter. ACP – Anglo Platinum Converting Process, SCF – Slag Cleaning Furnace, MC – Magnetic Concentrating.

At the smelter, incoming ore concentrate from the concentrators is dried in one of four flash driers (Figure 26), mixed with a limestone flux, and then fed into the two Hatch six-in-line electric resistance furnaces mentioned above. Smelting of the concentrate in these furnaces produces a melt with a high slag to matte ratio (at Waterval this is around 4:1).

Figure 26: One of the flash driers at Waterval Smelter. Photograph courtesy of Rustenburg Platinum Mines Ltd, Waterval Smelter.

The resulting matte is granulated and used as feed for the Ausmelt converting process. Furnace slag is tapped continuously and granulated in water. Some, but not all is then milled and floated in the slag plant to recover entrained matte, and hence reduce PGE and base metal losses.

Converter slag is granulated, blended with concentrate, and treated in the slag cleaning furnace. This is a smaller furnace with three electrodes. Slag cleaning furnace matte is granulated and fed to the converters, and the slag is granulated, blended with six-in-line furnace slag, and treated in the slag plant.

Converter matte is tapped into ladles and poured into moulds, which are holes in the ground. A lid is placed over the mould and the matte is allowed to cool slowly over a number of days. This allows all the PGE to concentrate into alloy phases, which can be removed by magnetic separation at the Base Metal Refinery.

At the start of sampling for this research (1999), the Peirce-Smith converters were still in operation and there was no slag cleaning furnace.

Some of the converter slag was returned to the six-in-line furnaces as slag (later blows) and reverts (slag plus ladle skulls). A certain amount of converter slag was sent directly to the slag plant.

The process is designed to concentrate PGE. The route that the base metals follow is not dissimilar, but these are more sensitive to the oxidation potential in the system. Thus converting (oxidising) increases base metal dissolution in the slag phase, and the slag cleaning furnace (reducing) decreases dissolution. The higher degree of turbulence present in the converter slag bath also leads to an increase in mechanical entrainment of matte into slag which results in losses of PGE and base metals. In theory, these will be recovered in the slag cleaning furnace where quiescent settling conditions should prevail.

The furnace and converting processes are described in more detail below, as these form the main study areas of the project.

4.3 ELECTRIC FURNACE SMELTING (SIX-IN-LINES)

Primary smelting of Anglo Platinum concentrates is carried out in four furnaces at three smelters. The history and present function of the two electric furnaces at Waterval Smelter have been described in the literature (MOSTERT & ROBERTS, 1973, JACOBS, 2006).

The furnaces are of Hatch design and are rated at 39 MVA (34 MW). Both are 8 x 26 m in size, and current passes between three pairs of Söderberg electrodes, situated down the length of the furnace (hence the name 'six-in-line'). The electrodes are 1.25 m in diameter and consist of a metal shell containing carbon paste. As the electrodes are consumed within the furnace, more shell and paste are added on top of the furnace roof. The furnaces are heated when current passes through the slag layer, which has a set resistance. The interdependence of slag composition, conductivity, viscosity, and liquidus temperature in electric furnaces of this type has been emphasised – these must be carefully controlled (ERIC & HEJJA, 1995, ERIC, 2004).

As mentioned earlier, blended ore concentrate is dried in the flash driers and mixed with limestone flux. Smaller amounts of recycles (Slag Plant concentrate) and refinery press cake may be added to the ore concentrate before flash drying. The feed mix is then fed into the furnaces by pneumatic transfer and enters

through the roof. Other materials, such as converter slag and reverts, are also batch-fed into the furnaces on occasion.

Primary smelting is limited to melting, and there is normally little oxidation or reduction in these furnaces. The ore concentrate, which contains base metal sulphides and gangue silicates, melts to form a base metal sulphide matte layer and, on top of this, a silicate slag layer. The furnaces are commonly maintained with a 'black top' – in other words, a concentrate layer floats on top of the molten bath.

The amount of sulphur (as sulphide minerals) in furnace feed is in excess of that required to form furnace matte. Sulphur vapour, sulphur dioxide, sulphur trioxide, and carbon monoxide gases report to off-gas. Furnace dust is removed by ceramic filters and the cleaned gas is directed to the Tower Plant.

Matte from the furnaces is tapped into ladles and granulated in water. It is then stored prior to being used as converter feed. Furnace slag is tapped continuously and granulated in water. This is then collected by rake classifiers, dewatered and stored before treatment in the Slag Plant, where the slag is milled and floated (Figure 27). Flotation concentrate is returned to the furnaces.

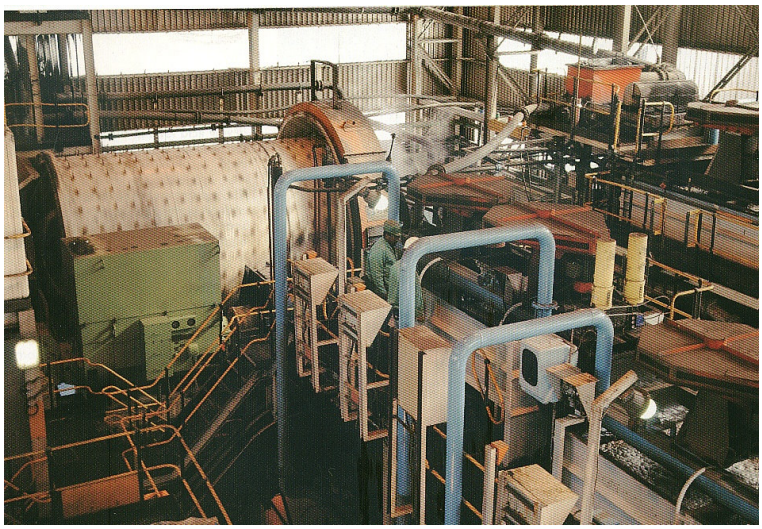

Figure 27: The Slag Plant consists of a ball mill, primary and secondary rougher flotation cells, but no cleaner cells. Concentrate is returned to the furnace with the flue dust and the tailings are dumped on the slimes dam. Photograph courtesy of Rustenburg Platinum Mines Ltd, Waterval Smelter.

Nickel recovery and the type of losses experienced in the Slag Plant have been documented (ANDREWS, 2005).

4.4 CONVERTING

The Peirce-Smith converters that were in use at the smelter until 2004 employed tilting vessels where air was blown into furnace matte to oxidise iron from the matte into the slag phase. A brief description of the process in 2000 has been documented (WICKS, 2000). By then six converters were in operation, each 10 feet in diameter and 25 feet in length. Each was lined with direct bonded chrome-magnesia refractory. Tuyeres were at and angle of 7º up, and punched with Galt punchers.

Two ladles of furnace matte would be poured into a converter, then air was injected to 'blow' the matte down to approximately 13 % iron. Silica was added to aid slag production and iron was oxidised according to the following reactions –

$$FeS + 1.5\ O_2 \rightarrow FeO + SO_2$$

$$2\ FeO + SiO_2 \rightarrow Fe_2SiO_4$$

$$3\ FeO + 0.5\ O_2 \rightarrow Fe_3O_4$$

After this more ladles of matte would be added and blowing repeated until five to six ladles of matte had been converted. The final 'blow' was required to bring iron levels in the converter matte down to 3 %. Approximately 30 t of nickel and copper-rich converter matte were produced per Peirce-Smith converter and this was poured into ladles and later slow cooled.

The slag produced during the process was raked off and solidified to produce material rich in fayalite (Fe_2SiO_4) and magnetite (Fe_3O_4). As can be seen from the reactions above, another by-product of the reaction was sulphur dioxide gas (SO_2). This was treated in the Acid Plant to produce sulphuric acid.

Peirce-Smith converters, by nature of their design, are not easy to adapt for strict SO_2 emission control (Figure 28). This fact, along with tightening emission control regulations, led to the decision to install two Ausmelt converters on a new site at the smelter and to phase out the use of the older converters.

Figure 28: Furnace matte being poured into one of the Peirce Smith converters. Photograph courtesy of Rustenburg Platinum Mines Ltd, Waterval Smelter.

Advantages of the Ausmelt process are reduced fugitive emissions, increased off-gas stability as feed to the New Acid Plant, and more consistent product quality.

The operation of the ACP (Anglo Platinum Converting Process) converters (Ausmelt technology) at Waterval Smelter has been described (VIVIERS & HINES, 2005, JACOBS, 2006). The ACP reactors are vertical vessels with copper waffle coolers in the slag zone. Feed (furnace matte), silica flux and air/oxygen mixtures are introduced to the ACP reactor through a submerged lance.

Basically, the reactions to produce converter matte and a fayalitic slag are the same as those described under Peirce-Smith converting. There is better control of over-oxidation by coal addition –

$$Fe_3O_4 + C \rightarrow CO + 3\ FeO$$

and the coal also acts as a heat generator according to the reaction –

$$C + 0.5\ O_2 \rightarrow CO$$

Converter matte is tapped into ladles and slow cooled (Figure 29) before being crushed and dispatched to the Base Metal Refinery. Converting not only leads to iron removal, increasing the base metal content of the matte, but also reduces sulphur. The resulting nickel-copper matte, which forms upon slow cooling, contains an alloy phase that concentrates the PGE, allowing them to be recovered by magnetic separation and subsequent hydrometallurgical processes.

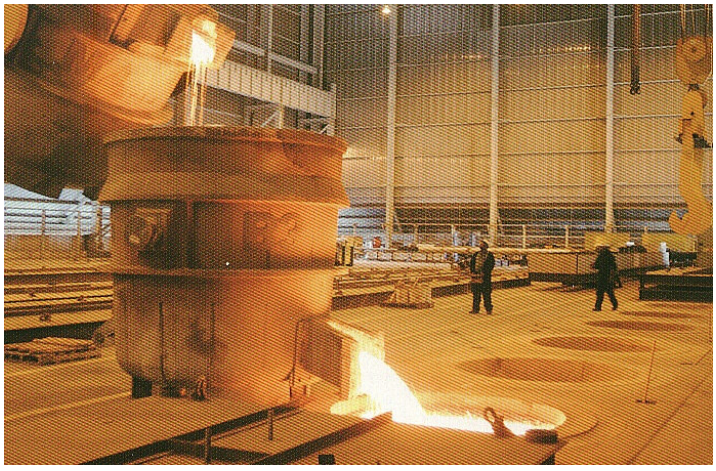

Figure 29: Converter matte is poured into moulds to form slow cooled ingots. Photograph courtesy of Rustenburg Platinum Mines Ltd, Waterval Smelter.

Over 14 000 t of furnace matte is converted per month. Even although matte from all three Anglo Platinum smelters (four electric furnaces and the slag cleaning furnace) can be processed by one ACP converter, a second was commissioned during 2006 to act mainly as a back up.

Converter slag (Waterval ACP Converter Slag or WACS) is tapped and granulated in water and, after dewatering and drying is used as feed for the slag cleaning furnace described below.

4.5 SLAG CLEANING (PYROMETALLURGICAL)

Treatment of WACS in the slag cleaning furnace (SCF) has been described in the literature (JACOBS, 2006, JOUBERT *et al,* 2005).

The SCF, which is situated close to the electric furnaces, is a twelve-metre diameter circular furnace with three 1.4 m diameter Söderberg electrodes. The SCF is a Pyromet furnace and is rated at 30 MVA (23 MW). Copper waffle coolers (here Pyromet Maxicoolers) are in contact with the slag bath, chrome-magnesia bricks line the hearth and are in contact with matte, and the flat roof is lined with suspended super-duty (aluminium silicate) bricks.

WACS and concentrate are fed into the furnace through roof ports. The concentrate, or occasionally furnace matte, is added to increase sulphur in the feed, which is required for matte fall. Concentrate for the SCF has a dedicated flash drier and limestone flux is not added. Silica and coke as well as reverts are also roof-fed. Silica is added to modify the slag properties, and coke is a reductant.

The reduction of the base metal oxides in the WACS is accomplished in two ways. The greater affinity of iron for oxygen as compared to that of nickel, copper and cobalt, allows selective reduction involving iron sulphides –

$$NiO + FeS \rightarrow NiS + FeO$$

$$Cu_2O + FeS \rightarrow Cu_2S + FeO$$

$$CoO + FeS \rightarrow CoS + FeO$$

and then iron forms fayalite as follows –

$$2\ FeO + SiO_2 \rightarrow Fe_2SiO_4$$

Magnetite ($Fe^{III}_2O_3{\cdot}Fe^{II}O$) can be reduced as shown below –

$$3\ Fe_3O_4 + FeS \rightarrow 10\ FeO + SO_2$$

after which FeO reacts to form fayalite as above and SO_2 leaves in the off-gas.

Coke also reacts to reduce metal oxides.

$$NiO + C \rightarrow Ni + CO$$

$$Cu_2O + C \rightarrow 2\ Cu + CO$$

$$CoO + C \rightarrow Co + CO$$

$$Fe_3O_4 + C \rightarrow 3\ FeO + CO$$

Carbon monoxide (CO) gas joins the SO_2 in the off-gas, which is treated in the Gas Cleaning Plant.

Matte is tapped and granulated in water along with electric furnace (six-in-line) matte. Both products then proceed to the ACP converters.

Slag is tapped and granulated in water (Figure 30). This product is further treated in the Slag Plant in combination with electric furnace (six-in-line) slag.

Since its commissioning in 2003, the SCF has been operated in batch and continuous mode, and has been used to treat widely varying feeds including WACS, Peirce-Smith converter slag, reverts and furnace matte. Its versatility lies in that it can be operated as a primary melting furnace for concentrate when stockpiles are high, as a slag cleaning furnace for the converters, or occasionally as the 'smelter dustbin'.

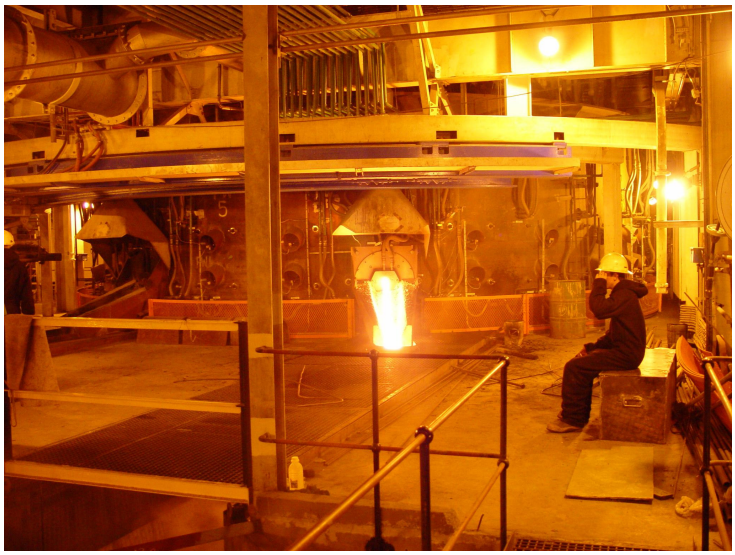

Figure 30: Tapping slag from the slag cleaning furnace. Photograph taken by R. Hundermark and displayed courtesy of Rustenburg Platinum Mines Ltd, Waterval Smelter.

4.6 PROCESS FLOW AND MASS BALANCES

The processes in 1999 and 2005 (during the two main furnace sampling campaigns), as well as the slag cleaning furnace process, are shown in the flow sheets (Figs 31 to 37). Approximate values for base metal contents are also shown. The data in the flow sheets was calculated from monthly composite reports. Often, especially in 1999, internal streams were not analysed at the smelter, so data are either estimated or unavailable.

Mass balance calculations for the 2005 campaign periods associated with the flow sheets are shown in Tables 6 to 9. These were calculated from data in the smelter month end reports, and the monthly composite analyses reported from PF Retief Laboratories. Analysis results, especially for cobalt, may be understated.

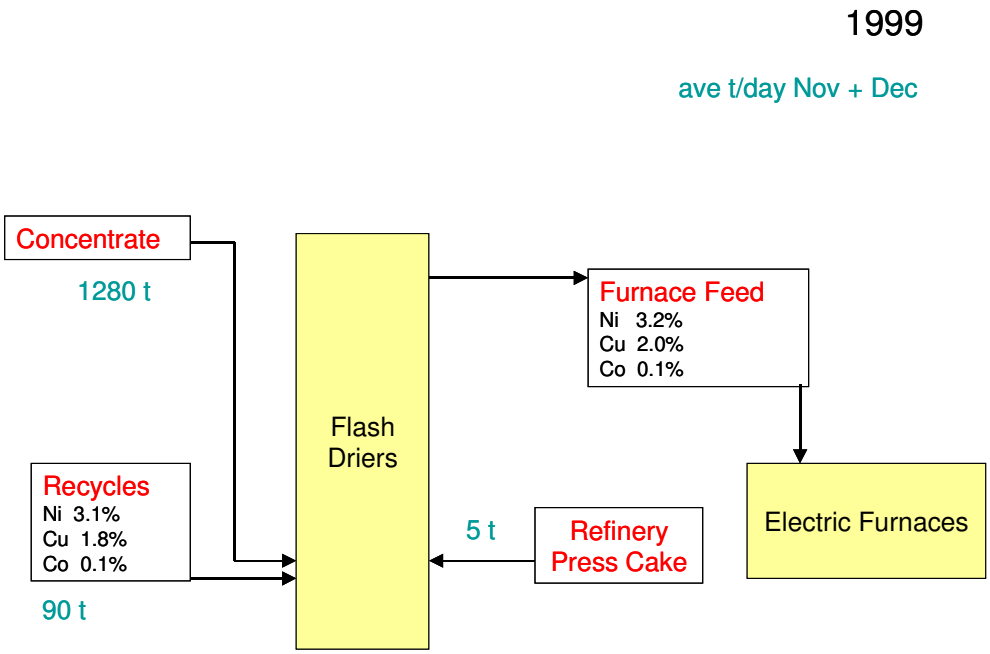

Figure 31: Flow sheet showing the flash drier process in 1999. Tonnages and base metal compositions have been included where available.

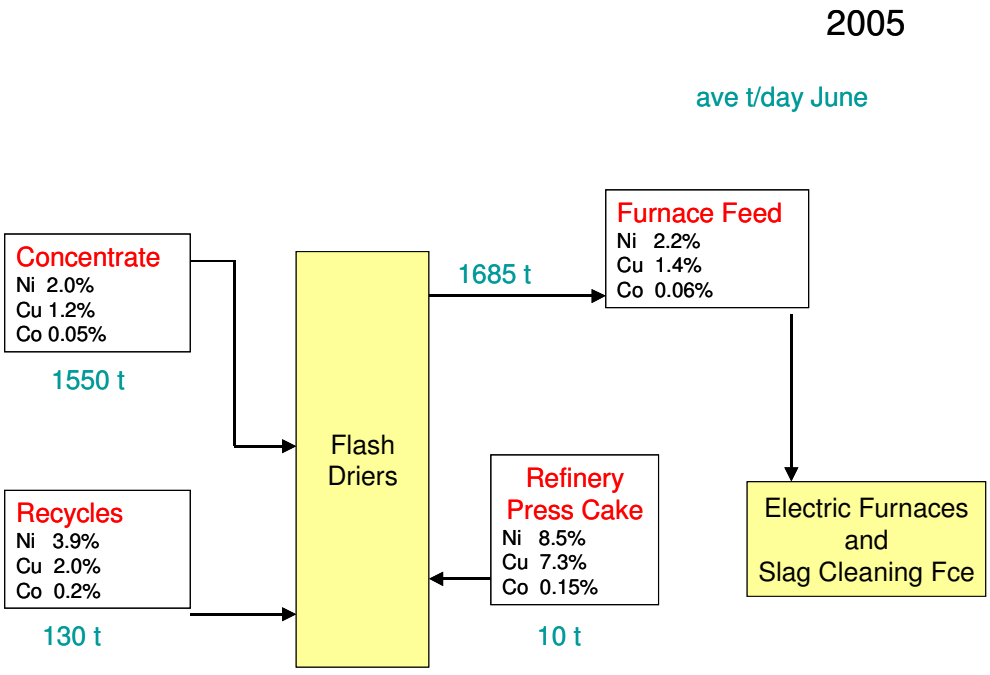

Figure 32: Flow sheet showing the flash drier process in 2005. Tonnages and base metal compositions have been included where available.

Table 6: Base metal mass balance calculations over the flash driers for June 2005.

	Cu	Ni	Co
Mass % in concentrate	1.21	1.98	0.05
Mass % in press cake	3.06	9.96	0.08
Mass % in recycles	1.30	2.42	0.16
Mass in 1548 t concentrate (t)	18.74	30.70	0.81
Mass in 11 t press cake (t)	0.34	1.10	0.01
Mass in 136 t recycles (t)	1.77	3.29	0.22
Mass in total feed (t)	20.85	35.09	1.04
Mass % in feed (calculated)	**1.23**	**2.08**	**0.06**
Mass % in feed (measured)	**1.35**	**2.21**	**0.06**

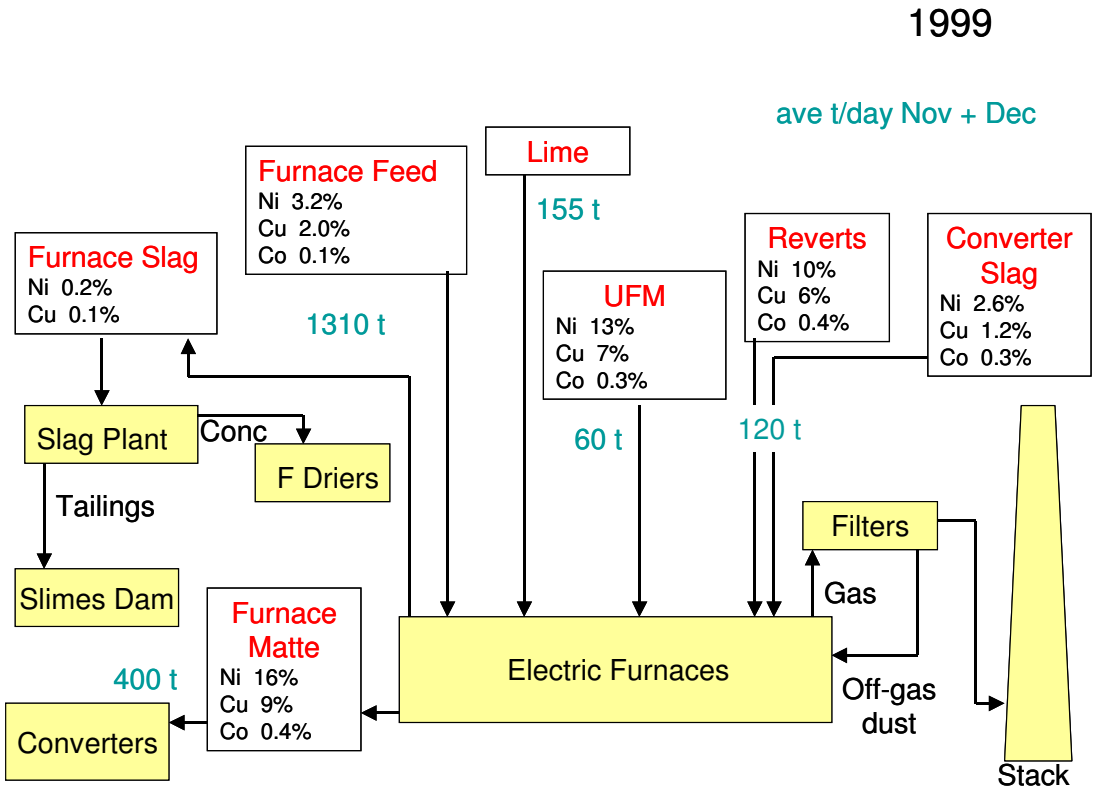

Figure 33: Flow sheet showing the electric furnace process in 1999. Tonnages and base metal compositions have been included where available. (UFM - Union Furnace Matte).

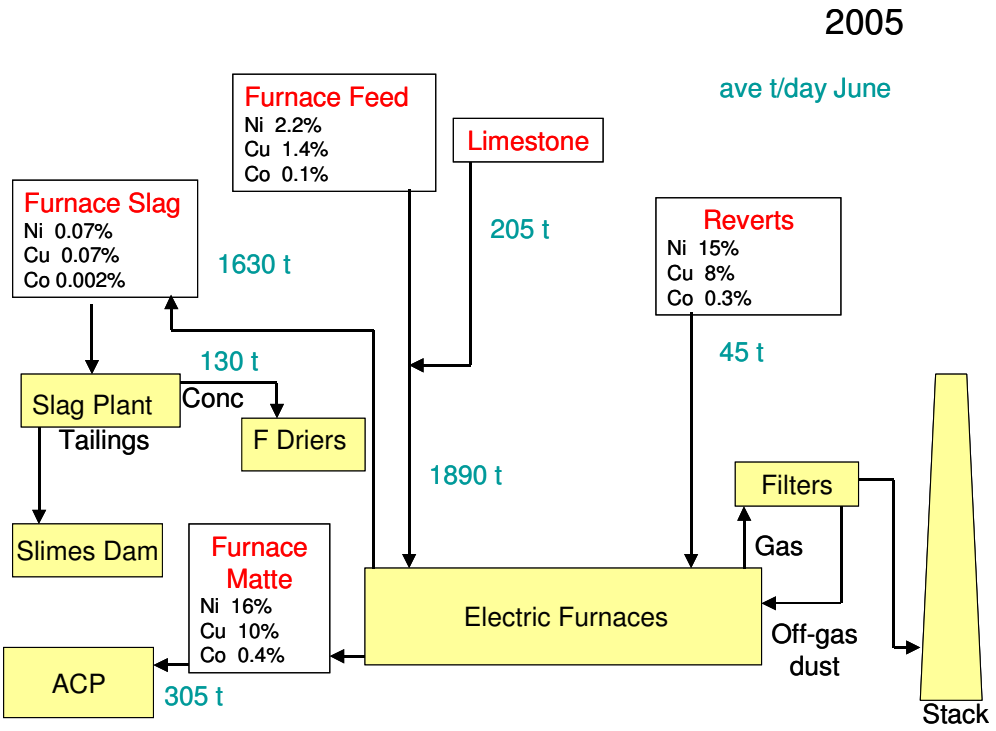

Figure 34: Flow sheet showing the electric furnace process in 2005. Tonnages and base metal compositions have been included where available. (ACP – Anglo Platinum Converting Process).

Table 7: Base metal mass balance calculations over the six-in-line furnaces for June 2005.

Input	Cu	Ni	Co
Mass % in feed	1.35	2.21	0.06
Mass % in reverts	7.00	15.20	0.30
Output			
Mass % in matte	9.10	16.30	0.30
Mass % in slag	0.07	0.07	0.00(2)
Input			
Mass in 1888 t feed (t)	25.49	41.72	1.13
Mass in 45 t reverts (t)	3.15	6.84	0.14
Total input (t)	**28.64**	**48.56**	**1.27**
Output			
Mass in 304 t matte (t)	27.66	49.55	0.91
Mass in 1629 t slag (t)	1.14	1.14	0.04
Total output (t)	**28.80**	**50.69**	**0.95**

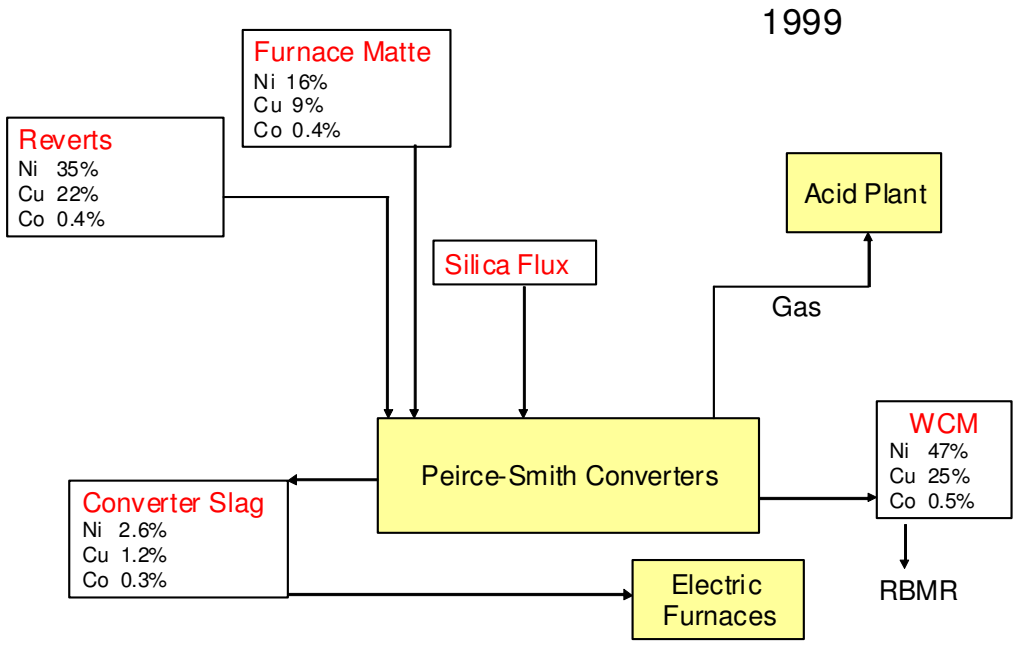

Figure 35: Flow sheet showing the converter process in 1999. Base metal compositions have been included where available. (WCM – Peirce Smith converter matte, RBMR – Rustenburg Base Metal Refinery).

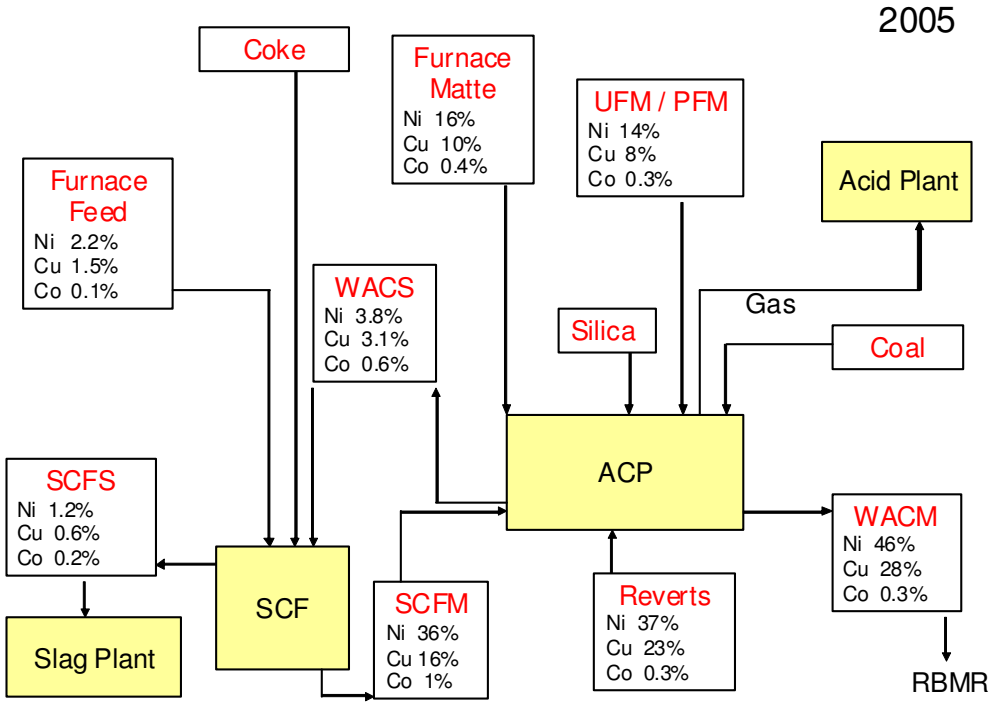

Figure 36: Flow sheet showing the converter process in 2005. Base metal compositions have been included where available. (UFM – Union Furnace Matte, PFM – Polokwane Furnace Matte, WACM – converter matte, WACS – converter slag, ACP – Anglo Platinum Converting Process, SCF – Slag Cleaning Furnace, SCFM – Slag Cleaning Furnace Matte, SCFS – Slag Cleaning Furnace Slag, RBMR – Rustenburg Base Metal Refinery).

Table 8: Base metal mass balance calculations over the converters for June 2005.

Input	Cu	Ni	Co
Mass % in furnace matte	9.10	16.30	0.30
Mass % in UFM+PFM	7.78	13.59	0.31
Mass % in SCF matte (estimate)	*16.00*	*36.00*	*1.00*
Output			
Mass % in converter matte	26.70	46.50	0.28
Mass% in converter slag	1.70	4.30	0.40
Input			
Mass in 305 t furnace matte (t)	27.76	49.72	0.92
Mass in 257 t UFM+PFM (t)	19.99	34.93	0.80
Mass in 35 t SCF matte (estimate)	*5.60*	*12.60*	*0.35*
Total input (t)	**53.35**	**97.24**	**2.06**
Output			
Mass in 140 t converter matte (t)	38.18	66.50	0.40
Mass in 360 t converter slag (t)	6.12	15.48	1.44
Total output (t)	**44.30**	**81.98**	**1.84**

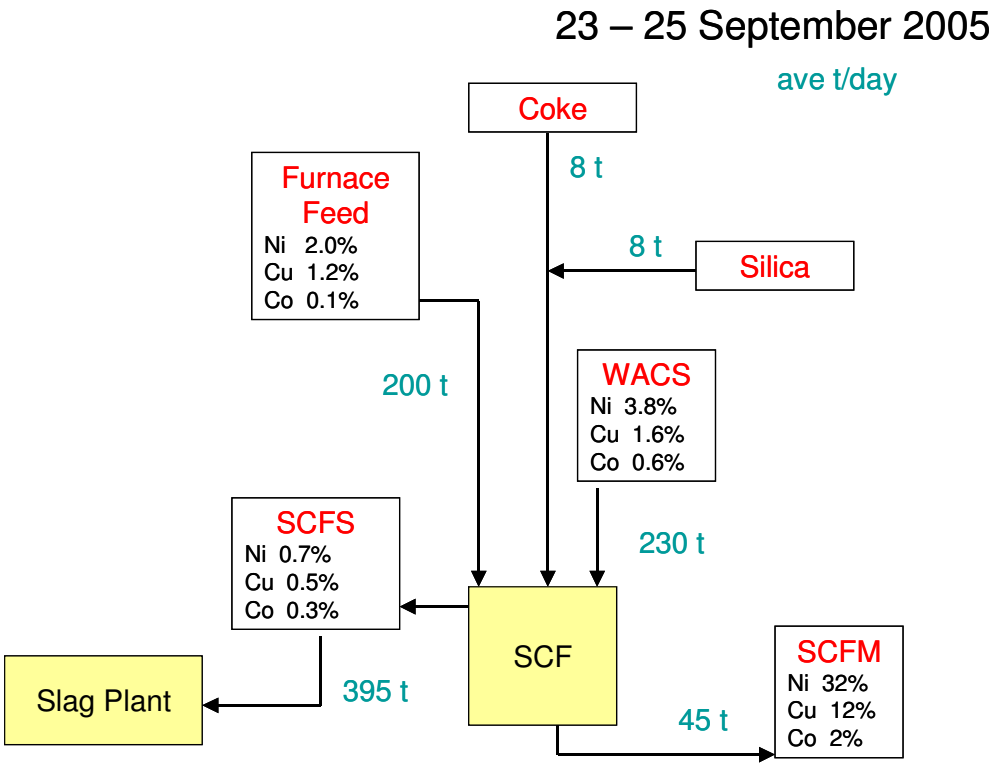

Figure 37: Flow sheet showing the slag cleaning furnace process in 2005. Tonnages and base metal compositions have been included where available. (WACS – converter slag, SCF – Slag Cleaning Furnace, SCFM – Slag Cleaning Furnace Matte, SCFS – Slag Cleaning Furnace Slag).

Table 9: Base metal mass balance calculations over the slag cleaning furnace for September 2005.

Input	Cu	Ni	Co
Mass % in feed concentrate	1.17	2.02	0.11
Mass % in converter slag	1.56	3.76	0.55
Output			
Mass % in SCF matte	12.40	31.60	1.67
Mass % in SCF slag	0.48	0.71	0.26
Input			
Mass in 201 t feed concentrate (t)	2.35	4.06	0.22
Mass in 230 t converter slag (t)	3.59	8.65	1.27
Total input (t)	**5.94**	**12.71**	**1.49**
Output			
Mass in 43 t SCF matte (t)	5.33	13.59	0.72
Mass in 396 t SCF slag (t)	1.90	2.80	1.03
Total output (t)	**7.23**	**16.39**	**1.75**

Although the mass balance calculations agree reasonably well for the flash driers and the six-in-line electric furnaces, this is not true for the converters. Apart from the habit of stockpiling, practices such as the return of unrecorded amounts of high grade reverts (reject ingots, matte ladle skulls, *etc.*) to the converters are probably responsible for the discrepancies.

The mass balance over the slag cleaning furnace should be in better agreement. A problem may have been experienced with the load cells, leading to inaccurate tonnage recordings.

The values quoted for cobalt in all the flow sheets and mass balance tables should be treated with caution due to questionable analytical accuracy in determining small amounts of this element.

The average matte and slag compositions during the 1999 and 2005 campaigns are shown in Tables 10 and 11. These were averaged from the samples taken at the time and therefore are not of exactly the same composition as shown in the flow sheets and mass balance tables.

Table 10: The average compositions (in mass %) of matte during the campaigns. For comparison purposes, the results have been normalised after removing contaminants from entrained slag and refractory. Also included are the average matte-tapping temperatures (Temp) in °C.

Date	Furnace	Fe	Co	Ni	Cu	S	Temp
1999	1	44.14	0.49	17.59	9.35	28.43	1330
1999	2	43.99	0.52	17.87	9.44	28.19	1306
2005	1	41.32	0.39	17.53	11.14	29.61	1394
2005	2	41.60	0.38	17.26	11.04	29.72	1384
2005	SCF	30.71	1.76	33.34	13.08	21.10	1239

Table 11: The average compositions (in mass %) of slag during the campaigns. For comparison purposes, the results have been normalised. Also included are the average slag-tapping temperatures (Temp) in °C.

Date	Furnace	FeO	Co	Ni	Cu	S	MgO	Al_2O_3	SiO_2	CaO	Cr_2O_3	Temp
1999	1	20.28	0.04	0.17	0.09	0.45	17.61	4.24	46.31	9.51	1.30	1448
1999	2	23.74	0.06	0.15	0.08	0.46	16.14	3.82	45.23	9.36	0.96	1460
2005	1	14.21	0.02	0.14	0.08	0.29	21.99	5.44	47.88	8.47	1.47	1523
2005	2	13.35	0.02	0.14	0.07	0.31	21.26	5.40	47.60	10.51	1.35	1495
2005	SCF	47.21	0.26	0.72	0.48	0.71	8.03	2.95	35.60	1.94	2.10	1508

A decrease in slag nickel and cobalt content for the six-in-line furnaces is evident between 1999 and 2005.

5 SAMPLING

5.1 ELECTRIC FURNACE (SIX-IN-LINE) SAMPLING

5.1.1 Sampling overview

During the initial campaign (November-December 1999), samples of granulated slag were collected on a weekly basis from the two electric furnaces. The electric furnaces are large and residence time is estimated to be two to four days – hence the weekly sampling times.

More frequent sampling was employed in November 2004 when sampling Furnace 1 over the introduction of reverts addition. Fortuitously, this campaign also encompassed an unplanned lime addition spike.

The campaign run on both furnaces during May and June 2005 was the most rigorous; again the furnaces were sampled weekly over four weeks.

Finally, sounding bar samples were taken from Furnace 2 in October 2006 and Furnace 1 in September 2007 to check for compositional variation of slag and entrained matte with depth in the furnace.

The sampling schedule for the six-in-line electric furnaces is shown in Tables A1–A3 and A5 in Appendix A.

5.1.2 Sampling methodology (six-in-lines)

Granulated slag samples were taken from the upper end of the rake classifiers by collecting a cut over one fin (Figure 38). This is the method used for metal accounting. Residence time in the rake classifiers is claimed to be 5 to 10 minutes providing that the rakes are adjusted to minimise the dead zone, although previous tracer work suggests that there may be slightly more spread of peaked information as compared to samples taken at the tap hole. The advantage of taking samples from the classifier is that superior quenching will have taken place.

Figure 38: Slag was sampled from the ends of the rake classifiers, by taking a cut across the fins. Photograph taken by the author, and displayed courtesy of Rustenburg Platinum Mines Ltd, Waterval Smelter.

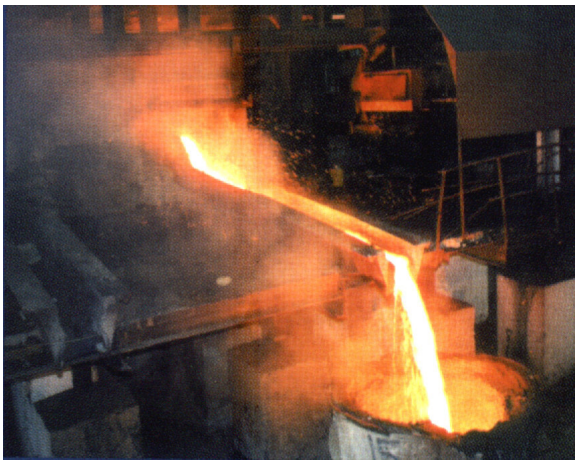

Figure 39: Matte spoon samples were taken from the ladle. Photograph courtesy of Rustenburg Platinum Mines Ltd, Waterval Smelter.

Spoon samples of slag were taken at the slag tap hole, and matte spoon samples from the ladle (Figure 39).

Feed samples were taken from the flash driers, and recycles from the belt filter (for slag plant concentrate) in the concentrate storage shed. Reverts were sampled from the bins on the furnace roof where they are stored prior to being fed into the furnaces.

Sounding bar samples are collected on an iron bar that is lowered into the furnace to measure the slag, matte and hearth build-up levels. After cooling, the bar is marked off in 10 cm sections and the samples chipped off and collected on a shovel.

5.2 SLAG CLEANING FURNACE SAMPLING

5.2.1 Sampling overview

The slag cleaning furnace is relatively small and has a shorter residence time than the electric furnaces (approximately one day). When the furnace was first installed it was run in batch mode, usually over two to three days. More recently the furnace has been run continuously.

Slag samples were collected during seven early optimisation runs (2003–2004), and more rigorous sampling took place when operation had stabilised to some extent (2005). Of the seven early trials, only four are reported here, being confined to those run with ACP converter slag, and without PS converter slag and revert addition, due to uncertainty as to the true feed composition.

The sampling schedule for the 2005 slag cleaning furnace campaign is shown in Table A4 in Appendix A.

5.2.2 Sampling methodology (SCF)

As with the electric furnaces, granulated slag samples were taken from the upper end of the rake classifiers by collecting a cut over one fin. Because the slag cleaning furnace runs at temperatures closer to the liquidus, crystallinity is unavoidable when slag is taken from the tap holes, even with rapid hand granulation.

Concentrate samples were taken from the flash drier, converter slag from the silo, and matte spoon samples were collected from the ladle.

6 ANALYTICAL TECHNIQUES

6.1 OVERVIEW

Crushed spoon, as well as granulated, samples were split and pulverised for chemical analysis and X-ray diffraction (XRD), and also prepared as polished sections. These were examined using the ore microscope, and imaged on the scanning electron microscope (SEM).

Concentrate feed, reverts and recycle samples were examined on the SEM, and also on the QEMSCAN. The sulphide phases present in selected concentrates were quantitatively analysed on the electron microprobe using wavelength dispersive X-ray (WDX) spectroscopy.

The granulated slag samples were run on the Minerals Liberation Analyser (MLA) for modal analyses, as well as for matte size and composition. Slag oxide and silicate phases were analysed by means of WDX on the electron microprobe.

Matte phases present in spoon samples were characterised using energy dispersive X-ray (EDX) analysis on the SEM (SEM-EDX), and optical modal analysis.

6.2 CHEMICAL ANALYSIS

Bulk chemical analysis results were determined at Anglo Research, although some samples were outsourced to Mintek, and at P.F. Retief Laboratory (Kroondal).
The methods used were base metal fusion and inductively coupled plasma – mass spectrometry (ICP-MS) for Mg, Al, Si, Ca, Ti, Cr, Fe, Co, Ni and Cu, LECO for sulphur, and Atomic Absorption Spectroscopy for sodium.
Some idea of the error in matte and slag analysis results using these techniques are provided in Tables 12 and 13.

Table 12: The percentage error (%) at averaged slag composition for the 2005 six-in-line furnace slag samples. N/s = not supplied.

	Na_2O	MgO	Al_2O_3	SiO_2	K_2O	CaO	Ti	Cr_2O_3	Fe	Co	Ni	Cu	S
Ave	0.38	21.48	5.32	46.72	0.228	8.28	0.16	1.44	10.82	0.024	0.135	0.076	0.282
±%	0.2	1.74	1.56	1.7	n/s	0.7	0.2	1.14	0.2	5.5	1	1.25	18

Table 13: The percentage error (%) at averaged slag composition for the 2005 six-in-line furnace matte samples.

	Mg	Al_2O_3	Si	Ca	Cr_2O_3	Fe	Co	Ni	Cu	S
Ave	<0.3	1.28	<0.23	<0.17	0.965	39.95	0.378	16.8	10.68	28.38
±%	11	1.56	3.7	28	1.14	0.62	5.5	1	3	1

Some of the early SCF samples were analysed at the ACP Robolab at the smelter – this employs X-ray Fluorescence (XRF) analysis.

6.3 X-RAY POWDER DIFFRACTION (XRD)

Samples were milled in the McCrone micronising mill to reduce particle size to 75 % passing 10 µm, the size required for good XRD resolution. The powders were then X-rayed on the Phillips PW1830 X-ray Diffractometer and processed using Diffrac Plus software.

XRD works on the Bragg angle diffraction principal (REYNOLDS, 1989). The resulting diffraction scan can be processed to produce structural, as distinct from compositional, data on the material analysed. (KLUG & ALEXANDER, 1974, JENKINS, 1989).

When the crystal size is too small or the material is amorphous (structureless) no pattern will be produced (as was the case in most of the granulated slag samples).

6.4 SECTION PREPARATION

Polished sections are polished mounts of particulate material prepared for ore microscopy, scanning electron microscopy, MLA, QEMSCAN and/or electron microprobe analysis.

Polished sections were prepared of unsized feed concentrate and recycles for QEMSCAN analysis using graphite addition for particle separation.

Matte and slag spoons, as well as reverts, were crushed to <3 mm for section preparation,

Granulated furnace, slag cleaning furnace, and converter slag samples were initially prepared using the Epovac technique, claimed to eliminate settling. To test whether this did indeed apply to matte/slag mixtures, samples of 'clean' furnace slag and pure furnace matte were prepared to produce predetermined volumes on the image analyser. The relative densities of the slag and matte were measured on the AccuPyc 1330 pycnometer for mass to volume conversion, and the results are shown in Table 14.

Table 14: Relative densities of Furnace 2 granulated matte and slag samples.

Sample type	*Date*	*RD (sd)*	*Temperature*
Matte	12 April 2006	4.95 (0.02)	23.1° C
Slag	13 April 2006	2.98 (0.04)	24.3° C

The results of image analysis on the resulting sections are shown in Table 15. The matte modal percentage is much higher than actual, so the Epovac technique is not effective in this case, probably due to the relatively coarse grain size and the large difference in relative densities.

Table 15: Averaged image analysis results for Epovac and vertically mounted sections.

Prepared volume %		Measured volume % Epovac		Measured volume % vertical mounts	
matte	slag	matte	slag	matte	slag
2	98	8	92	5	95
10	90	37	63	13	87
25	75	64	36	33	67
50	50	82	18	58	42

Following this discovery, all the 2005 slag sections were remade as vertical sections (or bottle mounts). This involves setting the slag in resin, during which it will settle, then cutting the section in half vertically and remounting on its side. The results of image analysis on vertical sections prepared from the same test sections are also shown in Table 15. These are closer to, but not identical to, the true modal percentages. The test situation was the worst-case scenario, containing large matte particles, and only three sections of each were measured on the image analyser. Smaller matte entrainment areas and multi-section measurement on the automated electron microscopes would minimise this type of error.

After ultrasonic treatment to remove adhering concentrate, the sounding bar samples were hand picked to select pieces representing a full bath profile. These were carefully mounted so that the inner and outer boundaries were defined.

6.5 SCANNING ELECTRON MICROSCOPY

This technique is the basis of CC-SEM (computer-controlled scanning electron microscopy) analysis. Imaging, analysis, and applications of this technique are described by GOLDSTEIN *et al.,* (1981).

The scanning electron microscope (SEM) used for energy-dispersive X-ray (EDX) analysis and back-scattered electron (BSE) imaging was the JEOL JSM-5400 at Anglo Research (Figure 40). This is operated using Thermo-NORAN VANTAGE software (version 4.01). The instrument operates by scanning an electron beam across the surface of a sample, and processing the back-scattered electrons emitted to produce an image where the intensity is sensitive to the atomic number of the phase under the beam. Spot analysis of phases is also possible when characteristic X-radiation is emitted and analysed using an EDX detector.

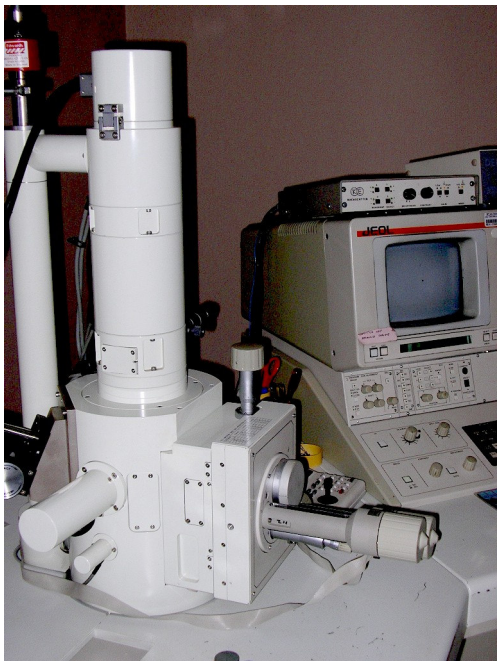

Figure 40: The JEOL scanning electron microscope.

Matte and entrained matte phases, and other finely-intergrown samples were analysed on the SEM because the image resolution is superior to that of the microprobe. Analysis is standardless and the results are normalised, but matte analysis results were checked by using standards as unknowns, and the results were reasonably accurate, as shown in the example below – run during the 2005 furnace and slag cleaning furnace matte analyses (Table 16).

Table 16: JEOL SEM-EDX analysis of microprobe standards (mass %). These points are on five different positions per standard.

Standard	*S*	*Fe*	*Ni*	*Cu*	*Pt*
$CuFeS_2$	35.8	30.6		33.6	
	35.6	30.0		34.4	
	35.7	30.6		33.7	
	35.7	31.2		33.1	
	35.7	30.6		33.7	
EDX average	**35.7**	**30.6**		**33.7**	
Actual	**35.0**	**30.5**		**34.5**	
NiS	37.0		63.0		
	36.8		63.2		
	36.9		63.1		
	36.6		63.4		
	36.5		63.5		
EDX average	**36.8**		**63.2**		
Actual	**35.3**		**64.7**		

6.6 AUTOMATED SCANNING ELECTRON MICROSCOPY

Two different computer-controlled SEM (CC-SEM) systems were used to characterise the samples. QEMSCAN instrumentation processed the concentrate/flash drier products, recycles and revert samples, and the Minerals Liberation Analyser (MLA) was set up to examine entrained matte phases in the slag samples. Although both of these systems are predominantly used for mineral liberation studies in flotation research, they can be adapted for other purposes.

Quantitative evaluation of minerals by scanning electron microscopy (QEM*SEM, and later QEMSCAN) techniques, and their applications, have been described by a number of authors (GOTTLIEB *et al.,* 2000, PIRRIE *et al.,* 2004, SUTHERLAND & GOTTLIEB, 1991). MLA is a similar technique, the basics of which are described by GU (2003).

In the present study, linear point analysis on the CC-SEMs was used to produce modal phase analyses of the samples. The systems employ both BSE imaging and EDX point short count acquisition. The EDX spectra are processed, and compared against a database to identify the mineral phase under the beam. Modal percentages are computed over many particles in a similar method to linear analysis in metallography. The results are obtained in volume per cent and are converted to mass per cent using the relative densities of the phases concerned. Generally, sufficient points are processed to produce reliable modal percentages even although the samples are analysed in section. Results are checked against chemistry. For particle sizing and association, a stereological factor may be introduced while processing the data.

The QEMSCAN used in this study consists of a LEO SEM with integrated QS software (Figure 47).

Automated sizing, modal analysis and EDX analysis of entrained matte (EM) phases in slag were performed on a system consisting of a Quanta 600 SEM with integrated MLA software (Figure 48). Spectra were initially acquired on the slag phases and stored as standards.

The combination of phase size with composition was achieved using the Latti measurement mode, where a phase is programmed to trigger a "long count" X-ray analysis, the results being comparable with a high quality quantitative EDX measurement. The method combines back-scattered electron (BSE) image analysis and EDX phase area analysis to provide automated quantitative analysis results (FANDRICH, *et al.,* 2007). Although this technique was mainly used to identify trends, the EDX results were adjusted against chalcopyrite ($CuFeS_2$) and millerite (NiS) microprobe standards before comparisons were made to bulk matte compositions. The system is still being developed for this type of work. Early in the study, the MLA was used to record the position and size of entrained matte phases, and the author had to relocate and analyse the phases manually. Size and area analysis of the 2005 furnace slag EM phases were acquired simultaneously and later combined by software processing. At this stage the fully automated mode does not run successfully on SCF slag EM, due to high EM density.

The “long count” results are reported using confidence intervals – the method of calculation is described in Appendix C. Also detailed in the Discussion (Page 116) is the Saltykov method for relating phase size in section to relative volume.

Figure 47: One of the QEMSCANs.

Figure 48: Operating one of the MLAs.

6.7 ELECTRON MICROPROBE ANALYSIS

The theory behind, and applications of, electron microprobe (EMP) analysis have been described by various authors (RUCKLIDGE, 1976, VILJOEN & JOHNSON, 1983, GOLDSTEIN *et al*, 1981, REED, 1996).

The electron microprobe operates using the same principle as the SEM, but has the capability of performing quantitative WDX analysis. This involves calibrating on, and checking of, standards and allows the composition of major elements in microscopic phases to be determined to within ± 2% relative, and of trace

elements to within ± 5% relative. Microprobe results are reported with mean (average) values and standard deviation, and the methods of obtaining these are described in Appendix C.

It should be noted that in all results reported as oxides (for the microprobe and the SEM), oxygen is not measured, but is calculated by stoichiometry.

All the WDX analyses for the project were performed on the JEOL 733 Superprobe at Anglo Research (Figure 49). This instrument utilises three WDX spectrometers, an EDAX energy dispersive X-ray (EDX) detector for simultaneous determination of all elements heavier than boron, and an integrated software system (Advanced Microbeam Probe for Windows version 4.52).

Of the WDX spectrometers, one contains a lighter element crystal (TAP) and a gas flow detector. This was used to analyse sodium, magnesium, aluminium and silicon. Unfortunately, for the slag analysis, all the transition metals had to be analysed on one spectrometer (LIF crystal) because the third spectrometer had to be set up with PET for calcium and sulphur. This caused relatively long total analysis times.

At the time of the analysis, the gain and high voltage settings had to remain constant for all elements analysed per spectrometer, because these could only be set manually. This produced high detection limits for sodium and titanium.

Figure 49: The JEOL 733 Superprobe, which was used for all the electron microprobe determinations.

The analysis conditions and standards that were chosen for the quantitative major and trace element WDX analysis of the slag and spinel phases are shown in Tables 17 and 18, and the detection limits of the base metals are shown in Table 19. The methods of calculating detection limits for trace elements are given in Appendix C.

The microprobe accelerating voltage was set at 20 kV with a specimen current of 20 nA. Pulse Height Analyser (PHA) windows were set up on aluminium and sulphur to cut out higher order interference, and on

nickel, copper and sulphur to reduce the detection limits. Software correction was used to strip counts from the tail of the first order Fe K_β peak from the Co K_α peak – background adjustments are usually made (ANDREWS, 1999) but these were not required in this case.

Table 17: Microprobe WDX analysis conditions for slag and spinel determination.

Element	X-ray line	Crystal	Peak position (mm)	Background offset (mm)	Peak/background counting time (secs)
Na	K-α	TAP	129.47	± 4	40/20
Mg	K-α	TAP	107.51	± 4	20/10
Al	K-α	TAP	90.66	± 4	20/10
Si	K-α	TAP	77.47	± 5	20/10
S	K-α	PET	172.10	± 4	20/10
Ca	K-α	PET	107.60	± 4	20/10
Ti	K-α	LIF	191.01	± 5	20/10
Cr	K-α	LIF	159.31	± 5	20/10
Fe	K-α	LIF	134.72	± 5	20/10
Co	K-α	LIF	124.49	± 5	40/20
Ni	K-α	LIF	115.20	± 4	40/20
Cu	K-α	LIF	107.12	+4, -5	40/20
Co	K-α	LIF	124.49	± 4	200/100
Cu	K-α	LIF	107.12	+4, -5	80/20

Table 18: Standards used for WDX analysis of slag and spinel phases.

Element	Primary Standard	Formula	Secondary standard	Formula
Na	Albite	$NaAlSi_3O_8$		
Mg	Periclase	MgO	Olivine	$(Mg,Fe)_2SiO_4$
Al	Corundum	Al_2O_3	Chromite	$(Mg,Al,Cr,Fe)_3O_4$
Si	Quartz	SiO_2	Olivine	$(Mg,Fe)_2SiO_4$
S	Anhydrite	$CaSO_4$		
Ca	Wollastonite	$CaSiO_3$		
Ti	Rutile	TiO_2		
Cr	Eskolaite	Cr_2O_3	Chromite	$(Mg,Al,Cr,Fe)_3O_4$
Fe	Hematite	Fe_2O_3	Chromite	$(Mg,Al,Cr,Fe)_3O_4$
Co	Cobalt oxide (syn)	CoO		
Ni	Bunsenite	NiO		
Cu	Cuprite	Cu_2O		

Table 19: Detection limits (3σ) of the minor and trace elements, in ppm.

Counting times	Element	Detection limit	Oxide	Detection limit
Normal	Na	420	Na_2O	565
Normal	S	230	SO_3	575
Normal	Ti	860	TiO_2	1435
Normal	Co	160	CoO	200
Normal	Ni	170	NiO	220
Normal	Cu	200	Cu_2O	220
Long	Co	80	CoO	100
Long	Cu	150	Cu_2O	170

Wherever possible, positions were preprogrammed on the slag glass phase and the instrument was able to run these analyses automatically. This was successful for the electric furnace slag samples and most of the SCF slag samples. Where microcrystallinity had developed or where tiny entrained matte particles were plentiful, as in some SCF slag and all converter slag samples, the phases had to be positioned on manual. All furnace slag spinel and most of the SCF and converter slag spinel and magnetite were positioned manually.

Base metal-containing sulphide minerals in flash drier product (furnace feed) were also analysed on the electron microprobe, and the element set up, standards and detection limits are shown in Tables 20 to 22.

Table 20: Microprobe WDX analysis conditions for sulphide determination.

Element	X-ray line	Crystal	Peak position (mm)	Background offset (mm)	Peak/background counting time (secs)
As	L-α	TAP	105.59	± 4	40/20
S	K-α	PET	171.97	± 4	20/10
Fe	K-α	LIF	134.6	± 4	20/10
Co	K-α	LIF	124.50	± 4	40/20
Cu	K-α	LIF	107.22	± 4	40/20
Ni	K-α	LIF	115.4	± 4	40/20

Unfortunately, no troilite (FeS) standard was available. This would have been more suitable for pyrrhotite analysis.

Table 21: Standards used for WDX analysis of feed sulphide minerals.

Element	Primary Standard	Formula
As	Arsenopyrite	FeAsS
S	Pyrite	FeS_2
Fe	Pyrite	FeS_2
Co	Cobalt sulphide	CoS
Cu	Chalcopyrite	$CuFeS_2$
Ni	Millerite	NiS

Table 22: Detection limits (3σ) of the sulphide analysis elements, in wt %.

Element	Detection limit
As	0.217
S	0.040
Fe	0.060
Co	0.025
Cu	0.027
Ni	0.032

In the event, arsenic was not detected in any of the feed sample sulphides, and so is not reported.

6.8 MÖSSBAUER SPECTROSCOPY

The Mössbauer effect is the recoil-free emission and resonant absorption of γ-rays by specific atomic nuclei in solids (MÖSSBAUER, 1958, quoted in HAWTHORNE, 1988). The theory behind Mössbauer Spectroscopy

has been described in detail in the literature (HAWTHORNE, 1988, SWARTZENDRUBER & BENNETT, 1986).

The Mössbauer effect has been detected in over one hundred isotopes, but one of the most commonly used isotopes is ^{56}Fe, the isotope used in the present study.

Selected samples were analysed by Mössbauer Spectroscopy at the Chemical Engineering Department of the North-West University (Potchefstroom Campus). This was in order to establish the Fe^{2+} / Fe^{3+} ratio, which provides information on the pO_2 conditions present in the slag samples.

The analyses were performed on a Halder Mössbauer Spectrometer fitted with a proportional counter filled to 2 atm with xenon (Figures 50 and 51). Spectra are obtained by Doppler scanning, *i.e.* by measuring a count rate as a function of the relative velocity between a γ-ray source and an absorber. The γ-rays were emitted from a 50 mCi ^{57}Co source, and the velocity scale was calibrated using an α-iron standard. The spectra, collected at room temperature, were recorded in a multi-channel analyzer and processed using the PC-Moss II computer program. The spectra were least squares fitted with superimposed Lorenzian lines, whilst the species present were identified by virtue of their quadrupole and isomer shifts, and hyperfine magnetic field splitting, and the amount of each constituent present was determined from the areas under the relevant peaks.

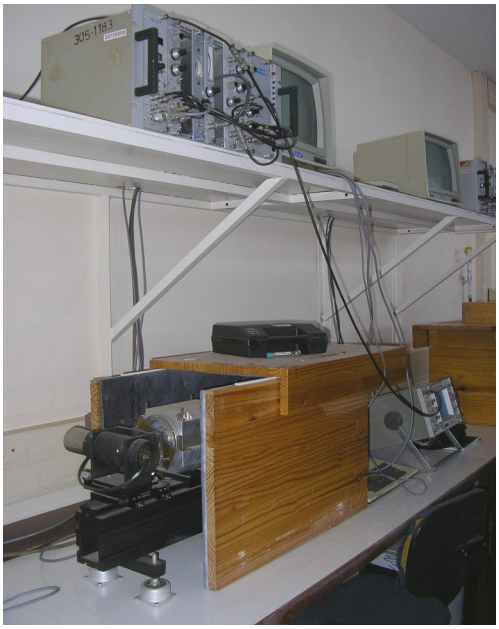

Figure 50: The Mössbauer Spectroscope at North West University.

Figure 51: A closer view of the instrument.

6.9 FactSage MODELLING

The modelling program used in this project was FactSage – the thermochemical software and databases are described by BALE and co-workers (2002).

The various slag-matte systems were modeled using the Equilib Module (in FactSage version 5.4.1). Normalised matte compositions (Fe, Ni, Cu, Co and S) were entered, followed by major elements as determined by electron microprobe analysis of the slag glass (six-in-line slag) and by chemistry (SCF slag). These included MgO, Al_2O_3, SiO_2, CaO and FeO for the six-in-lines and also Cr_2O_3 for the SCF.

Temperature ranges of 1300 – 1550 °C (six-in-lines) and 1200 – 1500 °C (SCF) were selected to include the range of tapping temperatures recorded at the smelter, and pressure was set at 1 atm.

The solution species used were FTmis–MATT (matte), FTmisc–FCCS (alloy), FToxid–SLAGA (slag) and FToxid–SPIN (spinel – SCF). The program calculates the activity and mass fraction of various elemental, oxide and sulphide species in the slag, including FeO-Fe_2O_3-FeO, NiO-NiS, Cu_2O-Cu_2S and CoO-CoS.

From this data, the predicted distribution of these elements in slag can be calculated, as well as the relative amount of sulphidic and oxidic dissolution.

7 RESULTS

The samples taken from the six-in-line and slag cleaning furnaces are described in Tables A1 to A5 in Appendix A. WS numbers (Waterval Smelter sampling labels) have been retained where these were assigned, in order to facilitate access to furnace operation parameters.

7.1 ELECTRIC FURNACES (six-in-line)

The results of the 1999, 2004 and 2005 campaigns are dealt with below. It should be emphasized that the 1999 campaign was essentially a slag characterisation exercise, so matte and feed data had to be taken from the metal accounting reports and monthly composites written at that time.

The results of sounding bar sampling during 2006 and 2007 to establish entrained matte and slag compositional variation with depth in the slag bath are also included in this section.

7.1.1 Furnace feed

The main component of six-in-line furnace feed is blended ore concentrate. Other materials added to the furnaces are limestone (flux), liquid converter slag (1999), reverts (the remnants of run-outs and ladle skulls), Union and Polokwane furnace mattes, recycles or "belt filter product" (slag plant concentrate, sometimes with off-gas solids), and, occasionally, filter press cake from the refineries.

Flash drier products contain ore concentrate, recycles and press cake, but limestone and reverts are added later.

The composition of limestone flux is shown in Table 23.

Table 23: Results of chemical analysis, in mass %, of the limestone flux in use during 2005. Please note that carbonate was not analysed.

Limestone	MgO	Al_2O_3	SiO_2	CaO	Fe
May 2005	1.63	1.41	9.22	46.00	0.99

The impurities in this material are mainly quartz, feldspar and iron oxides.

7.1.1.1 Flash drier product

The results of chemical analysis of the 2004 and 2005 flash drier products are shown in Tables A6 and A7 in Appendix A, and averaged in Table 24 below.

Table 24: The average compositions of the flash drier product samples (in mass %). The 1999 results are from monthly composites, the 2004 same-day samples (both analysed at P.F. Retief laboratories in Rustenburg) and the 2005 samples were analysed at Anglo Research.

Date	MgO	Al_2O_3	SiO_2	CaO	Cr_2O_3	Fe	Co	Ni	Cu	S	Ni:Fe	Ni:Cu
1999	14.65	3.81	36.50	5.18	0.70	14.75	0.07	3.22	1.95	8.57	0.22	1.65
2004	15.60	3.32	36.81	2.33	1.02	18.47	0.12	5.18	1.74	10.06	0.28	2.98
2005	13.80	3.87	33.30	3.54	1.27	18.40	0.14	4.20	2.66	10.12	0.23	1.58

The base metals occur in the concentrates as major or trace elements in a number of different ore minerals, such as pentlandite ($(Ni,Fe)_9S_8$), pyrrhotite ($Fe_{1-x}S$), chalcopyrite ($CuFeS_2$), pyrite (FeS_2), millerite (NiS), and

bornite (Cu_5FeS_4). The concentrates consist mainly of silicate and oxide minerals – the mineral contents of the 2005 samples are shown in Table 25.

Table 25: The results of QEMSCAN analysis of the 2005 flash drier product samples, in mass %.

Mineral/phase	WS1997	WS2013	WS2021
Total sulphides	**20.6**	**38.0**	**29.6**
Pentlandite	7.4	14.6	11.8
Millerite	0.2	0.6	0.1
Pyrite	1.1	2.5	1.5
Pyrrhotite	5.3	9.1	8.6
Chalcopyrite	6.0	10.4	7.1
Bornite	0.5	0.6	0.3
Other sulphides + PGM's	0.1	0.2	0.2
Iron oxides	**5.6**	**7.5**	**6.7**
Chromite	**3.0**	**2.8**	**3.0**
Carbonates	**0.3**	**0.5**	**0.3**
Total silicates	**70.5**	**51.2**	**60.4**

The QEMSCAN results, as well as those of chemical analysis, show the 2005 samples to vary substantially in mineralogy and composition.

Although the mineralogical break-downs of the furnace feed samples may seem to be irrelevant, they are important for labile sulphur calculations, as well as smelting energy requirements. For the purpose of this project they provide information on base metal distribution in the feed. The results of sulphide microprobe analysis run on September 2005 flash drier product are reported in Table 56 (Page 87). These were used to compare the composition of sulphide feed with bulk matte and entrained matte in slag for both the six-in-line and the slag cleaning furnaces.

7.1.1.2 Reverts

The averaged results of chemical analysis of the reverts are shown in Tables A8 and A9 in Appendix A and averaged in Table 26 below.

Table 26: The average compositions of the reverts samples (in mass %). All the samples were analysed at Anglo Research.

Date	MgO	Al_2O_3	SiO_2	CaO	Cr_2O_3	Fe	Co	Ni	Cu	S	Ni:Fe	Ni:Cu
2004	2.98	4.32	20.68	1.77	2.84	26.55	0.30	13.26	7.12	9.08	0.50	1.86
2005	4.28	2.92	17.80	1.85	3.57	26.70	0.32	15.60	8.69	9.90	0.58	1.80

No reverts analyses are available for the 1999 campaign.

Reverts consist of a complex mixture of converter and furnace matte (nickel and iron-rich respectively), converter slag, electric furnace slag, silica, refractory material, chrome-rich furnace products containing chromium-bearing spinel (2004), and occasional nickel sulphide-sulphate masses (2005). BSE images of revert phases are shown in Figures 52 and 53. It should be noted that the samples were crushed to -3 mm prior to section preparation.

An attempt was made to determine the modal percentage and source of the various components by QEMSCAN, and the results of this exercise for the 2005 reverts samples are shown in Table 27.

Table 27: An example of the use of QEMSCAN to establish the source of reverts samples. The modal values are in mass %.

	Source			*Sample*			
Phase	Converter	SCF	Furnace	WS1998	WS2004	WS2023	WS2024
Heazlewoodite	X	x		15.2	14.9	10.7	22.2
Bornite	X	X	X	4.2	5.7	8.3	6.8
Djurleite	X	x		4.1	6.0	0.8	7.2
Pentlandite	x	X	X	7.4	5.4	27.2	3.0
Pyrrhotite/troilite			X	0.2	0.4	0.8	0.1
BMA, Cu	X	X	x	12.4	7.2	6.6	14.5
Total matte				**43.5**	**39.7**	**54.5**	**53.7**
Oxides	X	X	X	13.4	12.9	8.3	22.8
Low Cr spinel	x	x		1.4	1.5	0.5	2.1
Cr-Fe spinel		X	X	1.2	1.4	2.6	1.3
Total oxides				**15.6**	**15.8**	**11.3**	**26.2**
Silicate glass	x	X	X	7.5	10.1	9.8	1.8
High SiO_2	X			6.3	8.7	5.8	2.6
Mg olivine		X	X	0.4	0.4	1.0	0.1
Fayalite		x		9.6	12.5	10.9	12.9
Ol-pyroxene		X	X	11.8	7.4	2.1	0.3
Al-Ca-Fe silicate		x	X	0.5	0.5	0.4	0.2
Other silicates	X	X	X	3.1	4.0	2.1	0.5
Total silicates				**39.1**	**43.6**	**32.1**	**18.3**
Other				1.9	1.5	2.5	1.8

Although this method is not quantitative, it does allow some observations to be made – for example, sample WS2024 appears to contain a higher ratio of converter to furnace source material.

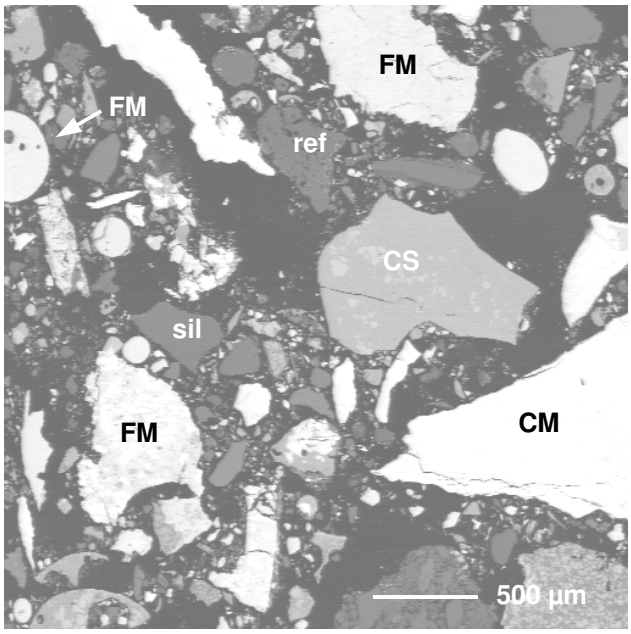

Figure 52: BSE image showing a typical area of a 2004 revert sample. Major phases here are furnace matte (FM), converter matte (CM), converter slag (CS), silica (sil), and refractory (ref). The black background material is resin.

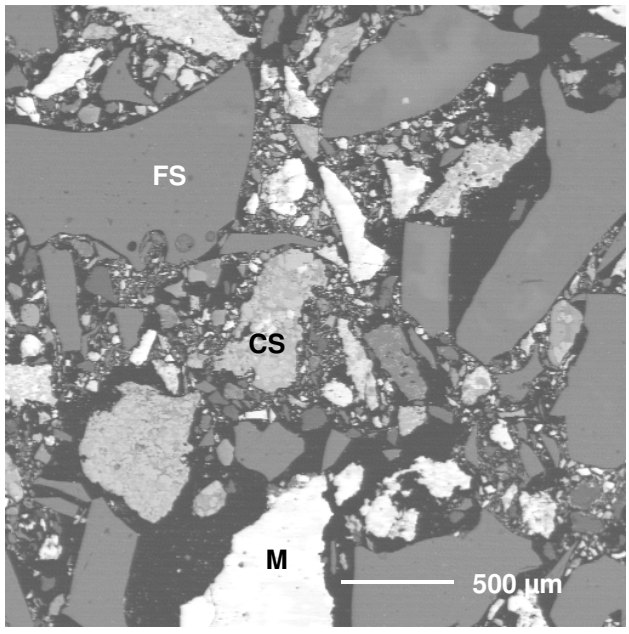

Figure 53: BSE image showing a 2005 revert sample at the same magnification. Furnace slag (FS), converter slag (CS), furnace and converter matte (M) are the most prevalent phases here.

7.1.1.3 Recycles

A small amount of recycles is sometimes added to the concentrate before flash drying. This material consists predominantly of slag plant concentrate, and so, in the later samples, contains furnace, and slag cleaning furnace, slag and matte, as well as off-gas solids. BSE images of the furnace recyles are shown in Figures 54 and 55.

The averaged results of chemical analysis of the 2005 recycle samples are shown in Table 28 and the full results are shown in Table A10 in Appendix A.

Table 28: The average compositions of the recycles (in mass %), as analysed at Anglo Research (2005). The 1999 results are taken from monthly composites analysed at P.F. Retief Laboratories in Rustenburg).

Date	MgO	Al_2O_3	SiO_2	CaO	Cr_2O_3	Fe	Co	Ni	Cu	S
1999	10.60	2.92	33.25	5.30	1.22	20.20	0.14	3.08	1.76	4.27
2005	11.70	3.66	35.5	5.77	1.66	24.00	0.15	2.50	1.29	2.27

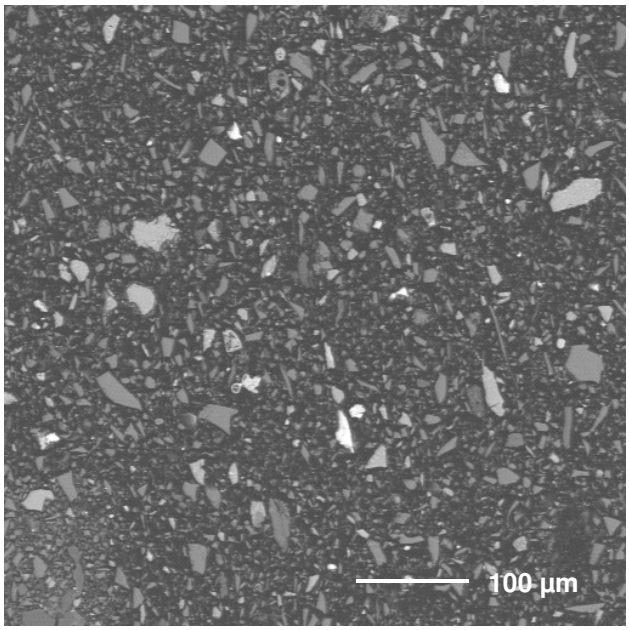

Figure 54: BSE image showing the fine-grained nature of recycles material. Here it consists mainly of furnace and slag cleaning furnace slag with minor matte or sulphide phases.

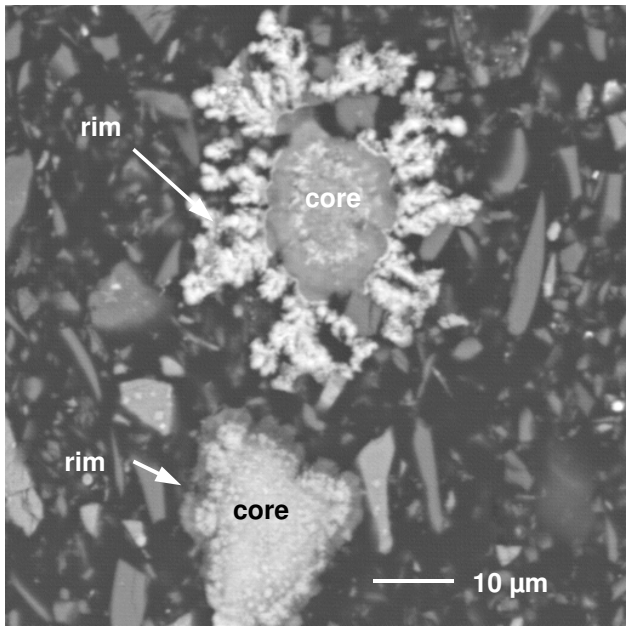

Figure 55: BSE image showing copper and copper-iron sulphides in a recycles sample. The upper particle has a core of covellite (CuS) and bornite, and a fringe of Cu_2S. The lower is a Fe>Cu-Ni sulphide-sulphate with a Cu sulphate rim.

The material is very fine-grained, but QEMSCAN modal analysis on these samples is shown in Table 29.

Table 29: QEMSCAN estimate of the source of the recycles. The modal values are in mass %.

	Source			*Sample*		
Phase	Converter	SCF	Furnace	WS1993	WS2014	WS2022
Heazlewoodite	X	x		1.8	1.8	0.5
Bornite	X	X	X	0.8	0.3	0.1
Djurleite	X	x		0.2	0.4	0.0
Pentlandite	x	X	X	4.8	6.5	2.0
Pyrrhotite/troilite			X	0.4	0.3	0.2
BMA, Cu	X	X	x	1.9	3.0	0.8
Total matte				**9.9**	**12.4**	**3.7**
Oxides	X	X	X	4.5	12.0	2.0
Low Cr spinel	x	x		0.1	0.3	0.0
Cr-Fe spinel		X	X	0.2	0.2	0.0
Total oxides				**4.8**	**12.5**	**2.0**
High silica + glass	x	X	X	55.4	37.4	84.2
Ol-pyroxene		X	X	13.7	2.7	4.2
Mg olivine		x	X	0.0	0.0	0.0
Fayalite	X	x		8.0	29.9	3.4
Al-Ca-Fe silicate		x	X	0.9	0.7	0.9
Other silicates	X	X	X	0.6	0.3	0.4
Total silicates				**78.6**	**71.1**	**93.2**
Other				6.6	4.0	1.1

The accuracy of this kind of analysis on material as fine as these samples is questionable, but it is possible to say, for example, that sample WS2014 contains more SCF slag flotation concentrate than sample WS2022, which is predominantly a low grade flotation concentrate produced from six-in-line slag.

7.1.1.4 Union furnace matte and Pierce Smith converter slag

These were added to the furnaces during the 1999 sampling campaign, and their compositions are reported in Table 30.

Table 30: The compositions (in mass %), of UFM and PSCS. The results are taken from monthly composites analysed at P.F. Retief Laboratories in Rustenburg.

	MgO	Al_2O_3	SiO_2	CaO	Cr_2O_3	Fe	Co	Ni	Cu	S
UFM	NR	NR	NR	NR	3.90	33.25	0.27	12.75	6.75	21.65
PSCS	1.31	0.69	25.90	0.74	0.74	48.80	0.33	2.83	1.29	2.83

NR = not reported.

The total mass % of the Union furnace matte is only 78.6 % – the balance probably consisted of silicates due to slag entrainment and casting contamination. The phases present in this material are the same as those reported for Waterval six-in-line furnace matte in the next section. The most common diiference is the higher spinel levels from Union, and occasional dissolved chromium in the iron sulphide phase.

The low total mass % of the converter slag is due to iron being reported as Fe rather than as FeO or Fe_2O_3. The Pierce Smith converter slag was added to the furnaces by molten transfer, so any description of the phases that formed upon cooling is not relevant.

7.1.2 Furnace matte

The full results of chemical analysis of the matte sampled in 1999, 2004 and 2005 are shown in Tables A11 to A13 in Appendix A. The normalised averages per furnace are shown in Table 31 below.

Table 31: The average compositions (in mass %) of matte during the electric furnaces campaign. For comparison purposes the results have been normalised after removing contaminants from entrained slag and refractory.

Date	Furnace	Fe	Co	Ni	Cu	S	Source*
Nov-Dec 1999	1	44.14	0.49	17.59	9.35	28.43	PFR
Nov-Dec 1999	2	43.99	0.52	17.87	9.44	28.19	PFR
Nov 2004	1	43.13	0.37	16.22	8.52	31.75	AR
May-June 2005	1	41.32	0.39	17.53	11.14	29.61	AR
May-June 2005	2	41.60	0.38	17.26	11.04	29.72	AR

*Source. Data from the 1999 campaign were obtained from same-day metal accounting samples analysed at PF Retief Laboratories in Rustenburg (PFR). Later matte samples were taken as part of the campaign and analysed at Anglo Research (AR).

Matte spoon samples solidify to form synthetic pentlandite ($(Fe,Ni,Cu)_9S_8$), troilite (FeS), bornite (Cu_5FeS_4) and base metal alloy (bma – Fe>Ni>Cu) at ambient temperature. Some of the bma plates contain platinum-rich cores. Typical BSE images of cast furnace matte are shown in Figures 56 and 57. Despite slow-cooling in the spoon, some of the phases in such samples are very finely-intergrown.

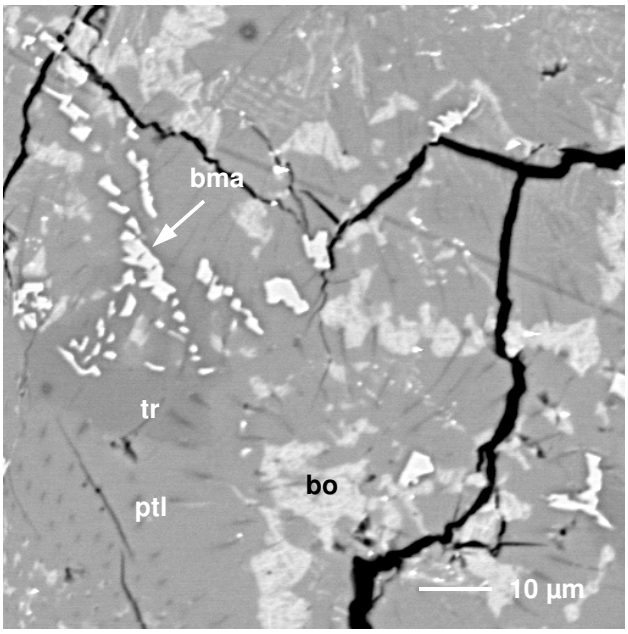

Figure 56: A typical area of furnace matte showing troilte (tr), pentlandite (ptl), bornite (bo) and base metal alloy (bma). Most of the matte shows cracking due to cooling and/or crushing and polishing. BSE image of matte sampled in 2004.

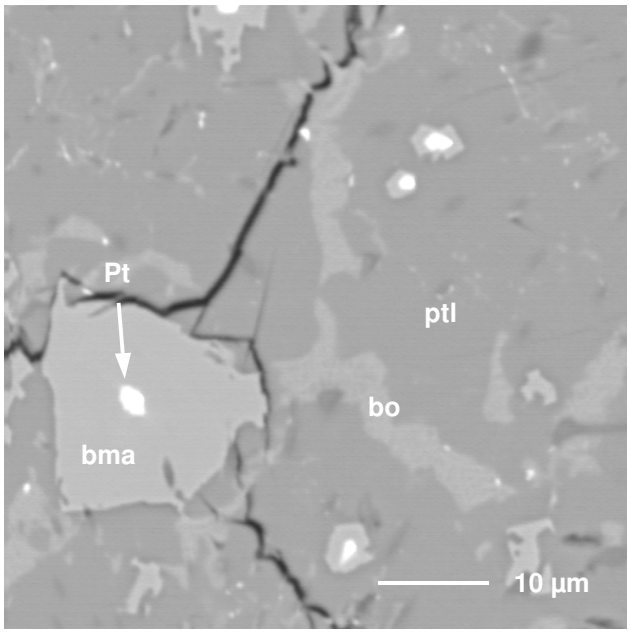

Figure 57: Platinum-rich cores (Pt) appear in many of the base metal alloy plates (bma). Other phases here are pentlandite (ptl) and bornite (bo). BSE image of matte sampled in 2004.

7.1.3 Furnace slag

Full results of chemical analysis for the 1999, 2004 and 2005 slag samples are given in Tables A14 to A16 in Appendix A. Averaged results are shown in Table 32 for comparison purposes. Note that it is not possible to distinguish between dissolved base metals and entrained sulphides using this technique.

Table 32: Averaged chemical composition of the furnace slag samples (values are in mass %). The average basicity (Bas) of the slag samples, as defined by (MgO + CaO)/(Al_2O_3 + SiO_2), is also shown.

	Fce	Cu	Ni	Co	Fe	Cr_2O_3	SiO_2	Al_2O_3	CaO	MgO	S	Bas
1999	1	0.09	0.17	0.04	16.09	1.33	47.27	4.33	9.71	17.97	0.46	0.54
1999	2	0.08	0.15	0.06	18.75	0.98	45.95	3.88	9.51	16.40	0.47	0.52
2004	1	0.06	0.06	0.01	9.68	1.42	51.20	5.04	6.04	20.00	0.27	0.46
2005	1	0.08	0.14	0.02	10.80	1.44	46.80	5.32	8.28	21.50	0.28	0.57
2005	2	0.07	0.14	0.02	10.20	1.33	46.80	5.31	10.33	20.90	0.30	0.60

The slag samples taken during 2004 and 2005 were also analysed for trace elements such as Na, K and Ti. These are reported in the Appendix tables. The most obvious difference between the slag composition in 1999 and those produced more recently is the higher Mg/Fe ratio of the recent samples.

The sulphur contents of the slag samples suggest that less matte is entrained in the more recent samples – they are "cleaner" slags. A BSE image of a relatively "dirty" granulated slag sample in section is shown in Figure 58 to illustrate the various forms of matte entrainment.

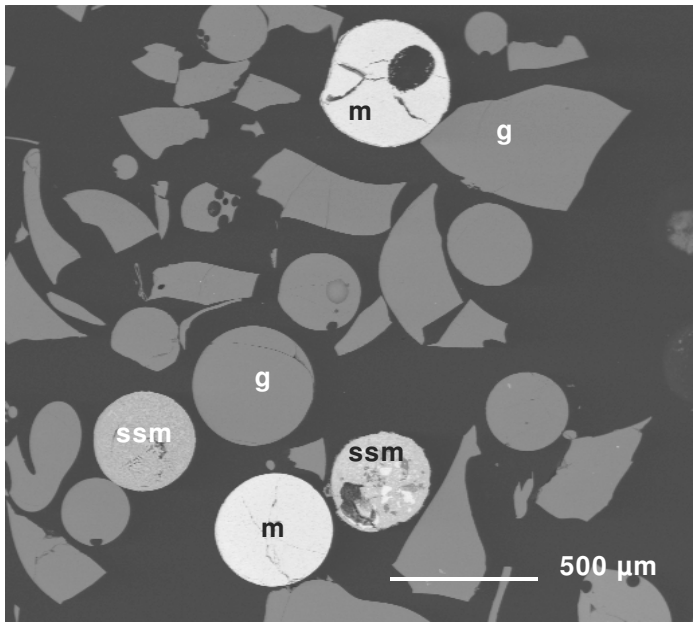

Figure 58: A BSE-image of 1999 granulated furnace slag showing the silicate glass phase (g), entrained matte granules (m) and spinel-slag±matte granules (ssm).

Granulated slag samples consist predominantly of an amorphous glass phase, compositionally a Mg-Al-Ca-Fe-Cr silicate, which also contains trace amounts of sulphur. Minor to trace phases such as slag spinel (M_3O_4, where M=Cr>Fe>Mg>Al), olivine needles ($(Mg,Fe)_2SiO_4$), and matte inclusions are found in the main glassy phase. When matte or spinel layer material has been tapped with the slag, a number of free matte granules and/or sulphide-bearing spinel-silicate composite particles form – as shown in Figure 58. The most

common occurrence of matte entrained in slag, however, is as smaller inclusions in the glass phase (see later).

Optical image analysis and QEMSCAN results show that, in terms of modal abundance, all the 1999 samples consist of 98 to 99 mass % glass phase, with the combined matte and spinel phases making up only 1 to 2 mass % of the sample.

The 2004 and 2005 granulated slag samples are all much 'cleaner' slag – that is, they contain even lower amounts of entrained matte. Spinel crystals are also very rare and localised, which shows that the slags were not chrome-saturated. Typical slag samples are shown in Figures 59 and 60.

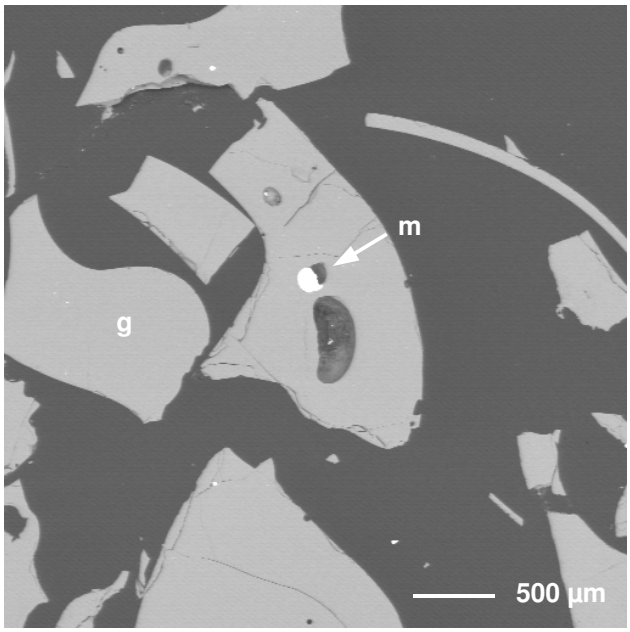

Figure 59: A general view of 2004 granulated slag. This consists almost entirely of glass (g) with trace amounts of entrained matte (m). Dark surrounding areas are resin. BSE image.

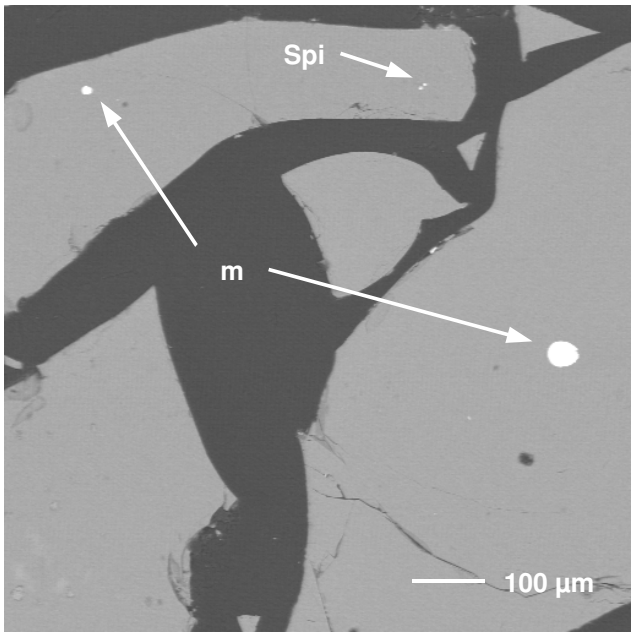

Figure 60: Typical BSE image of 2005 granulated slag showing matte (m), spinel (Spi) and silicate glass (g). The black areas are resin.

Modal analyses were not run on the 2004 slag samples, since the primary aim of the campaign was dissolved base metal in slag characterisation. Limited optical image analysis and QEMSCAN modals were run on the 1999 samples, and these averaged 0.52 % matte (optical) and 0.35 % matte (QEMSCAN – this is probably more accurate).

Modal analysis was carried out on the Minerals Liberation Analyser (MLA) and the results are shown in Table 33. The levels of entrained matte are underestimated using this method, because of the fact that tiny inclusions (<2 µm) are not picked up.

Table 33: The results of modal analysis of the furnace slag samples taken in 2005, in mass %.

	WS1989	WS1990	WS1999	WS2007	WS2008	WS2015	WS2020	WS2025
Furnace	1	2	2	1	2	1	2	1
Matte	0.03	0.03	0.02	0.02	0.09	0.00	0.03	0.01
Spinel	0.03	0.10	0.06	0.09	0.13	0.12	0.03	0.02
Silicate	99.94	99.87	99.92	99.89	99.78	99.88	99.94	99.97

The average matte content of Furnace 1 samples is 0.015 %, and of the Furnace 2 samples 0.042 %. Matte levels calculated from microprobe and chemistry results (Ni and Cu) for WS1989 and WS 2008 are 0.2–0.4 %. The calculation assumes that the total nickel and copper (from chemistry) minus the dissolved nickel and copper (as measured on the microprobe) equals the nickel and copper present as entrained matte sulphides. The amount of matte is then estimated using the entrained matte composition as a guideline.

The glass, spinel and entrained matte phases are described in more detail below.

7.1.3.1 Glass phase

Since the glass phase makes up nearly all of the samples, its composition approximates to the whole sample chemistry. Quantitative electron microprobe analyses were run on glass phases in all the granulated slag samples. The average results are presented in Table 34 to 36 below, and results in full are included in Appendix A, Tables A17 to A42. Please note that trace element averages are only calculated from values above the detection limit.

Table 34: Electron microprobe analysis results (in mass %) for the glass phase in the 1999 furnace slag samples. Each analysis is an average of twenty-five positions on the glass phase, and a grand average per furnace is included in the table.

Fce 1	MgO	Al_2O_3	SiO_2	CaO	SO_3	Cr_2O_3	FeO	CoO	NiO	Cu_2O	Total
FS1	16.88	3.99	46.63	6.47	0.89	0.80	23.27	0.063	0.135	0.085	99.21
FS2	15.65	3.91	45.29	10.28	0.94	0.67	22.44	0.098	0.138	0.063	99.48
FS3	16.63	4.75	45.64	10.79	0.76	1.01	19.44	0.077	0.176	0.082	99.35
FS4	19.30	5.13	48.41	11.08	0.66	1.04	13.50	0.020	0.069	0.042	99.24
FS5	20.92	5.18	48.60	9.31	0.60	1.00	13.75	0.021	0.122	0.060	99.56
Ave	**17.87**	**4.59**	**46.91**	**9.59**	**0.77**	**0.90**	**18.48**	**0.056**	**0.128**	**0.066**	**99.37**
Fce 2	MgO	Al_2O_3	SiO_2	CaO	SO_3	Cr_2O_3	FeO	CoO	NiO	Cu_2O	Total
FS6	15.86	3.73	45.66	5.89	1.06	0.87	26.54	0.070	0.152	0.095	99.92
FS7	15.88	3.83	45.25	7.64	0.98	0.92	23.77	0.098	0.175	0.082	98.61
FS8	14.21	4.15	42.65	13.68	1.06	0.55	22.44	0.070	0.122	0.068	99.00
FS9	16.49	4.07	45.86	8.08	1.08	0.73	23.05	0.069	0.174	0.084	99.67
Ave	**15.61**	**3.95**	**44.85**	**8.82**	**1.04**	**0.77**	**23.95**	**0.077**	**0.156**	**0.082**	**99.30**

Table 35: Results of electron microprobe analysis of the 2004 (Furnace 1) slag glass silicate phases (in mass %). Each analysis is the average of at least twenty positions (fifty each for WS1464 and 1479), and a grand average is included. Cobalt levels are not reported here because they fall on or under detection limit (here = 150 ppm).

Sample	Na_2O	MgO	Al_2O_3	SiO_2	CaO	SO_3	TiO_2	Cr_2O_3	FeO	NiO	Cu_2O	Total
WS1447	0.40	22.40	5.31	50.89	5.29	0.63	0.40	1.41	12.96	0.082	0.054	99.81
WS1451	0.32	23.45	5.05	52.23	4.87	0.65	0.23	1.41	11.60	0.070	0.057	99.94
WS1454	0.18	22.98	5.02	51.43	5.49	0.53	0.27	1.33	12.37	0.079	0.054	99.72
WS1459	0.36	23.44	5.07	52.01	4.81	0.56	0.25	1.30	12.23	0.081	0.047	100.16
WS1464	0.38	22.87	5.06	51.78	4.64	0.63	0.26	1.34	12.47	0.079	0.057	99.58
WS1465	0.32	22.52	4.91	51.37	5.17	0.50	0.31	1.34	12.63	0.076	0.038	99.21
WS1471	0.45	22.56	5.03	50.93	5.50	0.63	0.23	1.33	11.81	0.081	0.052	98.60
WS1478	0.28	21.76	4.86	50.06	8.77	0.68	0.26	1.24	12.04	0.090	0.056	100.08
WS1479	0.35	21.64	4.93	49.73	9.01	0.69	0.24	1.18	11.96	0.079	0.048	99.86
Ave	**0.34**	**22.62**	**5.03**	**51.16**	**5.95**	**0.61**	**0.27**	**1.32**	**12.23**	**0.08**	**0.052**	**99.66**

The blue figures indicate slag produced before the reverts addition commenced. Figures after this do not show any elevation in iron content. Note also the elevated CaO content in the last two samples (in purple). This was caused by incorrect limestone addition.

Table 36: Results, in mass %, of electron microprobe analysis of the 2005 slag silicate phases. Each result is the average of forty analysis positions, and grand averages are included for both furnaces.

Fce 1	Na_2O	MgO	Al_2O_3	SiO_2	CaO	SO_3	TiO_2	Cr_2O_3	FeO	NiO	Cu_2O	Total
WS1989	0.38	21.57	5.24	48.72	6.99	0.63	0.26	1.59	13.09	0.097	0.071	98.64
WS2007	0.38	20.75	5.24	48.47	7.77	0.66	0.31	1.62	13.69	0.106	0.079	99.07
WS2015	0.34	20.12	5.14	48.01	9.07	0.69	0.29	1.47	14.01	0.102	0.066	99.31
WS2025	0.33	21.64	5.34	49.81	6.58	0.67	0.30	1.53	12.40	0.076	0.055	98.73
Ave	**0.36**	**21.02**	**5.24**	**48.75**	**7.60**	**0.66**	**0.29**	**1.55**	**13.30**	**0.095**	**0.068**	**98.94**
Fce 2	Na_2O	MgO	Al_2O_3	SiO_2	CaO	SO_3	TiO_2	Cr_2O_3	FeO	NiO	Cu_2O	Total
WS1990	0.37	21.09	5.11	48.04	9.80	0.69	0.28	1.42	11.95	0.088	0.065	98.90
WS1999	0.35	20.72	5.35	47.83	9.42	0.75	0.28	1.61	12.75	0.094	0.065	99.22
WS2008	0.38	20.40	5.17	47.59	9.61	0.59	0.27	1.30	13.17	0.098	0.062	98.64
WS2020	0.31	20.58	4.98	47.24	10.46	0.69	0.21	1.42	12.69	0.098	0.054	98.73
Ave	**0.35**	**20.70**	**5.15**	**47.68**	**9.82**	**0.68**	**0.26**	**1.44**	**12.64**	**0.095**	**0.062**	**98.87**

The cobalt content of the slag was lower in 2005 than during the investigation run in 1999, so low that it fell below minimum detection limit. Longer counting times were used to reanalyse four selected samples, and cobalt levels are shown in Table 37 and in full in Tables A43 to A46 in the Appendix.

Table 37: Results, in mass %, of long count electron microprobe cobalt analysis of the 2005 slag silicate glass phases. Each result is the average of twenty analysis positions.

Sample	Furnace	Average CoO %
WS1989	1	0.017
WS2025	1	0.014
Average	1	0.016
WS1990	2	0.014
WS2020	2	0.016
Average	2	0.015

Areas with no obvious micro-inclusions of sulphide or spinel were chosen for the glass analyses and the individual results displayed low standard deviation. When compared to the sample chemistry these results imply, therefore, that in many samples, most of the copper, nickel and sulphur in the slag are actually chemically bound in the glass phase, rather than as sulphides. The exceptions are in sample FS5 (1999), where a relatively large amount of matte has been entrained in the slag, and, to a lesser extent, in sample FS4 (1999) which contained a relatively high number of coarse matte particles.

Rare olivine needles were detected in the glass phases of all the slag samples. The magnesia content of the olivine varies from 30 to 45 mass % MgO in the 1999 slags, but is higher in the 2005 slags.

7.1.3.2 Spinel phases

Three types of spinel (oxides with the general formula M_3O_4, where M can be one or a combination of Mg, Al, Fe, Cr, Ti, *etc.*) occur in the granulated slag samples. Magnetite (Fe_3O_4) and magnetites with small chromium, magnesium and aluminium contents are found in entrained matte particles, and in composite matte-slag-spinel or slag-spinel granules (Figures 61 and 62). In both the 1999 and 2005 slags, the spinel in finely-intergrown slag-spinel granules is magnetite. The origin of these granules is obscure, but there has been a suggestion that they could form during oxygen lancing at the slag tap hole.

A few relatively large compositionally zoned spinel phases appear in the glass phase. Their core composition is usually close to that of feed (or refractory) chromites from which they have probably been assimilated.

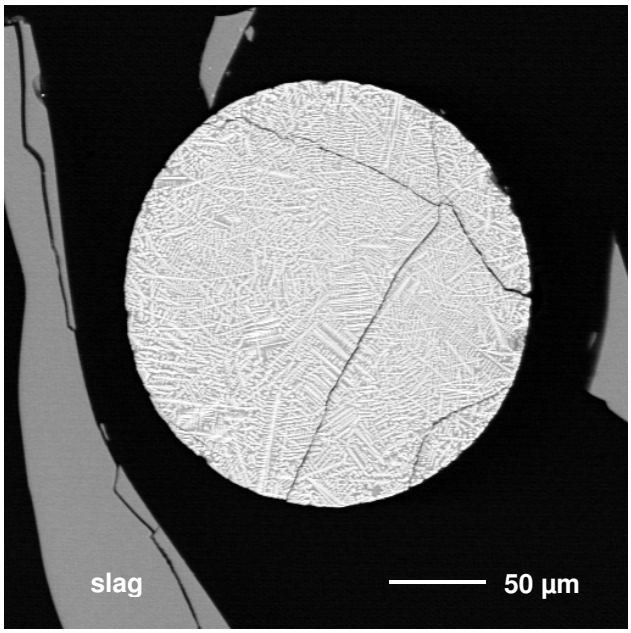

Figure 61: A magnetite-slag granule in slag sampled from Furnace 1 in 2005. It is surrounded by black mounting resin and pieces of granulated slag. BSE image.

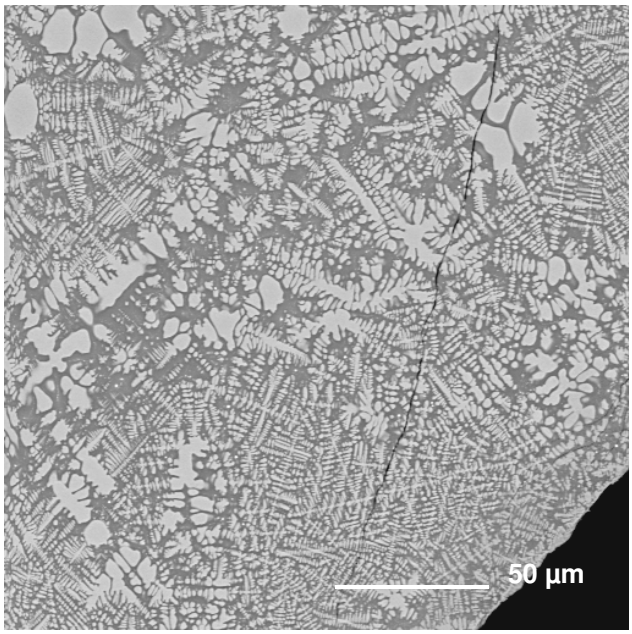

Figure 62: Detail of a spinel-slag granule in the 1999 slag. The spinel crystals (lighter phase) are close to pure magnetite in composition. BSE image.

The most common spinel is slag spinel, which is found in the glass phase and shows much higher chromium content than feed chromite (Figures 63 and 64). Microprobe analysis results for 1999 slag spinel and typical feed material are shown in Table 38 below, and full results are presented in Table A47 in the Appendix.

Table 38: Electron microprobe results averaged from twenty particles of the common slag spinel phase in the 1999 furnace slag samples. Results are in mass %.

Type	MgO	Al_2O_3	SiO_2	TiO_2	Cr_2O_3	MnO	FeO	CoO	NiO	Total
Slag	9.36	5.30	0.04	0.20	59.74	0.11	22.59	0.106	0.132	97.58

NB: Totals are low because some of the iron in chromite is present as Fe_2O_3.

The scarcity and small size of slag spinel crystals found in the later slag samples made microprobe analysis difficult. Spinel was not analysed in the 2004 slags. Average compositions gathered from twenty crystals over two 2005 samples are shown in Table 39, and in full in Table A48 in the Appendix.

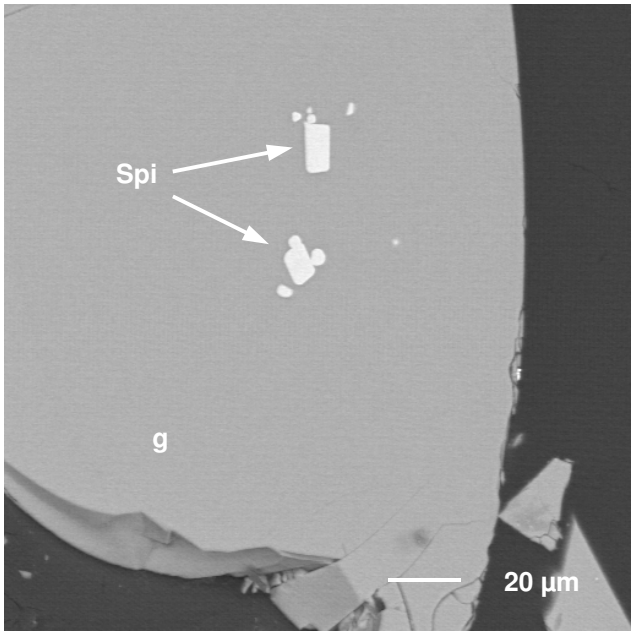

Figure 63: Spinel crystals are small and difficult to find in the 2005 slag samples. The BSE image shows spinel (Spi) in glass (g). Black areas are resin.

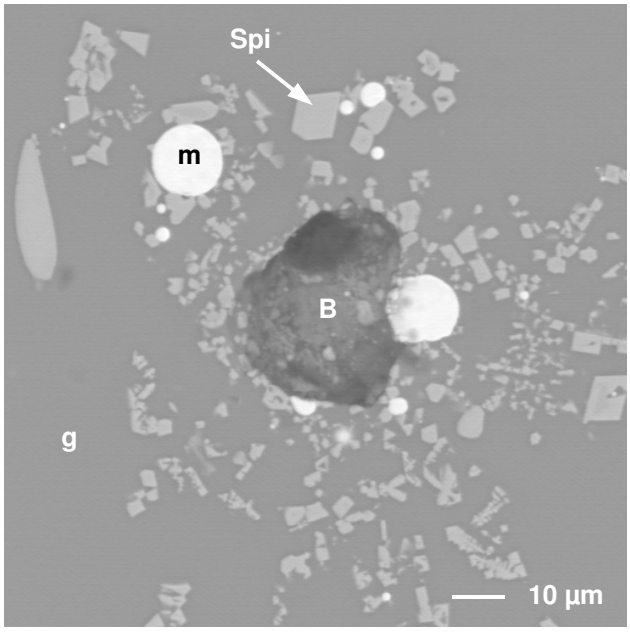

Figure 64: Rare spinel crystals (Spi) and entrained matte (m) phases associated with a gas bubble (B) in the silicate glass (g). BSE image of a 2004 slag sample.

Table 39: Averaged electron microprobe results from spinel phases in the 2005 slag samples (in mass %). Copper was not detected above 0.015% in any of the spinels.

Sample	MgO	Al_2O_3	SiO_2	CaO	TiO_2	Cr_2O_3	FeO	CoO	NiO	Total
WS1990	15.21	6.09	0.37	0.29	0.29	65.86	12.27	0.025	0.116	100.52
WS2020	14.94	6.28	0.59	0.50	0.54	64.95	13.41	0.034	0.108	101.35

In this case the high total mass % in sample WS2020 is probably due to the high relief and small size of the spinel crystals in the slag (as are the CaO and SiO_2 analysis components).

There is evidence to suggest that the larger slag spinels were present as solids in the liquid slag (referred to in the literature as *primary spinels*). Smaller slag spinels probably crystallised when the slag was cooled.

7.1.3.3 Entrained matte and sulphide phases

The amount of entrained sulphide, or matte, particles present in the slag samples is highly variable, but usually small – under one percent.

Matte or sulphide material may become attached to or enclosed in the glass phase (Figure 65), or form free granules which generally have a rim of iron oxide (Figure 66). Such matte granules are virtually identical to those found in granulated furnace matte.

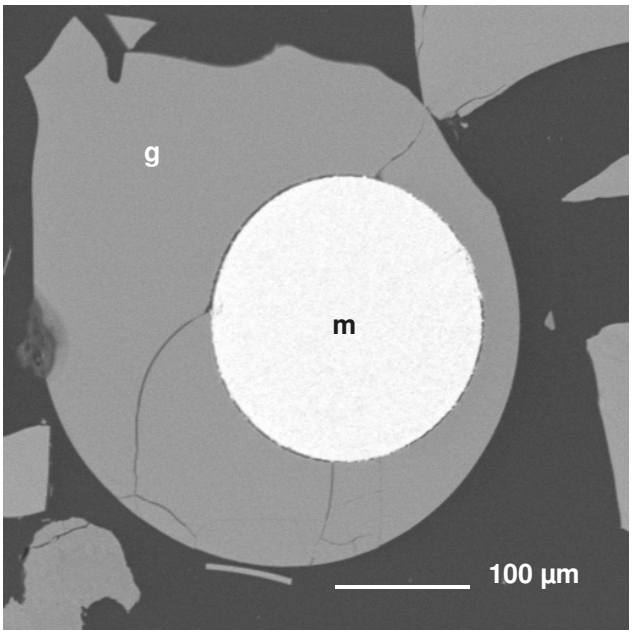

Figure 65: A matte inclusion (m) inside a glassy slag particle (g). BSE image.

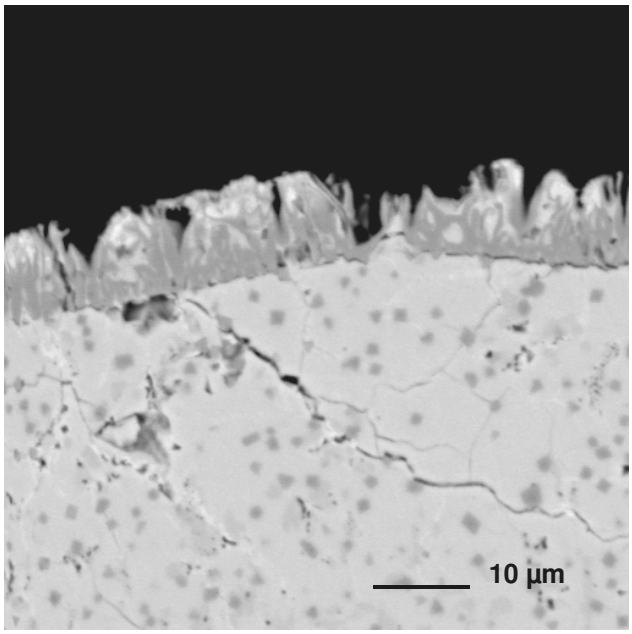

Figure 66: BSE image showing detail of a free matte granule. Lighter areas within the granule are sulphides and darker spots are magnetite. The rim of the granule consists of iron oxides.

The entrained matte consists of very fine-grained intergrowths of synthetic pentlandite ($(Fe,Ni,Cu)_9S_8$), troilite (FeS) or pyrrhotite ($Fe_{1-x}S$) and copper-iron sulphides interspersed with tiny magnetite and/or matte spinel crystals. Sometimes veins of copper metal are present, as well as tiny BMA plates (these are usually too small to resolve with the SEM). Matte may also be incorporated into composite particles with olivine, spinel and silicates. These are the spinel-slag-matte granules referred to earlier (Figure 67). The final mode of occurrence of sulphide/matte phases is as tiny inclusions in the glass phase (Figure 68). It is unlikely that such tiny sulphides would be liberated during milling and flotation.

Most of the matte particles in all of the furnace slag samples are under 15 µm in size. Larger particles of 500 µm – 1 mm do occur in some of the samples and these tend to skew the size distribution, according to the "nugget effect".

The 2004 slag samples were not processed for entrained matte size, but results for the 1999 and 2005 samples are shown in Tables 40 and 41.

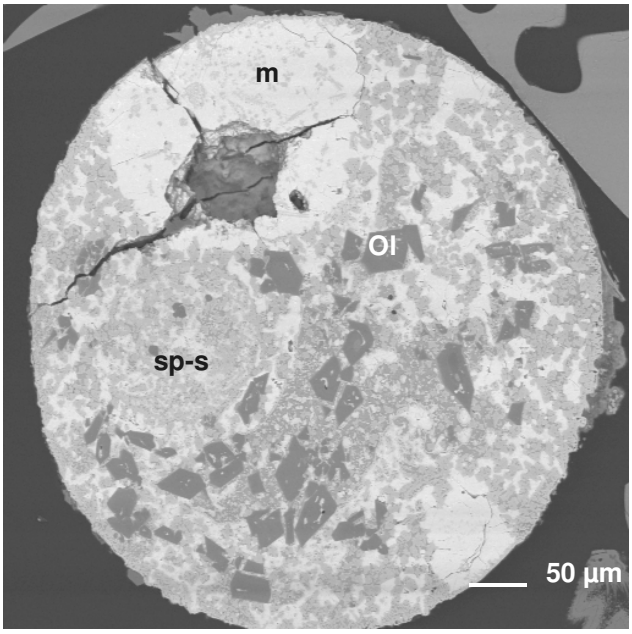

Figure 67: Matte (m) associated with spinel and slag areas (sp-s) as well as olivine (Ol) crystals. The matte consists of pentlandite with copper-rich veins and the iron-rich spinel contains small amounts of Cr, Al and Mg. BSE image.

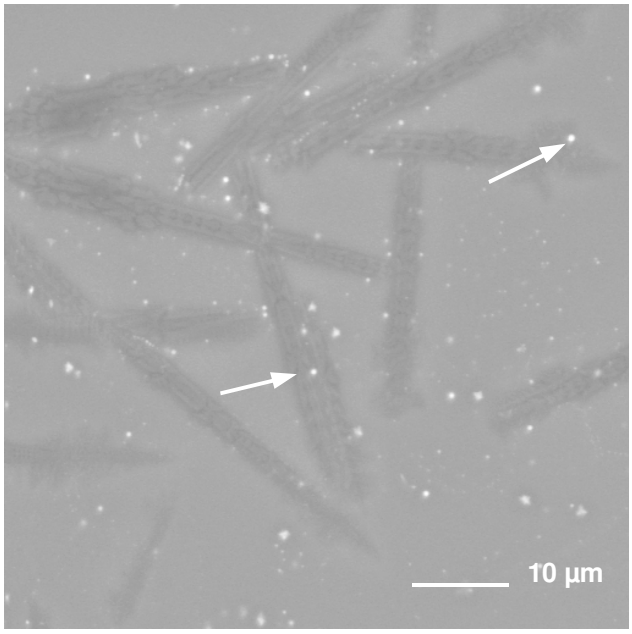

Figure 68: Tiny matte inclusions (arrowed) in the slag which, in this instance, consists of glass and darker olivine crystals. BSE image.

Table 40: Results (in mass %) of an early MLA size analysis of entrained matte in the 1999 slag samples (combined per furnace). Since the magnification was set to include a relatively large size range for large and small matte particles, the limit of resolution is around 2 µm (i.e. entrained matte under this size was not measured).

Furnace	1	2
2–5 µm	6.7	7.4
5–10 µm	9.5	21.3
10–27 µm	15.6	21.8
27–75 µm	21.1	23.2
75–212 µm	21.3	15.0
212–300 µm	25.8	11.2

Table 41: Results (in mass %) of MLA size analysis of entrained matte in the 2005 slag samples. Since the magnification was set to include a relatively large size range for large and small matte particles, the limit of resolution is around 2 µm (i.e. entrained matte under this size was not measured).

	WS1989	WS1990	WS1999	WS2007	WS2008	WS2015	WS2020	WS2025
Furnace	1	2	2	1	2	1	2	1
2–5 µm	3.0	3.5	13.1	7.0	2.8	6.1	15.1	3.9
5–10 µm	4.3	6.9	21.9	13.9	4.5	9.4	27.4	7.1
10–27 µm	7.3	14.5	18.1	33.4	5.3	14.8	32.6	4.2
27–75 µm	13.2	10.5	12.1	45.7	12.9	69.7	24.9	18.2
75–212 µm	18.4	64.6	34.8	0.0	31.1	0.0	0.0	66.6
212– 300 µm	53.8	0.0	0.0	0.0	43.4	0.0	0.0	0.0
No. particles	647	722	383	297	1068	127	482	168

The red figures in the tables indicate material that is not likely to be liberated and recovered in the slag plant. Some of the material in the green figure size range may be recovered, and the coarser fractions should, theoretically, be recoverable.

Two slag samples (one from each furnace) from the 1999 and 2005 campaigns were selected for long count analysis on the MLA. The results of the long count entrained matte phase analysis are shown in Tables 42 and 43 with fuller results in Tables A49 to A50 in Appendix A. The 1999 samples were acquired in a semi-automatic fashion, and the 2005 results were fully automatic (apart from the processing).

Table 42: Results, in normalised mass %, of averaged EDX area scans on entrained matte in two of the 1999 slag samples. The averages were calculated on over 100 phases in each sample. The (normalised) compositions of bulk matte from same-day samples are shown for comparison.

Sample	Furnace	S	Co	Fe	Ni	Cu
FS1 average	1	33.1	2.4	38.9	19.0	6.7
Bulk matte	1	28.1	0.5	44.4	17.4	9.2
FS6 average	2	32.7	1.1	37.0	21.1	8.1
Bulk matte	2	27.8	0.5	42.8	18.6	9.8

Table 43: Results, in normalised mass %, of averaged EDX area scans on entrained matte in two of the 2005 slag samples. The averages were calculated on over 500 phases in each sample. The (normalised) compositions of bulk matte from same-day samples are shown for comparison.

Sample	Furnace	S	Co	Fe	Ni	Cu
WS1989 average	1	32.7	0.7	34.3	22.3	10.0
Bulk matte	1	29.7	0.4	41.1	17.1	11.7
WS2008 average	2	31.8	0.7	32.5	24.2	10.8
Bulk matte	2	29.5	0.4	41.4	17.7	11.0

The EM compositions in the tables above were also related to droplet size. The results of this exercise are also presented in Tables A49 to A50 in Appendix A, and referred to in the Discussion.

The results of the microscope search and SEM-EDX analysis of coarser entrained matte "nuggets" for the 2005 samples are shown in Table 44. The combination of the SEM-EDX and MLA results for confidence interval calculation is shown in Table A51 (Appendix A), and the plots are referred to in the Discussion.

Table 44: Results, in normalised mass %, of averaged EDX area scans on larger entrained matte phases (>50 µm) in two of the 2005 slag samples. The averages were calculated on 127 phases (WS1989) and 169 phases (WS2008). The (normalised) compositions of bulk matte from same-day samples are shown for comparison.

Sample	Furnace	S	Co	Fe	Ni	Cu
WS1989 average	1	33.0	0.4	37.2	21.2	8.2
Bulk matte	1	29.7	0.4	41.1	17.1	11.7
WS2008 average	2	31.2	0.4	36.5	21.7	10.2
Bulk matte	2	29.5	0.4	41.4	17.7	11.0

7.1.4 Sounding bar results

Sounding bar samples are difficult to collect and great care must be taken with the interpretation of results. A dipped sounding bar can provide a depth profile of the furnace, but only the central area of the material that attaches to the bar is likely to represent the bath at that measured level. A sample collected from any given level on the bar, therefore, will contain a small amount of representative material sheathed in slag picked up on the way down and then on the way up again. In addition, feed concentrate is usually assimilated onto the

outside of the upper samples as the bar passes through the black top. This explains why chemistry results, such as those shown in Table 45, show very little differentiation.

A careful mineralogical examination, which involves cutting sections across samples and examining curvature and texture, can be more useful. An example of a sounding bar "skin" in section is shown in Figure 69.

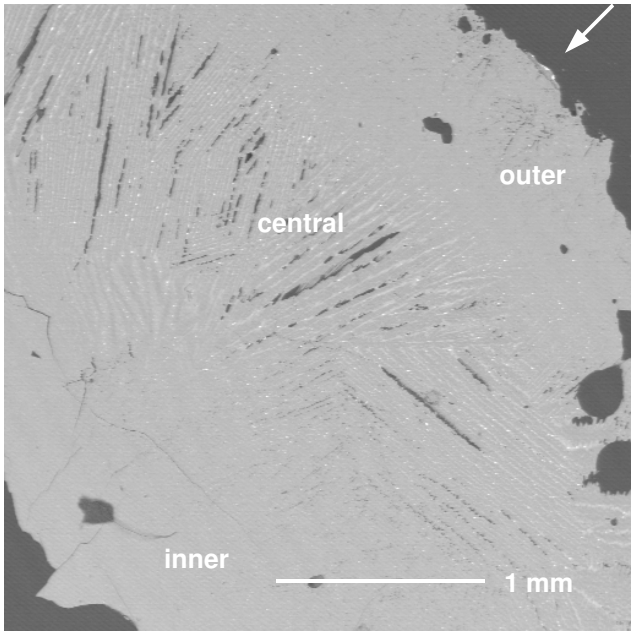

Figure 69: BSE image showing the zones of a sectioned sample after peeling from the sounding bar. This sample is from the upper slag bath and no larger entrained matte phases are present. Note the central slow-cooled or cast area which is the most representative of the slag bath at this depth. There is some evidence here of concentrate having been assimilated onto the outer edge of the sample (arrow). Black areas are mounting resin.

The slag bath was sampled successfully during the October 2006 campaign, and analysis across some of the samples are shown in Table 46, and more fully in Tables A52 to A54 in the Appendix. No obvious variation in slag composition is evident, either from top to base of the slag on the sounding bar, or from the inner layers to the outer.

When the mineralogical examination picked up an olivine-rich base layer and very little matte, enquiries were made which revealed that the furnace had been down for maintenance and switched back on the day before sampling. Very little entrained matte was recorded - some phases which were analysed were tiny, and may have formed during casting. The averaged results from the middle and lower slag bath are shown in Table 47 and given in full in Table A55 of Appendix A.

Table 45: The results of chemical analysis (in mass %) as received, as well as sample depth in the furnace (in cm), of the sounding bar samples taken from Furnace 2 in October 2006.

Name	Depth	MgO	Al_2O_3	SiO_2	S	CaO	Cr_2O_3	Fe	Ni	Cu
SB1	0–10	21.41	5.03	49.67	0.49	5.95	1.62	10.77	0.24	0.19
SB2	10–20	21.49	4.99	50.00	0.32	5.97	1.53	10.61	0.13	0.12
SB3	20–30	21.42	5.03	50.26	0.29	5.87	1.50	10.51	0.12	0.12
SB4	30–40	21.34	4.97	49.83	0.29	5.89	1.47	10.48	0.12	0.11
SB5	40–50	21.48	4.97	50.07	0.27	5.86	1.47	10.52	0.12	0.11
SB6	50–60	21.56	4.96	50.27	0.28	5.94	1.45	10.53	0.13	0.11
SB7	60–70	20.99	5.03	49.81	0.29	5.87	1.49	10.49	0.16	0.15
SB8	70–80	21.26	5.03	49.91	0.28	5.91	1.49	10.46	0.11	0.11
SB9	80–90	21.12	4.95	49.92	0.28	5.90	1.44	10.35	0.12	0.11
SB10	90–100	21.28	5.07	50.27	0.28	5.81	1.49	10.43	0.10	0.10
SB11	100–110	21.59	5.06	50.28	0.27	6.02	1.49	10.54	0.12	0.11
SB12	110–120	21.28	5.05	50.24	0.28	5.93	1.50	10.41	0.12	0.12
SB13	120–130	21.34	5.01	49.79	0.28	5.87	1.48	10.42	0.12	0.11
SB14	130–140	21.24	5.04	50.20	0.26	5.93	1.50	10.39	0.11	0.11
SB15	140–150	21.49	5.00	50.11	0.28	5.86	1.47	10.45	0.12	0.11
SB16	150–160	27.23	3.66	45.42	0.85	4.65	2.30	10.39	0.38	0.26

Table 46: The averaged results (in normalised mass %) of EMP area scan profiles across pieces from selected sounding bar samples taken from Furnace 2 in October 2006. Here profiles are those taken from the inside of the bar outwards. Inner areas are closest to the bar, central are coarser and representative of the depth, and outer are at the outside edge of the sample.

Name	Profile		MgO	Al_2O_3	SiO_2	SO_3	CaO	Cr_2O_3	FeO	NiO	Cu_2O
SB1	1	inner	21.5	5.3	51.8	0.2	6.0	1.8	13.3	0.1	0.1
		central	24.1	4.8	51.0	0.1	5.5	2.0	12.4	0.1	0.1
		outer	22.5	5.5	50.4	0.3	6.2	1.8	13.2	0.1	0.1
	2	inner	21.8	5.7	51.5	0.2	6.1	1.5	13.1	0.1	0.1
		central	22.4	5.7	50.3	0.2	6.4	1.5	13.2	0.1	0.1
		outer	21.4	5.8	49.4	0.3	7.0	1.8	14.1	0.1	0.1
	3	inner	21.8	5.2	51.1	0.3	6.0	1.9	13.4	0.1	0.1
		outer	21.7	5.4	51.5	0.3	6.4	0.8	13.6	0.2	0.1
SB10	1	inner	21.7	5.2	50.9	0.4	6.4	1.4	13.9	0.1	0.1
		central	21.6	5.4	50.5	0.4	6.4	1.5	13.9	0.1	0.2
		outer	21.7	5.4	50.9	0.3	6.5	1.5	13.3	0.2	0.1
	2	inner	21.9	5.6	49.6	0.4	6.7	1.9	13.8	0.1	0.1
		central	22.6	5.9	49.1	0.3	6.8	1.3	13.9	0.1	0.1
		outer	21.9	5.4	50.1	0.2	6.5	1.6	14.0	0.1	0.1
SB15	1	inner	21.5	5.5	50.6	0.3	6.5	1.4	13.9	0.1	0.1
		central	21.8	5.6	50.5	0.2	6.6	1.3	13.8	0.1	0.1
		outer	21.7	5.3	50.5	0.4	6.4	1.9	13.5	0.2	0.1
	2	inner	21.8	5.4	50.9	0.3	6.4	1.5	13.5	0.2	0.1
		central	21.5	5.8	50.8	0.3	6.5	1.2	13.7	0.1	0.1
	3	inner	22.4	5.3	52.1	0.2	5.8	1.7	12.4	0.0	0.1
		central	22.0	5.2	52.4	0.2	5.9	1.9	12.5	0.0	0.0
		outer	21.4	5.4	52.0	0.2	6.3	1.4	13.2	0.1	0.1

Table 47: The averaged results (in normalised mass %) of SEM-EDX area analysis of entrained matte in selected sounding bar samples taken from Furnace 2 in October 2006. The results have been corrected against standards.

Name	Depth (cm)	S	Fe	Ni	Cu
SB10	90–100	31.7	41.4	18.9	8.1
SB15	140–150	30.6	43.7	17.3	8.4
Bulk matte		30.9	42.4	16.6	9.6

The sampling in September 2007 was more successful, and samples near the base of the slag bath were concentrated on for a compositional profile of entrained matte. Phases likely to represent entrained matte droplets were analysed and the results are shown in Table A56 of Appendix A. The averaged results are shown in Table 48. Insufficient matte phases were observed in samples higher than SB5 for representative analysis - these were mainly tiny sulphides formed from casting. It is important to note that all sounding bar samples are slow cooled or cast to some extent. This means that the composition of the entrained matte phases is unlikely to be exactly that of the original matte droplet in the liquid melt. The results should be sufficiently representative, however, to establish trends with depth in the slag bath.

One aspect of the 2007 samples was the very high chrome and crystallised spinel levels in the lower samples. These have, to a certain extent, impeded matte fall and allowed more matte phases to be analysed (Figure 70). A number of large residual olivines were also present (Figure 71) – apparently a relic from the furnace being run at a low temperature for tap hole maintenance four days previously. The composition of these, as well as spinels and areas of slag, are shown in Table 49, and used for a temperature estimate in the Discussion.

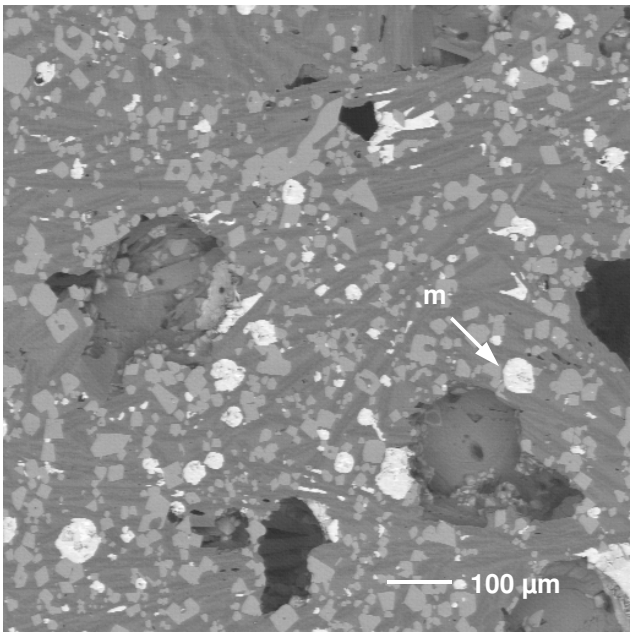

Figure 70: Matte phases (m) trapped in a pocket of spinel (medium grey). The darker grey phases are slag and the black areas are pores. BSE image of an area of sample SB5.

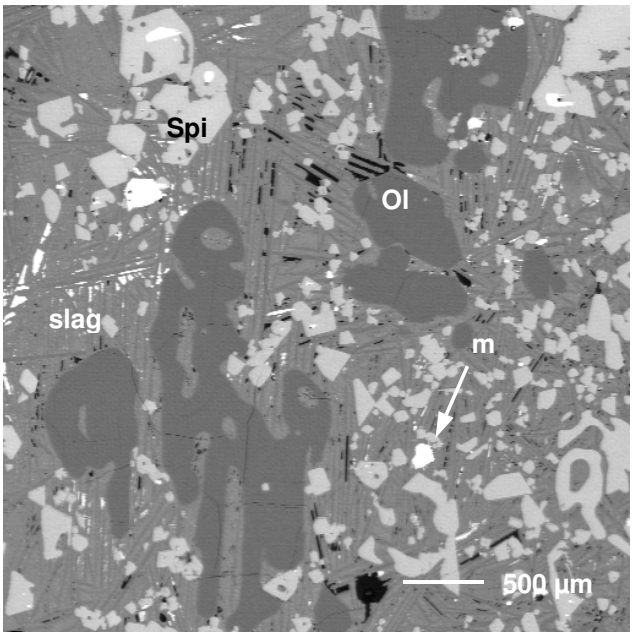

Figure 71: BSE image showing large residual olivine phases (Ol) in a lower slag bath sample (SB1). Other phases present are spinel (Spi), matte (m) and finely-intergrown slag olivine/pyroxene and matrix phases (slag).

Table 48: The averaged results (in normalised mass %) of SEM-EDX area analysis of entrained matte in selected sounding bar samples taken from Furnace 1 in September 2007. The results have been corrected against standards. Note that in this trial, samples were numbered from the base, not the top, of the bar.

Name	Depth	S	Fe	Co	Ni	Cu
SB5	78–88	29.2	35.5	0.5	27.7	7.3
SB3	95–105	30.9	38.9	0.4	20.1	9.7
SB1	150–155	31.1	41.4	0.4	18.8	8.3
Bulk matte		30.9	42.4	0.4	16.6	9.6

Table 49: The averaged results (in normalised mass %) of SEM-EDX analysis of residual olivine, spinel and slag (area) in selected sounding bar samples taken from Furnace 1 in September 2007.

Phase	Name	MgO	Al_2O_3	SiO_2	S	CaO	Cr_2O_3	FeO
Slag	SB3	20.7	5.4	49.0	0.4	9.7	1.7	13.1
Olivine	SB3	48.0		42.5			0.7	8.8
	SB1	46.5		42.1			0.6	10.8
Spinel	SB3	13.8	5.8				67.5	13.0
	SB1	10.9	2.8				70.5	15.8

7.2 SLAG CLEANING FURNACE (SCF)

7.2.1 Early work

Samples were received during 2003–2005 from a number of trial runs after the furnace was commissioned. These were batch runs and the samples were usually grab samples and only of slag. The results were compared with Robolab matte analysis from the same run to give some idea of optimum feed and process conditions. The feed components are shown in Table 50, Tables 51 to 53 show the calculated feed composition, and the base metal and sulphur levels in the matte and dissolved in slag. The September 2005 campaign parameters are also included for comparison.

Table 50: SCF feed components 2003–2005 (%).

	May 2003	June 2003	Feb 2004	June 2004	Sep 2004	Feb 2005	Sep 2005
Converter slag*	43	62	88	69	76	76	51
Concentrate	57	38	10	29	21	23	45
Silica	0	0	0	0	0	0	2
Coke	0	0	2	2	3	1	2

*In the early runs converter slag consisted of slag from the ACP reactor and from the Peirce-Smith converters. The latter contain more sulphur.

Table 51: Calculated base metal and sulphur content of the SCF feed (mass %).

	Fe	Co	Ni	Cu	S
May 2003	29.7	0.2	4.9	2.3	4.9
June 2003	35.4	0.2	6.7	2.8	3.2
Feb 2004	43.6	0.3	4.7	2.1	2.5
June 2004	38.4	0.3	3.3	1.4	2.4
Sep 2004	36.5	0.2	3.3	1.3	2.0
Feb 2005	40.6	0.4	3.9	1.6	2.0
Sep 2005	30.8	0.3	2.8	1.3	2.6

Table 52: Base metal and sulphur content of the resultant SCF matte (mass %). All these samples were analysed at the Robolab (XRF), apart from the Sep 2004 and 2005 matte samples, which were analysed by base metal fusion and ICP-MS, and LECO for sulphur. Where available, the amount of base metal alloy in the solidified matte is shown – this was measured using optical image analysis.

	Fe	Co	Ni	Cu	S	% Alloy
May 2003	17.9	0.5	35.9	14.5	26.6	9
June 2003	19.4	0.6	34.9	15.6	24.4	26
Feb 2004	16.2	0.6	36.1	15.8	24.6	11
June 2004	19.9	1.0	38.0	16.2	24.3	nd*
Sep 2004	43.4	1.5	29.6	11.2	12.5	50
Feb 2005	24.0	1.0	30.4	17.1	22.4	nd
Sep 2005	29.1	1.7	31.6	12.4	20.0	24

*nd = not determined.

Table 53: Dissolved base metals and sulphur in the SCF slag glass, as determined on the electron microprobe (mass %).

	Co	Ni	Cu	S
May 2003	0.23	1.21	0.38	0.24
June 2003	0.17	1.05	0.32	0.51
Feb 2004	0.31	1.02	0.52	0.20
June 2004	0.13	0.19	0.31	0.71
Sep 2004	0.07	0.08	0.34	0.96
Feb 2005	0.24	0.48	0.37	0.46
Sep 2005	0.23	0.24	0.24	0.50

The results tabulated above give an indication of the effect of adding larger amounts of carbon (coke), which produces more reducing conditions (*e.g.* September 2004 *vs.* February 2005). The dissolution of nickel and cobalt in the slag falls, but that of sulphur increases. The resulting lower sulphur matte contains more alloy.

Results of the more detailed campaign run on this furnace in 2005 are reported below. The sample names and descriptions are listed in Table A4 in Appendix A.

7.2.2 SCF feed (September 2005)

In September 2005, feed to the SCF consists of flash drier product, granulated converter slag, silica and carbon (reductant).

7.2.2.1Silica flux

No chemical analysis was run on this material, but the data specification suggests that it should contain at least 98.4% SiO_2, the balance of impurities being iron, aluminium and magnesium phases.

7.2.2.2 Flash drier product

The averaged composition of the flash drier product is shown in Table 54, and reported in full in Table A57 in Appendix A.

Table 54: Averaged results of chemical analysis of the flash drier product (concentrate) samples, in mass %. The samples were analysed at Anglo Research.

MgO	Al_2O_3	SiO_2	CaO	TiO_2	Cr_2O_3	Fe	Co	Ni	Cu	S	Ni:Fe	Ni:Cu
17.8	4.37	40.90	3.78	0.23	1.96	14.15	0.11	2.02	1.17	4.60	0.14	1.73

The mineral content, as determined by QEMSCAN, of the two samples are shown in Table 55.

Table 55: The results of QEMSCAN analysis of the flash drier product samples, in mass %.

Mineral/phase	WS2088	WS2089
Total sulphides	**14.6**	**14.7**
Pentlandite	6.0	6.0
Millerite	0.2	0.2
Pyrite	0.7	0.7
Pyrrhotite	3.2	3.1
Chalcopyrite	3.0	3.1
Bornite	0.1	0.1
Other sulphides	1.4	1.5
PGM's	**0.6**	**0.7**
Iron oxides	**6.0**	**5.7**
Chromite	**4.3**	**4.3**
Carbonates	**0.8**	**0.8**
Total silicates	**73.7**	**73.8**

The QEMSCAN results, as well as those of chemical analysis, show the two samples to be almost identical in composition and mineral content. The relative amount of sulphide minerals in the feed, and the sulpur content, are considerably lower than in the six-in-line furnace feeds sampled in May-June 2005. The SCF feed composition was the more in line with the average at that time.

The most common sulphide minerals in the flash drier product were analysed on the electron microprobe. The results are shown in Tables A58 to A61 in Appendix A, and the averaged results in Table 56 below.

Table 56: Averaged results of electron microprobe analysis of the major sulphide minerals in the flash drier product, in mass %.

Mineral	Fe	Co	Cu	Ni	S	Total
Pentlandite	31.34	0.56	0.00	33.28	34.54	99.72
Chalcopyrite	30.37	0.00	33.84	0.00	36.19	100.40
Pyrrhotite	60.45	0.00	0.02	0.43	39.98	100.88
Pyrite	45.20	0.52	0.03	0.05	54.19	99.99

The results in Table 56 were used to compare feed sulphide composition with that of bulk matte and entrained matte of the SCF and six-in-line furnaces.

7.2.2.3 Granulated converter slag

The results of chemical analysis of the converter slag feed samples are shown in full in Table A62 in Appendix A, and averaged results are shown in Table 57.

Table 57: Averaged results of chemical analysis of the converter slag, in mass %.

MgO	Al_2O_3	SiO_2	CaO	TiO_2	Cr_2O_3	Fe	Co	Ni	Cu	S	Ni:Fe	Ni:Cu
0.61	1.46	25.49	0.30	0.09	1.86	47.95	0.55	3.76	1.56	1.09	0.08	2.41

The basicity of the WACS samples, as defined by (MgO + CaO)/(Al_2O_3 + SiO_2), ranges from 0.02 to 0.05, with the average being 0.03.

These slag samples consist predominantly of iron silicate glass, chrome-bearing spinel and magnetite. Smaller amounts of entrained matte are also present (Figures 72 and 73). The silicate phase is sometimes glassy, but often displays some crystal development.

The results of modal analysis run on the MLA are shown in Table 58. There is reasonable agreement with chemistry, but some underestimation of matte due to the very small size of some of the entrained phases.

Table 58: The results of modal analysis of the converter slag samples, in mass %.

Phase	WS2099	WS2100	WS2101	WS2102	WS2103	WS2104	WS2105	WS2106
Matte	3.7	2.7	2.2	3.6	2.8	1.6	2.8	3.4
Magnetite	9.2	7.1	7.1	10.0	10.0	6.7	9.2	6.3
Spinel	2.4	3.2	2.7	2.0	2.4	2.4	2.4	3.1
Silicate	84.7	87.0	88.0	84.4	84.8	89.3	85.6	87.2

The average matte content of the converter slag samples is 2.8 %, and combined magnetite + spinel averages at 10.8 %.

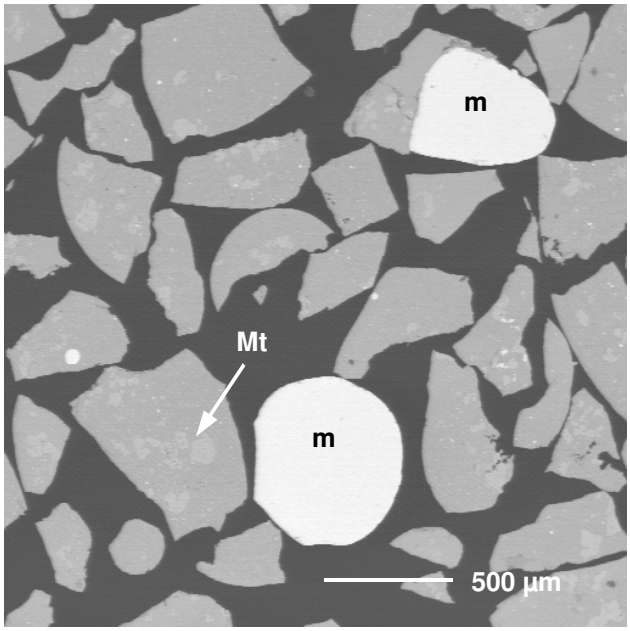

Figure 72: This view of a typical converter slag sample shows relatively coarse matte (m) and smaller spinel/magnetite (Mt) inclusions. Dark areas are resin. BSE image.

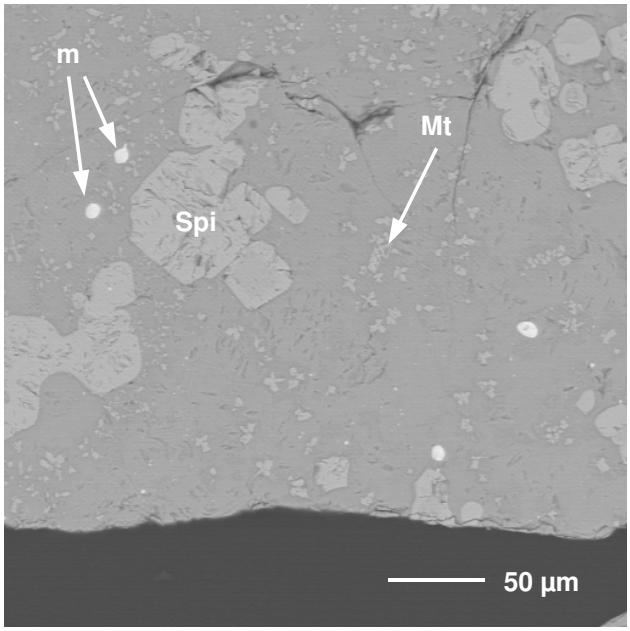

Figure 73: Fine inclusions of matte (m) and magnetite (Mt) are present in the converter slag granules, as well as the larger spinel (Spi) crystals which are occasionally compositionally zoned. BSE image.

Since the converter slag is only considered as feed material to the SCF here, a detailed mineralogical study was not warranted, and only two of the samples were analysed on the electron microprobe. The results of the analysis of glassy areas of silicate, and the larger spinel and magnetite crystals in these samples are presented in Tables A63 to A67 in Appendix A, and averaged in Tables 59 and 60.

Table 59: Results, in mass %, of electron microprobe analysis of silicate phases in two of the converter slag samples. Each result is the average of twenty analysis positions. A grand average for September 2005 is shown.

Sample	MgO	Al_2O_3	SiO_2	CaO	Cr_2O_3	FeO	CoO	NiO	Cu_2O	SO_3	Total
WS2100	0.62	1.26	28.53	0.26	0.17	64.52	0.68	2.23	0.69	0.66	99.63
WS2103	0.50	1.15	29.72	0.27	0.14	63.85	0.73	2.22	0.60	0.41	99.57
Sep 05	0.56	1.21	29.12	0.27	0.16	64.18	0.71	2.23	0.64	0.53	99.60

Table 60: Results, in mass %, of electron microprobe analysis of the larger converter slag spinel and magnetite phases. Each result is the average of ten analysis positions. Grand averages for September 2005 are shown.

Sample		MgO	Al_2O_3	SiO_2	TiO_2	Cr_2O_3	FeO	CoO	NiO	Cu_2O	Total
WS2100	Magnetite	0.24	2.16	0.45	0.21	16.18	68.07	0.67	5.19	0.05	*93.08
WS2103		0.14	1.68	0.55	0.16	12.98	71.98	0.68	5.72	0.04	93.83
Sep 05	Magnetite	0.19	1.92	0.50	0.18	14.58	70.02	0.68	5.45	0.03	93.54
WS2100	Spinel	0.76	0.02	0.08	0.15	65.63	30.90	0.78	1.69	0.04	99.91
WS2103		0.38	0.02	0.12	0.22	65.10	31.37	0.75	1.63	0.09	99.57
Sep 05	Spinel	0.57	0.02	0.10	0.18	65.36	31.14	0.76	1.66	0.07	99.74

* Magnetite totals are low because most of the iron is present as Fe_2O_3.

Semi-quantitative SEM analyses of entrained matte areas in two of the converter slag samples are shown in full in Table A68 in Appendix A, and averaged in Table 61.

Table 61: Results, in mass %, of EDX area scans on entrained matte in two of the converter slag samples. Each result is an average of ten analyses. The results are semi-quantitative and normalised.

Sample	S	Fe	Ni	Cu
WS2100	24.2	4.4	46.4	25.0
WS2103	24.1	4.2	46.6	25.1
Sep 05	24.2	4.3	46.5	25.1

It should be emphasised that the compositions in Table 37 provide only a rough idea, and that many more analyses would be required to provide a complete picture.

7.2.3 SCF matte

The full results of chemical analysis of the matte samples are shown in Table A69 in Appendix A. Averaged results are presented in Table 62 below.

Table 62: Averaged results, in mass %, of chemical analysis of the SCF matte samples.

MgO	Al_2O_3	SiO_2	CaO	Cr_2O_3	Fe	Co	Ni	Cu	S
0.18	1.37	1.26	0.15	0.22	29.1	1.67	31.6	12.4	20.0

The following phases were identified in the matte spoon samples – base metal alloy (bma) containing up to 3 % Pt, synthetic pentlandite ($(Ni,Fe,Cu)_9S_8$), and bornite (Cu_5FeS_4), sometimes intergrown with copper sulphide approximating to Cu_2S. No troilite (FeS) or heazlewoodite (Ni_3S_2) were detected. Minor oxide phases such as magnetite stringers (Fe_3O_4) and wustite (FeO) are present in all the samples, as well as

variable amounts of entrained slag and/or refractory phases – see the backscattered electron (BSE) images in Figures 74 and 75.

The results of modal analysis of the alloy and sulphide phases are shown in Table 63.

Table 63: Results of modal analysis, run on the optical image analyser, of the matte samples, in mass %.

Sample	Pentlandite	Cu-Fe sulphides	Base metal alloy
WS2108	50.3	24.6	25.2
WS2110	51.2	24.9	23.9
WS2111	52.1	19.7	28.2
WS2112	56.6	22.1	21.3
WS2113	53.6	17.7	28.6
WS2115	58.5	18.1	23.4
WS2116	56.3	21.0	22.7
WS2120	57.4	20.5	22.2
Average	54.5	21.1	24.4

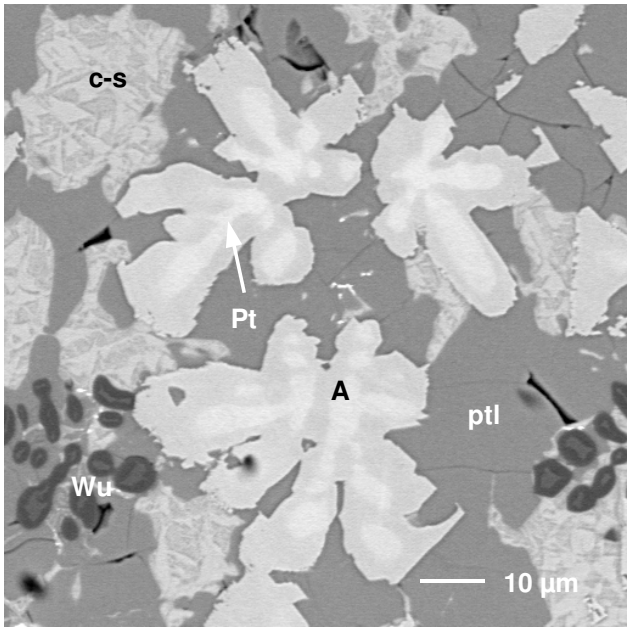

Figure 74: High contrast BSE image of SCF matte showing base metal alloy (A) with Pt-rich cores (Pt) and wustite (Wu) surrounded by pentlandite (ptl) and copper-iron sulphides (c-s).

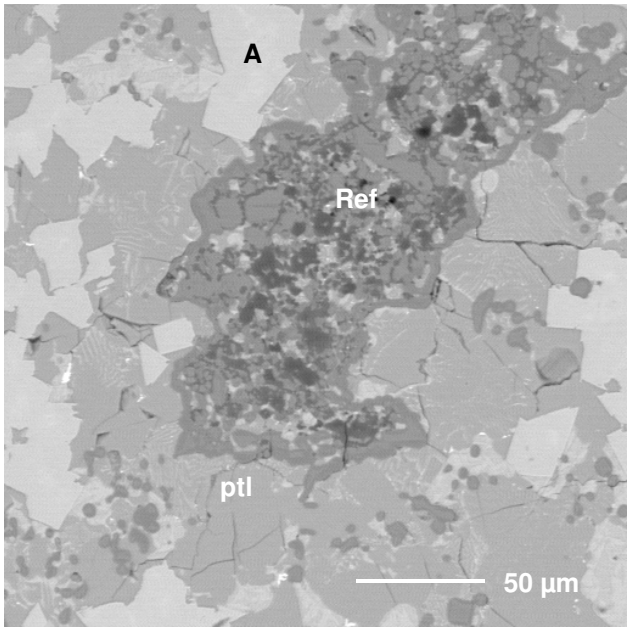

Figure 75: A refractory inclusion (Ref) consisting of Al-Fe-Cr oxide material in SCF matte. Surrounding phases are predominantly pentlandite (ptl) and base metal alloy (A). BSE image.

7.2.4 SCF slag

Full chemical analysis of the SCF slag samples are shown in Table A70 in Appendix A. The results are averaged in Table 64 below.

Table 64: Results of averaged chemical analysis of the SCF slag samples, in mass %. The average basicity (Bas) of the slag samples, as defined by (MgO + CaO)/(Al_2O_3 + SiO_2), is also shown.

MgO	Al_2O_3	SiO_2	CaO	TiO_2	Cr_2O_3	Fe	Co	Ni	Cu	S	Bas
7.97	2.93	35.34	1.93	0.15	2.08	36.43	0.26	0.71	0.48	0.70	0.26

The basicity of the SCF slag samples, as defined by (MgO + CaO)/(Al_2O_3 + SiO_2), ranges from 0.23 to 0.28, with the average being 0.26, as shown in the Table.

All the samples consist predominantly of iron-magnesium silicate glass, and spinel. Smaller amounts of entrained matte (Ni-Cu-Fe sulphide and bma) are also present. The silicate phase is usually glassy, as in electric furnace slag, but in some areas slower quenching has occurred, and some crystallisation is evident. The general appearance of SCF slag is shown in Figure 76 – this should be compared to the converter slag shown in Figure 18 earlier. The large size range of entrained matte in SCFS (<1 to 600 µm) is illustrated in Figures 77 and 78.

Modal analysis was carried out on the MLA, and the results are shown in Table 65. There is reasonable agreement with the chemistry results. The levels of entrained matte, however, are underestimated because tiny inclusions (<2 µm) are not picked up by this method.

Table 65: The results of modal analysis of the SCF slag samples, in mass %.

Phase	WS2090	WS2091	WS2092	WS2093	WS2094	WS2095	WS2096	WS2097	WS2098
Matte	0.2	0.2	0.2	0.2	0.1	0.5	0.4	0.2	0.2
Spinel	2.5	2.0	2.0	2.7	1.9	1.8	2.0	2.9	2.8
Silicate	97.3	97.8	97.8	97.1	98.0	97.7	97.6	96.9	97.0

The average matte content of the SCF slags is 0.24 %, and spinel is 2.3 %.

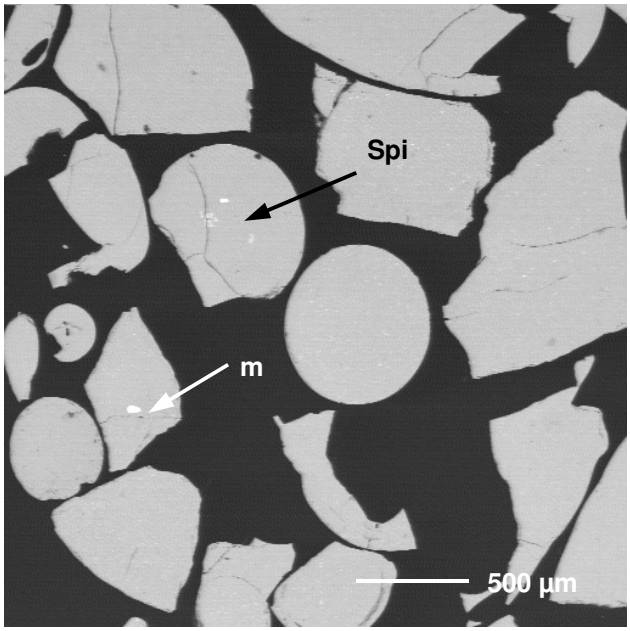

Figure 76: Typical view of a SCF slag sample showing silicate granules with occasional entrained matte (m) and spinel (Spi) phases. Dark areas are resin. BSE image.

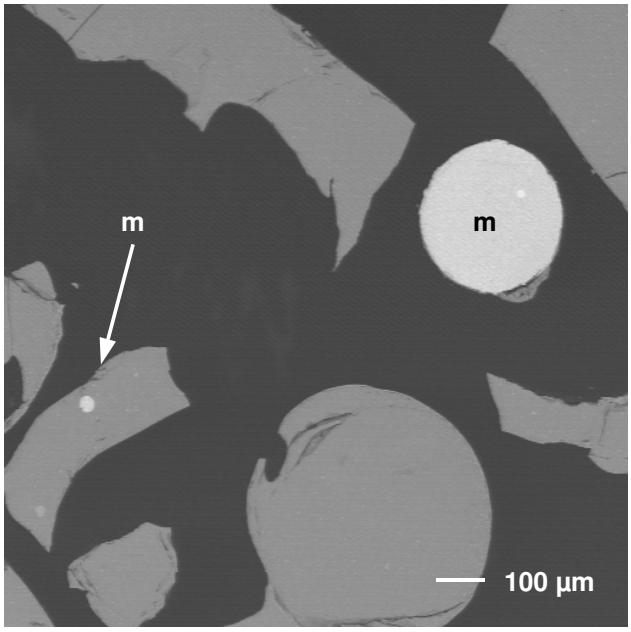

Figure 77: BSE image of SCF slag showing a large entrained matte (m) granule, as well as a more common entrained matte inclusion (arrowed) in the silicate phase. Dark areas are resin.

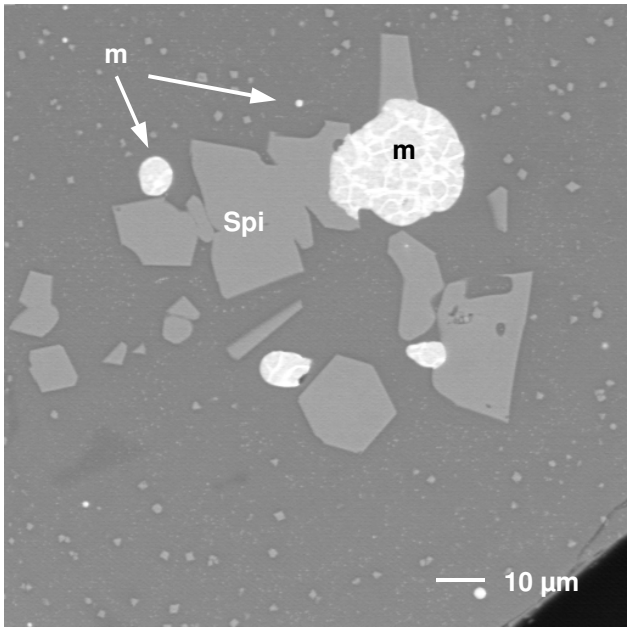

Figure 78: A higher magnification BSE image showing small entrained matte particles (m) as well as spinel crystals (Spi) in a silicate granule. Entrained matte phases less than 5 µm in diameter are unlikely to be recovered in the slag plant.

7.2.4.1 Glass and spinel phases

The results of electron microprobe analysis of glassy silicate areas and the larger spinel crystals in selected samples are presented in Tables A71 to A82 in Appendix A, and averaged in Tables 66 and 67 below.

Table 66: Results, in mass %, of electron microprobe analysis of the SCF slag silicate phases. Each result is the average of twenty analysis positions. A grand average for September 2005 is shown.

Sample	MgO	Al_2O_3	SiO_2	CaO	TiO_2	Cr_2O_3	FeO	CoO	NiO	Cu_2O	SO_3	Total
WS2090	8.28	3.12	37.02	1.99	0.16	0.81	45.77	0.30	0.33	0.31	1.36	99.35
WS2091	9.65	3.11	38.23	2.27	0.17	0.85	43.33	0.26	0.26	0.24	1.06	99.38
WS2092	8.60	3.22	37.05	2.04	0.17	0.83	45.31	0.28	0.25	0.24	1.42	99.38
WS2095	9.18	2.98	37.68	2.19	0.17	0.72	45.01	0.30	0.34	0.26	0.87	99.61
WS2096	9.01	2.98	37.31	1.96	0.17	0.80	45.20	0.32	0.35	0.26	1.26	99.51
WS2098	9.45	3.08	37.77	2.15	0.17	1.22	43.21	0.26	0.28	0.30	1.50	99.34
Sep 05	9.03	3.08	37.51	2.10	0.17	0.87	44.64	0.29	0.30	0.27	1.24	99.43

Table 67: Results, in mass %, of electron microprobe analysis of the larger SCF slag spinel phases. Each result is the average of ten analysis positions. A grand average for September 2005 is shown.

Sample	MgO	Al_2O_3	SiO_2	TiO_2	Cr_2O_3	FeO	CoO	NiO	Cu_2O	Total
WS2090	3.54	2.27	0.11	0.21	61.41	30.63	0.44	0.39	0.04	98.93
WS2091	4.32	3.84	0.15	0.21	57.96	32.18	0.36	0.45	0.04	99.40
WS2092	4.77	4.46	0.18	0.21	58.03	30.86	0.29	0.30	0.12	99.08
WS2095	4.91	4.08	0.15	0.18	59.80	29.69	0.27	0.22	0.03	99.27
WS2096	4.96	3.33	0.19	0.19	59.99	30.01	0.30	0.35	0.04	99.22
WS2098	4.77	3.38	0.15	0.21	59.81	30.11	0.30	0.26	0.01	98.90
Sep 05	4.55	3.56	0.15	0.20	59.50	30.58	0.33	0.33	0.02	99.13

7.2.4.2 Entrained matte phases

Entrained matte size distributions are shown in Table 68.

Table 68: Results (in mass %) of MLA size analysis of entrained matte in the SCF slag samples. Since the magnification was set to include a relatively large size range for large and small matte particles, the limit of resolution is around 2 µm (i.e. entrained matte under this size was not measured). Due to the large size range of entrained matte in these samples, the results of two runs on each were merged.

Size (µm)	WS2090	WS2091	WS2092	WS2095	WS2096	WS2098
<4.8	4.6	3.8	26.9	15.4	6.0	1.9
4.8–9.5	3.3	3.5	13.8	5.6	2.9	1.2
9.5–26.9	18.0	10.3	15.9	11.4	14.2	7.6
26.9–75	24.1	19.7	19.2	21.4	28.4	14.5
75–212	21.1	44.9	24.2	38.8	31.7	27.3
212–600	28.9	17.8	0	7.3	16.8	47.6
No. particles	1406	907	2463	2664	1943	1144

The red figures in Table 66 indicate material that is not likely to be liberated and recovered in the slag plant, whereas *some* of the materials in the green figure size range may be recovered.

Despite running a number of trials, it was found that it is currently not possible to use the long count method of correlating SCFS EM composition with size, as was done with the six-in-line slag samples. This is due to the frequent presence of many tiny entrained matte inclusions in the same field, which cannot be separately tagged due to stage resolution.

The EM composition results of four of the runs, however, are shown in Tables 69 and 70 below. The slag samples were run at two different cut-off sizes (2 and 7 µm), and will be referred to in the Discussion. The compositional results are reported in full in Table A83 in Appendix A.

Table 69: Results, in normalised mass %, of MLA-EDX area scans on entrained matte in two of the SCF slag samples. The averages were calculated from 519 phases in WS2091, and 837 in WS2098. The (normalized) compositions of same-day bulk matte samples are shown for comparison. The cut-off size is approximately 2 µm.

Sample	S	Fe	Co	Ni	Cu
WS2091 EM	23.4	15.3	1.8	38.9	20.6
WS2013 bulk matte	20.9	30.5	1.8	33.8	12.9
WS2098 EM	26.0	16.8	1.8	38.8	16.6
WS2120 bulk matte	22.0	29.1	1.7	33.0	14.2

Table 70: Results, in normalised mass %, of MLA-EDX area scans on entrained matte in the same SCF slag samples set at a different "magnification". The averages were calculated from 307 phases in WS2091, and 292 in WS2098. The (normalized) compositions of same-day bulk matte samples are shown for comparison. The cut-off size is approximately 7 µm.

Sample	S	Fe	Co	Ni	Cu
WS2091 EM	24.3	17.0	2.0	41.9	14.8
WS2013 bulk matte	20.9	30.5	1.8	33.8	12.9
WS2098 EM	26.2	17.7	1.8	38.9	15.4
WS2120 bulk matte	22.0	29.1	1.7	33.0	14.2

7.3 MÖSSBAUER SPECTROSCOPY RESULTS

Full results of Mössbauer Spectroscopy are shown in Tables A84 to A86 in Appendix A. The Fe^{3+}/Fe^{2+} ratios of the slag samples as calculated from relative peak intensities are shown in Tables 71 and 72.

7.3.1 Six-in-line furnaces

From 89 to 91 % (1999) and 95 to 97 % (2005) of the iron in the slag samples occurs as Fe^{2+}. No magnetite (Fe_3O_4) was detected (so virtually all the iron is present in the silicate glass), but the Fe^{3+}/Fe^{2+} ratios show that conditions were more oxidizing in the 1999 slag samples.

Table 71: Fe^{3+}/Fe^{2+} ratios as calculated from Mössbauer analysis of the 1999 and 2005 slag samples.

Furnace (1999)	*Sample*	*Fe^{3+}/Fe^{2+}*
1	FS1	0.099
	FS3	0.124
2	FS6	0.111
	FS8	0.124
Average 1999		**0.114**
Furnace (2005)	*Sample*	*Fe^{3+}/Fe^{2+}*
1	WS1989	0.042
	WS2007	0.031
	WS2015	0.031
	WS2025	0.031
2	WS1990	0.031
	WS1999	0.053
	WS2008	0.042
	WS2020	0.031
Average 2005		**0.036**

The extent of the isomer and quadrupole splitting in these samples suggest that iron in the slag glass is both tetrahedrally and octahedrally coordinated – this will be dealt with in more detail later.

7.3.2 Slag cleaning furnace.

The Fe^{3+}/Fe^{2+} ratios of the SCF slag samples as calculated from relative peak intensities are shown in Table 47, and two samples of converter slag feed are included for comparison.

Table 72: Fe^{3+}/Fe^{2+} ratios as calculated from Mössbauer analysis of SCF and converter slag samples.

SCF slag	*Sample*	*Fe^{3+}/Fe^{2+}*
	WS2090	0.031
	WS2091	0.031
	WS2095	0.075
	WS2098	0.042
Average		**0.058**
Converter slag	*Sample*	*Fe^{3+}/Fe^{2+}*
	WS2100	0.282
	WS2103	0.294
Average		**0.288**

From 93 to 97 % of the iron in the SCF slag samples occurs as Fe^{2+}. No magnetite (Fe_3O_4) was detected, so most iron is present in the silicate glass.

Approximately 78 % of the iron in the converter slag feed is present as Fe^{2+}. Magnetite (or spinel) has given rise to all the Fe^{3+} component in the converter slag, suggesting that iron in the silicate glass is mostly as Fe^{2+}. The Fe^{3+}/Fe^{2+} ratios in the slag were calculated assuming a 2:1 Fe^{3+}/Fe^{2+} ratio in magnetite – any chromium or nickel substitution in the magnetite/spinel would alter this ratio to some extent. The Fe^{3+}/Fe^{2+} ratio of the converter slag confirms that conditions were more oxidising than in the SCF slag produced from it (and the concentrate) by reduction with carbon.

7.4 FACTSAGE MODELLING OF SLAG-MATTE EQUILIBRIUM

Slag-matte base metal and sulphur distributions as calculated assuming that slag is in equilibrium with bulk matte are shown below.

7.4.1 Six-in-line furnaces – slag in equilibrium with bulk matte

The distributions of the base metals and sulphur between six-in-line slag and bulk matte, as predicted using the FactSage Equilibrium model, are shown in full in Tables A87 to A89 in Appendix A. Average values for predicted and measured $L_{s/m}$ are shown in Tables 73 – 75 below. These calculations are for equilibrium between bulk slag and bulk matte, and hence control of the pO_2 by the Fe_{matte}/FeO_{slag} couple.

Table 73: Average base metal and sulphur distributions (L) between slag and matte for the 1999 samples. The average matte tapping temperatures were 1330 ºC (Furnace 1) and 1306 ºC (Furnace 2).

Furnace	L_{Co} measured	L_{Co} predicted		
	1450–1460 ºC*	1550 ºC	1400 ºC	1300 ºC
1	0.1355	0.0260	0.0223	0.0200
2	0.1192	0.0285	0.0243	0.0218
Furnace	L_{Ni} measured	L_{Ni} predicted		
	1450–1460 ºC	1550 ºC	1400 ºC	1300 ºC
1	0.0068	0.0012	0.0008	0.0006
2	0.0068	0.0013	0.0009	0.0007
Furnace	L_{Cu} measured	L_{Cu} predicted		
	1450–1460 ºC	1550 ºC	1400 ºC	1300 ºC
1	0.0070	0.0042	0.0028	0.0020
2	0.0076	0.0046	0.0030	0.0022
Furnace	L_S measured	L_S predicted		
	1450–1460 ºC	1550 ºC	1400 ºC	1300 ºC
1	0.0122	0.0131	0.0095	0.0073
2	0.0149	0.0149	0.0109	0.0084

*Average slag tapping temperatures 1450 ºC (Furnace 1) and 1460 ºC (Furnace 2).

Table 74: Base metal and sulphur distributions (L) between slag and matte for the 2004 samples. The average matte tapping temperature was 1376 ºC.

Furnace	L_{Co} measured	L_{Co} predicted		
	1495 ºC*	1550 ºC	1400 ºC	1300 ºC
1	nd	0.0233	0.0211	0.0199
Furnace	L_{Ni} measured	L_{Ni} predicted		
	1495 ºC	1550 ºC	1400 ºC	1300 ºC
1	0.0039	0.0013	0.0009	0.0007
Furnace	L_{Cu} measured	L_{Cu} predicted		
	1495 ºC	1550 ºC	1400 ºC	1300 ºC
1	0.0055	0.0027	0.0017	0.0012
Furnace	L_S measured	L_S predicted		
	1495 ºC	1550 ºC	1400 ºC	1300 ºC
1	0.0076	0.0086	0.0059	0.0044

*Average slag tapping temperature 1495 ºC.

Table 75: Base metal and sulphur distributions (L) between slag and matte for the 2005 samples. The average matte tapping temperatures were 1394 ºC (Furnace 1) and 1384 ºC (Furnace 2).

Furnace	L_{Co} measured	L_{Co} predicted		
	1523–1495 ºC*	1550 ºC	1400 ºC	1300 ºC
1	0.0358	0.0213	0.0189	0.0175
2	0.0361	0.0199	0.0175	0.0161
Furnace	L_{Ni} measured	L_{Ni} predicted		
	1523–1495 ºC	1550 ºC	1400 ºC	1300 ºC
1	0.0044	0.0010	0.0007	0.0005
2	0.0044	0.0009	0.0007	0.0005
Furnace	L_{Cu} measured	L_{Cu} predicted		
	1523–1495 ºC	1550 ºC	1400 ºC	1300 ºC
1	0.0056	0.0024	0.0020	0.0015
2	0.0049	0.0031	0.0020	0.0014
Furnace	L_S measured	L_S predicted		
	1523–1495 ºC	1550 ºC	1400 ºC	1300 ºC
1	0.0091	0.0089	0.0062	0.0047
2	0.0093	0.0097	0.0067	0.0050

*Average tapping temperatures 1523 ºC (Furnace 1) and 1495 ºC (Furnace 2).

As can be seen from the results above, the predicted $L_{s/m}$ distribution of the base metals in the six-in-line furnaces is lower than that measured, but for sulphur it is relatively accurate.

7.4.2 Slag cleaning furnace – slag in equilibrium with bulk matte

The distributions of the base metals and sulphur between SCF slag glass and bulk matte, and slag spinel and bulk matte, as predicted using the FactSage Equilibrium model, are shown in full in Tables A90 and A91 in Appendix A. Averaged values for predicted and measured $L_{s/m}$ are shown in Tables 76 and 77 below. The calculations were as noted in section 7.4.1.

Table 76: Average base metal and sulphur distributions (L) between slag glass and matte for the SCF samples. The average matte tapping temperature was 1236 ºC.

Furnace	L_{Co} measured	L_{Co} predicted		
	1508 ºC*	1550 ºC	1400 ºC	1300 ºC
SCF	0.1297	0.0560	0.0486	0.0419
Furnace	L_{Ni} measured	L_{Ni} predicted		
	1508ºC	1550 ºC	1400 ºC	1300 ºC
SCF	0.0072	0.0025	0.0019	0.0014
Furnace	L_{Cu} measured	L_{Cu} predicted		
	1508ºC	1550 ºC	1400 ºC	1300 ºC
SCF	0.0184	0.0127	0.0096	0.0071
Furnace	L_S measured	L_S predicted		
	1508ºC	1550 ºC	1400 ºC	1300 ºC
SCF	0.0237	0.0422	0.0377	0.0329

*Average slag tapping temperature 1508 ºC.

Table 77: Average base metal and sulphur distributions (L) between slag spinel and matte for the SCF samples. The average matte tapping temperature was 1236 ºC.

Furnace	L_{Co} measured	L_{Co} predicted		
	1508 ºC*	1550 ºC	1400 ºC	1300 ºC
SCF	0.1485	0.0566	0.0546	0.0525
Furnace	L_{Ni} measured	L_{Ni} predicted		
	1508ºC	1550 ºC	1400 ºC	1300 ºC
SCF	0.0079	0.0020	0.0018	0.0017
Furnace	L_{Cu} measured	L_{Cu} predicted[#]		
	1508ºC	1550 ºC	1400 ºC	1300 ºC
SCF	0.0014	0.0000	0.0000	0.0000

*Average slag tapping temperature 1508 ºC.

[#] No copper is predicted to partition into spinel.

The distribution coefficients for the base metals are again underestimated in the slag cleaning furnace, whereas sulphur is slightly overestimated.

7.4.3 Base metal dissolution types in slag

The relative degrees of sulphidic and oxidic base metal dissolution are also predicted using the model. The results are shown in Tables A92 to A95 in Appendix A, and the average results are shown in Tables 78 to 81 below. This confirms that the base metals dissolve as oxides in the slag.

Table 78: The average percentages of base metal dissolution in slag silicate that is sulphidic in the 1999 slag samples, as predicted by FactSage.

	% Co as sulphide					
Furnace	1300 ℃	1350 ℃	1400 ℃	1450 ℃	1500 ℃	1550 ℃
1	0.88	1.01	1.15	1.29	1.44	1.59
2	0.99	1.15	1.30	1.45	1.62	1.78
	% Ni as sulphide					
Furnace	1300 ℃	1350 ℃	1400 ℃	1450 ℃	1500 ℃	1550 ℃
1	0.88	1.01	1.15	1.28	1.44	1.59
2	1.01	1.16	1.30	1.46	1.60	1.77
	% Cu as sulphide					
Furnace	1300 ℃	1350 ℃	1400 ℃	1450 ℃	1500 ℃	1550 ℃
1	0.81	0.93	1.05	1.18	1.31	1.45
2	0.91	1.05	1.17	1.33	1.48	1.63

Table 79: The average percentages of base metal dissolution in slag silicate that is sulphidic in the 2004 EF slag samples, as predicted by FactSage.

	% Co as sulphide					
Furnace	1300 ℃	1350 ℃	1400 ℃	1450 ℃	1500 ℃	1550 ℃
1	0.62	0.72	0.83	0.94	1.07	1.21
	% Ni as sulphide					
Furnace	1300 ℃	1350 ℃	1400 ℃	1450 ℃	1500 ℃	1550 ℃
1	0.62	0.72	0.83	0.95	1.07	1.21
	% Cu as sulphide					
Furnace	1300 ℃	1350 ℃	1400 ℃	1450 ℃	1500 ℃	1550 ℃
1	0.57	0.66	0.76	0.85	0.99	1.10

Table 80: The average percentages of base metal dissolution in slag silicate that is sulphidic in the 2005 EF slag samples, as predicted by FactSage.

	% Co as sulphide					
Furnace	1300 ℃	1350 ℃	1400 ℃	1450 ℃	1500 ℃	1550 ℃
1	0.60	0.70	0.80	0.91	1.01	1.14
2	0.63	0.73	0.85	0.97	1.07	1.21
	% Ni as sulphide					
Furnace	1300 ℃	1350 ℃	1400 ℃	1450 ℃	1500 ℃	1550 ℃
1	0.60	0.69	0.80	0.90	1.03	1.15
2	0.63	0.74	0.86	0.97	1.09	1.23
	% Cu as sulphide					
Furnace	1300 ℃	1350 ℃	1400 ℃	1450 ℃	1500 ℃	1550 ℃
1	0.63	0.64	0.74	0.83	0.94	1.03
2	0.56	0.67	0.77	0.79	1.00	1.11

Table 81: The average percentages of base metal dissolution in slag silicate that is sulphidic in the 2005 SCF slag samples, as predicted by FactSage.

	% Co as sulphide			
Furnace	1200 °C	1300 °C	1400 °C	1500 °C
SCF	2.46	3.00	3.42	3.87
	% Ni as sulphide			
	1200 °C	1300 °C	1400 °C	1500 °C
SCF	2.46	3.02	3.45	3.89
	% Cu as sulphide			
	1200 °C	1300 °C	1400 °C	1500 °C
SCF	2.33	2.70	3.13	3.54

8 DISCUSSION

8.1 DISTRIBUTION OF BASE METALS IN SMELTER FEED AND PRODUCTS

The degree of enrichment of the base metals during processing at Waterval Smelter may be assessed from average base metal levels in the smelter feed (ore concentrate) and final product (converter matte), as well as the intermediate mattes and slags analysed in this study. These are shown in Table 82.

Table 82: Base metal levels (in mass %) in smelter feed and products, based on figures for 2005.

Material	Nickel	Copper	Cobalt
Ore concentrate (feed)	2.0	1.2	0.1
Six-in-line furnace matte	16.3	9.1	0.30
SCF matte	31.6	12.4	1.67
Converter matte	46.5	26.7	0.28
Six-in-line slag	0.14	0.07	0.02
SCF slag	0.71	0.48	0.26
Converter slag	3.76	1.56	0.55

The ore concentrate contains far more sulphide minerals than run of mine ore. For example, the average sulphide mineral content of the five flash drier products analysed during the 2005 campaigns was 24 %, whereas the sulphides in Waterval ore (the main feed source for Waterval Smelter) were running at 0.8 % (Merensky) and 0.2 % (UG-2) at that time. The origin of these sulphides from a silicate melt with associated oxide crystallization can be compared to matte formation in a huge, pressurised natural furnace. Due to the extremely small “matte fall”, however, and the fact that the deposit has been cast (crystallised) rather than granulated, virtually all the nickel, copper and cobalt in the system reports to the sulphide minerals. The situation is not so clear-cut in the furnaces of this study because there is a much higher matte/melt ratio, and no slag casting. This leads to the incorporation of higher base metal levels into the granulated slag.

The range of sulphide mineral contents in the five dried concentrates referred to above was surprisingly large – from 15 % to 38 %, the higher values occurring in late May and early June 2005. The composition of material being added to the furnaces is supposed to be maintained at a steady level with respect to sulphide and chrome content, by means of blending. It seems that such control was not being practised at that time, probably because of low stock levels.

As was outlined Chapters 3 and 4, most of the base metals in Anglo Platinum six-in-line and slag cleaning furnaces report to the matte.

A compositional change is evident between that of the feed sulphide to the six-in-line furnaces and the resulting matte. This involves a reduction in sulphur (on average 36 to 32 %) and iron (39 to 33 %), and an increase in nickel (14 to 23 %) and copper (10 to 11 %). The reasons for this are the loss of labile sulphur to off-gas, and the preferential dissolution of iron into the slag. Sulphur, nickel, copper and particularly, cobalt, also dissolve in the slag, but not to the same degree as iron.

The situation in the slag cleaning furnace is more complex. Feed materials include ore concentrate as described above, and also converter slag. The converters work by oxidising most of the iron out of the matte to form the slag with silica flux addition (see section 4.4) which results in the formation of an iron-rich slag.

Turbulence in the bath and magnetite formation also lead to relatively high levels of matte entrainment. Due to the oxidized nature of the slag, and the closer-to-liquidus operation, granulated converter slag usually contains spinel and magnetite crystals, and high levels of dissolved base metals. Pyrometallurgical reduction in the slag cleaning furnace is designed to reduce dissolved base metals out of the slag with carbon addition, and also to settle the resulting sulphide phases under more quiescent conditions than those present in the ACP reactor. During the 2005 campaign, levels of nickel in slag were reduced from 3.8 to 0.7 %, copper from 1.6 to 0.5 % and cobalt from 0.6 to 0.3 %. These remain higher than those in the slags of the six-in-line furnaces.

The losses of base metals to slag in the six-in-line and slag cleaning furnaces are of two types – losses by predominantly oxidic dissolution in the slag, and losses as unsettled entrained sulphide matte. Since neither the six-in-line nor the slag cleaning furnace slags are treated further by pyrometallurgical reduction, losses by dissolution in slag are not recoverable. Slag from the slag cleaning furnace, and a limited amount of six-in-line slag is currently milled and floated in the Slag Plant where at least the coarser entrained matte particles should be recovered. Most of the six-in-line slag is dumped, however, so this option is not available. Given these facts, it is obvious that the best approach to reducing base metal (and associated PGE) losses to slag lies in process optimisation to minimise the dissolution of base metals, and to maximise the settling of entrained matte.

8.2 DISSOLVED BASE METALS

This study of the nature of base metal losses has relied heavily on both chemical and mineralogical analytical techniques. Some are well established, but others are new, at least to the field of pyrometallurgy. The results of the experimental work on dissolved base metals are evaluated and interpreted in this section.

The viability of analysing quenched slag phases and drawing conclusions about molten slags and the matte droplets therein should not be taken for granted. The quenching method used, as well as the analytical technique may well influence the conclusions – this is discussed with respect to microprobe measurement of dissolved base metals below, and later under Mössbauer spectroscopy (Section 8.4).

The slag samples used in this study were rapidly quenched in water, apart from the sounding bar samples – these were dip samples and some microcrystallinity is evident. The glass silicate and, in some samples, slag spinel, were analysed on the electron microprobe to determine the dissolved base metal content. Electron microprobe analysis excites a volume of material with a diameter of approximately 2 µm and any microcrystallinity can be picked up when the standard deviation of results is excessive. These areas were avoided and the silicate glass samples, which were analysed for base metal dissolution, were regarded as homogenous.

According to JALKANEN *et al.,* (2003) copper metal particles which precipitate during the quenching of high grade copper slag are "too small to be avoided by the electron beam in EPMA". The photomicrograph which accompanies this statement, however, shows phases large enough to be avoided easily, providing that the microprobe in question has a BSE imaging facility. The lack of dissolved base metal-sulphur trends in the slags of this study rule out the presence of submicroscopic base metal sulphide particles in areas analysed by the microprobe. The presence of very tiny metallic particles, however, could theoretically go undetected. It

seems unlikely that such particles would be present in the six-in-line slags as even the smallest entrained matte particles contain around 30 % sulphur. The case may not be so watertight in the SCF slags – in some of these a small amount of low-sulphur phases such as copper metal and Ni>>Fe>Cu (alloy?) were detected by the MLA. It is likely that these were residual converter slag inclusions, but some could represent metals reduced out of the slag by the action of carbon. Any extremely small metal, alloy or sulphide phase that is encountered in the slag glass is most likely to be a quench product. It can then be argued that these were dissolved in the silicate melt prior to quenching, and that microprobe measurement *must* assimilate these values to assess dissolved base metal and sulphur levels.

The standard deviations of the microprobe analysis results for the base metals are indeed relatively high, although this varies from one tap to the next, and even between furnaces. The deviations fall in line with those of other trace elements such as sodium and titanium. The standard deviation of homogeneous area glass analysis reflects the variation between different slag granules, rather than within granules, which suggests that there may be slight compositional variation within the quenched slag.

The amount of dissolved base metals as a percentage of total slag base metal in the six-in-line furnaces can be calculated from the microprobe results and chemical analysis. These levels are shown in Table 83 below.

Table 83: The averaged relative amounts of dissolved base metals in slag for the 1999 and 2005 six-in-line samples. Results are as a percentage of total element content in slag. Cobalt is not reported for the earlier samples, as the chemical analysis results were known to be inaccurate.

Year	Furnace	Dissolved Ni (%)	Dissolved Cu (%)	Dissolved Co (%)
1999	1	61	63	
1999	2	81	88	
2005	1	56	79	51
2005	2	55	78	48

The calculation assumes that both analytical techniques are accurate, and that the amount of spinel in the samples is negligible. In the case of the SCF slags reported in Table 84 below, nickel and cobalt are dissolved in the spinel phase as well as the silicate glass. The accuracy of the cobalt values could be questionable.

Table 84: The averaged relative amounts of dissolved base metals in slag for the 2005 SCF samples. Results are as a percentage of total element content of the slag.

Year	Dissolved Ni (%)	Dissolved Cu (%)	Dissolved Co (%)
2005	37	52	88

The lower dissolved nickel and copper in the SCF slag compared to those in the six-in-line slag is not due to a lower pO_2 in slag but rather to the different feed composition.

The electron microprobe results may be plotted to test a relationship between the dissolved base metal and sulphur content in the slag glass. Composite examples of this are shown for nickel in Figures 79 to 81. Plots of this kind for the base metals of all three furnaces are shown in Figures B1 to B3 in Appendix B.

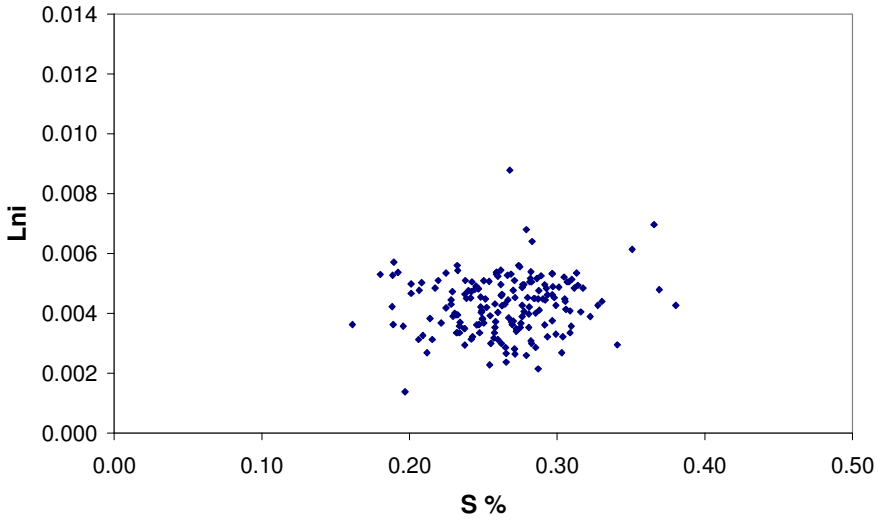

Figure 79: The relationship between L_{Ni} and dissolved sulphur in Furnace 1 slag (2005). The plot is a composite of data from WS1989, 2007, 2015 and 2025.

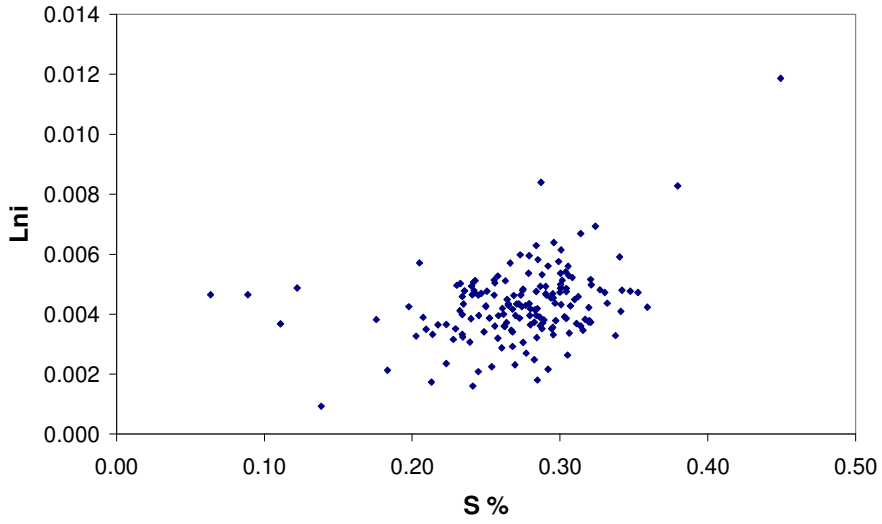

Figure 80: The relationship between L_{Ni} and dissolved sulphur in Furnace 2 slag (2005). The plot is a composite of data from WS1990, 1999, 2008 and 2020. The outlying points all come from WS2008, where some microcrystallinity may have been present.

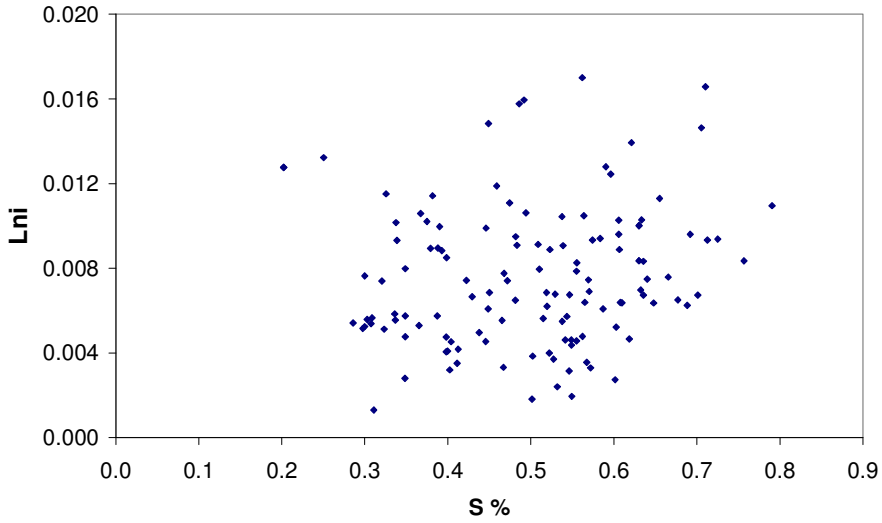

Figure 81: The relationship between L_{Ni} and dissolved sulphur in SCF slag (2005). The plot is a composite of data from all six SCF slag samples. Note the scale difference between this plot and those in Figures 79 and 80.

Given that the outliers in the Furnace 2 plot (Figure 80) probably arise from microcrystallinity in one sample, the dissolved nickel in the slags does not display any obvious relationship with sulphur. This is confirmed by FactSage modeling, which shows very little nickel dissolution to be sulphidic in these slags. A similar pattern is evident for copper and cobalt.

It is interesting to compare the plots here, and in Appendix B, to illustrate differences between the six-in-line and the SCF slag dissolution plots, taking note of scale differences. The values for base metal distribution and dissolved sulphur exhibit far more spread in the SCF slag, and are also much higher, on average, than those in the six-in-line samples.

Prior to 2001, reverts, mainly in the form of Peirce Smith converter slag, used to be returned to the six-in-line electric furnaces on a regular basis. At that time, the major effect of this, apart from hearth build-up in the furnace, was to raise the iron levels of the resultant slag and to dissolve more base metals as silicate and oxide phases. Microprobe analysis results confirm that the amount of dissolved base metals, particularly nickel and cobalt, was higher. This could be due to the lower Mg/Fe in the slag or the lower smelting temperature, but the predominant reason is likely to be the higher pO_2 in the slag bath during 1999 as compared to 2005 (see Figure 82). This is confirmed by the calculations presented in section 8.5.

The practice of returning large amounts of reverts to the furnaces was discontinued in 2001, and limited to occasional until 2007, when relatively large amounts of granulated converter slag (WACS) were returned to both six-in-line furnaces during a period when problems were being experienced with the SCF. Certain operational problems were reported, but unfortunately no slag samples were made available for analysis.

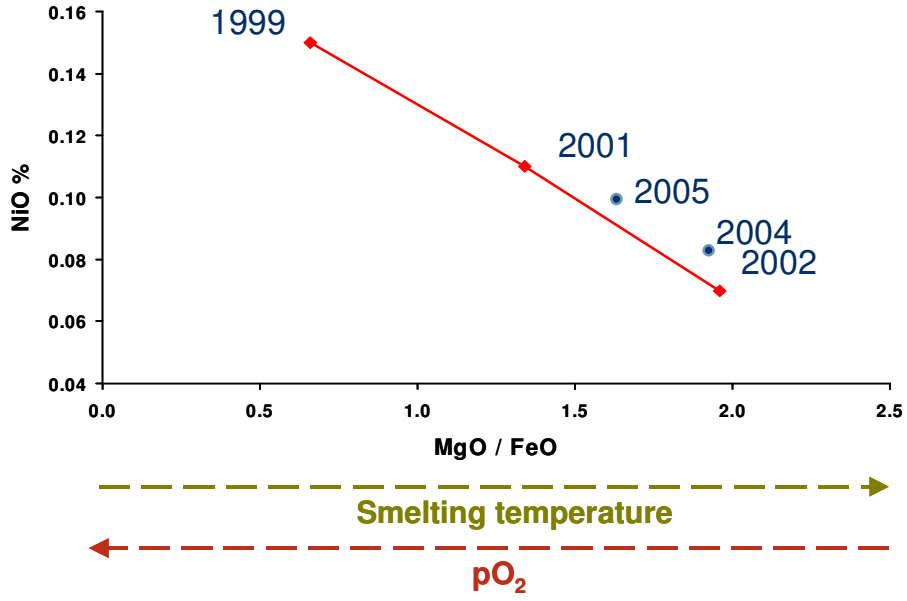

Figure 82: The original graph was presented by the author in 2004 to explain the reduction in dissolved nickel when converter slag return to the furnaces was discontinued. The MgO/FeO ratio in slag increases when the amount of converter slag returned to the furnaces falls, but this also increases the required smelting temperature. In addition, the pO_2 of the slag is higher when converter slag forms part of the feed. The situation is complex, with many interacting factors determining base metal dissolution.

Examination of the chemistry and mineralogy of the slag samples taken from Furnace 1 over the 2004 revert addition does not show evidence of increasing slag iron levels, or of increased base metal loss to silicate phases. The main reasons for this are the amounts of reverts added, and their composition. When Peirce-Smith converter reverts were added to the furnaces as part of the process before 2001, a larger tonnage was involved (up to 90 tons per day), and this consisted primarily of converter slag and entrained matte. Smaller amounts (on average 30 tons/day) were added during the 2004 sampling campaign, and the reverts consisted mainly of furnace ladle skulls, with a smaller amount of converter ladle skulls.

Smelter chemistry results for the flash drier daily composites show a deviation from 'normal feed' composition on 3 and 4 November. The fact that there is no real increase in copper and PGE levels, but only in nickel, iron and sulphur suggests that a relatively large amount of some material, such as refinery press cake, must have been added to the feed. This information was not relayed to the persons involved in running the trial, and it does serve to illustrate one of the many difficulties experienced in running plant trails of this nature. Fortunately, due to the time delay between the flash driers and the furnace, the effect of this departure from the norm on the furnace products sampled was minimal, although it could have been responsible for the unexpected drop in slag chrome levels. This was recorded during the afternoon and night shifts of November 5, despite high-chrome reverts addition.

An interesting aspect of the trial results is the surge in slag calcium levels which took place around the afternoon of 4 November. The cause of this is supposed to have been a larger-than-usual limestone addition to the furnace after stocks had been exhausted. It is curious that no evidence can be seen of increased levels of base metals dissolved in the slag silicate at higher slag calcium content (or basicity), as this

contradicts the available literature (ERIC *et al.*, 1994, and others). It must be remembered, however, that a large-scale platinum furnace is a complex system, and that one result of increased lime addition may have been a drop in smelting temperature – a slight fall in slag tapping temperature *was* recorded. This could also affect the amount of base metal dissolving in the silicate phase, as would the base metal and iron content of the bulk matte, and/or the pO_2 of the slag (NAGAMORI, 1974, WANG *et al.*, 1974, ERIC, 2004).

Electron microprobe area scans on the slag silicate phases run on the sounding bar samples from Furnace 2 in 2006 show no significant change in slag composition with depth in the slag bath. This is confirmed by the chemistry results, and agrees with the findings of earlier workers (URQUHART *et al.,* 1976).

The results of the initial FactSage equilibrium modelling exercises show that dissolved base metal levels in the furnace and SCF slags are underpredicted, for example as shown in Figure 83. The levels of sulphur, however, are accurately predicted (Figure 84).

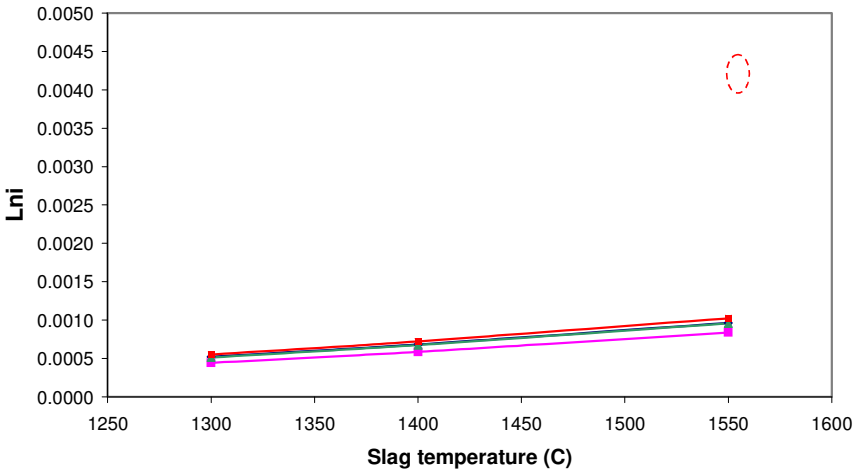

Figure 83: The predicted nickel dissolution in slag, shown as the distribution coefficient (L_{Ni}), for the Furnace 2 (2005) slag samples. The levels measured on the electron microprobe are shown by the red dotted elipse. The levels of copper and cobalt are also underpredicted by the model.

Other modelling exercises included the prediction of the amount of spinel which should form in the SCF slag samples. This was predicted to be about one half of that measured by modal analysis. Predictions of the major element distribution between SCF slag and spinel proved to be very close to the actual microprobe measurements, but nickel and cobalt levels in spinel were again underestimated (See Figures 85 and 86).

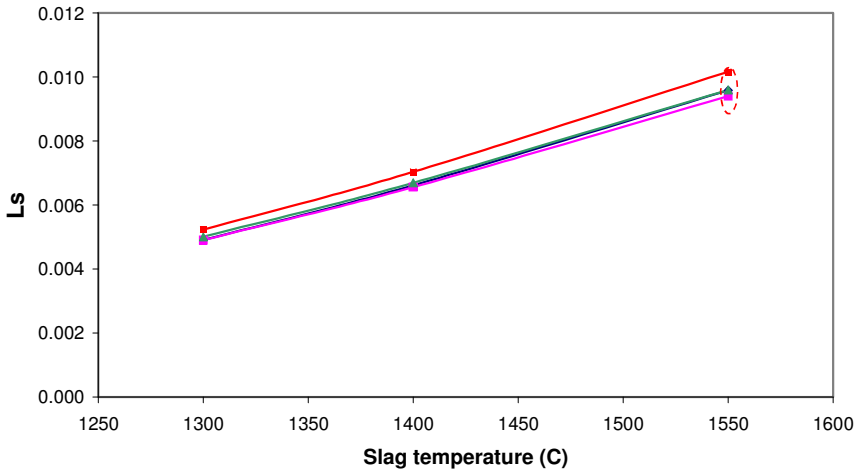

Figure 84: The predicted sulphur dissolution in slag, shown as the distribution coefficient (L_S), for the Furnace 2 (2005) slag samples. The levels measured on the electron microprobe are shown by the red dotted elipse.

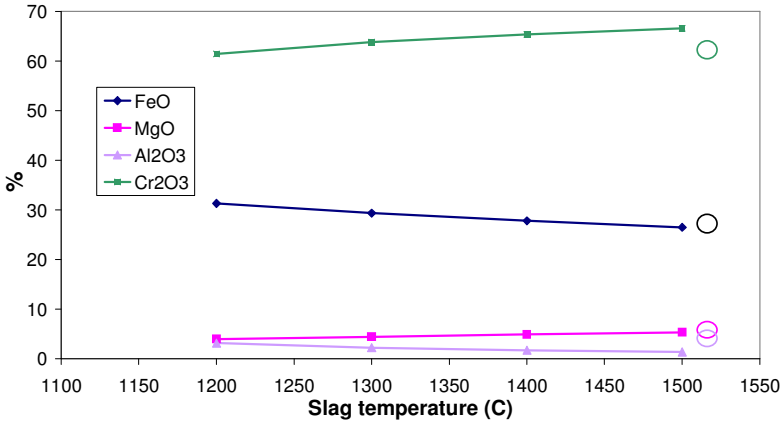

Figure 85: Plot showing the major element distribution into spinel in the 2005 SCF slag samples, as predicted by FactSage. The levels measured on the electron microprobe are shown by open circles.

FactSage also provides an insight into base metal coordination in the spinel crystals in the 1200–1500 °C temperature range. Co^{2+} prefers tetrahedral sites at all temperatures, and Co^{3+} (which would only be present in tiny amounts) would show octahedral preference. Ni^{2+} shows roughly equal site preference, but slightly favours octahedral at 1200 °C, and tetrahedral at 1500 °C.

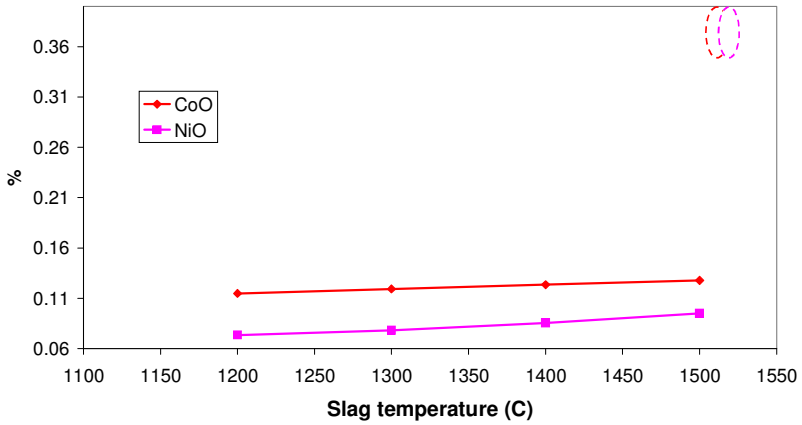

Figure 86: Plot showing the base metal distribution into spinel in SCF slag (2005), as predicted by FactSage (copper does not partition into spinel in this case). The levels measured on the electron microprobe are shown by open dotted circles.

The reasons for the underpredictions in the initial modelling attempts were not immediately apparent, since the base metal activity coefficients arrived at by *FactSage* were in agreement with those of other workers, and authorities in the field (*e.g.* SAHOO & REDDY, 1984, HOLZHEID *et al.,* 1996, LI & TSUKIHASHI, 2001, TAN & NEUSCHUTZ, 2001).

8.3 ENTRAINED MATTE IN SLAG

Matte droplets entrained in furnace and SCF slag are preserved as spherical or near-spherical phases in the quenched slag silicate glass. These were sized and analysed on the MLA to produce information on particle size distribution and droplet composition and, in the case of the six-in-lines, the relationship between the two.

During this project time was spent not only by the author, but also by Anglo Research MLA mineralogists and the technical staff of JKTech in Australia to adapt the Latti method, developed for mineral processing work, for use on entrained matte phases in slag. Although not fully automated, the result was successful for the six-in-line furnace slag samples, mainly due to the relatively small amount of entrained matte. The accuracy of the EDX area analysis, as tested on microprobe standards, was impressive. Ideally, to provide acceptable statistics, many more matte phases should have been analysed than 500 per sample, but instrument time is at a premium, and the data was sufficient to provide an overview of the size-composition trends in the six-in-line furnace slag samples, as described below.

Although data were acquired successfully for the 2005 SCF slag samples, processing ran in to difficulties because of the presence of multiple matte phases per frame, even with coarse cut-off sizes. This means that it is only possible to report the relationship between entrained matte size and composition for the six-in-line furnaces and not for the SCF. Other useful information was gleaned from the results, however, and is also included in this section.

The compositional variation of entrained matte phases is far greater in SCF slag than in six-in-line slag. The spread can be compared in two different ways – Fe *vs.* S plots, and element fraction plots. For example Fe

vs. S plots for entrained matte in the two six-in-line slag samples analysed on the MLA are shown in Figures 87 and 88.

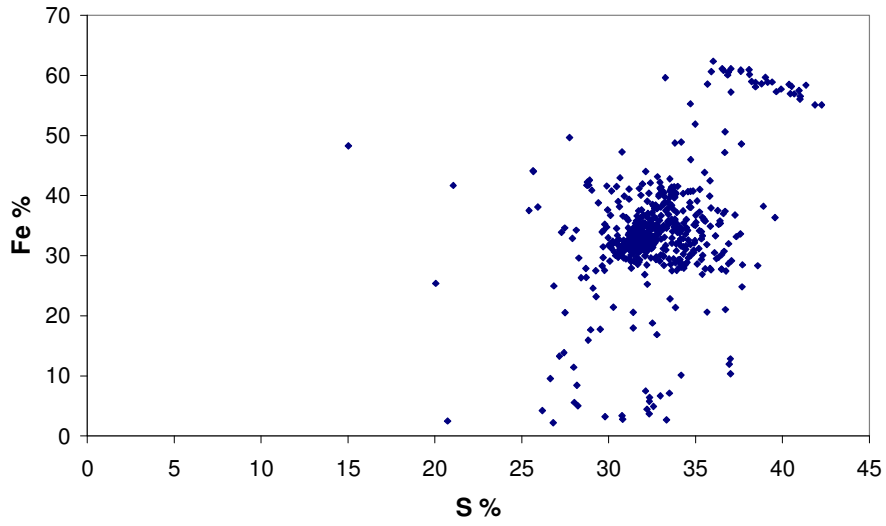

Figure 87: The compositional spread of entrained matte composition in WS1989 slag (Furnace 1, 2005) shown by the variation of iron with sulphur.

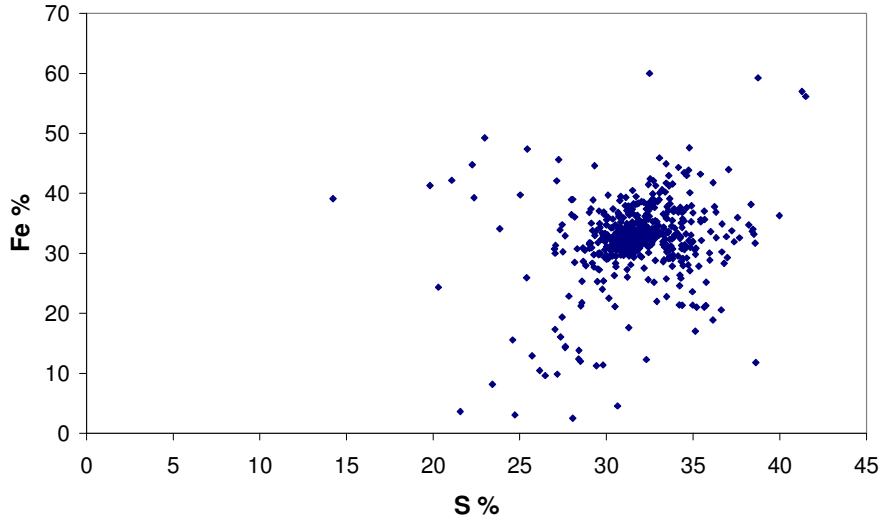

Figure 88: The compositional spread of entrained matte composition in WS2008 slag (Furnace 2, 2005) shown by the variation of iron with sulphur.

The plots reveal that entrained matte phases in sample WS1989 are not homogeneous in composition – a small group of higher Fe+S (and therefore lower Ni+Cu) phases, possibly from feed material, is separate from the main composition group. Sample WS2008 is more homogeneous. A similar trend can be picked up from the element fraction plots taking, for example, copper distribution in the entrained matte of the same slag samples (Figures 89 and 90). Here the Furnace 1 population is definitely bimodal in distribution. Histograms of this type for nickel, copper and sulphur can be seen in Figures B4 to B7 in Appendix B.

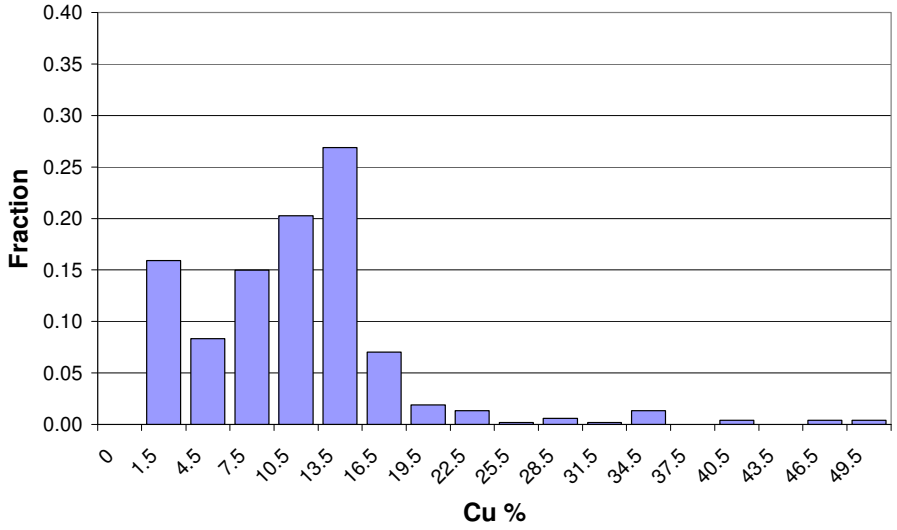

Figure 89: Copper compositional distribution in the entrained matte phases of WS1989 slag (Furnace 1, 2005).

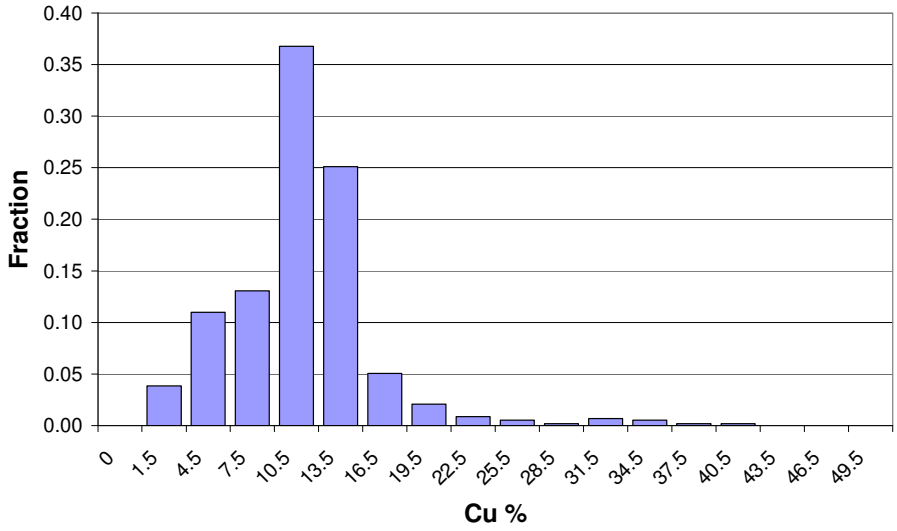

Figure 90: Copper compositional distribution in the entrained matte phases of WS2008 slag (Furnace 2, 2005).

The spread of entrained matte composition in the SCF slag samples is much greater than that of the six-in-line slags, as shown on the same scale in Figure 91 and in the histogram showing the nickel distribution in Figure 92. It appears that partly unreacted entrained sulphide phases from feed (slag and concentrate) are still present, as well as uncoalesced metallic phases formed by reduction.

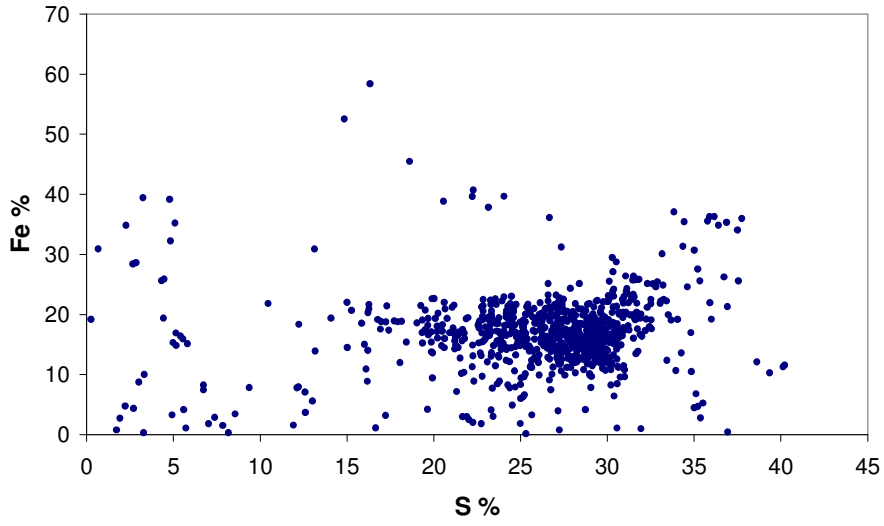

Figure 91: The compositional spread of >2 µm entrained matte composition in WS2098 SCF slag (2005) shown by the variation of iron with sulphur.

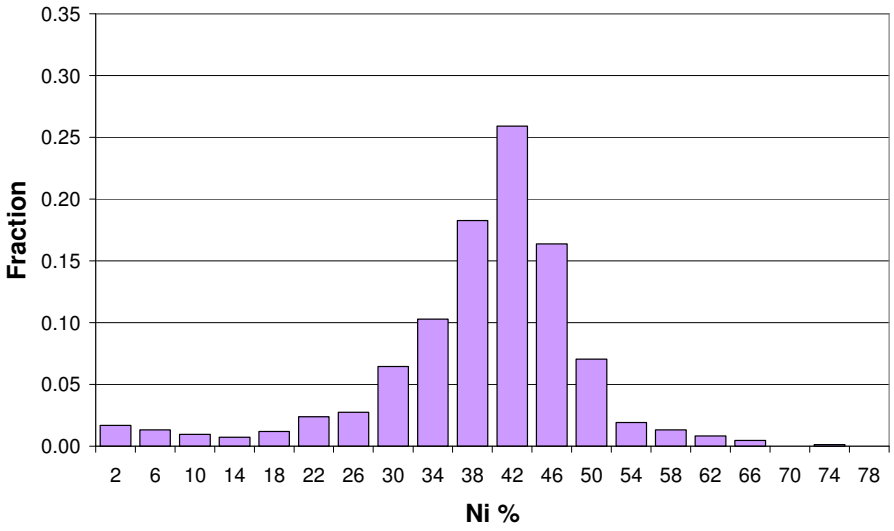

Figure 92: Nickel compositional distribution in the entrained matte phases of WS2098 SCF slag (2005).

Although it is not possible to report the relationship between entrained matte size and composition for the SCF, average matte compositions can still be estimated. Further information on the SCF slag entrained matte phases can be obtained by comparing the 2 µm cut-off plot as shown in Figure 91 with that of the 7 µm cut-off plot acquired on the same sample (Figure 93).

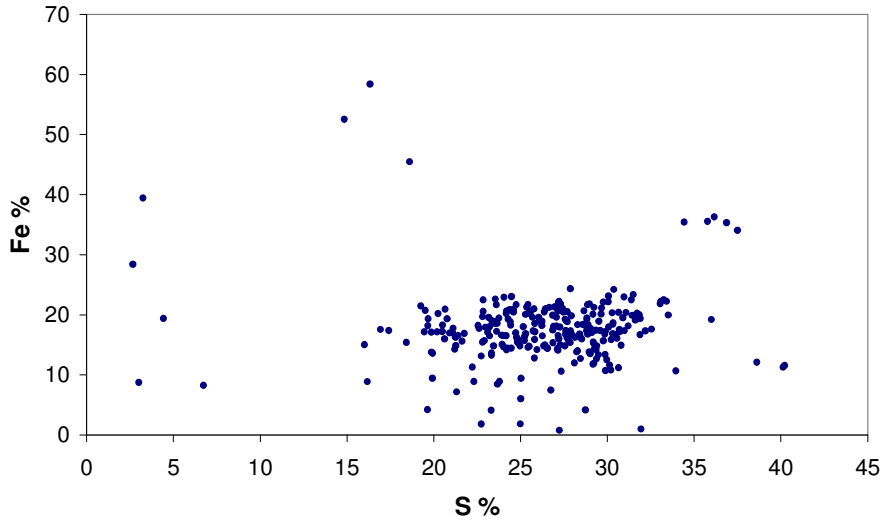

Figure 93: The compositional spread of >7 µm entrained matte composition in WS2098 SCF slag (2005) shown by the variation of iron with sulphur. This figure should be compared with the finer-sized distribution in Figure 91.

When the plots are compared, it is possible to show that many of the smallest phases are of low S+Fe composition – these are often grouped together, and may represent tiny alloy particles being reduced out of the slag.

Base metal content is plotted against entrained matte apparent diameter for the 1999 and 2005 six-in-line slag samples and shown in Figures B8 to B11 in Appendix B. No obvious dependence of size upon composition is evident, although a trend may be suspected. Confidence intervals were calculated for size groups as described in Appendix C, and plots of these are plotted in Figures B12 and B13 in Appendix B. The confidence intervals overlap so there is no significant relationship between composition and size. A small number of larger entrained matte phases are present in the slag samples, but are so sparse that they will not usually be picked up by MLA analysis – these are known as “nuggets”. Since the author was convinced that there must be a trend towards bulk matte composition in the largest of these, the manual SEM-EDX search and analysis exercise was run. The results were incorporated into the diameter plots which are plotted in Figures 94 and 95 below.

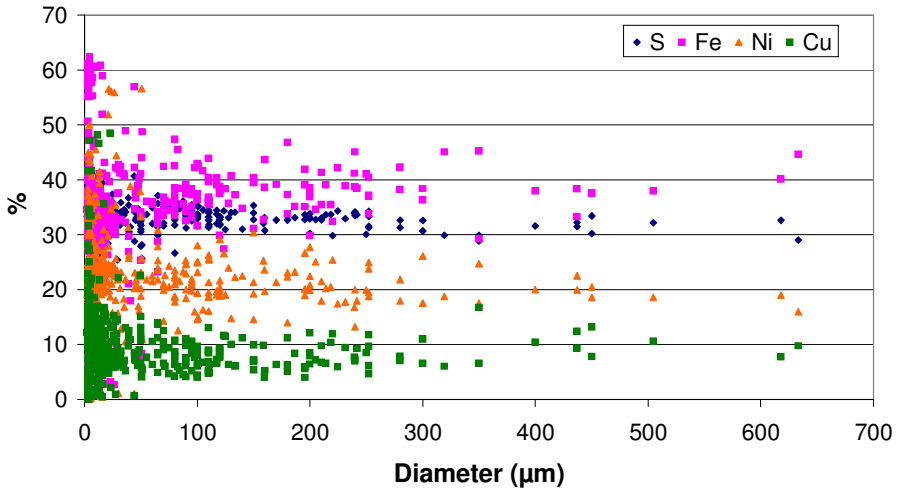

Figure 94: Entrained matte compositional variation with droplet diameter in WS 1989 slag (Furnace 1, 2005) as determined by MLA and SEM analysis.

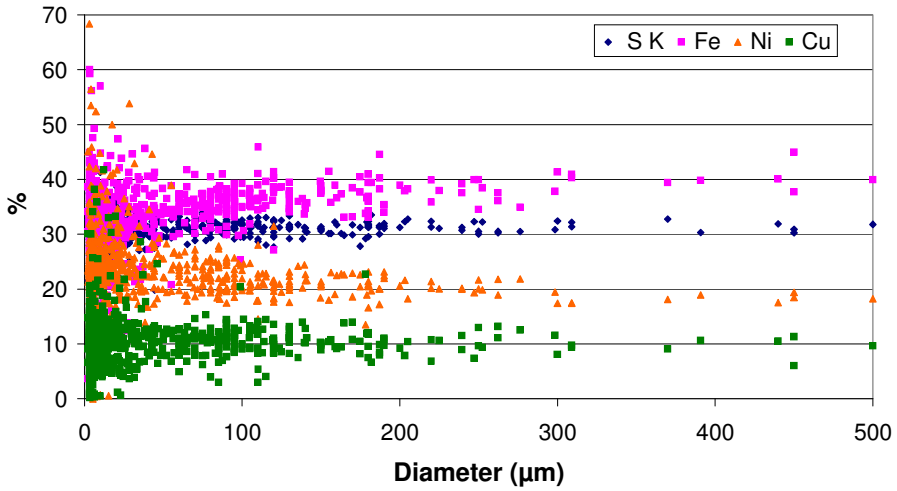

Figure 95: Entrained matte compositional variation with droplet diameter in WS 2008 slag (Furnace 2, 2005) as determined by MLA and SEM analysis.

The results were also added in to the size groups for confidence interval calculation. The final figures are shown in Table A51 (Appendix A) and plotted in Figures B14 and B15 in Appendix B. Trends only are still shown in WS1989 because the intervals are so broad due to the bimodal distributions described earlier. A far clearer picture can be seen in WS2008, which was the more homogenous sample. The confidence interval plots for nickel and iron in sample WS2008 are shown in Figures 96 and 97. A definite trend towards bulk matte composition is demonstrated.

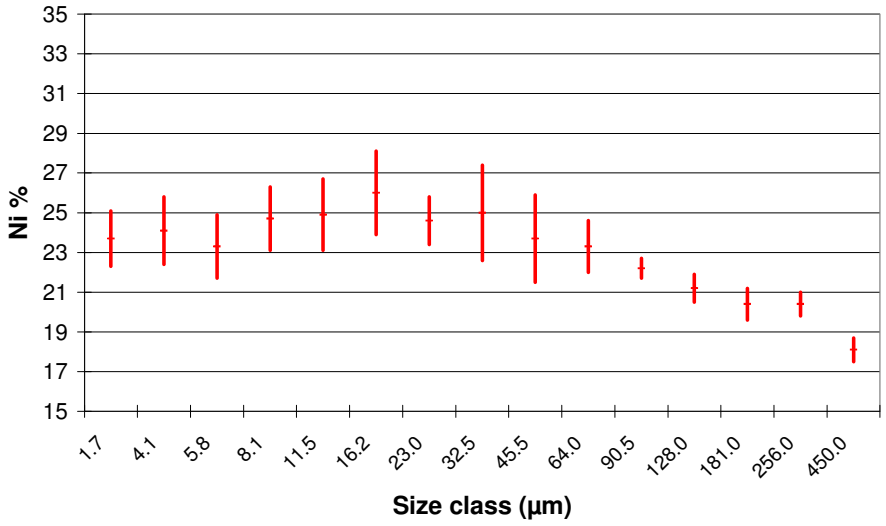

Figure 96: Confidence interval plot of entrained matte nickel content with increasing droplet size class for WS2008 slag (Furnace 2 , 2005) as determined by MLA and SEM analysis.(Size classes based on apparent diameters from polished sections).

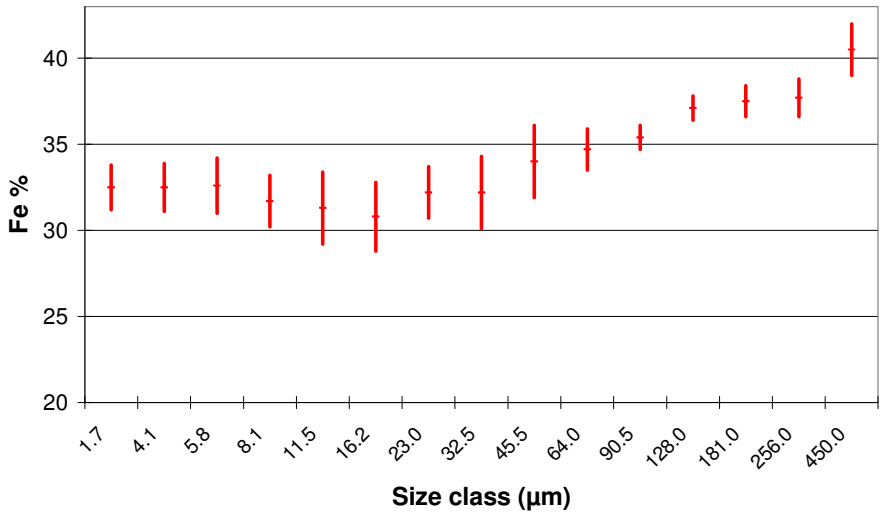

Figure 97: Confidence interval plot of entrained matte iron content with increasing droplet size class for WS2008 slag (Furnace 2, 2005) as determined by MLA and SEM analysis. (Size classes based on apparent diameters from polished sections).

Although the confidence intervals allow some statistical treatment of the results, it should be remembered that the entrained matte droplet diameters as measured on the MLA and SEM are, in fact, not true diameters, but those apparent in section (which will be equal to, or less than, the true diameter).

The size distribution of the entrained matte phases in the six-in-line furnaces and the SCF are easier to examine when grouped and plotted on a logarithmic or $\sqrt{2}$ scale. Examples of such plots are shown in Figures 98 and 99 and also in Figures B16 in Appendix B. The low size cut-off of the MLA is at 1 – 2 µm, but

the shape of the size distributions suggest that there are many tiny matte inclusions that are smaller than this. Although numerous, these will not contribute a great deal to the total matte mass percentage.

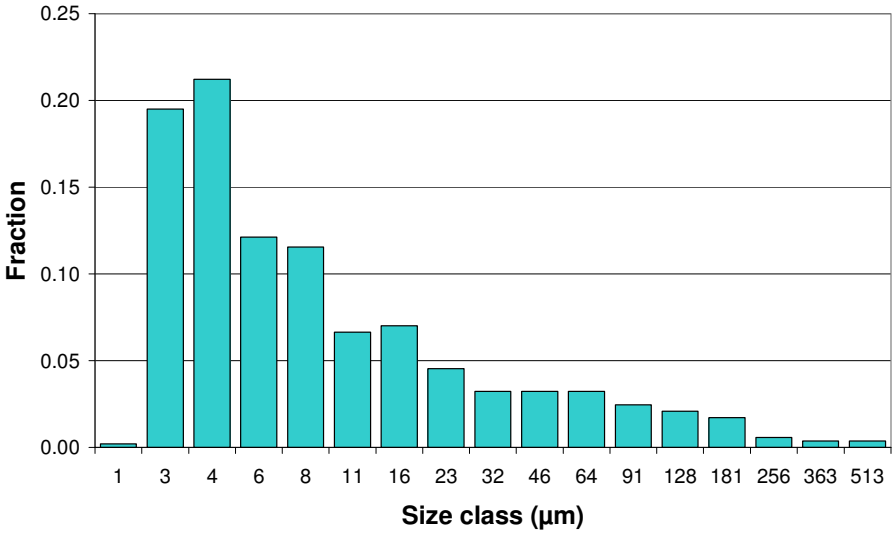

Figure 98: √2 size distribution of entrained matte droplets in WS1989 slag (Furnace 1). The cut-off size here was around 2 µm.

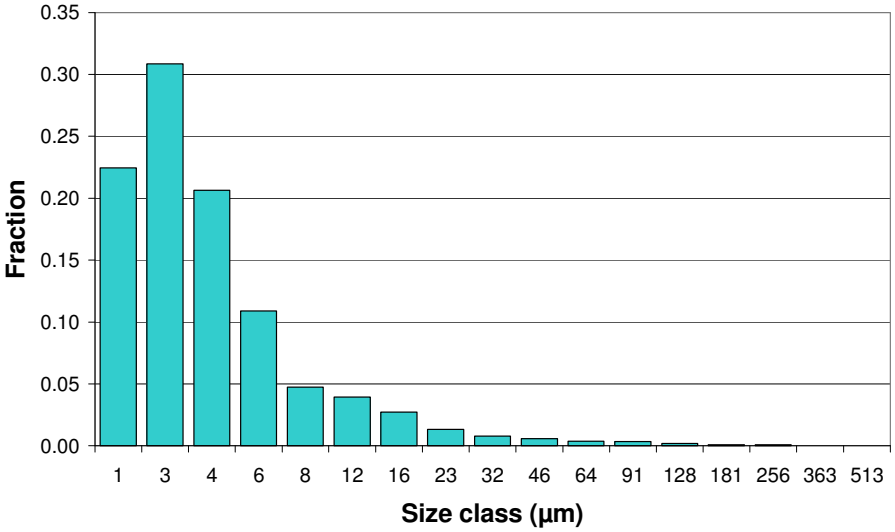

Figure 99: √2 size distribution of entrained matte droplets in WS2091 SCF slag, with cut-off size just under 2 µm.

According to WEHR & SHAW (2002), area distributions acquired on phases in section "yield consistently low estimates for mean particle size, but the error is least for coarsely-binned spheres". Fortunately, nearly all the entrained matte phases are spherical, or a close approximation, which facilitates a stereological comparison. The method used to test the relationship between entrained matte droplet composition and size was adapted from that of SALTYKOV (1967) and is described below.

In order to test a possible relationship between the composition of suspended sulphide droplets and their size, it was necessary to correct the observed two-dimensional size distribution (as measured on polished planes which were presumed to intersect the sulphide droplets randomly). The droplets were assumed to be spherical (which is reasonable, given the circular appearance of the droplets in polished section). The geometry of the intersection of different polishing planes with a sphere is illustrated in Figure 100a. As this figure shows, a random polishing plane through a sphere gives a circular area with a radius which is smaller than that of the sphere; for example, a plane at a distance h_1 from the centre of the sphere gives a circular section with a radius of l_1, and one at a distance of (h_1+h_2) gives a radius of l_2. The effect of this is that, when apparent particle sizes are measured from a 2D section, the measured particle size distribution is shifted to smaller sizes than the actual (3D) distribution. Correcting for this requires a method to account for the larger particles which, when sectioned away from their centres, contribute to the observed number of particle sections of a given (smaller) size.

In this work, the method of SALTYKOV (1967) was used to estimate the 3D size distribution from the measured 2D areas. Using this method, the observed particle sections are divided into a number of size intervals (up to 12, in the published version of his method). The lower bound of each particle size interval is related to the upper bound by $d_{i+1} = (10^{-f})\ d_i$, with f taken to be 0.1 in the example published by Saltykov (1967). This means that the largest observed diameter is taken to be $10^{0.1\times(12-1)} = 12.6$ times as large as the smallest observed diameter. Starting with the largest particles, the contribution of the particles, in each size interval, to observed smaller sections, is subtracted consecutively. This method is aided by the observation that, for a sphere of given diameter, the majority of random sections through the sphere have diameters which are close to the true diameter of the sphere (in Figure 100a, the fraction of sections which have radii which lie between l_1 and r is equal to h_1/r, the fraction which have radii between l_1 and l_2 is equal to h_2/r, and so forth). This is illustrated by Figure 100b, which gives the distribution of the observed section areas. Figure 100b also illustrates the area intervals which were used in this work, with a larger area ratio than that given in the paper by Saltykov (1967). This larger area ratio was necessary because the ratio of the largest to smallest observed diameters was 81 in this work (rather than 12.6 as used by Saltykov), hence requiring $f = 0.1735$.

The method of successively correcting for the effect of large particles on observed smaller sections is then as follows –

$$N_{V1} = (1/d_1)(s_1 N_{A1})$$
$$N_{V2} = (1/d_2)(s_1 N_{A2} - s_2 N_{A1})$$
$$N_{V3} = (1/d_3)(s_1 N_{A3} - s_2 N_{A2} - s_3 N_{A1})$$
$$\vdots$$
$$N_{V12} = (1/d_{12})\ (s_1 N_{A12} - s_2 N_{A11} - s_3 N_{A10} - s_4 N_{A9} - s_5 N_{A8} - s_6 N_{A7} - s_7 N_{A6} - s_8 N_{A5} - s_9 N_{A4} - s_{10} N_{A3} - s_{11} N_{A2} - s_{12} N_{A1})$$

In this expression, N_{Ai} is the number of particle sections with diameters between d_i and d_{i+1} which are observed on the random planes, N_{Vi} is the actual number of particles with diameter d_i in the material (that is, the required true size distribution), and s_1 to s_3 are the coefficients of the Saltykov calculation. In this work, these coefficients were recalculated for the size ratios (corresponding to $f = 0.1735$) as required here. The original Saltykov coefficients (for $f = 0.1$) were also recalculated, for comparison. The values for $f = 0.1$ were found to be identical to those given in the original paper, except for slight differences in s_6 to s_{12}, which coefficients appear to have been affected by truncation errors in the original paper. These values are summarised in Table 85.

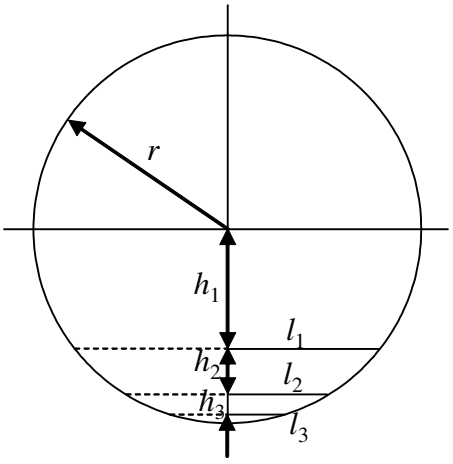

Figure 100a: Geometry of the intersection of polishing planes with a spherical particle (radius r), with the planes at various distances (h_1, h_1+h_2, $h_1+h_2+h_3$) from the centre of the sphere, giving circular sections with radii l_1, l_2 and l_3 (adapted from UNDERWOOD, 1970).

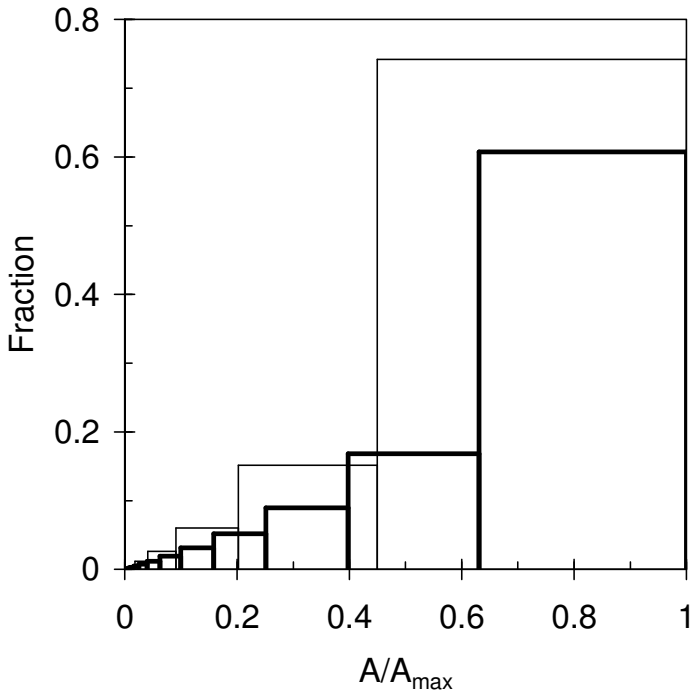

Figure 100b: Distribution of the areas of random sections through a sphere. Heavy line: area interval ratio of $10^{0.2}$ (as used by SALTYKOV, 1967); thin line: area interval $10^{0.347}$ (as used in this work, to give a larger ratio of large to small observed sections).

Table 85: Coefficients (s_i) for the calculation of the true size distribution by means of the SALTYKOV (1967) method, for f = 0.1 (as in the original Saltykov paper), and f = 0.1735 (as used for the sulphide droplet size distribution in this work).

	f = 0.1		*f* = 0.1735
i	this work	Saltykov	this work
1	1.646121	1.6461	1.348133
2	0.456123	0.4561	0.275113
3	0.11619	0.1162	0.053416
4	0.041495	0.0415	0.013822
5	0.017271	0.0173	0.004005
6	0.007795	0.0079	0.001221
7	0.003684	0.0038	0.000381
8	0.00179	0.0018	0.00012
9	0.000884	0.0010	3.81E-05
10	0.000441	0.0003	1.21E-05
11	0.000222	0.0002	3.87E-06
12	0.000112	0.0002	1.23E-06

Examination of volume fraction plots such as those shown in Figure 101, and in Figure B17 in Appendix B, shows that trends are consistent over various entrained matte compositional groups, with the exception of a few "nuggets" of > 200 µm diameter, which skew the volume distribution. Note that the x axis is plotted on a log scale. The trends indicate that the composition-size relationships derived from the number of determinations in this study can be taken as a meaningful reflection of the facts: high-nickel particles are less common in the larger size group.

The entrained matte phases analysed at different depths in the six-in-line furnace slag bath during the 2007 sounding bar investigation were also processed for confidence interval plots (as shown in Figures 102 to 104, and Figure B18 in Appendix B). This treatment shows a significant variation towards bulk matte composition as the slag-bulk matte interface is approached. The presence of such a large amount of spinel could have led to matte being captured from the bulk matte below. There does seem to be a gradual compositional trend from the entrained matte analysed higher in the bath, however, to that near the interface.

The conclusion from the data sets is that the larger entrained matte particles, and the matte particles from lower in the slag layer contain less nickel (and are closer to bulk matte composition). Interestingly, this trend is not found for copper.

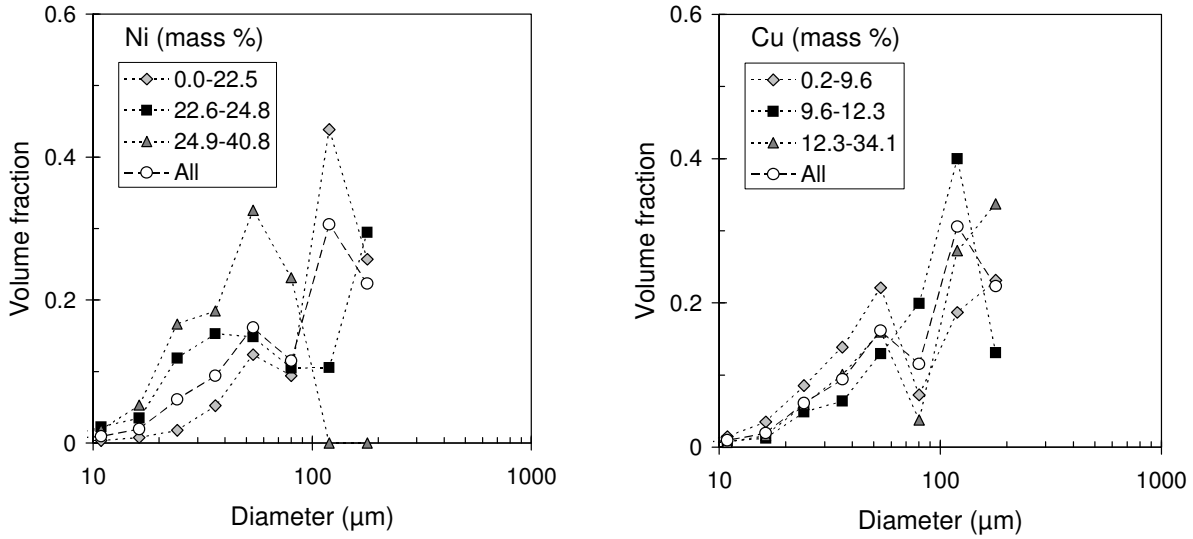

Figure 101: A comparison of the volume fractions of entrained matte nickel and copper in high, medium and low levels, compared to the total for WS2008.

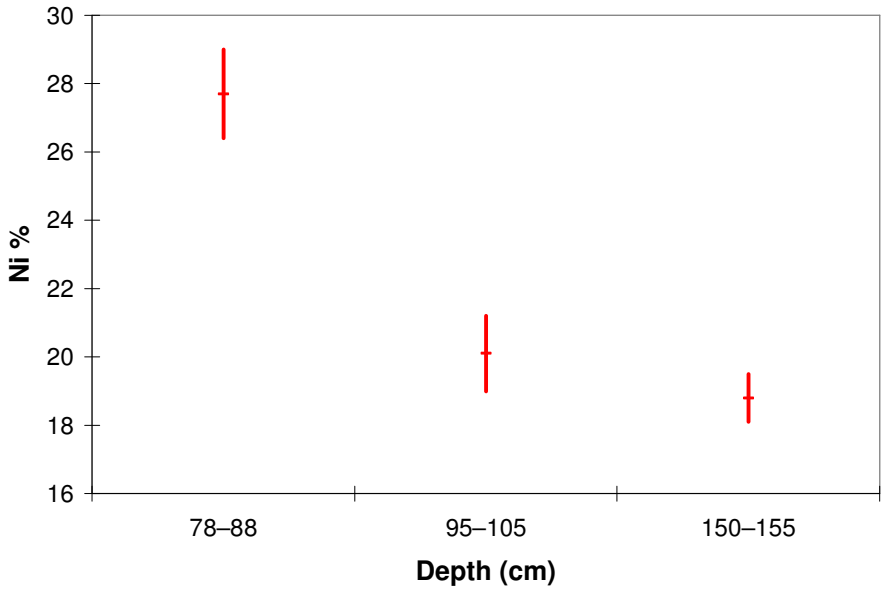

Figure 102: Confidence interval plot of entrained matte nickel content with depth in the slag bath for the 2007 sounding bar samples (Furnace 1) as determined by SEM analysis.

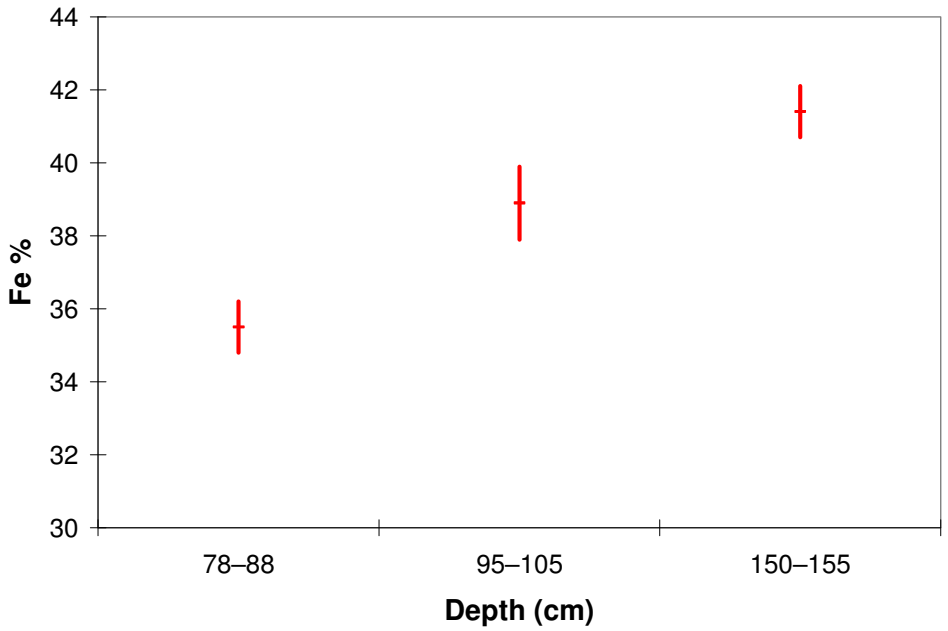

Figure 103: Confidence interval plot of entrained matte iron content with depth in the slag bath for the 2007 sounding bar samples (Furnace 1) as determined by SEM analysis.

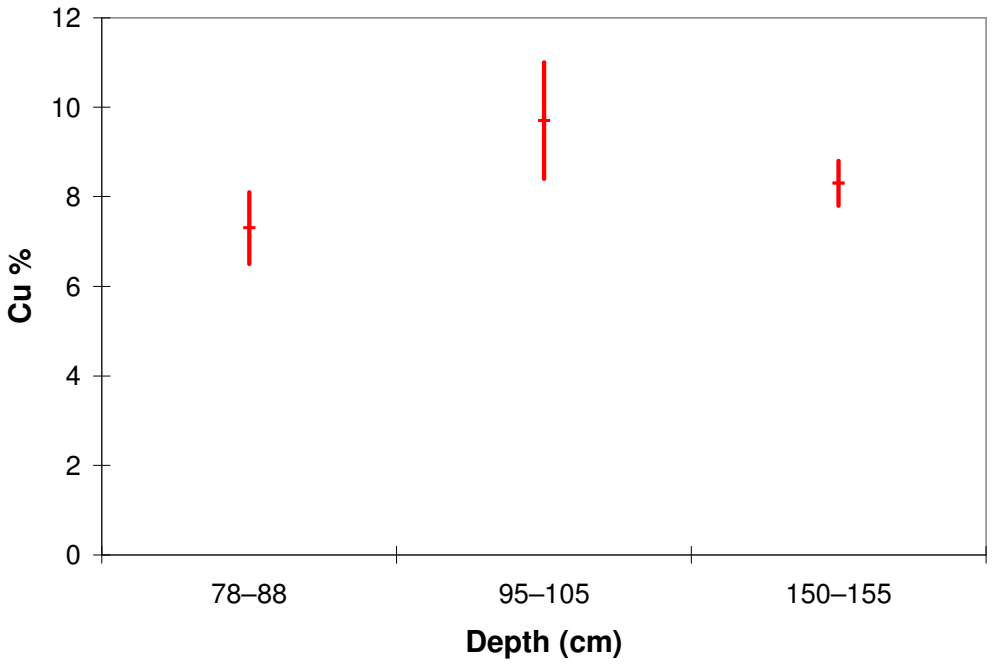

Figure 104: Confidence interval plot of entrained matte copper content with depth in the slag bath for the 2007 sounding bar samples (Furnace 1) as determined by SEM analysis.

If the composition of the 2005 entrained matte phases, as measured on the MLA, is averaged for a slag sample and compared to that of bulk matte sampled on the same day or shift, the entrained matte is nickel-rich and iron-poor compared to bulk matte. This applies to the 1999 and 2005 six-in-line and the 2005 SCF samples, and has implications for slag-matte equilibrium. The average entrained matte compositions are also

not intermediate between feed sulphide and bulk matte compositions – in other words, the droplets have not achieved this composition through partial melting during settling. If the droplets have equilibrated with the surrounding slag and display a nickel-rich, iron-poor composition, then there cannot be equilibrium between the slag and bulk tapped matte.

The entrained matte droplets in tapped slag represent phases that have not coalesced and settled during the allotted time, the lowest value of which may loosely be defined as the residence time of the slag between the electrode closest to the slag tap hole and the tap hole itself. Using the information displayed in Table 5 (Page 30), an approximate settling time in the slag bath can be estimated (Table 86).

Table 86: An estimate of the time required (in minutes) for matte droplets to settle 1 m through the slag bath. Slag viscosities were taken as 0.3 and 0.1 Pa.s (six-in-line and SCF respectively), and ΔRD as 1.0 and 2.2.

Drop diameter	Six-in-line slag	SCF slag
1 mm	6.1	<1
100 µm	612	93
10 µm	61162	9267

The depth of one metre was chosen for comparison purposes; in fact the average depth of the SCF slag bath is 1.2 m. That of the six-in-lines is currently around 1 m (shallower than that described by ERIC (2004).

The origin of entrained matte in slag is discussed further in Section 8.7.

8.4 Fe^{3+}/Fe^{2+} MEASUREMENT FOR SLAG pO_2 AND OTHER MÖSSBAUER INFORMATION

Since the initial FactSage modelling results suggested that there must be a higher than predicted oxygen activity in the slag in order to achieve the dissolved base metal levels that were measured on the microprobe, samples were submitted for Mössbauer Spectroscopy.

The use of this technique for slag and glass measurement of iron speciation, and hence pO_2, is currently widely accepted. It is also possible to measure the Fe^{3+}/Fe^{2+} ratio in PGE smelter slag using chemical methods, such as HF/HCl digestion followed by potassium dichromate titration (HUNDERMARK, 2002), or a combination of wet chemistry and XRF (DU TOIT *et al.,* 2005), but these are generally reported to be complex and sometimes unreliable. Comparisons between wet chemical results and those from Mössbauer Spectroscopy are given by DYAR (1985) as well as by MYSEN and co-workers (1985). These authors suggest that a higher Fe^{3+}/Fe^{2+} ratio is determined on glass using Mössbauer than wet chemistry, but it is not known which technique is inaccurate. It is also suggested that the presence of Al^{3+} decreases the Fe^{2+} component, whereas Ca^{2+} and Mg^{2+} may increase it. These effects may be counteracted by the use of molar basicity corrections during pO_2 calculation at the iron redox equilibrium (YANG & BELTON, 1997).

The Fe^{3+}/Fe^{2+} ratios determined on the 2005 six-in-line furnace slag samples of this study fall into a similar range as those determined with the XRF-wet chemistry technique by DU TOIT and co-workers (2005). One factor not mentioned in the discussions on technique preference is that other sources of iron are present in the slag samples, such as iron in entrained matte, and occasionally in crystalline olivine. Wet chemical and XRF methods rely on the determination of ferrous and total iron, with ferric being calculated by difference, and the distinction between ferric and sulphide iron would not be made. The data available from Mössbauer allows some discrimination as to the type of iron present –*e.g.* Fe in glass, Fe in magnetite, Fe as metal, *etc.*

Whereas the amount of sulphide iron in six-in-line slag samples is usually negligible, this would not necessarily be the case for SCF or converter slag.

It should also be considered that the rate and type of quenching of a silicate melt might affect the homogeneity of the resulting glass, as well as the valency and coordination of the transition metals, according to certain workers involved in lunar glass research (DYAR & BIRNIE, 1984, DYAR, 1985, DYAR *et al.,* 1987). Even ageing has been shown to reduce the Fe^{3+} component of Mössbauer spectra of air-quenched glass – after one year the peak corresponding to Fe^{3+} in these samples was substantially reduced, and after two years it had vanished. The same cannot be said of the water-quenched samples of this study – the 1999 slag samples were analysed eight years after production and the Fe^{3+} component was still present, allowing the levels of higher pO_2 in the earlier samples to be confirmed.

The Mössbauer spectra obtained, including the isomer shift and quadrupole splitting for the quenched slag samples of this study, are almost identical to those found for naturally-occuring Mg-Fe-Al-Ca silicate glasses. The Fe^{3+}/Fe^{2+} ratio is therefore also similar, and AP six-in-line slag glass corresponds closely to the melted USGS (United States Geological Survey) basalt standard. From the Mössbauer parameters, the iron coordination in the silicate glass of the slags of this study is both tetrahedral and octahedral (for Fe^{2+}), and probably tetrahedral for Fe^{3+}. The cobalt coordination is likely to be similar to Fe^{2+}, whereas nickel could resemble both Fe^{2+} and Fe^{3+} displaying tetrahedral and octahedral, or distorted octahedral, coordination.

The method of calculating pO_2 from the Fe^{3+}/Fe^{2+} ratio relies on the following data –

For the reaction $FeO + 0.25O_2 = FeO_{1.5}$ $\quad K = a_{FeO1.5}/a_{FeO} \cdot (pO_2)^{0.25}$,

and therefore $pO_2 = (a_{FeO1.5}/a_{FeO} \cdot K_2)^4$

The values of a_{FeO} and $a_{FeO1.5}$ are available from FactSage.

Calculation of pO_2 in the six-in-line and SCF slag samples from the Mössbauer results assumes the redox couple $(FeO)^{slag}/(FeO_{1.5})_{slag}$ as distinct from the $[Fe]_{matte}/(FeO)_{slag}$ which was used in the preliminary modelling exercises. It therefore produces a result that is independent of slag-bulk matte equilibrium. Use of the two redox couples is explained in more detail in the next section.

8.5 CALCULATION OF THE BASE METAL DISTRIBUTION IN SLAG

8.5.1 Reactions and equilibrium constants

It is assumed that oxidic dissolution of the base metals predominates (see Page 8), so the dissolution equilibria for the base metals are given by:

$Ni + 0.5\ O_2 = NiO$

$Cu + 0.25\ O_2 = CuO_{0.5}$

$Co + 0.5\ O_2 = CoO$

For these equilibria, the metallic species (Ni, Cu, and Co) are dissolved in the matte, and the oxides (NiO, $CuO_{0.5}$ and CoO) in the slag. The partial pressure of oxygen can be established by various couples, as discussed later in this section.

The method of equilibrium dissolution calculation is illustrated below, taking nickel as example.

The equilibrium constant for dissolution is given by:

$$K_{\mathrm{Ni}} = \frac{a_{\mathrm{NiO}}}{a_{\mathrm{Ni}}\sqrt{p_{O_2}}}$$

where a_{NiO} is the activity of NiO in the slag, a_{Ni} is the activity of Ni in the matte, and p_{O_2} is the prevailing oxygen activity.

The activity of NiO can be written as follows in terms of the activity coefficient and molar masses of NiO and slag:

$$a_{\mathrm{NiO}} = \gamma_{\mathrm{NiO}} X_{\mathrm{NiO}} = \frac{\gamma_{\mathrm{NiO}}(\%\mathrm{NiO})/M_{\mathrm{NiO}}}{100/M_{\mathrm{slag}}}$$

where X_{NiO} is the mole fraction of NiO in the slag, γ_{NiO} is the activity coefficient of NiO in the slag, (%NiO) is the mass percentage of NiO in the slag, M_{NiO} is the molar mass of NiO, and M_{slag} is the average molar mass of the slag.

Substitution then gives the following expression for the percentage NiO in the slag; the expressions for $CuO_{0.5}$ and CoO are also shown.

$$(\%\mathrm{NiO}) = \frac{100M_{\mathrm{NiO}}}{\gamma_{\mathrm{NiO}}M_{\mathrm{slag}}} K_{\mathrm{Ni}} a_{\mathrm{Ni}} \sqrt{p_{\mathrm{O}2}}$$

$$(\%\mathrm{CuO}_{0.5}) = \frac{100M_{\mathrm{CuO}_{0.5}}}{\gamma_{\mathrm{CuO}_{0.5}}M_{\mathrm{slag}}} K_{\mathrm{Cu}} a_{\mathrm{Cu}} \left(p_{\mathrm{O}2}\right)^{0.25}$$

$$(\%\mathrm{CoO}) = \frac{100M_{\mathrm{CoO}}}{\gamma_{\mathrm{CoO}}M_{\mathrm{slag}}} K_{\mathrm{Co}} a_{\mathrm{Co}} \sqrt{p_{\mathrm{O}2}}$$

Equilibrium constants were found from the FactSage database, using liquid reference states for the matte and slag species. The equilibrium constants are summarised in Table 87 below:

Table 87: Equilibrium constants for base metal dissolution. The equilibrium constants are given in the form ln K = A/T + B, where T is the absolute temperature. Reference states are the pure liquids for the metal and oxide species.

Reaction	*A (K)*	*B (-)*
Ni + 0.5 O_2 = NiO	23018	-8.015
Cu + 0.25 O_2 = $CuO_{0.5}$	7408.3	-2.663
Co + 0.5 O_2 = CoO	25511	-7.384

8.5.2 Activities and activity coefficients in slag and matte

The activity coefficients of the base metal oxides in the slag were calculated using the model "SlagA" in the FToxid database of FactSage (v. 5.5). The activity coefficients were found from the calculated activities at

0.1% (mass basis) of the oxides in the slag, for a temperature of 1500°C. Tables 88 and 89 below summarise the slag compositions and activity coefficients.

Table 88: Summarised slag compositions (mass percentages), showing major components only. The Fe_2O_3 content was found from the total FeO_x content, and the Fe^{3+}/Fe^{2+} ratio analysed by Mössbauer spectroscopy.

Case	Furnace	Year	Slag	MgO	Al_2O_3	SiO_2	CaO	FeO	Fe_2O_3
a	1	1999	FS1	16.88	3.99	46.63	6.47	21.2	2.3
b	2	1999	FS6	15.86	3.73	45.66	5.89	23.9	2.9
c	1	2005	WS1989	21.57	5.24	48.72	6.99	12.6	0.59
d	2	2005	WS2008	20.4	5.17	47.59	9.61	12.6	0.59
e	SCF	2005	WS2091	9.65	3.11	38.23	2.27	42.0	1.45
f	SCF	2005	WS2098	9.45	3.08	37.77	2.15	41.5	1.94

Table 89: Activity coefficients and activities in the slags as listed in Table 88, with average slag molar mass. Reference states are the pure liquid for NiO, $CuO_{0.5}$, CoO and FeO, and pure solid for $FeO_{1.5}$.

Case	γ_{NiO}	$\gamma_{CuO0.5}$	γ_{CoO}	a_{FeO}	$\gamma_{FeO1.5}$	M_{slag} (g/mol)
a	3.25	4.93	1.21	0.191	10.62	58.1
b	2.96	4.72	1.16	0.210	9.38	58.6
c	4.34	5.44	1.34	0.127	16.50	56.1
d	4.65	5.70	1.50	0.139	16.20	56.3
e	2.32	4.13	1.00	0.366	6.15	62.3
f	2.27	4.07	0.98	0.359	5.94	62.4

The activities of the matte species were found from the analysed matte compositions, using the model "MATT" in the FTmisc database. The matte compositions and activities are summarised in Tables 90 and 91. At this stage, the composition of entrained matte from MLA results was considered as well as bulk matte composition. It should be noted that the higher sulphur content of the entrained matte results in a much larger sulphur activity, and substantially smaller metal activities.

Table 90: Compositions of entrained matte (from MLA analyses) and bulk matte, for the years and furnaces as listed in Table 88.

Case	Entrained matte					Bulk matte				
	S	Fe	Co	Ni	Cu	S	Fe	Co	Ni	Cu
a	33.1	38.9	2.4	19	6.7	28.1	44.4	0.5	17.4	9.2
b	32.7	37.0	1.1	21.1	8.1	27.8	42.8	0.5	18.6	9.8
c	32.7	34.3	0.7	22.3	10.0	29.7	41.1	0.4	17.1	11.7
d	31.8	32.5	0.7	24.2	10.8	29.5	41.4	0.4	17.7	11.0
e	23.4	15.3	1.8	38.9	20.6	20.9	30.5	1.8	33.8	12.9
f	26.0	16.8	1.8	38.8	16.6	22	29.1	1.7	33	14.2

Table 91: Activities in the mattes of which the compositions are summarised in Table 90. The reference states are pure liquid metals for Fe, Cu, Ni and Co. The partial pressure of S_2 is in atm. Values are for the typical slag tapping temperature of 1500°C.

Case	Entrained matte					Bulk matte				
	a_{Fe}	a_{Cu}	a_{Ni}	a_{Co}	p_{S2}	a_{Fe}	a_{Cu}	a_{Ni}	a_{Co}	p_{S2}
a	0.013	0.0065	0.035	0.0028	0.483	0.191	0.0422	0.135	0.0042	0.0020
b	0.012	0.0075	0.035	0.0012	0.597	0.184	0.0452	0.141	0.0041	0.0021
c	0.006	0.0071	0.025	0.0005	1.610	0.096	0.0344	0.104	0.0022	0.0084
d	0.010	0.0101	0.036	0.0007	0.642	0.106	0.0344	0.110	0.0023	0.0070
e	0.073	0.1048	0.231	0.0134	0.002	0.279	0.1212	0.292	0.0209	0.0003
f	0.036	0.0513	0.139	0.0073	0.015	0.239	0.1175	0.275	0.0187	0.0004

8.5.3 Oxygen activities

Two possible redox couples were considered as indicators of the oxygen activity. These were the combinations $[Fe]_{matte}/(FeO)_{slag}$ (as used in the initial modelling exercise, but this time for bulk and entrained matte), and $(FeO)_{slag}/(FeO_{1.5})_{slag}$ (as calculated from the Mössbauer results). The equilibrium constants of the two reactions for these couples are summarised in Table 92.

Table 92: Equilibrium constants for reactions which indicate the oxygen activity. The equilibrium constants are given in the form ln K = A/T + B, where T is the absolute temperature. Reference states are the pure liquids for the Fe and FeO, and pure solid for $FeO_{1.5}$.

Reaction	*A (K)*	*B (-)*
$Fe + 0.5\ O_2 = FeO$	29362	-6.171
$FeO + 0.25\ O_2 = FeO_{1.5}$	20783	-9.424

The oxygen activity was estimated from the activities of FeO and $FeO_{1.5}$ in the slag (using the data as given in Tables 84 and 85), and the Fe activities in the matte (Table 90). Because the Fe activities are very different in the entrained and bulk matte, the predicted oxygen activities differ. The oxygen activity as predicted from the Fe^{3+}/Fe^{2+} reaction gave a third value, which was larger than the oxygen activities predicted for the two Fe-FeO equilibria. These predicted oxygen activities are summarised in Table 93.

Table 93: Predicted oxygen activities (pO_2, in atm), for different redox couples, as calculated from the equilibrium constants of Table 89 and the activities summarised in Tables 88 and 90. "EM" denotes entrained matte and "BM" is bulk matte. The first two columns of values are for equilibrium between $[Fe]_{matte}$ and $(FeO)_{slag}$, and the third column is for equilibrium between $(FeO)_{slag}$ and $(FeO_{1.5})_{slag}$.

Case	BM/slag	EM/slag	Fe^{3+}/Fe^{2+}
a	$9.5x10^{-10}$	$1.9x10^{-7}$	$8.78x10^{-5}$
b	$1.2x10^{-9}$	$3.1x10^{-7}$	$9.72x10^{-5}$
c	$1.6\ x10^{-9}$	$3.6x10^{-7}$	$1.01x10^{-5}$
d	$1.6\ x10^{-9}$	$1.8x10^{-7}$	$6.69x10^{-6}$
e	$1.6\ x10^{-9}$	$2.3x10^{-8}$	$1.69x10^{-7}$
f	$2.1\ x10^{-9}$	$9.2\ x10^{-8}$	$5.62x10^{-7}$

8.5.4 Calculated base metal dissolution

Plots can be produced from this data such as those shown in Figure 105 and in Figures B19 to B21 in Appendix B. The levels of dissolved base metals corresponding to bulk matte-slag and entrained matte-slag

equilibria may be read off at the Fe/FeO and Fe^{3+}/Fe^{2+} buffers (or redox pairs). The levels obtained for all eighteen cases are summarised in Table 94.

Table 94: Predicted levels of base metal dissolution (in mass %) at both buffers for bulk matte-slag and entrained matte-slag equilibria for all the samples modelled, as compared to those measured on the microprobe.

Year	Furnace	Base metal oxide	Bulk matte equilibrium (BME)		Entrained matte equilibrium (EME)		Measured	Best fit
			Fe/FeO	Fe^{3+}/Fe^{2+}	Fe/FeO	Fe^{3+}/Fe^{2+}		
1999	1	NiO	0.0237	7.212	0.0883	1.8759	0.135	EME, Fe/FeO
1999	2	NiO	0.0305	8.569	0.1195	2.1144	0.152	EME, Fe/FeO
1999	1	Cu_2O	0.0266	0.464	0.0155	0.0714	0.085	EME, Fe^{3+}/Fe^{2+}
1999	2	Cu_2O	0.0315	0.528	0.0209	0.0878	0.095	EME, Fe^{3+}/Fe^{2+}
1999	1	CoO	0.0115	4.580	0.1449	3.0772	0.063	BME, Fe/FeO
1999	2	CoO	0.0175	4.907	0.0782	1.3846	0.070	EME, Fe/FeO
2005	1	NiO	0.0186	1.457	0.0669	0.3544	0.097	EME, Fe/FeO
2005	2	NiO	0.0182	1.164	0.0616	0.3784	0.098	EME, Fe/FeO
2005	1	Cu_2O	0.0233	0.207	0.0186	0.0427	0.071	EME, Fe^{3+}/Fe^{2+}
2005	2	Cu_2O	0.0222	0.177	0.0211	0.0523	0.062	EME, Fe^{3+}/Fe^{2+}
2005	1	CoO	0.0098	0.772	0.0312	0.1652	0.016	BME, Fe/FeO
2005	2	CoO	0.0091	0.586	0.0287	0.1761	0.014	BME, Fe/FeO
2005	SCF a	NiO	0.0874	0.892	0.2622	0.7042	0.26	EME, Fe/FeO
2005	SCF b	NiO	0.0960	1.564	0.3211	0.7932	0.28	EME, Fe/FeO
2005	SCF a	Cu_2O	0.0974	0.311	0.1641	0.2689	0.24	EME, Fe^{3+}/Fe^{2+}
2005	SCF b	Cu_2O	0.1022	0.412	0.1148	0.1801	0.30	BME, Fe^{3+}/Fe^{2+}
2005	SCF a	CoO	0.1116	1.139	0.2716	0.7294	0.26	EME, Fe/FeO
2005	SCF b	CoO	0.1162	1.892	0.2991	0.7389	0.26	EME, Fe/FeO

NiO dissolution in Furnace 2 slag, 1999.

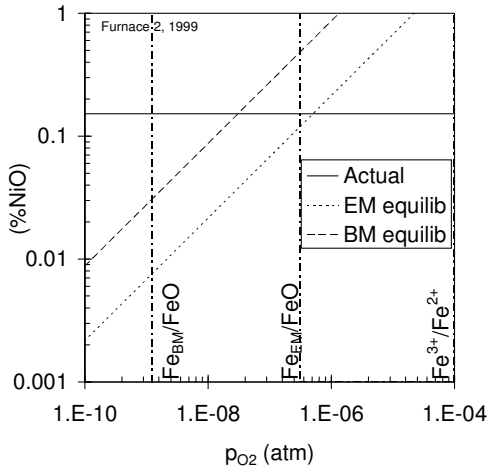

NiO dissolution in Furnace 2 slag, 2005.

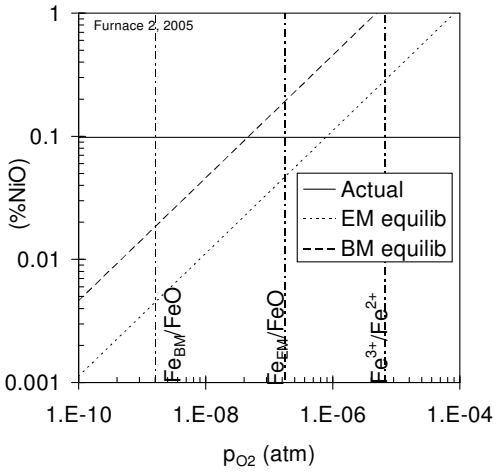

NiO dissolution in SCF slag, 2005.

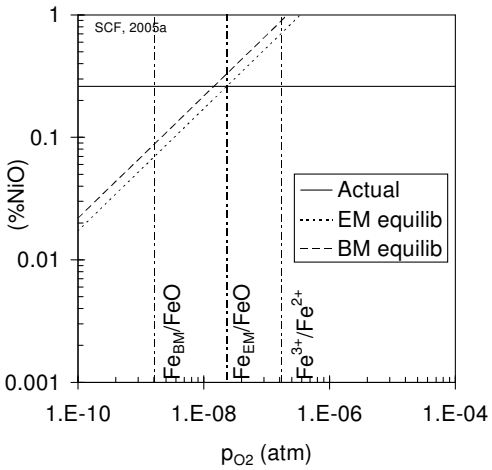

Cu_2O dissolution in Furnace 2 slag, 1999.

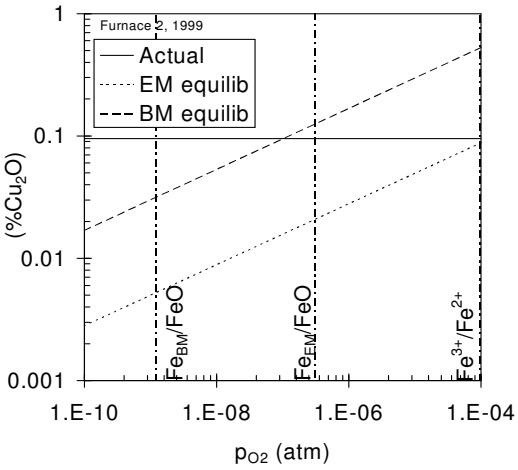

Cu_2O dissolution in Furnace 2 slag, 2005.

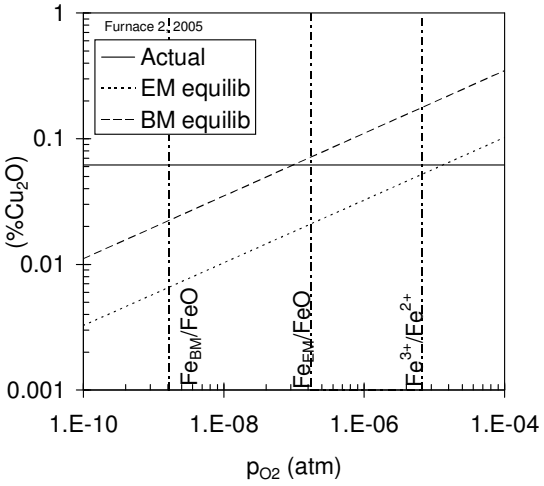

Cu_2O dissolution in SCF slag, 2005.

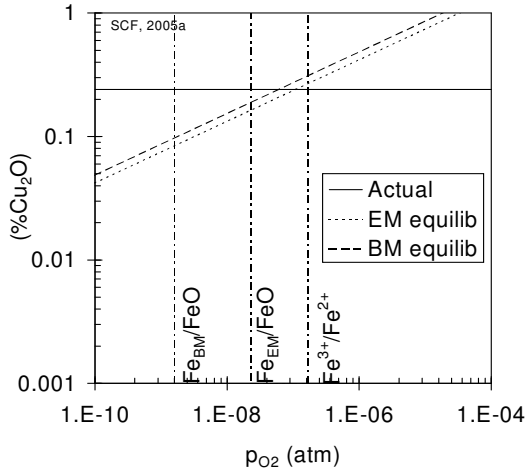

Figure 105: Base metal dissolution plots for Furnace 2 (1999 and 2005) and SCF (2005) slag. Dissolved base metal oxide levels can be measured at the intersections of the Fe_{BM}/FeO and Fe^{3+}/Fe^{2+} buffers with the bulk matte equilibrium line, or of the Fe_{EM}/FeO and Fe^{3+}/Fe^{2+} buffers with the entrained matte equilibrium line. The levels so obtained can be compared with the actual base metal oxide levels measured on the microprobe.

In all cases, for the six-in-line furnaces, nickel and copper dissolution is best predicted assuming slag in equilibrium with entrained matte. Copper usually lies close to the Fe^{3+}/Fe^{2+} buffer, whereas nickel falls between the buffers, usually closer to the Fe/FeO buffer. As far as cobalt is concerned, it should be emphasised that measurement of small amounts of cobalt are unlikely to be accurate, especially in entrained matte droplets due to the interference between iron and cobalt in MLA-EDX. It is probable that the behaviour of cobalt approximates that of nickel.

As sulphur prediction in slag was reasonable in the earlier modelling exercises, subsequent prediction using slag-entrained matte equilibrium might be expected to be overestimated. In fact this is not the case. A small increase in the sulphur levels in entrained over bulk matte causes a relatively large increase in sulphur activity. This means that the effect of higher pO_2 for equilibrium with entrained matte is counteracted.

Entrained matte-slag equilibrium is again the best fit for nearly all of the SCF slag samples, the exception being copper in WS2098. The SCF predictions should be treated with a certain amount of caution, however, since the entrained matte droplet composition could not be related to droplet size.

8.6 SLAG-MATTE EQUILIBRIA IN THE FURNACES

At first the concept of slag not being in equilibrium with bulk matte in the furnaces may seem strange. One requirement of equilibrium, however, would be that the two phases are at the same temperature, and they are not, except, presumably, close to the slag-matte boundary. There is a tapping temperature difference of over 100 °C between bulk matte and slag.

Temperature profiles have been described for six-in-line nickel smelting furnaces (SHENG *et al.,* 1998). These are shown for matte and slag in Figure 106. Mathematical modelling results were compared to measured plant data, and these corresponded well for the slag, which was "thermally homogenized". Temperatures do fall off in the vicinity of the slag-matte interface, and it appears that the matte profile cannot be accurately predicted due to some form of thermal layering.

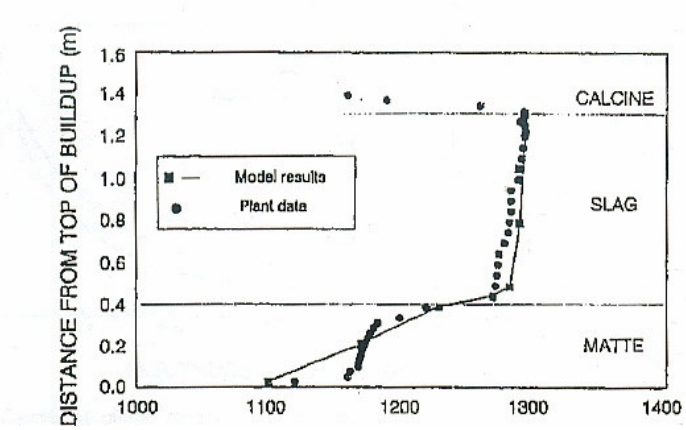

Figure 106: Comparison between the calculated bath temperature profile and plant data (after Sheng et al., 1998). The x axis is temperature in °C.

The furnace studied was used to smelt a nickel calcine, but there are similarities to the furnaces of this study. The thermal homogeneity of the slag was ascribed to stirring – mainly from CO bubbles produced at the

electrode surfaces, rather than to “natural convection”. Conditions in nickel calcine, or nickel laterite-smelting furnaces can be quite reducing. Entrained metal droplets can contain both carbon and silicon, and the silicon can reduce iron from the slag in the same way as FeS can reduce nickel during nickel sulphide smelting.

Data for thermal profiles through the slag of South African PGE-producing furnaces are reproduced by ERIC (2004) - see Figure 107. The six-in-line furnace in the study appears to be one of the Anglo Platinum furnaces at Waterval Smelter, but the measurements predate the upgrade of the furnaces from 19 MW to 34 MW between 1994 and 1998. At that time, Mg/Fe ratios in the slag were lower, and the smelting temperatures were therefore lower than those recorded during the present study, but the profile is likely to take a similar form.

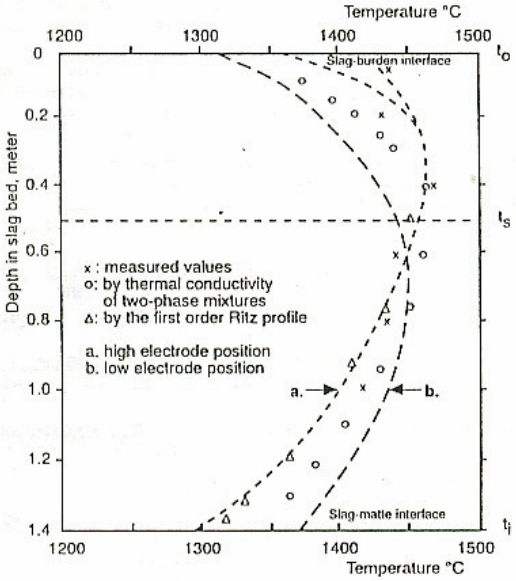

Figure 107: A comparison of measured and predicted vertical temperature gradients in a six-in-line PGE furnace (after Eric, 2004). The profile was produced for two electrode positions and calculated values from thermal conductivity data and the Ritz profile away from the electrode reaction zone were used to supplement measured data – see Page 35.

Present-day tapping practice in the six-in-line furnaces forbids slag tapping to less than 20 cm above the matte-slag interface and to less than 30 cm from the overlying concentrate. This means that all the entrained matte in the tapped slag samples would be at a considerably higher temperature than that of the bulk matte.

Sounding bar slag analysis results from this study do not show any major variation in slag composition with height in the six-in-line slag bath, although samples from close to the slag-matte interface are difficult to analyse. The entrained matte droplets which were analysed in the sounding bar samples demonstrated a trend towards bulk matte composition with depth as mentioned earlier.

It is interesting that residual Mg-rich olivine phases were recorded in the lower parts of the slag bath in these samples. These form above the matte when the furnace cools due to temporary power shut downs. The fact that such phases were still present days after power up, and with normal slag and matte tapping

temperatures, shows that the lower slag bath is considerably cooler than slag at tapping levels. FactSage modelling of the olivine and surrounding slag composition puts the temperature within a range of 1400 to 1450 ºC. Around the time of taking the sounding bar samples, slag and matte tapping temperatures were 1490 °C and 1370 °C respectively.

8.7 ORIGIN OF ENTRAINED MATTE IN SLAG

The compositions of entrained and bulk matte have already been tabulated in Table 90. These are shown again for Furnace 2 (2005) in Table 95 below, where the composition of sulphides in the feed is also given.

Table 95: The normalised compositions of entrained matte, same day bulk matte, and the sulphide portion of the concentrate for WS2008 (Furnace 2, 2005) in mass %.

	S	Fe	Co	Ni	Cu
Entrained matte	31.8	32.5	0.7	24.2	10.8
Bulk matte	29.5	41.4	0.4	17.7	11.0
Flash Drier product	37.4	38.0	0.2	14.0	10.3

The entrained matte phases contain more nickel and less iron than both bulk matte and feed sulphides. There is also considerably more sulphur in the feed, but some of this would be labile and would have volatilised during smelting. Flash drier product includes concentrate and recycles from the slag plant, but not reverts (described in section 7.1.1.2). These will raise the overall nickel content of the feed, and lower the iron, but calculations from QEMSCAN data show that, at the tonnages concerned, the effect should not exceed +1 % Ni and -1% Fe, even taking dissolved nickel into account.

The non-settled matte droplets in the tapped six-in-line furnace slag could represent material that has reacted for a longer period and thus equilibrated with the slag, but calculations do not predict this. These droplets may actually have originated from specific sulphide minerals in the feed concentrate, which did not coalesce and settle as easily as others. Certain sulphides may be entrained into and/or react with the slag more easily than others due to surface and interfacial tension factors (TOGURI & IP, 1993). The sulphide/slag interfacial tension of matte increases with nickel content, which suggests that nickel-rich sulphides should coalesce easily (drops reduce their energy more by coalescing). Sulphur decreases the surface tension of the matte, however, which would act against coalescence, and this may be the dominant effect.

The suspended droplets become nickel-rich because iron has been oxidised out of the entrained matte – it has a greater tendency to do this than nickel, copper and cobalt. In the case of the slag cleaning furnace, carbon may have the ability to reduce nickel directly from the slag. The main nickel-bearing sulphide mineral in Anglo Platinum concentrates is pentlandite ($(Fe,Ni)_9S_8$), but this contains on average 33 % Ni – greater than the 22 % of the entrained matte average. Obviously some degree of reaction or diffusion between the entrained sulphide and the surrounding slag bath must have taken place. The fact that copper levels do not become as elevated in the unsettled droplets as those of nickel is curious, and this may point to a link with specific sulphide minerals in the feed.

Since oxidation of the ore concentrate overlying the slag bath is not extensive, the first step of incorporation of exposed sulphides into the slag may be melting, as all the sulphides melt at temperatures well below that of the slag. If so, the nickel-iron and copper-iron sulphides would melt before the pyrrhotite (~FeS) and this could also be responsible for a certain amount of nickel enrichment over copper, and nickel and copper over iron, in sulphides entering the slag.

No real compositional variation in the melt was evident from the sounding bar results, and this is in agreement with earlier sounding bar work on the Waterval six-in-line furnaces (URQUHART *et al.* , 1976). It is possible that closer to the electrodes the profile differs, due to the evolution of CO gas from the electrode tip which would lower pO_2 locally. This effect appears to be subordinate to slag mixing in the six-in-line furnaces, but may be more important in the Slag Cleaning Furnace. Sounding bar samples were not taken from this furnace due to technical difficulties at the time of sampling. The slag bath is deeper and, in theory, more quiescent.

The ability of FeS in matte droplets to reduce slag Fe^{3+} to Fe^{2+}, followed by a disproportion reaction to produce a fine precipitation of metallic copper in high grade copper smelting, as described by JALKANEN and co-workers (2003), is not an important factor in the slags of this study. Tiny low-sulphur alloy phases, as detected in the slag cleaning furnace slag, either contain considerable iron, and are likely to have formed by direct reduction from slag by carbon reductant, or are nickel-rich and originate from unreacted entrained matte from the converter slag feed.

Molten FeS can also reduce nickel from the slag (resulphidation) under favourable conditions. Suspended matte droplets in the six-in-line furnace slag do contain less iron and more nickel than the feed (as would be expected from a nickel resulphidation reaction), but the droplets also contain less iron and more nickel than the bulk matte. In other words, entrained matte droplet composition is not intermediate between feed sulphide and bulk matte composition (as shown above in Table 94). The changes in droplet composition, as observed in the sounding bar samples, can therefore not be explained by progressive reaction of matte droplets with the slag during their descent – in fact, such droplets gain iron and lose nickel as the bulk matte boundary is approached. It should be mentioned again that neither the slag compositional profile nor the degree of nickel sulphidation are known for the Slag Cleaning Furnace.

Finally, to complicate the picture, of the fourteen feed loading bins situated above the six-in-line furnaces, two are situated directly above the settling zone (between the electrode closest to the slag tap holes and the end of the furnace). Sulphides in concentrate (or other furnace additives) fed in such positions would have less time to react, coalesce and settle into the bulk matte than material fed further towards the matte end of the furnace. The loading bins feed sporadically, which implies that more feed-related sulphides may be present in certain tapped slag samples than in others. This may be the reason for the bimodal compositional distributions recorded in the matte droplets of the 2005 Furnace 1 slag (WS1989). There is also evidence of an unreacted ore concentrate component in the SCF slag samples. The broad range of matte droplet compositions in these samples suggests contributions from feed (converter slag and ore concentrate) as well as matte entrained in SCF slag and also, possibly, alloy reducing out of slag. The slag appears to have been tapped before the reduction, coalescence and settling processes had reached completion. The trial was a

three-day process, rather than the continuous process of the six-in-line furnaces, but potentially more efficient slag cleaning could have been achieved (see below).

8.8 PROCESS OPTIMISATION

"The removal of matte from slag is a complex phenomenon including several simultaneous steps, namely: chemical reactions, mass transfer between droplet surface and slag, dissolving mechanisms, and separation due to physiochemical properties of the slag; viscosity, density, diffusivity, thermodynamic properties, *etc.*" (FAGERLUND & JALKANEN, 1999).

8.8.1 Six-in-line furnaces

Although PGE losses to the six-in-line furnaces are relatively small, base metal losses can be substantial. Over 50 % of nickel and cobalt, and over 75 % of copper in these slags are present as dissolved metals in the silicate phases. There is little leeway for lowering these levels using the current process, as slag reduction would be impractical due to the configuration of the off-gas system (CO could ignite with sparks from the electrostatic precipitator). As has been demonstrated in this study, however, any practice that increases slag pO_2, such as converter slag addition, should be discouraged.

Mechanical losses to slag were often considerable in the early days of the project (1999). These were usually caused by poor tapping practice, and larger matte inclusions were recovered by milling and flotation. All the slag samples examined from the 2005 trials were very "clean" which is just as well, because most of the slag is no longer processed in the Slag Plant. The data gleaned from the six-in-line furnace slags in this study, however, is vital for the understanding of, and for future optimisation of, the SCF.

8.8.2 Slag cleaning furnace

As mentioned above, there is more potential for process optimisation in the SCF than in the six-in-line furnaces.

Chemistry and microprobe results for the early SCF trial samples lead to the following conclusions –

- Coke addition reduces the dissolved base metals in the SCF slag (especially Ni and Co), increases dissolved sulphur in slag and increases the amount of alloy in the SCF matte,
- Higher concentrate in the feed produces higher sulphur in the matte (increases matte fall),
- Higher converter slag in the feed produces lower sulphur in the matte, and increases the amount of alloy.

A balance has to be reached considering all these factors. There is no point in over-reducing the feed to remove more dissolved base metals from the slag as this will produce high alloy content in the matte. This leads to furnace operation problems, as the alloy tends to "freeze" at normal smelting temperatures.

The use of a round furnace for slag cleaning will produce more turbulent conditions than would be found in a rectangular furnace. The argument for this is that better mixing and reduction will occur and that there should

be more chance of droplet coalescence and settling. Problems may arise if there is insufficient settling time, and if slag viscosity leads to high matte entrainment in slag. The silica addition, which was introduced in 2005, was supposed to reduce the liquidus temperature of the slag. It is possible that increasing the amount of concentrate in the latter half of the year may have raised slag silica above ideal levels, and led to an increase in slag viscosity. Such additions should be closely monitored and recalculated with each change in feed composition.

As far as the SCF products are concerned, the sulphur levels in the matte produced during the 2005 trial averages around twenty per cent, and this is suitable to limit alloy formation. The target for total nickel in SCF slag is <1 %, so the average slag nickel in the slag is acceptable. Over 35 % of nickel, over 45 % of copper, and over 80 % of cobalt in these slag samples are present as dissolved metals in the silicate and oxide phases.

The entrained matte size distribution in the SCF slag samples varies widely from one sample to the next. This could be due to the effect of sporadic large matte granules. It is apparent, however, that a considerable amount of entrained matte in some of the samples is too fine to be recovered – there is more fine matte in these samples than in previously produced SCF slag. A higher residence time is required so that the slag cleaning process can near completion.

Recommendations given to plant personnel after the results of the SCF trial became available included a re-assessment of silica addition, and its affect on the slag viscosity, and an increase of settling time. The latter impacts upon throughput tonnages, and changing the tap hole height may be considered at a future date.

8.9 MODELLING OF DISSOLVED BASE METAL LEVELS

The software model in common use at Anglo Platinum smelters is the CSIRO Multi Phase Equilibrium (MPE) model (ZHANG *et al.,* 2002). Preliminary evidence suggests that this model also underpredicts nickel and copper dissolution in slag.

Although it is now known that base metal dissolution can be quite accurately predicted by FactSage (and other similar models), there is a problem in that the input data required is not easily available. If distribution at entrained matte equilibrium is to be calculated, the average composition (and possibly the average weighted composition, if this changes with droplet size) of the entrained matte phases would need to be determined first using the MLA, and at least occasional Fe^{3+}/Fe^{2+} measurements made, especially for copper estimation.

In practice it would be quicker and easier just to measure the dissolved base metal content of the slag directly using the electron microprobe, as is currently the case. Such analyses are not made on a routine basis, however, and the turn-around time is certainly nowhere that needed for process control.

It would be in the interest of Anglo Platinum to investigate further model development, which could be reconciled with microprobe data at suitable intervals. A preliminary trial of this nature during the course of this study involved an attempt at relating feed chemistry to slag and entrained matte compositions, but this was not successful. It now appears that the answer may involve linking the feed mineralogy with the entrained matte composition, due to the preferential entrainment and coalescence behaviour mentioned earlier.

9 CONCLUSIONS

In this study a combination of chemical, Mössbauer, and electron microbeam techniques has been used successfully to define the base metal distribution in Anglo Platinum furnace slags. These include a new technique, the MLA Latti method, applied here for the relationship between entrained matte droplet size and composition in slag.

The information gathered was employed to optimise FactSage modelling predictions of slag pO_2 and base metal dissolution in six-in-line and slag cleaning furnace slag samples. The model, as well as similar software in use at the smelters, tends to underpredict base metal levels in slag when bulk matte-slag equilibrium is assumed.

The results of this study have shown that tapped six-in-line furnace slag is not in equilibrium with bulk matte, but rather with entrained matte. At the base of the slag bath, close to the bulk matte-slag boundary, slag (which is not tapped) may attain equilibrium with the matte, and entrained matte phases approach bulk matte composition.

The methods described in this thesis have already been used for process optimisation in the slag cleaning furnace. The SCF slag examined in this study shows high levels of entrained sulphides, the origin of which are both feed and product-related. It can only be concluded that insufficient residence time has curtailed reaction, coalescence and settling, but a slag viscosity factor may also be involved.

10 RECOMMENDATIONS FOR FUTURE WORK

Opportunities for future work lie in three main areas. Firstly, in further testing of the slag cleaning furnace now that the process has become continuous, with analytical treatment similar to that used in this study. It is an accepted fact that there is room for SCF process improvement and a sampling campaign is already at the planning stage.

Secondly, more development work on CC-SEM analysis of the entrained matte in slag, and similar applications, is required. The strength of the MLA Latti method is in the accuracy of the SEM-EDX long count analysis results, but for trends it would be easier to adapt QEMSCAN 'sip' files for this task. The advantage of using QEMSCAN here would be the established statistical software.

Thirdly, modelling software needs to be adapted for more accurate dissolved base metal prediction

11 REFERENCES

ALTMAN, R. & KELLOGG, H.H. (1972). Solubility of copper in silica-saturated iron silicate slag. *Trans. Inst. Mining. Metall.,* **81C**: 163–175.

ALTMAN, R, SCHLEIN, W. & SILVA, C. (1976). The influence of spinel formation on copper loss in smelter slags. *Int. Symp. Copper Extr. and Refining. 1976. Proceedings of Extractive Metallurgy of Copper 1976* **1**: 276–316. New York:AIME.

AMMANN, P.R., KIM, J.J. & LOOSE, T.A. (1979). The Kennecott Process for nickel slag cleaning. *Journ. Metals,* **1**, No. 2: 20–25.

ANDREWS, L. (1999). Accurate electron microprobe determination of cobalt in iron-bearing sulphide and sulpharsenide bioleach samples. *Proc. MSSA* **29**: 7.

ANDREWS, L. (2005). Factors affecting nickel recovery from slags produced during platinum smelting. *Trans. Inst. Min. Metall. C,* **114** no. 3: C130–C134.

ANGLO PLATINUM LIMITED (2008). Annual report 2007: 174.

BALE, C.W., CHARTRAND, P., DECTEROV, S.A., ERIKSSON, G., HACK, K., BEN MAHFOUD, R., MELANCON, J., PELTON, A.D. & PETERSEN, S. (2002). FactSage thermochemical software and databases. *Calphad,* **26**, No. 2: 189–228.

BARNETT, S.C.C. & JEFFES, J.H.E. (1977). Recovery of nickel from Thompson Smelter electric furnace slag. *Trans. Inst. Min. Metall.C,* **86**: C155–C157.

BARNETT, S.C.C. (1979). The methods and economics of slag cleaning. *Mining Mag. May 1979*: 408–417.

BEATTIE, P. (1994). Systematics and energetics of trace-element partitioning between olivine and silicate melts: Implications for the nature of mineral/melt partitioning. *Chem. Geol.* **117**: 57–71.

BISWAS, A.K & DAVENPORT, W.G. (1976). Extractive metallurgy of copper. New York: Pergamon Press.

BROWN, G.E., FARGES, F. & CALAS (1994). X-ray scattering and X-ray spectroscopy studies of silicate melts. *In* Stebbins, McMillan and Dingwell (eds) *Structure, dynamics and properties of silicate melts, Reviews in mineralogy* **32**: 372–381. Michigan: Mineralogical Society of America.

CHAKRABORTY, S (1994). Diffusion in silicate melts. *In* Stebbins, McMillan and Dingwell (eds) *Structure, dynamics and properties of silicate melts, Reviews in mineralogy* **32**: 483–495. Michigan: Mineralogical Society of America.

CHEN, C., ZHANG, L. & JAHANSHAHI, S. (2004). Review and thermodynamic modelling of CoO in iron silicate-based slags and calcium ferrite-based slags. *Proceedings of the VII Int. Conf. on Molten Slags, Fluxes and Salts*: 509–515. Cape Town: the SAIMM.

CHOI, N. & CHO, W.D. (1997). Distribution behaviour of cobalt, selenium and tellurium between nickel-copper-iron matte and silica-saturated iron silicate slag. *Metall. and Materials Trans. B, vol* **28B**: 429–438.

CHOO, R.T.C. & TOGURI, J.M. (1992). The electrodynamic behaviour of metal and metal sulphide droplets in slags. *Can. Metall. Quarterly* **31** no.2: 113–126.

CLIFT, R., GRACE, J.R. & WEBER, M.E. (1978). Bubbles, drops and particles: 30–46. London: Academic Press.

COLSON, R.O., FLODEN, A.M., HAUGEN, T.R., MALUM, K.M., SAWARYNSKI, M., NERMOE, N.K.B., JACOBS, K.E. & HOLDER, D. (2005). Activities of NiO, FeO and O^{2-} in silicate melts. *Geochim et*

Cosmochim Acta **69,** no. 12: 3061–3073.

CONOCHIE, D.S. & ROBERTSON, D.G.C. (1980). Ternary interfacial energy diagram. *Trans. IMM C,* **89**: C61–C64.

CRAMER, L. A. (2001). The extractive metallurgy of South Africa's platinum ores. *J.O.M.* **53***, no. 10*: 14–18.

D.M.E. (Department: Minerals and Energy) (2006/7). South Africa's mineral industry. Pretoria: the D.M.E.

DAVEY, T.R.A. & WILLIS, G.M. (1985). Metal, matte and slag solution thermodynamics. *In* Kudryk, V. and Rao, Y.K. (eds), *Physical chemistry of extractive metallurgy:* Proceedings of an international symposium: 23–39. Warrendale, PA: AIME Books.

DECTEROV, S.A., JUNG, I.H., JAK, E., KANG, Y.B., HAYES, P. & PELTON, A.D. (2004). Thermodynamic modelling of the Al_2O_3-CaO-CoO-CrO-Cr_2O_3-FeO-Fe_2O_3-MgO-MnO-NiO-SiO_2-S system and applications in ferrous process metallurgy. *Proc. VII Int. Conf. on Molten Slags, Fluxes and Salt*: 839–850. Cape Town: the SAIMM.

DEGEL, R., SCHREITER, T., SCHMEIDEN, H. & KEMPKEN, J. (2006). Rectangular furnace design and revolutionary DC-slag cleaning technology for the PGM industry. *In Proc. International Platinum Conference 'Platinum Surges Ahead'*: 237–245. Johannesburg: the SAIMM.

DEMETRIO, S., AHUMADA, J., DURAN, M.A., MAST, E., ROJAS, U., SAHUEZA, J, REYES, P. & MORALES, E. (2000). Slag cleaning: The Chilean copper smelter experience. *JOM Aug 2000*: 20–25.

DUCRET, A.C. & RANKIN, W.J. (2002). Liquidus temperatures and viscosities of FeO-Fe_2O_3-SiO_2-CaO-MgO slags at compositions relevant to nickel matte smelting. *Scandinavian Journ. Metall.* **31**: 59–67.

DRAKE, M.J. & HOLLOWAY, J.R. (1981). Partitioning of Ni between olivine and silicate melt: the 'Henry's Law problem' re-examined. *Geochim. et Cosmochim. Acta* **45**: 431–437.

DU TOIT, A.J., GAYLARD, P., JAHANSHAHI, S. & NELL, J. (2005). Iron redox equilibria and sulphide capacity of PGM melter-type slags. *Proc. Pyrometallurgy 05, Cape Town.* 16 pp.

DYAR, M.D.& BIRNIE, D.P. (1984). Quench media effects on iron partitioning and ordering in a lunar glass. *Journ. Non-crystalline Solids* **67**: 397–412.

DYAR, M.D. (1985). A review of Mossbauer data on inorganic glasses: The effects of composition on iron valency and coordination. *Amer. Miner.* **70**: 304–316.

DYAR, M.D., NANEY, M.T. & SWANSON, S.E. (1987). Effects of quench methods on Fe^{3+}/Fe^{2+} ratios: A Mossbauer and wet-chemical study. *Amer. Miner.* **72**: 792–800.

ERIC, R.H. (2004). Slag properties and design issues pertinent to matte smelting electric furnaces. *Journ. SAIMM,* October 2004: 499–510.

ERIC, R.H. & HEJJA, A.A. (1995). Dimensioning, scale-up and operating considerations for six electrode electric furnaces. Part I: Current and heat flow in the slag. *Proc. EPD Congress.*

ERIC, R.H. & HEJJA, A.A. (1995). Dimensioning, scale-up and operating considerations for six electrode electric furnaces. Part II: Design and scale-up considerations for furnaces treating PGM-containing copper-nickel concentrates. *In* Warren, G.W. (ed) *Proc. EPD Congress:* 239–257. The Minerals, Metals and Materials Society.

ERIC, R.H., HEJJA, A.A. & HOWAT, D.D. (1994). Metal losses to the slag and matte-slag separation in electric smelting of copper-nickel concentrates. *In* Warren, G.W. (ed.) *Proc. EPD Congress:* 641–

656. The Minerals, Metals and Materials Society.

FAGERLUND, K.O. & JALKANEN, H. (1999). Some aspects on matte settling in copper smelting. *Proc.Copper 99 Int. Conf.* **VI**: 539–551.

FAGERLUND, K.O. & JALKANEN, H. (2000). Microscale simulation of settler processes in copper matte smelting. *Metall. Materials Trans. B,* ***31B***: 439–451.

FANDRICH, R., GU, Y., BURROWS, D. & MOELLER, K. (2007). Modern SEM-based mineral liberation analysis. *Int. J. Miner. Process* **84**: 310–320.

FARGES, F. & BROWN, G.E. (1996). An empirical model for the anharmonic analysis of high-temperature XAFS spectra of oxide compounds with applications to the coordination environment of Ni in NiO, γ-Ni_2SiO_4 and Ni-bearing Na-disilicate glass and melt. *Chem. Geol.* **128**: 93–106.

FLOYD, J.M. & MACKEY, P.J. (1981). Developments in the pyrometallurgical treatment of slag: a review of current technology and physical chemistry. *Proceedings of Extraction Metallurgy* **81**: 345–371. London: IMM.

FONT, J.M., HINO, M. & ITAGAKI, K. (1999). Phase equilibrium and minor elements distribution between iron-silicate base slag and nickel-copper-iron matte at 1573K under high partial pressures of SO2. *Materials Trans. JIM,* **40***,* no. 1: 20–26.

FONT, J.M., HINO, M. & ITAGAKI, K. (1998). Minor element distribution between iron-silicate base slag and Ni_3S_2-FeS matte under high partial pressures of SO_2. *Materials Trans. JIM* **39***,* no.8: 834–840.

FONT, J.M., ROGHANI, G., HINO, M. & ITAGAKI, K. (1998). Solubility of copper or nickel in iron silicate base slag equilibrated with Cu_2S-FeS or Ni_3S_2-FeS matte under high partial pressures of SO_2. *Metall. Rev. MMIJ* 15, no. 1: 75–86.

FONT, J.M., HINO, M. & ITAGAKI, K. (2000). Phase equilibrium and minor element distribution between Ni_3S_2-FeS matte and calcium ferrite slag under high partial pressures of SO_2. *Metall. And Materials Trans. B,* **31B**: 1231–1239.

FONTANA, A., ILUNGA, M., SEGERS, L., TWITE, K. & WINAND, R. (1989). Properties of ferrous silicate slags associated with copper flash smelting and electric furnace processes. *Proceedings of Extraction Metallurgy* **89**: 147–164. London: IMM.

FRANCIS, R.D. (1990). Sulfide globules in mid-ocean ridge basalts (MORB) and the effect of oxygen abundance in Fe-S-O liquids on the ability of those liquids to partition metals from MORB and komatiite magmas. *Chem. Geol* **85**:199-213.

GASKELL, D.R., PALACIOS, J. & SOMSIRI, C. (1990). The physical chemistry of copper mattes. *Proc. The Elliot Symposium:* 151–162. Cambridge, MA: Iron and Steel Society.

GAYE, H. & LEHMANN, J. (1995). Sulphide capacities. *In* Eisenhuttenleute, V.D. (ed.) *Slag Atlas, 2nd edition:* 258. Verlag Stahleisen GmbH.

GBOR, P.K., MOKRI, V. & JIA, C.Q. (2000). Characterization of smelter slags. *J. Environ. Sci. Health* **A35** (2): 147–167.

GOLDSTEIN, J.I., NEWBURY, D.E., ECHLIN, P., JOY, D.C., FIORI, C. & LIFSHIN, E. (1981). Scanning electron microscopy and X-ray microanalysis. New York and London: Plenum Press.

GOTTLIEB, P., WILKIE, G., SUTHERLAND, D., HO-TUN, E., SUTHERS, S., PERERA, K., JENKINS, B., SPENCER, S., BUTCHER, A. & RAYNER, J. (2000). Using quantitative electron microscopy for process mineralogy applications. *JOM, April 2000*: 24–25.

GRIMSEY, E.J. & LIU, X. (1994). The activity coefficient of cobalt oxide in silica-saturated iron silicate

slags. *Metall. and Materials Trans. B,* **26B**: 229–233.

GU, Y. (2003). Automatede scanning electron microscope based mineral liberation analysis: An introduction to JKMRC/FEI Mineral Liberation Analyser. *Journ. Miner. & Materials Charact. & Eng.* **2**, no. 1: 33–41.

HAKLI, T.A. & WRIGHT, T.L. (1967). The fractionation of nickel between olivine and augite as a geothermometer. *Geochim. et Cosmochim. Acta* **31**: 877–884.

HAWTHORNE, F.C. (1988). Mossbauer Spectroscopy. *In* Hawthorne, F.C. (ed.), *Spectroscopic methods in mineralogy and geology*, Reviews in mineralogy **18**: 255–340. Michigan: Mineralogical Society of America.

HEJJA, A.A. & ERIC, R.H. (1996). Flow and settling phenomena in matte smelting electric furnaces. *In* Warren, G.W. (ed) *Proc. EPD Congress:* 27–41. The Minerals, Metals and Materials Society.

HEINRICH, G. (1989). On the utilization of nickel smelter slags. *C.I.M. Bulletin, Jan 1989*: 87–91.

HENAO, H.M., HINO, M. & ITAGAKI, K. (2002). Phase equilibrium between Ni-S melt and slags under controlled partial pressure. *In* Stephens and Sohn (eds). *Sulfide Smelting 2002*: 523–531. The minerals, metals and materials society.

HIRSCHMANN, M.M. & GHIORSO, M.S. (1994). Activities of nickel, cobalt and manganese silicates in magmatic liquids and applications to olivine/liquid and to silicate/metal partitioning. *Geochim. et Cosmochim. Acta,* **58** no. 19: 4109–4126.

HOFIREK, Z. & HALTON, P. (1990). Production of high quality electrowon nickel at Rustenburg Base Metals Refiners (Pty.) Ltd. *Proc. Int Symp. Electrometall. Plant Practice*: 233–251. Montreal, Canada: Canadian Instituite of Metallurgy.

HOLZHEID, A. & PALME, H. (1996). The influence of FeO on the solubilities of cobalt and nickel in silicate melts. *Geochim. et Cosmochim. Acta* **60** no. 7: 1181–1193.

HOLZHEID, A., PALME, H. & CHAKRABORTY, S. (1997). The activities of NiO, CoO and FeO in silicate melts. *Chemical Geology* **139**: 21-38.

HUGHES, S. (2000). Applying Ausmelt technology to recover Cu, Ni and Co from slags. *J.O.M. Aug 2000*: 30–33.

HUNDERMARK, R.J. (2002). Electrical conductivity of melter type slags. M.Eng. Dissertation, University of Cape Town.

HUNDERMARK, R.J., JAHANSHAHI, S. & SUN, S. (2004). The oxidation state dependence of the electrical conductivity of high iron containing slags. *Proc.7th Int. Symp. of Molten Slags, Fluxes and Salts* : 487–492. Cape Town: the SAIMM.

IMRIS, I. (2003). Copper losses in copper smelting slags. *In* Kongoli, F., Itagaki, K., Yamauchi, C. and Sohn, H.Y. (eds) *Yazawa Int Symp on Metallurgical and Materials Processing: Principles and Technologies* **1**: 359–373. The Minerals, Metals and Materials Society.

IP, S.W. & TOGURI, J.M. (1992). Entrainment behaviour of copper and copper matte in copper smelting operations. *Metall. Trans. B vol* **23B**: 303–311.

IP, S.W. & TOGURI, J.M. (1993). Surface and interfacial tension of the Ni-Fe-S, Ni-Cu-S and fayalite slag systems. *Metall. Trans. B vol* **24B**: 657–668.

IP, S.W. & TOGURI, J.M. (2000). Entrainment of matte in smelting and converting operations. *In* Kaiura, G., Pickles, C., Utigard, T. and Vahed, A. (eds), *J.M. Toguri Symp. Fundamentals of Metallurgical Processing*: 291–302. Ottowa, Canada: Met. Soc.

ITAGAKI, K. (2003). Distribution of minor elements in sulfide smelting. *In* Kongoli, F., Itagaki, K., Yamauchi, C. and Sohn, H.Y. (eds) *Yazawa Int Symp on Metallurgical and Materials Processing: Principals and Technologies*. The Minerals, Metals and Materials Society.

ITOH, S., CHOO, R.T.C., & TOGURI, J.M. (1995). Electrocapillary motion of copper and nickel matte droplets on fayalite-based slag surfaces. *Can. Metallurgical Quarterly* **34**, no. 4: 319–330.

JACOBS, M. (2006). Process description and abbreviated history of Anglo Platinum's Waterval Smelter. *In* Jones, R.T. (ed.) *Southern African Pyrometallurgy 2006*: 17–28. Johannesburg: the SAIMM.

JALKANEN, H., VEHVILAINEN, J. & POIJARVI, J. (2003). Copper in solidified copper smelter slags. *Scandinavian Journ. Metall.* **32**: 65–70.

JANA, D. & WALKER, D. (1997). The influence of sulfur on partitioning of siderophile elements. *Geochim. et Cosmochem. Acta* **61,** no. 24: 5255–5277.

JENKINS, R. (1989). Instrumentation and experimental procedures. *In* Bish, D.L. and Post, J.E. (eds). *Reviews in Mineralogy* **20**: *Modern powder diffraction*:19–71. Washington: The Mineralogical Society of America.

JONES, R.T. (1999). Platinum smelting in South Africa. *S.A. Journ. Sci.* **95**: 525–534.

JONES, R.T., HAYMAN, D.A. & DENTON, G.M. (1996). Recovery of cobalt, nickel and copper from slags using DC–AC furnace technology. *Proc. Int. Symp. On Challenges of Process Intensification, Montreal, Canada*: 16 pp.

JONES, R.T., DENTON, G.M., REYNOLDS, Q.G., PARKER, J.A.L. & VAN TONDER, G.J.J. (2001). Recovery of cobalt from slag in a DC arc furnace at Chambishi, Zambia. *Proc. Copper Cobalt Nickel and Zinc Recovery conference, Zimbabwe*: 10 pp.

JOUBERT, H., NOURSE, R.B., MASTERS, B. & HUNDERMARK, R. (2005). Copper cooling design, installation and operational results for the slag cleaning furnace at Waterval Smelter, Rustenburg Platinum, South Africa. *In* Donald, J. and Schoneville, R. (eds) *Proc. 44th Annual conference of Metallurgists of CIM. Nickel and Cobalt 2005 – Challenges in Extraction and Production*: 19– 35. Calgary, Canada: CIM.

KAIURA, G.H., JACKSON, J.F. & LAINE, R.O. (1989). None-ferrous metal recovery. *US Patent no. 4814004.*

KAPTAY, G. (2001). Discussion of 'Microscale simulation of settler processes in copper matte smelting'. *Metall. Mat. Trans. B* **32B**: 555–557.

KATYAL, A. & JEFFES, J.H.E. (1989). Activities of cobalt and copper oxides in silicate and ferrite slags. *Proc. 3rd Int. Conf. on Molten Slags and Fluxes.* London:46–55.

KEPPLER, H. (1992). Crystal field spectra and geochemistry of transition metal ions in silicate melts and glasses. *Amer. Miner.* **77**: 62–75.

KIM, H.G. & SOHN, H.Y. (1998). Effects of CaO, Al2O3 and MgO additions on the copper solubility, ferric/ferrous ratio, and minor element behaviour of iron silicate slags. *Metall. and Materials Trans. B* **29B**: 583–590.

KLUG, H.P. and ALEXANDER, L.E. (1974). X-ray diffraction procedures. J. Wiley and Sons Inc., New York, 996 pp.

LEEMAN, W.P. & LINDSTROM, D.J. (1978). Partitioning of Ni^{2+} between basaltic and synthetic melts and olivines – an experimental study. *Geochim. et Cosmochim. Acta* **42**: 801–816.

LI, G. & TSUKIHASHI, F. (2001). Distribution equilibria of Fe, Co and Ni between MgO-saturated FeOx-

MgO-SiO2 slag and Ni alloy. *ISIJ International* **41**:1303–1308.

LIOW, J.L., JUUSELA, M., GRAY, N.B., & SUTALO, I.D. (2003). Entrainment of a two-layer liquid through a taphole. *Metall. & Materials Trans. B* **34B**: **821–832.**

MACKAY, R., CORDERO, D., ESTEBAN, J. & ALVEAR, G.R. (2000). Continuous improvement of the Teniente slag cleaning process. *Proc. Int. Conf. Molten Slags Fluxes and Salts,* 19 pp.

MACKEY, P.J. (1982). The physical chemistry of copper smelting slags – a review. *Can. Metall. Quarterly* **21**, no.3: 221–260.

MACLEAN, W.H. & SHIMAZAKI, H. (1976). The partition of Co, Ni, Cu and Zn between sulfide and silicate liquids. *Econ. Geol.* **71**: 1049–1057.

MARU, H.C., WASAN, D.T. & KINTNER, R.C. (1971). Behaviour of a rigid sphere at a liquid-liquid interface. *Chem. Eng. Science,* **26**: 1615–1628.

MARUYAMA, T., FURUI, N., HAMAMOTO, M. & SUNAMOTO, T. (2003). The copper loss in slag of flash smelting furnace in Tamano Smelter. *In* Kongoli, F., Itagaki, K., Yamauchi, C. and Sohn, H.Y. (eds) *Yazawa Int Symp on Metallurgical and Materials Processing: High temperature metals production* **2**: 337–347. The Minerals, Metals and Materials Society.

MATOUSEK, J.W. (1982). The pyrometallurgical winning of cobalt. *CIM Bulletin* **75** no. 848: 121–127.

MILLS, K.C. (1995). Structure of liquid slags. *In* Eisenhuttenleute, V.D. (ed.) *Slag Atlas, 2nd edition:* 1–9. Verlag Stahleisen GmbH.

MINTO, R. & DAVENPORT, W.G. (1972). Entrapment and flotation of matte in molten slags. *Trans. Inst. Min. Metall.,* **81**: C36–C41.

MINTO, R. & DAVENPORT, W.G. (1973). *Discussion of* Entrapment and flotation of matte in molten slags. *Trans. Inst. Min. Metall.,* **82**: C59–C62.

MONTENEGRO, V., FUJISAWA, T., WARCZOK, A. & RIVEROS, G. (2003). Effect of magnetic field on the rate of slag reduction in an electric furnace. *In* Kongoli, F., Itagaki, K., Yamauchi, C. and Sohn, H.Y. (eds) *Yazawa Int Symp on Metallurgical and Materials Processing: High temperature metals production* **2**: 199–209. The Minerals, Metals and Materials Society.

MOSTERT, J.C. & ROBERTS, P.N. (1973). Electric smelting at Rustenburg Platinum Mines Limited of nickel-copper concentrates containing platinum-group metals. *Journ. SAIMM.* **73**: 290–299.

MYSEN, B.O., VIRGO, D., NEUMANN, E.R. & SEIFERT, F.A. (1985). Redox equilibria and the structural states of ferric and ferrous iron in melts in the system CaO-MgO-Al_2O_3-SiO_2-Fe-O: Relationships between redox equilibria, melt structure and liquidus phase equilibria. *Amer. Miner.* **70**: 317–331.

NAGAMORI, M. & MACKEY, P.J. (1978). Thermodynamics of copper matte converting: Part I. Fundamentals of the Noranda Process. *Metall. Trans. B,* **9B**: 255–265.

NAGAMORI, M. & MACKEY, P.J. (1978). Thermodynamics of copper matte converting: Part II. Distribution of Au, Ag, Pb, Zn, Ni, Se,Te, Bi, Sb and As between copper, matte and slag in the Noranda Process. *Metall. Trans. B,* **9B**: 567–579.

NAGAMORI, M. (1974). Metal losses to slag: Part I. Sulfidic and oxidic dissolution of copper in fayalite slag from low grade matte. *Metall. trans.* **5**: 531–538.

NAGAMORI, M. (1974). Metal losses to slag: Part II. Oxidic dissolution of nickel in fayalite slag and thermodynamics of continuous converting of nickel-copper matte. *Metall. Trans.* **5**:539–548.

NELL, J. (2001). Modelling of selected chemical and physical properties of a slag cleaning furnace

operation. *Mintek CC no. C3243M,* 6 September 2001, 20 pp.

NELL, J. (2004). Melting of platinum group metal concentrates in South Africa. *Journ. SAIMM,* August 2004: 423–428.

NELSON, L.R., STOBER, F., NDLOVU, J., DE VILLIERS, LPvS, & WANBLAD, D. Role of technical innovation on production delivery at the Polokwane Smelter. *In* Donald, J. and Schoneville, R. (eds) *Proc. 44th Annual conference of Metallurgists of CIM. Nickel and Cobalt 2005 – Challenges in Extraction and Production*: 91– 116. Calgary, Canada: CIM.

PAGADOR, R.U. & ITAGAKI, K. (1996). Dissolution of nickel and copper in FeOx-SiO_2-MgO slag equilibrated with nickel alloy. *Metall. Rev. of MMIJ* **13**: 90–103.

PAGADOR, R.U., HINO, M. & ITAGAKI, K. (1999). Distribution of minor elements between MgO saturated FeO_x-MgO-SiO_2 or FeO_x-CaO-MgO-SiO_2 slag and nickel alloy. *Materials Trans. JIM,* **40,** no. 3: 225–232.

PEACH, C.L., MATHEZ, E.A. & KEAYS, R.R. (1980). Sulfide melt-silicate melt distribution coefficients for noble metals and other chalcophile elements as deduced from MORB: Implications for partial melting. *Geochim. et Cosmochim. Acta* **54**: 3379–3389.

PELTON, A.D., ERIKSSON, G & ROMERO-SERRANO, A. (1993). Calculation of sulphide capacities of multicomponent slags. *Metall. Trans. B* **24B**: 817–825.

PIRET, N.L. (2000). Cleaning copper and Ni/Co slags: The technical, economic and environmental aspects. *J.O.M. Aug 2000*: 18.

PIRRIE, D., BUTCHER, A.R., POWER, M.R., GOTTLIEB, P. & MILLER, G.L. (2004). Rapid quantitative mineral and phase analysis using automated scanning electrontron microscopy (QEMSCAN); potential applications in forensic geoscience. *In* Pye, K. and Croft, D.J. (eds) *Forensic Geoscience: Principles, Techniques and Applications.* London: The Geological Society.

POGGI, D., MINTO, R. & DAVENPORT, W.G. (1969). Mechanisms of metal entrapment in slags. *Journ. Metals Nov 1969*: 40–45.

RAJAMANI, V. & NALDRETT, A.J. (1978). Partitioning of Fe, Co, Ni and Cu between sulfide liquid and basaltic melts and the composition of Ni-Cu sulfide deposits. *Econ. Geol.* **73**:82–93.

RAJCEVIC, H.P. & OPIE, W.R. (1982). Development of electric furnace slag cleaning at a secondary copper smelter. *Journ. Metals,* **34**, no. 3: 54–56.

REDDY, R.G. (2003). Impurity capacity of metallurgical slags. *In* Kongoli, F., Itagaki, K., Yamauchi, C. and Sohn, H.Y. (eds) *Yazawa Int Symp on Metallurgical and Materials Processing: Materials Processing Fundamentals and New Technologies* **2**: 199–209. The Minerals, Metals and Materials Society.

REED, S.J.B. (1996). Electron microprobe analysis and scanning electron microscopy in geology. Cambridge: Cambridge University Press.

REYNOLDS, R.C. (1989). Principles of powder diffraction. *In* Bish, D.L. and Post, J.E. (eds). Reviews in Mineralogy **20:** Modern powder diffraction: 1–17. The Mineralogical Society of America, Washington.

RUCKLIDGE, J.C. (1976). Electron microprobe instrumentation. *In* Smith, D.G.W. (ed.) Microbeam techniques: 1–44. Edmonton, Alberta: Can. Mineral. Assoc.

RUDDLE, R.W., TAYLOR, B. & BATES, A.P. (1966). The solubility of copper in iron silicate slags. *Inst. Min. Metall. C*: C1–C12.

SAFFMAN, P.G. & TURNER, J.S. (1956). On the collision of drops in turbulent clouds. *Journ. Fluid Mechanics,* **1**: 16–30.

SAHOO, P. & REDDY, R.G. (1984). Activity coefficient of nickel oxide in FeO-NiO-$FeO_{1.5}$-$AlO_{1.5}$-SiO_2 slag at 1573K. *In* Fine, H.A. and Gaskell, D.R. (eds) *Proc. 2nd Int. Symp. on Metallurgical Slags and Fluxes 1984*: 533–545. Metall. Soc. Of AIME.

SAKAI, T., IP, S.W. & TOGURI, J.M. (1997). Interfacial phenomena in the liquid copper-calcium ferrite slag system. *Metall. Materials Trans B,* **28B**: 401–407.

SALTIKOV, S.A. (1967). The determination of the size distribution of particles in an opaque material from a measurement of the size distribution of their sections. *In* Elias, H. (ed.) *Proc. 2nd Int. Congress for Stereology April 1967:* 163–173. Chicago: International Congress for Stereology.

SHAHROKHI, H. & SHAW, J.M. (2000). Fine drop recovery in batch gas-agitated liquid-liquid systems. *Chem. Eng. Sci.* **55**: 4719–4735.

SHENG, Y.Y., IRONS, G.A. & TISDALE, D.G. (1998). Transport phenomena in electric smelting of nickel matte: Part II> Mathematical Modelling. *Metall. Trans. B* **29B**: 85–94.

SHIMPO, R., GOTO, S., OGAWA, O. & ASAKURA, I. (1986). A study on the equilibrium between copper matte and slag. *Can. Metall. Quarterly,* **25**, no. 2: 113–121.

SIMEONOV, S.R., SRIDHAR, R. & TOGURI, J.M.(1996). Relationship between slag sulfur content and slag metal losses in non-ferrous pyrometallurgy. *Can. Metall. Quarterly,* **35**, no. 5: 463–467.

SNELGROVE, W.R.N. & TAYLOR, J.C. (1980). The recovery of values from non-ferrous smelter slags. *Int. Symposium on Metallurgical Slags,* **2**. Halifax, Nova Scotia. 38 pp.

SRIDHAR, R., TOGURI, J.M. & SIMEONOV, S. (1997). Copper losses and thermodynamic considerations in copper smelting. *Meatll. And Materials Trans. B* **28B**: 191–200.

SUBRAMANIAN, K.N. & THEMELIS, N.J. (1972). Copper recovery by flotation. *JOM Apr 1972*: 33–38.

SUTHERLAND, D.N. & GOTTLIEB, P. (1991). Application of automated quantitative mineralogy in mineral processing. *Miner. Eng.* **4**: 753–762.

SWARTZENDRUBER, L.J. & BENNETT, L.H. (1986). Mossbauer Spectroscopy. *In* Materials characterization. Metals Handbook 9th edition, **10**. Ohio: Amer. Soc. for Metals.

TAKEDA, Y. (1997). Oxygen potential measurement of iron silicate slag-copper-matte system. *Proc. 5th Int. Conf. on Molten Slags, Fluxes and Salts*: 735–743. Warrendale.

TAKEDA, Y. (2000). Copper solubility in SiO_2-CaO-FeO_x slag equilibrated with matte. *Proc. 6th Int. Conf. on Molten Slags, Fluxes and Salts,* Stockholm/Helsinki: ISBN. 18 pp.

TAKEDA, Y. (2003). Thermodynamic evaluation of copper loss in slag equilibrated with matte. *In* Kongoli, F., Itagaki, K., Yamauchi, C. and Sohn, H.Y. (eds) *Yazawa Int Symp on Metallurgical and Materials Processing: Materials Processing Fundamentals and New Technologies* **1:** 341–357. The Minerals, Metals and Materials Society.

TAN, P. & NEUSCHUTZ, D. (2001). A thermodynamic model of nickel smelting and direct high-grade nickel matte smelting processes: Part I. Model development and validation. *Metall. and Materials Trans. B,* **32B**: 341–351

TAN, P. & NEUSCHUTZ, D. (2001). A thermodynamic model of nickel smelting and direct high-grade nickel matte smelting processes: Part II. Distribution behaviours of Ni, Cu, Co, Fe, As, Sb and Bi. *Metall. and Materials Trans. B,* **32B**: 353–361.

TASKINEN, P., SEPPAIA, K., LAUHEMEA, J. & POIJARVI, J. (2001). Oxygen pressure in the Outokumpu flash smelting furnace – Part 1: Copper flash smelting settler. *Trans. Inst. Min. Metall.* **C110**: C94–C100.

TASKINEN, P., SEPPAIA, K., LAUHEMEA, J. & POIJARVI, J. (2001). Oxygen pressure in the Outokumpu flash smelting furnace – Part 2: the DON process. *Trans. Inst. Min. Metall.* **C110**: C101–C108.

TEAGUE, K.C., SWINBOURNE, D.R. & JAHANSHAHI, S. (2001). A thermodynamic study on cobalt-containing calcium ferrite and calcium iron silicate slags at 1573K. *Metall. & Materials Trans. B,* **32B**: 47–54.

THEMELIS, N.J. & KELLOGG, H.H. (1983). Principles of sulfide smelting. *In Advances in sulfide smelting* **1**: 1–29. Warrendale, PA: The Society.

TOGURI, J.M. & IP, S.W. (1993). Surface and Interfacial Tension Studies in the matte/slag systems. *In* Steele, B.C.H. (ed.) *High Temperature Materials Chemistry*: 199–223. London: The Institute of Materials.

TSEMEKHMAN, L.S., RYABKO, A.G., TSYMBULOV, L.B., KNYAZOV, M.V., FOMICHEV, V.B., RYUMIN, A.A. & PAVLINOVA, L.A. (2003). Mechanisms of the cleaning of Cu-Ni-Co-containing slags by oxidizing-reduction gas mixtures. *In* Kongoli, F., Itagaki, K., Yamauchi, C. and Sohn, H.Y. (eds) *Yazawa Int Symp on Metallurgical and Materials Processing: High temperature metals production* **2**: 167–175.The Minerals, Metals and Materials Society.

UNDERWOOD, E.E. (1970). Particle and grain-size distributions. *In* Underwood, E. (ed.) *Quantitative Stereology:* 109–147. Reading, Massachusetts: Addison-Wesley.

URQUHART, R.C., RENNIE, M.S. & RABEY, C.C. (1976). The smelting of copper-nickel concentrates in an electric furnace. *Proc. Int. Symp. Extractive Metallurgy of Copper: Pyrometallurgical and Electrolytic Refining* **1**: 274–295. Las Vegas.

URQUHART, R.C., RENNIE, M.S., FORBES, A.W., ZAIDY, M.G., GRIESSEL, H.J., de KOCK, R. & BOSWELL, M.S. (1976). The smelting of copper-nickel concentrates in an electric furnace. *NIM Report No. 1664,* September 1974. 41 pp.

VILJOEN, E.A. & JOHNSON, J.A. (1983). Microbeam techniques in applied mineralogy. *Special Publications of the Geological Society of South Africa* **7**: 499–506.

VIRCIKOVA, E. & MOLNAR, L. (1992). Recovery of copper from dump slag by a segregation process. *Resources, conservation and recycling,* **6**: 133–138.

WANG, S.S., SANTANDER, N.H. & TOGURI, J.M. (1974). The solubility of nickel and cobalt in iron silicate slags. *Metall. Trans.* ***5***: 261–265.

WARCZOK, A. & RIVEROS, G. (2003). Effect of electric and magnetic fields on the metallic inclusions in a liquid slag. *In* Kongoli, F., Itagaki, K., Yamauchi, C. and Sohn, H.Y. (eds) *Yazawa Int Symp on Metallurgical and Materials Processing: High temperature metals production* **2**: 167–175.The Minerals, Metals and Materials Society.

WARCZOK, A. & UTIGARD, T.A. (1995). Settling of copper drops in molten slags. *Metall. Trans. B* **26B**:1165–1173.

WARCZOK, A., RIVEROS, G., ECHEVERRIA, P., DIAZ, C.M., SCHWARZE, H. & SANCHEZ, G. (2002). Factors governing slag cleaning in an electric furnace. *Can. Metall. Quarterly* **41***,* no. 4: 465–474.

WARCZOK, A. & RIVEROS, G., (2007). Slag cleaning in crossed electric and magnetic fields. *Minerals Engineering* **20**: 34–43.

WEHR, S.D. & SHAW, J.M. (2002). A note on the misuse of area images to obtain particle size information

in solid-solid systems. *Can. Metall. Quarterly* **41***,* no. 3: 365–372.

WHITTAKER, E.J.W. (1967). Factors affecting element ratios in the crystallization of minerals. *Geochim et Cosmochim Acta* **31**: 2275–2288.

WHYTE, R.N., ORLANS, J.R., HARRIS, G.B. & THOMAS, J.A. (1977). Development of a process for the recovery of electrolytic copper and cobalt from Rokana converter slag. *Advances in extractive metallurgy*: 57–68. London: Inst. Min. Metall.

WICKS, J.N. (2000). Smelter and converter practice at Waterval Smelter: Process challenges and innovations. *In Proc. of Developments in Non-ferrous Pyrometallurgy*: 1–10. Cape Town: the SAIMM.

XIA, J.L., AHOKAINEN, T. & KANKAANPAA, T. (2004). A CFD study of flows in slag cleaning furnaces. *Can. Metall. Quarterly* **43,** no.2: 145–152.

XIA, J.L., AHOKAINEN, T. & KANKAANPAA, T. (2004). Nickel droplet settling behaviour in an electric furnace. *Metall. and Materials Trans B,* **35B**: *839–845.*

YANG, L. & BELTON, G.R. (1998). Iron redox equilibria in $CaO\text{-}Al_2O_3\text{-}SiO_2$ and $MgO\text{-}CaO\text{-}Al_2O_3\text{-}SiO_2$ slags. *Metall. and Materials Trans B,* **29B**: *837–845.*

YAZAWA, A. (1979). Thermodynamic evaluations of extractive metallurgical processes. *Metall. Trans. B* **10B**:307–321.

ZHANG, L., JAHANSHAHI, S., SUN, S., CHEN, C., BOURKE, B., WRIGHT, S. & SOMERVILLE, M. (2002). CSIRO's multiphase reaction models and their industrial applications. JOM November 2002: 51–56.

APPENDIX A – TABLES

Table A1: Sample description and nomenclature – 1999 six-in-line furnace campaign.

Sample name	*Date*	*Furnace no.*	*Description*
FS1	29 November 1999	1	Granulated slag
FS2	3 December 1999	1	Granulated slag
FS3	13 December 1999	1	Granulated slag
FS4	20 December 1999	1	Granulated slag
FS5	22 December 1999	1	Granulated slag
FS6	29 November 1999	2	Granulated slag
FS7	3 December 1999	2	Granulated slag
FS8	13 December 1999	2	Granulated slag
FS9	22 December 1999	2	Granulated slag

Table A2: Sample description and nomenclature – 2004 six-in-line campaign. All the samples were taken from Furnace 1.

Sample name	*Date*	*Shift*	*Furnace additions*	*Description*
WS1445	2 November 2004	A	No revert addition	Matte spoon
WS1447		A		Granulated slag
WS1448		A		Reverts
WS1449	3 November 2004	M	Revert addition	Matte spoon
WS1451		M		Granulated slag
WS1452		A		Matte spoon
WS1454		A		Granulated slag
WS1455		A		Reverts
WS1456		N		Reverts
WS1457		N		Matte spoon
WS1459	4 November 2004	N		Granulated slag
WS1460		M		Reverts
WS1461		M		Reverts
WS1462		M		Matte spoon
WS1464		M		Granulated slag
WS1465		A		Granulated slag
WS1467		A		Matte spoon
WS1468		A		Reverts
WS1469		N		Matte spoon
WS1471	5 November 2004	N		Granulated slag
WS1474	5 November 2004	A	High lime addition	Matte spoon
WS1475		N		Matte spoon
WS1476		A		Reverts
WS1477		N		Reverts
WS1478		A		Granulated slag
WS1479		N		Granulated slag

Table A3: Sample description and nomenclature – 2005 six-in-line furnace campaign.

Sample name	*Date*	*Furnace no.*	*Description*
WS1922	5 May 2005		Limestone
WS1989	18 May 2005	1	Granulated slag
WS1990		2	Granulated slag
WS1993			Recycles
WS1995		1	Matte spoon
WS1997	19 May 2005		Flash drier product
WS1998			Reverts
WS1999	25 May 2005	2	Granulated slag
WS2000		2	Matte spoon
WS2003		1	Matte spoon
WS2004			Reverts
WS2007	27 May 2005	1	Granulated slag
WS2008	2 June 2005	2	Granulated slag
WS2009		2	Matte spoon
WS2012		1	Matte spoon
WS2013			Flash drier product
WS2014			Recycles
WS2015	3 June 2005	1	Granulated slag
WS2016	8 June 2005	1	Matte spoon
WS2018		2	Matte spoon
WS2020		2	Granulated slag
WS2021			Flash drier product
WS2022			Recycles
WS2023			Reverts
WS2024	2 June 2005		Reverts
WS2025	10 June 2005	1	Granulated slag

Table A4: Sample description and nomenclature – 2005 SCF campaign.

Name	*Date*	*Shift*	*Description*
WS2110	23 September 2005	M	Matte spoon
WS2120		A	Matte spoon
WS2088		A	Flash Drier product
WS2097		A	Granulated slag
WS2098		A	Granulated slag
WS2100		A	Converter slag feed
WS2115		N	Matte spoon
WS2096		N	Granulated slag
WS2116	24 September 2005	M	Matte spoon
WS2101		M	Converter slag feed
WS2112		A	Matte spoon
WS2093		A	Granulated slag
WS2090		A	Granulated slag
WS2105		A	Converter slag feed
WS2108		N	Matte spoon
WS2089		N	Flash Drier product
WS2092		N	Granulated slag
WS2103	25 September 2005	M	Converter slag feed
WS2113		A	Matte spoon
WS2091		A	Granulated slag
WS2094		A	Granulated slag
WS2102		A	Converter slag feed
WS2111		N	Matte spoon
WS2095		N	Granulated slag
WS2099		N	Converter slag feed
WS2106	Undated	–	Converter slag feed
WS2104		–	Converter slag feed

Table A5: Sample description and nomenclature – 2006 and 2007 sounding bar campaigns (six-in-line furnaces).

Furnace 2 October 2006		Furnace 1 September 2007	
Name	Depth (cm)	Name	Height (cm)
SB1	0–10	SB1	0–5
SB2	10–20	SB2	5–45
SB3	20–30	SB3	45–55
SB4	30–40	SB4	55–62
SB5	40–50	SB5	62–72
SB6	50–60	SB6	72–94
SB7	60–70	SB7	94–106
SB8	70–80	SB8	106–112
SB9	80–90	SB9	112–124
SB10	90–100	SB10	124–134
SB11	100–110	SB11	134–144
SB12	110–120	Top*	144–150
SB13	120–130		
SB14	130–140		
SB15	140–150		
SB16	150–160		

*This sample was lost.

Table A6: 2004 flash drier daily composite assay results (in mass %) as received from Waterval Smelter.

Date	MgO	Al_2O_3	SiO_2	CaO	Cr_2O_3	Fe	Co	Ni	Cu	S
1 Nov	17.40	3.68	40.82	2.61	1.45	15.16	0.07	2.80	1.77	7.17
2 Nov	16.73	3.70	39.72	2.44	1.24	15.96	0.08	3.13	1.94	7.89
3 Nov	12.66	2.24	29.01	1.54	0.30	25.88	0.24	10.38	1.57	18.11
4 Nov	14.62	3.07	34.51	2.20	0.80	20.41	0.15	6.65	1.67	11.74
5 Nov	16.57	3.90	40.00	2.86	1.30	14.94	0.07	2.95	1.77	5.39
Average	15.60	3.32	36.81	2.33	1.02	19.07	0.12	5.12	1.74	10.06

Table A7: Results of chemical analysis of the 2005 flash drier product (concentrate) samples, in mass %.

Sample	MgO	Al_2O_3	SiO_2	CaO	Cr_2O_3	Fe	Co	Ni	Cu	S
WS1997	15.9	3.78	36.9	4.14	1.30	15.4	0.11	2.76	1.97	6.95
WS2013	10.8	4.13	28.3	3.44	1.21	20.6	0.16	5.70	3.67	13.20
WS2021	14.7	3.69	34.6	3.05	1.29	19.3	0.14	4.14	2.34	10.20
Average	13.8	3.87	33.3	3.54	1.27	18.4	0.14	4.20	2.66	10.12

Table A8: Results of chemical analysis, as received, of the 2004 reverts samples, in mass

Sample	MgO	Al_2O_3	SiO_2	CaO	Cr_2O_3	Fe	Co	Ni	Cu	S
WS1448	3.00	4.34	23.1	2.05	2.47	27.2	0.31	11.5	5.90	7.69
WS1455	3.17	3.70	22.6	2.08	4.11	31.4	0.28	9.9	5.26	6.65
WS1456	2.88	4.01	21.0	1.56	2.96	27.9	0.29	12.2	6.58	8.42
WS1460	2.79	4.22	21.2	1.71	2.04	27.0	0.30	13.5	7.41	7.67
WS1461	2.76	4.17	21.0	1.69	1.56	24.0	0.29	15.1	8.47	9.02
WS1468	3.21	4.39	18.2	1.67	3.20	25.0	0.30	14.9	7.86	11.10
WS1476	2.92	4.90	19.5	1.61	3.03	25.4	0.31	14.1	7.32	10.70
WS1477	3.15	4.85	18.8	1.81	3.31	24.5	0.29	14.9	8.16	11.40
Average	2.98	4.32	20.7	1.77	2.84	26.6	0.30	13.3	7.12	9.08

Table A9: Results of chemical analysis of the 2005 revert samples, in mass %.

Sample	MgO	Al_2O_3	SiO_2	CaO	Cr_2O_3	Fe	Co	Ni	Cu	S
WS1998	5.99	4.31	21.0	2.28	3.32	23.6	0.34	15.2	7.86	8.58
WS2004	4.79	3.64	20.0	2.20	2.86	22.6	0.23	14.7	9.13	8.62
WS2023	4.70	2.57	17.2	2.22	4.57	31.6	0.35	12.0	6.28	12.50
WS2024	1.63	1.16	12.8	0.70	3.51	29.0	0.35	20.4	11.50	9.89
Average	4.28	2.92	17.8	1.85	3.57	26.7	0.32	15.6	8.69	9.90

Table A10: Results of chemical analysis of the recycles samples, in mass %.

Sample	MgO	Al_2O_3	SiO_2	CaO	Cr_2O_3	Fe	Co	Ni	Cu	S
WS1993	13.9	4.06	37.1	5.83	1.67	20.0	0.13	2.66	1.26	2.63
WS2014	6.9	2.59	30.7	4.34	1.72	32.9	0.23	3.37	1.80	2.58
WS2022	14.3	4.32	38.7	7.14	1.59	19.0	0.10	1.47	0.80	1.59
Average	11.7	3.66	35.5	5.77	1.66	24.0	0.15	2.50	1.29	2.27

Table A11: Results of chemical analysis, as received, of the 1999 matte samples, in mass %. The results are averaged per furnace.

Sample	MgO	Al_2O_3	SiO_2	CaO	Cr_2O_3	Fe	Co	Ni	Cu	S
29 Nov	0.30	5.55	1.85	0.21	0.60	40.60	0.49	15.86	8.35	25.70
3 Dec	0.83	3.07	3.53	1.00	0.46	39.80	0.42	15.12	8.44	25.10
13 Dec	0.01	1.45	0.55	0.22	0.52	40.85	0.44	17.15	8.79	26.95
Fce 1 ave	0.38	3.36	1.98	0.48	0.53	40.42	0.45	16.04	8.53	25.92
29 Nov	0.05	1.56	0.76	0.19	0.73	40.35	0.50	17.51	9.28	26.20
3 Dec	0.01	2.72	0.84	0.22	0.64	39.97	0.50	17.18	9.44	25.75
13 Dec	0.01	1.76	0.69	0.26	0.54	43.13	0.44	15.80	8.03	26.75
22 Dec	0.01	0.87	0.62	0.21	0.84	42.61	0.50	16.52	8.64	27.04
Fce 2 ave	0.02	1.73	0.73	0.22	0.69	41.52	0.49	16.75	8.85	26.44

Table A12: Results of chemical analysis, as received, of the 2004 matte samples, in mass %.

Sample	MgO	Al_2O_3	SiO_2	CaO	Cr_2O_3	Fe	Co	Ni	Cu	S
WS1445	<0.05	0.73	0.23	0.27	1.11	40.7	0.34	14.7	8.11	30.7
WS1449	<0.05	1.25	0.26	0.31	1.41	41.5	0.34	14.8	8.03	30.2
WS1452	<0.05	0.74	0.97	0.29	1.22	41.2	0.34	15.3	8.14	28.9
WS1457	<0.05	1.15	0.22	0.30	0.90	41.6	0.34	14.7	7.92	30.1
WS1462	<0.05	2.67	1.50	0.28	1.18	39.5	0.34	14.9	7.75	28.3
WS1467	<0.05	0.26	0.17	0.26	1.10	41.1	0.37	15.8	8.12	28.8
WS1469	<0.05	0.64	0.17	0.30	1.04	40.4	0.36	15.9	8.12	30.8
WS1474	<0.05	0.45	0.36	0.29	1.02	42.5	0.35	15.5	7.90	29.4
WS1475	<0.05	1.67	0.29	0.31	0.96	39.9	0.35	15.6	7.98	31.4
Average	<0.05	1.06	0.46	0.29	1.10	40.9	0.35	15.2	8.01	29.8

Table A13: Results, in mass %, of chemical analysis of the 2005 six-in-line matte spoon samples. The results are averaged per furnace.

Sample	Mg	Al_2O_3	Si	Ca	Cr_2O_3	Fe	Co	Ni	Cu	S
WS1995	<0.3	1.47	<0.23	<0.17	0.95	39.1	0.35	16.2	11.10	28.2
WS2003	<0.3	1.36	<0.23	<0.17	0.84	41.2	0.38	16.7	10.70	27.6
WS2012	<0.3	0.41	<0.23	<0.17	1.09	39.9	0.39	17.6	11.00	29.0
WS2016	<0.3	1.90	<0.23	<0.17	0.98	39.6	0.39	16.7	9.91	28.7
Ave F1	<0.3	1.29	<0.23	<0.17	0.97	40.0	0.38	16.8	10.68	28.4
Sample	Mg	Al_2O_3	Si	Ca	Cr_2O_3	Fe	Co	Ni	Cu	S
WS1996	<0.3	1.73	<0.23	<0.17	1.46	39.8	0.33	15.1	10.80	28.2
WS2000	<0.3	0.40	<0.23	<0.17	1.09	41.2	0.38	17.1	11.10	28.5
WS2009	<0.3	0.44	<0.23	<0.17	0.91	40.5	0.38	17.3	10.80	28.8
WS2018	<0.3	1.22	<0.23	<0.17	1.08	40.6	0.39	17.1	9.85	29.1
Ave F2	<0.3	0.95	<0.23	<0.17	1.14	40.5	0.37	16.6	10.64	28.6

Table A14: Results, in mass %, of chemical analysis of the 1999 six-in-line slag samples. The average per furnace is also shown.

Sample	Cu	Ni	Co	Fe	Cr_2O_3	SiO_2	Al_2O_3	CaO	MgO	S	Total
FS1	0.08	0.14	0.06	21.00	1.23	46.68	3.58	7.26	16.31	0.54	96.88
FS2	0.08	0.15	0.04	18.02	0.90	45.97	3.77	10.94	16.58	0.46	96.91
FS3	0.08	0.17	0.04	16.01	1.22	46.59	4.52	10.94	17.18	0.40	97.15
FS4	0.08	0.14	0.03	13.45	1.41	48.50	4.55	10.21	19.16	0.44	97.97
FS5	0.15	0.26	0.02	11.95	1.91	48.59	5.22	9.19	20.63	0.47	98.42
Ave F1	0.09	0.17	0.04	16.09	1.33	47.27	4.33	9.71	17.97	0.46	97.47
FS6	0.08	0.13	0.05	19.00	0.97	47.96	3.88	6.89	17.43	0.44	96.83
FS7	0.11	0.20	0.07	19.17	1.10	46.35	3.80	8.56	16.49	0.48	96.33
FS8	0.06	0.13	0.05	17.88	0.97	43.30	4.00	14.13	14.90	0.48	95.90
FS9	0.08	0.14	0.06	18.94	0.89	46.15	3.84	8.44	16.78	0.46	95.81
Ave F2	0.08	0.15	0.06	18.75	0.98	45.95	3.88	9.51	16.40	0.47	96.22

Table A15: Results of chemical analysis, in mass %, of the 2004 granulated slag samples, in mass %.

Sample	Na	MgO	Al_2O_3	SiO_2	K	CaO	Cr_2O_3	Fe	Co	Ni	Cu	S
WS1447	0.16	22.0	5.29	50.9	0.084	5.73	1.48	10.20	0.015	0.064	0.065	0.28
WS1451	0.21	23.0	5.06	52.3	0.091	4.97	1.45	9.17	0.012	0.051	0.058	0.27
WS1454	0.21	22.5	5.05	51.2	0.086	5.79	1.40	9.54	0.014	0.091	0.075	0.31
WS1459	0.21	22.7	5.06	51.9	0.088	4.84	1.48	9.69	0.014	0.054	0.059	0.25
WS1464	0.18	22.5	5.08	51.9	0.083	4.74	1.45	9.83	0.014	0.048	0.059	0.27
WS1465	0.16	22.3	5.08	51.7	0.082	5.14	1.44	10.10	0.015	0.053	0.057	0.27
WS1471	0.19	22.5	5.04	51.6	0.087	5.44	1.43	9.77	0.014	0.058	0.057	0.26
WS1478	0.16	21.3	4.81	49.5	0.086	8.78	1.34	9.39	0.013	0.052	0.051	0.28
WS1479	0.18	21.4	4.85	49.8	0.089	8.96	1.30	9.42	0.013	0.052	0.051	0.27
Average	0.18	22.2	5.04	51.2	0.086	6.04	1.42	9.68	0.014	0.058	0.059	0.27

Table A16: Results of chemical analysis of the slag samples in, mass %.

Sample	Na_2O	MgO	Al_2O_3	SiO_2	K_2O	CaO	Ti	Cr_2O_3	Fe	Co	Ni	Cu	S
WS1989	0.36	22.0	5.31	46.4	0.19	7.36	0.16	1.53	10.6	0.020	0.15	0.087	0.28
WS2007	0.40	21.2	5.28	46.2	0.23	8.67	0.16	1.49	11.2	0.030	0.14	0.087	0.28
WS2015	0.38	20.5	5.23	45.8	0.25	9.77	0.16	1.40	11.4	0.025	0.13	0.070	0.29
WS2025	0.39	22.2	5.45	48.5	0.24	7.30	0.16	1.35	10.1	0.020	0.12	0.062	0.28
Ave F1	0.38	21.5	5.32	46.8	0.23	8.28	0.16	1.44	10.8	0.023	0.14	0.077	0.28
WS1990	0.40	21.3	5.32	47.4	0.22	10.20	0.16	1.31	9.6	0.020	0.13	0.077	0.29
WS1999	0.38	20.6	5.53	46.2	0.22	9.73	0.16	1.51	10.4	0.021	0.13	0.070	0.30
WS2008	0.40	20.7	5.30	46.8	0.23	10.40	0.16	1.20	10.6	0.023	0.15	0.076	0.30
WS2020	0.38	21.0	5.08	46.7	0.23	11.00	0.16	1.28	10.3	0.023	0.14	0.066	0.29
Ave F2	0.39	20.9	5.31	46.8	0.23	10.33	0.16	1.33	10.2	0.022	0.14	0.072	0.30

Table A17: Results (in mass %) of electron microprobe analysis of twenty-five positions on the glass phase in sample FS1 (1999). The average (Ave) and standard deviation (s.d.) of all results over the detection limit are shown. Detection limits are quoted in section 6.7 – in this table one cobalt determination is below the limit.

	MgO	Al2O3	SiO2	CaO	SO3	Cr2O3	FeO	CoO	NiO	Cu2O	Total
Ave	16.88	3.99	46.63	6.47	0.89	0.80	23.27	0.068	0.135	0.085	99.21
s.d.	0.32	0.04	0.23	0.08	0.11	0.05	0.41	0.021	0.041	0.022	0.59

Table A18: Results (in mass %) of electron microprobe analysis of twenty positions on the glass phase in sample FS2 (1999). The average (Ave) and standard deviation (s.d.) of all results over the detection limit are shown. Detection limits are quoted in section 6.7 – in this table four cobalt and three nickel determinations are below the limit.

	MgO	Al2O3	SiO2	CaO	SO3	Cr2O3	FeO	CoO	NiO	Cu2O	Total
Ave	15.65	3.91	45.29	10.28	0.94	0.67	22.44	0.123	0.162	0.063	99.48
s.d.	0.30	0.05	0.39	0.13	0.34	0.10	0.35	0.090	0.145	0.033	0.48

Table A19: Results (in mass %) of electron microprobe analysis of twenty-two positions on the glass phase in sample FS3 (1999). The average (Ave) and standard deviation (s.d.) of the results are shown. All determinations were above the detection limit.

	MgO	Al2O3	SiO2	CaO	SO3	Cr2O3	FeO	CoO	NiO	Cu2O	Total
Ave	16.63	4.75	45.64	10.79	0.76	1.01	19.44	0.077	0.176	0.082	99.35
s.d.	0.26	0.07	0.47	0.14	0.26	0.06	0.63	0.023	0.043	0.025	0.77

Table A20: Results (in mass %) of electron microprobe analysis of twenty-one positions on the glass phase in sample FS4 (1999). The average (Ave) and standard deviation (s.d.) of all results over the detection limit are shown. Detection limits are quoted in section 6.7 – in this table eleven cobalt and five copper determinations are below the limit.

	MgO	Al2O3	SiO2	CaO	SO3	Cr2O3	FeO	CoO	NiO	Cu2O	Total
Ave	19.32	5.13	48.38	11.05	0.66	1.05	13.51	0.042	0.072	0.039	99.25
s.d.	0.41	0.05	0.49	0.12	0.07	0.03	0.20	0.013	0.028	0.009	0.71

Table A21: Results (in mass %) of electron microprobe analysis of twenty-two positions on the glass phase in sample FS5 (1999). The average (Ave) and standard deviation (s.d.) of all results over the detection limit are shown. Detection limits are quoted in section 6.7 – in this table eleven cobalt determinations are below the limit.

	MgO	Al2O3	SiO2	CaO	SO3	Cr2O3	FeO	CoO	NiO	Cu2O	Total
Ave	20.92	5.18	48.60	9.31	0.60	1.00	13.75	0.042	0.122	0.060	99.58
s.d.	0.39	0.07	0.66	0.16	0.12	0.05	0.47	0.017	0.036	0.015	1.28

Table A22: Results (in mass %) of electron microprobe analysis of twenty-three positions on the glass phase in sample FS6 (1999). The average (Ave) and standard deviation (s.d.) of all results over the detection limit are shown. Detection limits are quoted in section 6.7 – in this table five cobalt determinations are below the limit.

	MgO	Al2O3	SiO2	CaO	SO3	Cr2O3	FeO	CoO	NiO	Cu2O	Total
Ave	15.86	3.73	45.66	5.89	1.06	0.87	26.54	0.090	0.152	0.095	99.94
s.d.	0.40	0.05	0.61	0.10	0.28	0.10	0.53	0.058	0.081	0.045	0.56

Table A23: Results (in mass %) of electron microprobe analysis of twenty positions on the glass phase in sample FS7 (1999). The average (Ave) and standard deviation (s.d.) of all results are shown. For this table, all determinations were above the detection limit.

	MgO	Al2O3	SiO2	CaO	SO3	Cr2O3	FeO	CoO	NiO	Cu2O	Total
Ave	15.88	3.83	45.25	7.64	0.98	0.92	23.77	0.098	0.175	0.082	98.61
s.d.	0.42	0.07	0.30	0.21	0.15	0.04	0.40	0.020	0.049	0.026	0.68

Table A24: Results (in mass %) of electron microprobe analysis of twenty-nine positions on the glass phase in sample FS8 (1999). The average (Ave) and standard deviation (s.d.) of the results are shown. For this table, all determinations were above the detection limit (quoted in section 6.7).

	MgO	Al2O3	SiO2	CaO	SO3	Cr2O3	FeO	CoO	NiO	Cu2O	Total
Ave	14.21	4.15	42.65	13.68	1.06	0.55	22.44	0.070	0.122	0.068	99.00
s.d.	0.25	0.05	0.42	0.15	0.16	0.05	0.32	0.025	0.069	0.033	0.56

Table A25: Results (in mass %) of electron microprobe analysis of twenty-seven positions on the glass phase in sample FS9 (1999). The average (Ave) and standard deviation (s.d.) of the results are shown. For this table, all determinations were above the detection limit (quoted in section 6.7).

	MgO	Al2O3	SiO2	CaO	SO3	Cr2O3	FeO	CoO	NiO	Cu2O	Total
Ave	16.48	4.07	45.82	8.07	1.09	0.72	23.08	0.081	0.178	0.083	99.68
s.d	0.40	0.06	1.04	0.10	0.23	0.04	0.73	0.026	0.081	0.033	0.84

Table A26: Results (in mass %) of electron microprobe analysis of twenty-one positions on the glass phase in sample WS1447 (2004). The average (Ave) and standard deviation (s.d.) of all results over the detection limit are shown. Detection limits are quoted in section 6.7 – in this table eleven cobalt and six titanium determinations are below the limit.

	MgO	Al2O3	SiO2	CaO	SO3	Cr2O3	FeO	CoO	NiO	Cu2O	Na2O	TiO2	Total
Ave	22.40	5.31	50.89	5.29	0.63	1.41	12.96	0.028	0.082	0.054	0.398	0.550	99.83
s.d.	0.24	0.06	0.34	0.25	0.06	0.15	0.14	0.005	0.015	0.014	0.068	0.264	0.75

Table A27: Results (in mass %) of electron microprobe analysis of twenty-one positions on the glass phase in sample WS1451 (2004). The average (Ave) and standard deviation (s.d.) of all results over the detection limit are shown. Detection limits are quoted in section 6.7 – in this table sixteen cobalt and eight titanium determinations are below the limit.

	MgO	Al2O3	SiO2	CaO	SO3	Cr2O3	FeO	CoO	NiO	Cu2O	Na2O	TiO2	Total
Ave	23.45	5.05	52.23	4.87	0.65	1.41	11.60	0.028	0.070	0.057	0.323	0.353	99.95
s.d.	0.19	0.09	0.32	0.05	0.08	0.14	0.16	0.006	0.020	0.020	0.052	0.184	0.64

Table A28: Results (in mass %) of electron microprobe analysis of twenty-one positions on the glass phase in sample WS1454 (2004). The average (Ave) and standard deviation (s.d.) of all results over the detection limit are shown. Detection limits are quoted in section 6.7 – in this table sixteen cobalt, six sodium and six titanium determinations are below the limit.

	MgO	Al2O3	SiO2	CaO	SO3	Cr2O3	FeO	CoO	NiO	Cu2O	Na2O	TiO2	Total
Ave	22.98	5.02	51.43	5.49	0.53	1.33	12.37	0.023	0.079	0.054	0.249	0.375	99.73
s.d.	0.43	0.14	0.73	0.90	0.09	0.18	0.53	0.004	0.018	0.013	0.156	0.159	0.65

Table A29: Results (in mass %) of electron microprobe analysis of twenty-one positions on the glass phase in sample WS1459 (2004). The average (Ave) and standard deviation (s.d.) of all results over the detection limit are shown. Detection limits are quoted in section 6.7 – in this table fifteen cobalt, six sodium and seven titanium determinations are below the limit.

	MgO	Al2O3	SiO2	CaO	SO3	Cr2O3	FeO	CoO	NiO	Cu2O	Na2O	TiO2	Total
Ave	23.47	5.07	52.02	4.79	0.57	1.31	12.21	0.028	0.086	0.050	0.505	0.367	100.22
s.d.	0.33	0.15	0.28	0.13	0.07	0.14	0.22	0.005	0.023	0.013	0.286	0.166	0.61

Table A30: Results (in mass %) of electron microprobe analysis of sixty positions on the glass phase in sample WS1464 (2004) – Low CaO extreme. The average (Ave) and standard deviation (s.d.) of all results over the detection limit are shown. Detection limits are quoted in section 6.7 – in this table thirty-six cobalt and twenty-five titanium determinations are below the limit.

	MgO	Al2O3	SiO2	CaO	SO3	Cr2O3	FeO	CoO	NiO	Cu2O	Na2O	TiO2	Total
Ave	22.87	5.06	51.78	4.64	0.64	1.33	12.47	0.028	0.080	0.057	0.378	0.408	99.59
s.d.	0.20	0.07	0.24	0.06	0.08	0.14	0.15	0.006	0.021	0.020	0.197	0.200	0.66

Table A31: Results (in mass %) of electron microprobe analysis of twenty positions on the glass phase in sample WS1465 (2004). The average (Ave) and standard deviation (s.d.) of all results over the detection limit are shown. Detection limits are quoted in section 6.7 – in this table fourteen cobalt, one copper, one sodium and five titanium determinations are below the limit.

	MgO	Al2O3	SiO2	CaO	SO3	Cr2O3	FeO	CoO	NiO	Cu2O	Na2O	TiO2	Total
Ave	22.52	4.91	51.37	5.17	0.50	1.34	12.63	0.023	0.076	0.040	0.338	0.402	99.22
s.d.	0.31	0.15	0.39	0.13	0.13	0.10	0.17	0.003	0.038	0.012	0.137	0.252	0.64

Table A32: Results (in mass %) of electron microprobe analysis of twenty positions on the glass phase in sample WS1471 (2004). The average (Ave) and standard deviation (s.d.) of all results over the detection limit are shown. Detection limits are quoted in section 6.7 – in this table fifteen cobalt, four sodium, and seven titanium determinations are below the limit.

	MgO	Al2O3	SiO2	CaO	SO3	Cr2O3	FeO	CoO	NiO	Cu2O	Na2O	TiO2	Total
Ave	22.56	5.03	50.93	5.50	0.63	1.33	11.81	0.026	0.081	0.052	0.557	0.343	98.61
s.d.	0.55	0.32	0.78	0.99	0.08	0.07	0.50	0.005	0.019	0.015	0.182	0.202	0.33

Table A33: Results (in mass %) of electron microprobe analysis of twenty positions on the glass phase in sample WS1478 (2004). The average (Ave) and standard deviation (s.d.) of all results over the detection limit are shown. Detection limits are quoted in section 6.7 – in this table thirteen cobalt, two copper, six sodium and six titanium determinations are below the limit.

	MgO	Al2O3	SiO2	CaO	SO3	Cr2O3	FeO	CoO	NiO	Cu2O	Na2O	TiO2	Total
Ave	21.77	4.86	50.09	8.78	0.66	1.23	12.04	0.027	0.083	0.057	0.414	0.364	100.15
s.d.	0.48	0.39	0.44	0.09	0.12	0.12	0.16	0.006	0.026	0.012	0.210	0.176	0.78

Table A34: Results (in mass %) of electron microprobe analysis of fifty-five positions on the glass phase in sample WS1479 (2004) – High CaO extreme. The average (Ave) and standard deviation (s.d.) of all results over the detection limit are shown. Detection limits are quoted in section 6.7 – in this table thirty-nine cobalt and twenty-two titanium determinations are below the limit.

	MgO	Al2O3	SiO2	CaO	SO3	Cr2O3	FeO	CoO	NiO	Cu2O	Na2O	TiO2	Total
Ave	21.64	4.93	49.73	9.01	0.69	1.18	11.96	0.028	0.079	0.048	0.355	0.369	99.88
s.d.	0.16	0.06	0.22	0.07	0.07	0.12	0.14	0.010	0.016	0.011	0.045	0.153	0.48

Table A35: Results (in mass %) of electron microprobe analysis of fifty-threebpositions on the glass phase in sample WS1989 (2005). The average (Ave) and standard deviation (s.d.) of all results over the detection limit are shown. Detection limits are quoted in section 6.7 – in this table twenty-seven cobalt determinations are below the limit.

	MgO	Al2O3	SiO2	CaO	SO3	Cr2O3	FeO	CoO	NiO	Cu2O	Na2O	TiO2	Total
Ave	21.59	5.25	48.76	6.92	0.64	1.60	13.08	0.028	0.098	0.072	0.39	0.26	98.67
s.d.	0.25	0.13	0.56	0.75	0.08	0.15	0.21	0.007	0.014	0.015	0.08	0.09	0.44

Table A36: Results (in mass %) of electron microprobe analysis of forty-two positions on the glass phase in sample WS1990 (2005). The average (Ave) and standard deviation (s.d.) of all results over the detection limit are shown. Detection limits are quoted in section 6.7 – in this table thirty cobalt determinations are below the limit.

	MgO	Al2O3	SiO2	CaO	SO3	Cr2O3	FeO	CoO	NiO	Cu2O	Na2O	TiO2	Total
Ave	21.12	5.11	48.03	9.78	0.69	1.43	11.94	0.025	0.089	0.067	0.38	0.29	98.94
s.d.	0.17	0.07	0.41	0.11	0.06	0.11	0.18	0.007	0.017	0.014	0.06	0.20	0.65

Table A37: Results (in mass %) of electron microprobe analysis of forty-one positions on the glass phase in sample WS1999 (2005). The average (Ave) and standard deviation (s.d.) of all results over the detection limit are shown. Detection limits are quoted in section 6.7 – in this table eighteen cobalt determinations are below the limit.

	MgO	Al2O3	SiO2	CaO	SO3	Cr2O3	FeO	CoO	NiO	Cu2O	Na2O	TiO2	Total
Ave	20.72	5.35	47.83	9.42	0.75	1.61	12.75	0.027	0.094	0.065	0.35	0.28	99.23
s.d.	0.15	0.09	0.38	0.11	0.08	0.15	0.16	0.005	0.024	0.020	0.04	0.14	0.53

Table A38: Results (in mass %) of electron microprobe analysis of forty-one positions on the glass phase in sample WS2007 (2005). The average (Ave) and standard deviation (s.d.) of all results over the detection limit are shown. Detection limits are quoted in section 6.7 – in this table eighteen cobalt determinations are below the limit.

	MgO	Al2O3	SiO2	CaO	SO3	Cr2O3	FeO	CoO	NiO	Cu2O	Na2O	TiO2	Total
Ave	20.75	5.24	48.47	7.77	0.66	1.62	13.69	0.035	0.106	0.079	0.38	0.31	99.09
s.d.	0.19	0.06	0.31	0.16	0.10	0.12	0.26	0.015	0.021	0.016	0.04	0.16	0.68

Table A39: Results (in mass %) of electron microprobe analysis of forty positions on the glass phase in sample WS2008 (2005). The average (Ave) and standard deviation (s.d.) of all results over the detection limit are shown. Detection limits are quoted in section 6.7 – in this table twenty-four cobalt determinations are below the limit.

	MgO	Al2O3	SiO2	CaO	SO3	Cr2O3	FeO	CoO	NiO	Cu2O	Na2O	TiO2	Total
Ave	20.40	5.17	47.58	9.60	0.60	1.31	13.17	0.030	0.100	0.063	0.38	0.27	98.66
s.d.	0.72	0.11	0.45	0.28	0.16	0.17	0.13	0.008	0.036	0.023	0.05	0.13	0.48

Table A40: Results (in mass %) of electron microprobe analysis of forty-five positions on the glass phase in sample WS2015 (2005). The average (Ave) and standard deviation (s.d.) of all results over the detection limit are shown. Detection limits are quoted in section 6.7 – in this table twenty-three cobalt determinations are below the limit.

	MgO	Al2O3	SiO2	CaO	SO3	Cr2O3	FeO	CoO	NiO	Cu2O	Na2O	TiO2	Total
Ave	20.12	5.14	48.01	9.07	0.69	1.47	14.01	0.028	0.102	0.066	0.34	0.29	99.34
s.d.	0.28	0.06	0.31	0.11	0.11	0.17	0.18	0.006	0.019	0.015	0.03	0.20	0.64

Table A41: Results (in mass %) of electron microprobe analysis of forty positions on the glass phase in sample WS2020 (2005). The average (Ave) and standard deviation (s.d.) of all results over the detection limit are shown. Detection limits are quoted in section 6.7 – in this table thirteen cobalt determinations are below the limit.

	MgO	Al2O3	SiO2	CaO	SO3	Cr2O3	FeO	CoO	NiO	Cu2O	Na2O	TiO2	Total
Ave	20.58	4.99	47.26	10.46	0.69	1.41	12.69	0.028	0.096	0.056	0.31	0.21	98.77
s.d.	0.18	0.07	0.28	0.12	0.09	0.16	0.15	0.005	0.025	0.016	0.05	0.10	0.49

Table A42: Results (in mass %) of electron microprobe analysis of forty-four positions on the glass phase in sample WS2025 (2005). The average (Ave) and standard deviation (s.d.) of all results over the detection limit are shown. Detection limits are quoted in section 6.7 – in this table thirty-three cobalt determinations are below the limit.

	MgO	Al2O3	SiO2	CaO	SO3	Cr2O3	FeO	CoO	NiO	Cu2O	Na2O	TiO2	Total
Ave	21.64	5.34	49.81	6.58	0.67	1.53	12.40	0.027	0.076	0.055	0.33	0.30	98.75
s.d.	0.19	0.04	0.30	0.08	0.07	0.11	0.22	0.005	0.014	0.009	0.04	0.13	0.49

Table A43: Results (in mass %) of electron microprobe analysis of twenty-two positions on the glass phase in sample WS1989 (2005), using long counts for cobalt. The average (Ave) and standard deviation (s.d.) of all results over the detection limit are shown. Detection limits are quoted in section 6.7 – in this table three cobalt determinations are still below the limit.

	MgO	Al2O3	SiO2	CaO	SO3	Cr2O3	FeO	CoO	NiO	Cu2O	Total
Ave	21.62	5.30	49.74	7.12	0.74	1.68	13.12	0.017	0.111	0.079	99.53
s.d.	0.27	0.05	0.26	0.31	0.20	0.12	0.23	0.005	0.037	0.033	0.83

Table A44: Results (in mass %) of electron microprobe analysis of twenty-one positions on the glass phase in sample WS1989 (2005), using long counts for cobalt. The average (Ave) and standard deviation (s.d.) of all results over the detection limit are shown. Detection limits are quoted in section 6.7 – in this table five cobalt determinations are still below the limit.

	MgO	Al2O3	SiO2	CaO	SO3	Cr2O3	FeO	CoO	NiO	Cu2O	Total
Ave	21.18	5.20	48.87	10.57	0.70	1.44	12.10	0.014	0.091	0.063	100.23
s.d.	0.22	0.05	0.28	0.45	0.13	0.15	0.16	0.003	0.029	0.024	0.69

Table A45: Results (in mass %) of electron microprobe analysis of twenty-one positions on the glass phase in sample WS1989 (2005), using long counts for cobalt. The average (Ave) and standard deviation (s.d.) of all results over the detection limit are shown. Detection limits are quoted in section 6.7 – in this table one cobalt determination is still below the limit.

	MgO	Al2O3	SiO2	CaO	SO3	Cr2O3	FeO	CoO	NiO	Cu2O	Total
Ave	20.65	4.93	47.87	10.85	0.79	1.37	12.86	0.016	0.118	0.069	99.53
s.d.	0.18	0.05	0.27	0.53	0.14	0.15	0.20	0.004	0.028	0.016	0.69

Table A46: Results (in mass %) of electron microprobe analysis of twenty-one positions on the glass phase in sample WS1989 (2005), using long counts for cobalt. The average (Ave) and standard deviation (s.d.) of all results over the detection limit are shown. Detection limits are quoted in section 6.7 – in this table five cobalt determinations are still below the limit.

	MgO	Al2O3	SiO2	CaO	SO3	Cr2O3	FeO	CoO	NiO	Cu2O	Total
Ave	21.65	5.39	50.15	7.06	0.73	1.47	12.72	0.014	0.075	0.052	99.31
s.d.	0.18	0.06	0.24	0.34	0.13	0.14	0.21	0.005	0.016	0.012	0.51

Table A47: Results (in mass %) of electron microprobe analysis of twenty spinel crystals in three of the 1999 slag samples (FS4, 5 and 8). The average (Ave) and standard deviation (s.d.) of all results over the detection limit are shown. Detection limits are quoted in section 6.7 – in this table three titanium determinations are below the limit.

	MgO	Al2O3	SiO2	Cr2O3	FeO	TiO2	MnO	CoO	NiO	Total
Ave	9.36	5.30	0.04	59.74	22.59	0.20	0.114	0.106	0.132	97.58
s.d.	1.63	2.00	0.03	2.53	2.81	0.04	0.037	0.051	0.030	0.91

Table A48: Results (in mass %) of electron microprobe analysis of twenty slag spinel crystals in two of the 2005 slag samples. In all cases copper was below detection limit – for this table, all determinations were above the detection limit. CaO and SiO_2 were picked up from the surrounding glass phase because the spinel crystals were so small. The average (Ave) and standard deviation (s.d.) of the results are shown.

WS1990	MgO	Al2O3	SiO2	CaO	SO3	Cr2O3	FeO	CoO	NiO	TiO2	Total
Ave	15.21	6.09	0.37	0.29	0.04	65.86	12.27	0.025	0.116	0.29	100.57
s.d.	0.13	0.46	0.33	0.12	0.06	2.11	0.58	0.006	0.017	0.34	0.88
WS2020	MgO	Al2O3	SiO2	CaO	SO3	Cr2O3	FeO	CoO	NiO	TiO2	
Ave	14.94	6.28	0.59	0.50	0.08	64.95	13.41	0.034	0.108	0.54	101.43
s.d.	0.49	0.35	0.57	0.26	0.06	2.08	0.85	0.005	0.035	0.64	1.53

Table A49: Results of averaged EDX analysis (in mass %) with confidence intervals per size class for entrained matte in two of the 1999 slag samples.

FS1	S	Co	Ni	Cu	Fe	Size class (µm)	No particles
	32.0+/-0.7	2.4+/-0.1	18.1+/-0.6	7.8+/-1.3	39.7+/-1.8	0 to 4.8	21
	34.1+/-0.2	2.4+/-0.1	19.7+/-1.1	6.2+/-0.8	37.7+/-1.5	4.8 to 13.4	17
	33.7+/-0.5	2.4+/-0.1	21.9+/-5.2	5.4+/-0.6	36.7+/-5.6	13.4 to 19	15
	33.8+/-0.3	2.4+/-0.1	18.8+/-0.8	6.3+/-0.9	38.7+/-1.4	19 to 26.9	17
	33.2+/-0.3	2.4+/-0.1	19.6+/-1.9	6.4+/-0.8	38.4+/-2.3	26.9 to 53	15
	32.0+/-0.7	2.4+/-0.1	16.3+/-1.9	7.6+/-1.0	41.6+/-2.1	53 to 300	17
FS6	S	Co	Ni	Cu	Fe	Size class (µm)	No particles
	33.0+/-2.4	1.1+/-0.1	19.4+/-4.5	9.1+/-1.6	37.5+/-3.8	0 to 4.8	14
	32.7+/-0.3	1.0+/-0.1	20.1+/-1.7	8.7+/-0.8	37.4+/-1.7	4.8 to 9.5	29
	32.5+/-0.5	1.1+/-0.1	21.8+/-2.0	9.4+/-1.5	35.2+/-2.8	9.5 to 19	21
	33.1+/-0.4	1.1+/-0.1	22.0+/-1.4	6.0+/-0.7	37.8+/-1.2	19 to 38	25
	32.4+/-0.6	1.1+/-0.1	21.8+/-1.8	7.6+/-1.1	37.1+/-2.2	38 to 212	15

Table A50: Results of averaged EDX analysis (in mass %) with confidence intervals per size class for entrained matte in two of the 2005 slag samples.

WS1989	S	Co	Ni	Cu	Fe	Size class (µm)	No. particles
	33.1+/-0.5	0.7+/-0.0	20.6+/-1.7	10.6+/-1.3	35.0+/-1.8	0 to 3.4	104
	33.4+/-0.7	0.7+/-0.1	20.2+/-2.1	10.9+/-1.7	34.9+/-2.1	3.4 to 4.8	112
	32.8+/-0.9	0.6+/-0.1	22.8+/-2.6	10.3+/-2.0	33.5+/-2.6	4.8 to 6.7	64
	32.5+/-0.5	0.7+/-0.1	22.4+/-1.6	10.4+/-1.0	34.0+/-1.7	6.7 to 9.5	61
	32.7+/-0.6	0.7+/-0.1	23.2+/-1.7	10.8+/-1.9	32.6+/-2.4	9.5 to 19	72
	33.0+/-0.7	0.7+/-0.1	25.2+/-3.8	10.0+/-2.3	31.0+/-3.7	19 to 38	41
	32.1+/-1.0	0.8+/-0.1	24.6+/-3.7	10.0+/-1.7	32.6+/-4.3	38 to 75	34
	31.0+/-0.6	0.8+/-0.1	21.8+/-1.8	10.4+/-1.0	36.0+/-2.2	75 to 600	40
WS2008	S	Co	Ni	Cu	Fe	Size class (µm)	No. particles
	32.0+/-0.5	0.7+/-0.1	23.7+/-1.4	11.1+/-0.8	32.5+/-1.3	0 to 3.4	100
	32.8+/-0.6	0.7+/-0.1	24.1+/-1.7	9.8+/-1.0	32.5+/-1.4	3.4 to 4.8	93
	32.1+/-1.0	0.7+/-0.1	23.3+/-1.6	11.3+/-1.7	32.6+/-1.6	4.8 to 6.7	59
	31.7+/-0.5	0.7+/-0.1	24.7+/-1.6	11.2+/-1.3	31.7+/-1.5	6.7 to 9.5	60
	32.0+/-0.8	0.8+/-0.1	24.9+/-1.8	10.9+/-1.8	31.3+/-2.1	9.5 to 13.4	50
	31.4+/-0.8	0.7+/-0.1	26.0+/-2.1	11.1+/-1.6	30.8+/-2.0	13.4 to 19	49
	31.2+/-0.6	0.8+/-0.1	24.6+/-1.2	11.2+/-1.3	32.2+/-1.5	19 to 26.9	64
	31.1+/-0.7	0.7+/-0.1	25.0+/-2.4	10.9+/-1.6	32.2+/-2.1	26.9 to 38	38
	30.3+/-0.9	0.8+/-0.1	23.7+/-2.2	11.3+/-1.3	34.0+/-2.1	38 to 53	31
	30.9+/-0.4	0.8+/-0.1	20.9+/-1.1	11.7+/-1.2	35.7+/-1.3	53 to 150	30

Table A51: Results of averaged EDX analysis (in mass %) with confidence intervals per size class for entrained matte in two of the 2005 slag samples. Here the SEM-EDX results have been combined with those of the MLA, so that information about large particles is also displayed. These values should not be used for a size distribution.

WS1989	S	Fe cor	Co	Ni	Cu	Size class (µm)	No. particles
	33.1+/-0.5	35.0+/-1.8	0.7+/-0.0	20.6+/-1.7	10.6+/-1.3	0 to 3.4	104
	33.4+/-0.7	34.9+/-2.1	0.7+/-0.1	20.2+/-2.1	10.9+/-1.7	3.4 to 4.8	112
	32.8+/-0.9	33.5+/-2.6	0.6+/-0.1	22.8+/-2.6	10.3+/-2.0	4.8 to 6.7	64
	32.5+/-0.5	34.0+/-1.7	0.7+/-0.1	22.4+/-1.6	10.4+/-1.0	6.7 to 9.5	61
	32.5+/-0.9	30.4+/-3.8	0.7+/-0.1	24.8+/-2.8	11.5+/-3.4	9.5 to 13.4	35
	32.9+/-0.7	34.7+/-3.1	0.8+/-0.1	21.6+/-2.1	10.1+/-2.0	13.4 to 19	37
	33.3+/-0.9	27.2+/-5.2	0.6+/-0.1	28.3+/-5.5	10.5+/-3.7	19 to 26.9	24
	32.6+/-1.2	36.4+/-4.4	0.8+/-0.1	20.9+/-4.9	9.3+/-2.5	26.9 to 38	17
	32.0+/-1.4	32.2+/-5.8	0.8+/-0.2	25.6+/-5.2	9.4+/-2.2	38 to 53	18
	32.4+/-0.8	32.8+/-2.9	0.6+/-0.1	23.8+/-2.4	10.4+/-1.3	53 to 75	35
	33.0+/-0.6	36.3+/-1.9	0.5+/-0.1	21.9+/-1.6	8.4+/-0.8	75 to 106	47
	32.3+/-0.7	37.7+/-1.2	0.5+/-0.1	20.9+/-1.1	8.6+/-0.8	106 to 150	33
	32.3+/-0.6	37.4+/-1.6	0.5+/-0.1	21.4+/-1.4	8.3+/-1.3	150 to 212	31
	32.6+/-0.7	38.6+/-1.5	0.5+/-0.1	19.9+/-1.5	8.4+/-1.0	212 to 300	19
	31.0+/-0.8	38.0+/-2.3	0.5+/-0.1	20.2+/-1.4	10.2+/-1.5	>300	17
WS2008	S	Fe cor	Co	Ni	Cu	Size class (µm)	No. particles
	32.0+/-0.5	32.5+/-1.3	0.7+/-0.1	23.7+/-1.4	11.1+/-0.8	0 to 3.4	100
	32.8+/-0.6	32.5+/-1.4	0.7+/-0.1	24.1+/-1.7	9.8+/-1.0	3.4 to 4.8	93
	32.1+/-1.0	32.6+/-1.6	0.7+/-0.1	23.3+/-1.6	11.3+/-1.7	4.8 to 6.7	59
	31.7+/-0.5	31.7+/-1.5	0.7+/-0.1	24.7+/-1.6	11.2+/-1.3	6.7 to 9.5	60
	32.0+/-0.8	31.3+/-2.1	0.8+/-0.1	24.9+/-1.8	10.9+/-1.8	9.5 to 13.4	50
	31.4+/-0.8	30.8+/-2.0	0.7+/-0.1	26.0+/-2.1	11.1+/-1.6	13.4 to 19	49
	31.2+/-0.6	32.2+/-1.5	0.8+/-0.1	24.6+/-1.2	11.2+/-1.3	19 to 26.9	64
	31.1+/-0.7	32.2+/-2.1	0.7+/-0.1	25.0+/-2.4	10.9+/-1.6	26.9 to 38	38
	30.3+/-0.9	34.0+/-2.1	0.8+/-0.1	23.7+/-2.2	11.3+/-1.3	38 to 53	31
	31.1+/-0.4	34.7+/-1.2	0.6+/-0.1	23.3+/-1.3	10.3+/-0.7	53 to 75	36
	31.4+/-0.3	35.4+/-0.7	0.5+/-0.1	22.2+/-0.5	10.6+/-0.6	75 to 106	70
	31.0+/-0.3	37.1+/-0.7	0.5+/-0.1	21.2+/-0.7	10.2+/-0.6	106 to 150	38
	31.1+/-0.4	37.5+/-0.9	0.4+/-0.1	20.4+/-0.8	10.5+/-1.0	150 to 212	33
	31.1+/-0.5	37.7+/-1.1	0.4+/-0.2	20.4+/-0.6	10.5+/-1.2	212 to 300	13
	31.5+/-0.7	40.5+/-1.5	0.5+/-0.2	18.1+/-0.6	9.4+/-1.2	300 to 500	9

Table A52: Results (in mass %) of electron microprobe area analysis profiles across pieces of SB1 2006 sounding bar sample. The totals are low due to casting and pores, and the averages have been normalized in Table 44 on page?.

Piece1	MgO	Al2O3	SiO2	CaO	SO3	Cr2O3	FeO	NiO	Cu2O	Total
inner	20.40	5.52	51.22	6.13	0.190	0.92	13.39	0.094	0.065	97.93
inner	21.34	5.14	50.54	5.67	0.188	3.39	13.28	0.119	0.084	99.75
inner	21.38	5.08	51.86	5.96	0.093	2.33	12.82	0.083	0.046	99.64
inner	21.18	5.11	50.80	5.89	0.270	1.13	13.14	0.141	0.100	97.77
inner	21.44	4.99	50.09	5.93	0.137	0.92	12.84	0.031	0.040	96.40
central	21.63	4.30	45.75	4.90	0.110	1.82	11.10	0.057	0.048	89.72
outer	21.14	5.15	47.45	5.84	0.260	1.73	12.39	0.085	0.069	94.13
Piece 2	MgO	Al2O3	SiO2	CaO	SO3	Cr2O3	FeO	NiO	Cu2O	Total
inner	20.61	5.64	50.32	5.92	0.294	1.62	12.58	0.106	0.074	97.17
inner	21.18	5.24	48.46	5.77	0.177	1.25	12.47	0.107	0.041	94.70
central	21.53	5.22	46.16	5.66	0.210	1.17	12.09	0.068	0.052	92.17
central	20.52	5.53	48.19	6.28	0.256	1.68	12.71	0.097	0.069	95.33
outer	19.46	5.30	44.87	6.32	0.249	1.60	12.84	0.086	0.061	90.78
Piece 3	MgO	Al2O3	SiO2	CaO	SO3	Cr2O3	FeO	NiO	Cu2O	Total
inner	20.96	5.13	49.50	5.86	0.262	1.66	12.97	0.163	0.102	96.60
inner	20.99	5.03	49.55	5.80	0.362	1.30	12.92	0.142	0.072	96.15
inner	21.15	5.00	49.01	5.90	0.268	1.53	13.27	0.133	0.086	96.33
inner	21.32	5.07	49.83	5.86	0.325	2.78	12.55	0.132	0.090	97.95
outer	20.56	5.13	48.77	6.03	0.322	0.78	12.91	0.159	0.092	94.76

Table A53: Results (in mass %) of electron microprobe area analysis profiles across pieces of SB10 2006 sounding bar sample. The totals are low due to casting and pores, and the averages have been normalized in Table 44 on page?.

Piece 1	MgO	Al2O3	SiO2	CaO	SO3	Cr2O3	FeO	NiO	Cu2O	Total
inner	20.27	4.84	47.61	5.97	0.362	1.36	12.98	0.126	0.089	93.61
central	20.04	5.27	47.36	6.29	0.093	1.51	13.37	0.138	0.092	94.16
central	20.59	5.12	48.59	6.00	0.392	1.53	12.96	0.150	0.083	95.41
central	20.81	5.10	46.99	6.08	0.507	1.38	13.19	0.146	0.308	94.51
outer	20.80	5.10	48.14	6.11	0.345	1.51	12.70	0.144	0.102	94.95
outer	20.39	5.20	48.40	6.21	0.308	1.37	12.62	0.166	0.092	94.76
Piece 2	MgO	Al2O3	SiO2	CaO	SO3	Cr2O3	FeO	NiO	Cu2O	Total
inner	20.21	5.19	46.77	6.10	0.329	1.28	12.60	0.111	0.086	92.67
inner	19.10	4.90	42.48	5.98	0.331	2.12	12.17	0.092	0.092	87.26
central	20.32	4.95	43.12	5.63	0.272	1.18	12.02	0.110	0.125	87.73
central	19.06	5.01	43.29	6.00	0.371	0.61	12.60	0.116	0.076	87.13
central	19.71	5.07	42.43	5.78	0.239	1.24	11.42	0.067	0.086	86.05
central	18.68	5.18	40.21	5.94	0.212	1.48	11.68	0.011	0.055	83.44
outer	20.62	5.00	47.79	5.98	0.239	1.57	12.74	0.116	0.096	94.14
outer	20.10	4.98	45.33	6.01	0.203	1.44	13.22	0.157	0.083	91.53

Table A54: Results (in mass %) of electron microprobe area analysis profiles across pieces of SB15 2006 sounding bar sample. The totals are low due to casting and pores, and the averages have been normalized in Table 44 on page?.

Piece 1	MgO	Al2O3	SiO2	CaO	SO3	Cr2O3	FeO	NiO	Cu2O	Total
inner	20.12	4.93	46.81	6.08	0.224	1.28	12.51	0.151	0.073	92.18
inner	20.43	5.23	47.58	5.96	0.178	1.44	12.71	0.017	0.059	93.59
inner	20.18	4.84	46.87	5.94	0.257	1.29	12.84	0.025	0.079	92.32
inner	20.11	5.14	47.53	6.19	0.277	1.18	12.75	0.160	0.124	93.44
inner	19.75	5.02	47.02	6.11	0.503	1.27	12.98	0.281	0.171	93.11
inner	20.13	5.23	47.49	6.17	0.290	1.22	13.11	0.084	0.062	93.78
inner	19.48	5.26	47.03	6.28	0.502	1.59	13.65	0.116	0.183	94.08
central	20.74	4.97	47.29	5.94	0.447	1.54	13.24	0.245	0.167	94.59
central	20.18	5.19	47.13	6.40	0.033	0.66	13.50	0.084	0.090	93.26
central	19.96	5.18	46.67	6.37	0.436	1.81	13.36	0.092	0.093	93.97
central	20.42	5.12	47.04	6.03	0.293	1.05	12.81	0.083	0.051	92.90
central	19.85	5.10	47.22	6.73	0.378	1.50	13.84	0.058	0.057	94.75
central	21.52	5.03	47.67	5.71	0.367	1.58	12.74	0.139	0.093	94.85
central	21.11	4.84	47.48	5.97	0.182	1.12	12.60	0.064	0.033	93.41
central	19.08	6.07	47.00	6.94	0.119	1.28	13.45	0.094	0.050	94.08
central	23.15	4.52	48.39	5.01	0.159	1.86	11.25	0.057	0.033	94.42
central	17.43	6.67	46.64	6.97	0.000	0.69	13.45	0.064	0.055	91.97
central	19.41	5.70	46.99	6.31	0.231	1.38	12.92	0.101	0.035	93.08
central	21.27	4.72	47.72	5.63	0.000	0.99	12.15	0.135	0.033	92.65
central	20.33	4.84	46.48	6.23	0.166	0.86	12.79	0.045	0.108	91.86
outer	19.90	5.01	46.97	6.14	0.318	1.91	12.67	0.132	0.116	93.17
outer	20.26	5.16	47.81	6.06	0.259	1.34	12.90	0.257	0.076	94.12
outer	20.62	4.95	47.93	6.09	0.649	1.62	12.89	0.220	0.100	95.08
outer	21.05	5.02	48.08	6.01	0.269	1.78	13.11	0.072	0.053	95.45
outer	20.62	5.01	48.08	6.02	0.284	1.59	12.72	0.127	0.089	94.54
outer	20.47	5.00	47.76	5.96	0.395	1.79	12.80	0.238	0.126	94.54
outer	20.77	4.96	47.70	5.94	0.534	2.33	12.47	0.121	0.126	94.94

Table A54 (cont.)

Piece 2	MgO	Al2O3	SiO2	CaO	SO3	Cr2O3	FeO	NiO	Cu2O	Total
inner	20.54	5.02	47.25	6.07	0.431	1.32	12.80	0.247	0.096	93.77
inner	20.65	4.96	48.40	6.00	0.319	1.08	12.66	0.168	0.095	94.33
inner	21.02	5.09	49.06	6.03	0.077	1.56	12.88	0.119	0.084	95.91
inner	20.66	5.06	48.38	6.09	0.196	1.46	12.55	0.138	0.067	94.60
inner	21.02	4.92	48.60	5.61	0.392	1.54	12.84	0.126	0.064	95.10
inner	20.59	5.19	47.81	6.03	0.435	1.94	12.72	0.180	0.086	94.99
inner	20.26	5.16	47.76	6.28	0.272	1.30	12.83	0.110	0.057	94.02
inner	20.62	5.20	48.48	6.09	0.307	1.44	12.92	0.117	0.091	95.26
central	20.41	5.45	48.05	6.10	0.425	1.29	13.04	0.101	0.081	94.94
central	20.59	5.39	48.32	6.25	0.309	1.02	13.04	0.114	0.060	95.09
central	20.18	5.55	47.96	6.17	0.216	1.15	12.95	0.072	0.056	94.35
	edge under sample holder									
Piece 3	MgO	Al2O3	SiO2	CaO	SO3	Cr2O3	FeO	NiO	Cu2O	Total
inner	22.27	4.98	51.63	5.42	0.100	1.67	11.69	0.012	0.063	97.83
inner	21.82	5.34	50.91	5.60	0.303	1.47	12.19	0.012	0.041	97.69
inner	20.98	5.30	50.48	6.32	0.292	1.78	12.94	0.063	0.069	98.22
inner	22.62	5.10	51.31	5.54	0.080	1.74	11.91	0.083	0.037	98.42
centre	22.26	4.77	51.10	5.60	0.130	1.98	12.13	0.017	0.029	98.00
centre	20.75	5.34	51.57	5.96	0.199	1.66	12.32	0.055	0.042	97.89
outer	20.46	5.55	50.12	6.46	0.139	0.87	12.72	0.038	0.082	96.43
outer	20.82	5.27	50.66	6.15	0.189	1.27	12.73	0.062	0.062	97.20
outer	21.12	5.13	50.87	6.06	0.179	1.65	13.12	0.065	0.052	98.25
outer	21.06	5.07	50.96	6.05	0.199	1.50	12.86	0.077	0.080	97.86

Table A55: Results of averaged area EDX analysis (in mass %) on entrained matte in three of the 2006 sounding bar samples. Standard deviations (st dev) are also tabulated.

		S	Fe	Ni	Cu
SB 1	Average	30.8	43.0	18.8	7.4
	s.d.	2.4	4.5	4.9	5.3
SB10	Average	31.5	40.0	19.3	9.3
1	s.d.	2.8	4.8	4.0	4.7
	Average	31.9	42.5	18.5	7.1
2	s.d.	2.2	5.5	4.8	4.7
SB 15	Average	30.5	43.9	17.9	7.8
1	s.d.	2.3	7.6	7.2	8.8
2	Average	31.0	43.5	16.1	9.4
	s.d.	2.4	9.9	5.9	9.2

Table A56: Results of averaged area EDX analysis (in mass %) on entrained matte in three of the 2007 sounding bar samples. Standard deviation (s.d.) and confidence intervals (c.i.) are also tabulated.

		S	Fe	Ni	Cu	Co
SB5	Average	29.2	35.5	27.7	7.3	0.5
	s.d.	2.2	2.6	4.7	3.1	0.3
	c.i.	0.6	0.7	1.3	0.8	0.1
SB3	Average	30.9	38.9	20.1	9.7	0.4
	s.d.	1.4	3.6	4.0	4.7	0.2
	c.i.	0.4	1.0	1.1	1.3	0.1
SB1	Average	31.1	41.4	18.8	8.3	0.4
	st dev	1.2	3.8	3.8	2.8	0.2
	c.i.	0.2	0.7	0.7	0.5	0.0

Table A57: Results of chemical analysis of the September 2005 flash drier product (concentrate) samples, in mass %.

Sample	MgO	Al_2O_3	SiO_2	CaO	TiO_2	Cr_2O_3	Fe	Co	Ni	Cu	S
WS2088	17.6	4.26	40.8	3.77	0.23	1.96	14.5	0.11	1.97	1.15	4.59
WS2089	18.0	4.47	41.0	3.78	0.22	1.95	13.8	0.10	2.06	1.19	4.61
Average	17.8	4.37	40.90	3.78	0.23	1.96	14.15	0.11	2.02	1.17	4.60

Table A58: Results of microprobe analysis of thirty positions on pyrrhotite-troilite in the September 2005 flash drier product (concentrate) samples, in mass %. The average (Ave) and standard deviation (s.d.) of the results are shown. For this table, all copper determinations below the detection limit were set at zero. The copper values are very sporadic, and may represent sub micron-sized inclusions.

	S	Fe	Cu	Ni	Total
Ave	39.98	60.45	0.020	0.428	100.89
s.d.	1.07	1.25	0.030	0.461	0.64

Table A59: Results of microprobe analysis of fifty positions on pentlandite in the September 2005 flash drier product (concentrate) samples, in mass %. The average (Ave) and standard deviation (s.d.) of the results are shown. For this table, all determinations were above the detection limit.

	S	Fe	Co	Ni	Total
Ave	34.54	31.34	0.560	33.28	99.72
s.d.	0.61	1.70	0.226	1.79	1.06

Table A60: Results of microprobe analysis of forty positions on chalcopyrite in the September 2005 flash drier product (concentrate) samples, in mass %. The average (Ave) and standard deviation (s.d.) of the results are shown. For this table, all determinations were above the detection limit.

	S	Fe	Cu	Total
Ave	36.19	30.37	33.84	100.40
s.d.	0.49	0.34	0.68	0.95

Table A61: Results of microprobe analysis of twenty positions on pyrite in the September 2005 flash drier product (concentrate) samples, in mass %. The results are normalised, and average (Ave) and standard deviation (s.d.) of the results are shown. For this table, all cobalt, copper and nickel determinations below the detection limit were set at zero. The copper, cobalt and nickel values are very sporadic, and may represent sub micron-sized inclusions.

	S	Fe	Co	Cu	Ni
Ave	54.20	45.21	0.516	0.027	0.046
s.d.	0.63	0.74	0.534	0.027	0.062

Table A62: Results of chemical analysis of the converter slag used as SCF feed in September 2005, in mass %.

Sample	MgO	Al_2O_3	SiO_2	CaO	TiO_2	Cr_2O_3	Fe	Co	Ni	Cu	S
WS2099	0.43	1.47	25.1	0.24	0.08	1.89	48.1	0.58	4.03	1.66	1.19
WS2100	0.98	1.30	25.9	0.33	0.10	1.91	47.7	0.56	3.46	1.44	1.12
WS2101	0.44	1.95	25.4	0.37	0.11	1.74	48.1	0.48	3.78	1.55	0.92
WS2102	0.41	1.01	24.6	0.24	0.08	2.00	48.6	0.60	4.11	1.65	1.24
WS2103	0.42	1.03	24.6	0.24	0.08	1.99	48.9	0.60	4.09	1.63	1.24
WS2104	0.87	2.36	26.3	0.36	0.12	1.67	47.1	0.57	3.21	1.37	0.80
WS2105	0.65	1.25	25.3	0.27	0.08	1.79	47.8	0.53	4.02	1.70	1.16
WS2106	0.70	1.31	26.7	0.32	0.08	1.88	47.3	0.49	3.35	1.48	1.04
Average	0.61	1.46	25.49	0.30	0.09	1.86	47.95	0.55	3.76	3.10	1.09

Table A63: Results (in mass %) of electron microprobe analysis of twenty positions on the glass phase in converter slag sample WS2100 (2005). The average (Ave) and standard deviation (s.d.) of the results are shown. For this table, all determinations were above the detection limit, but titanium is not reported as it was not present over detection limit in any of the determinations.

	MgO	Al2O3	SiO2	CaO	SO3	Cr2O3	FeO	CoO	NiO	Cu2O	Total
Ave	0.62	1.26	28.53	0.26	0.66	0.17	64.52	0.681	2.233	0.689	99.63
s.d.	0.12	0.15	0.86	0.03	0.38	0.16	1.16	0.063	0.783	0.273	0.98

Table A64: Results (in mass %) of electron microprobe analysis of twenty positions on the glass phase in converter slag sample WS2103 (2005). The average (Ave) and standard deviation (s.d.) of the results are shown. For this table, all determinations were above the detection limit, but titanium is not reported, as it was not present over detection limit in any of the determinations.

	MgO	Al2O3	SiO2	CaO	SO3	Cr2O3	FeO	CoO	NiO	Cu2O	Total
Ave	0.50	1.15	29.72	0.27	0.41	0.14	63.85	0.726	2.222	0.597	99.57
s.d.	0.10	0.19	1.55	0.02	0.21	0.11	1.35	0.040	0.331	0.334	0.75

Table A65: Results (in mass %) of electron microprobe analysis of ten spinel crystals in converter slag sample WS2100 (2005). The average (Ave) and standard deviation (s.d.) of all results over the detection limit are shown. Detection limits are quoted in section 6.7 – in this table nine (WS2100) and five (WS2103) titanium determinations are below the limit.

WS2100	MgO	Al2O3	SiO2	Cr2O3	FeO	TiO2	CoO	NiO	Cu2O	Total
Ave	0.76	0.02	0.08	65.63	30.90	0.15	0.778	1.688	0.044	99.91
s.d.	1.39	0.04	0.07	1.19	2.15		0.170	0.564	0.024	0.96
WS2103	MgO	Al2O3	SiO2	Cr2O3	FeO	TiO2	CoO	NiO	Cu2O	Total
Ave	0.38	0.02	0.12	65.10	31.37	0.22	0.750	1.632	0.095	99.57
s.d.	0.22	0.02	0.16	1.47	0.50	0.09	0.16	0.42	0.07	0.97

Table A66: Results (in mass %) of electron microprobe analysis of twenty magnetite crystals in converter slag sample WS2100 (2005). The average (Ave) and standard deviation (s.d.) of all results over the detection limit are shown. Detection limits are quoted in section 6.7 – in this table ten titanium and nine copper determinations are below the limit. The total mass % is low because some of the iron is present as Fe_2O_3.

	MgO	Al2O3	SiO2	Cr2O3	FeO	TiO2	CoO	NiO	Cu2O	Total
Ave	0.24	2.16	0.45	16.18	68.07	0.21	0.671	5.187	0.049	93.08
s.d.	0.07	0.81	0.10	4.02	3.60	0.05	0.032	1.190	0.030	0.74

Table A67: Results (in mass %) of electron microprobe analysis of twenty-two magnetite crystals in converter slag sample WS2103 (2005). The average (Ave) and standard deviation (s.d.) of all results over the detection limit are shown. Detection limits are quoted in section 6.7 – in this table eleven titanium and thirteen copper determinations are below the limit. The total mass % is low because some of the iron is present as Fe_2O_3.

	MgO	Al2O3	SiO2	Cr2O3	FeO	TiO2	CoO	NiO	Cu2O	Total
Ave	0.14	1.68	0.55	12.98	71.98	0.16	0.682	5.719	0.039	93.83
s.d.	0.04	0.29	0.10	2.33	2.14	0.02	0.032	0.273	0.011	0.87

Table A68: Results of EDX analysis (in mass %) of twenty entrained matte phases in the converter slag samples (2005). The average (Ave) and standard deviation (s.d.) of the results are shown.

WS2100	S	Fe	Ni	Cu
Ave	24.2	4.4	46.5	25.0
s.d.	0.5	1.1	0.9	1.3
WS2103	S	Fe	Ni	Cu
Ave	24.1	4.2	46.7	25.1
s.d.	0.3	0.2	0.7	0.8

Table A69: Results, in mass %, of chemical analysis of the 2005 SCF matte spoon samples.

Sample	MgO	Al_2O_3	SiO_2	CaO	Cr_2O_3	Fe	Co	Ni	Cu	S
WS2108	<0.05	2.62	0.60	0.13	0.06	28.7	1.70	32.2	12.4	19.5
WS2110	0.14	3.62	1.15	0.14	0.18	28.4	1.66	31.2	12.2	19.4
WS2111	<0.05	0.24	0.36	0.14	0.05	29.6	1.77	32.8	12.8	20.7
WS2112	1.25	0.79	6.01	0.36	1.18	30.6	1.46	26.9	10.5	17.8
WS2113	<0.05	0.31	0.32	0.11	0.05	29.9	1.81	33.1	12.6	20.5
WS2115	<0.05	2.60	0.80	0.10	0.13	27.9	1.63	32.2	12.5	20.2
WS2116	0.08	0.42	0.54	0.09	0.08	29.6	1.68	32.4	12.6	20.6
WS2120	<0.05	0.38	0.33	0.16	0.05	28.2	1.63	32.0	13.8	21.3
Average	0.18	1.37	1.26	0.15	0.22	29.1	1.67	31.6	12.4	20.0

Nd = not determined.

Table A70: Results of chemical analysis of the SCF slag samples in mass %.

Sample	MgO	Al_2O_3	SiO_2	CaO	TiO_2	Cr_2O_3	Fe	Co	Ni	Cu	S
WS2090	6.96	2.94	33.8	1.76	0.15	2.03	38.1	0.29	0.91	0.57	0.74
WS2091	8.86	3.05	36.5	2.18	0.15	2.06	34.7	0.23	0.48	0.36	0.64
WS2092	7.75	3.10	35.3	1.88	0.15	2.05	37.1	0.25	0.58	0.44	0.71
WS2093	7.85	3.18	35.2	1.92	0.16	2.02	36.7	0.26	0.56	0.46	0.70
WS2094	8.42	3.00	36.1	2.07	0.16	2.03	35.6	0.25	0.62	0.41	0.65
WS2095	8.52	2.82	35.8	2.08	0.16	2.18	35.3	0.26	0.68	0.46	0.67
WS2096	8.18	2.98	35.8	1.90	0.15	1.82	36.5	0.27	0.65	0.43	0.70
WS2097	6.91	2.51	33.8	1.62	0.14	2.29	38.0	0.31	1.28	0.72	0.84
WS2098	8.29	2.83	35.8	1.95	0.16	2.25	35.9	0.25	0.61	0.46	0.69
Average	7.97	2.93	35.34	1.93	0.15	2.08	36.43	0.26	0.71	0.48	0.70

Table A71: Results (in mass %) of electron microprobe analysis of twenty-seven positions on the glass phase in SCF slag sample WS2090. The average (Ave) and standard deviation (s.d.) of all results over the detection limit are shown. Detection limits are quoted in section 6.7 – in this table fourteen titanium determinations are below the limit.

	MgO	Al2O3	SiO2	CaO	SO3	Cr2O3	FeO	TiO2	CoO	NiO	Cu2O	Total
Ave	8.28	3.12	37.02	1.99	1.36	0.81	45.77	0.16	0.296	0.326	0.309	99.35
s.d.	0.26	0.07	0.52	0.04	0.33	0.41	0.46	0.03	0.021	0.121	0.101	0.67

Table A72: Results (in mass %) of electron microprobe analysis of twenty-one positions on the glass phase in SCF slag sample WS2091. The average (Ave) and standard deviation (s.d.) of all results over the detection limit are shown. Detection limits are quoted in section 6.7 – in this table seven titanium determinations are below the limit.

	MgO	Al2O3	SiO2	CaO	SO3	Cr2O3	FeO	TiO2	CoO	NiO	Cu2O	Total
Ave	9.65	3.11	38.23	2.27	1.06	0.85	43.33	0.17	0.263	0.264	0.244	99.38
s.d.	0.23	0.05	0.59	0.13	0.20	0.41	0.46	0.02	0.021	0.133	0.082	0.74

Table A73: Results (in mass %) of electron microprobe analysis of twenty-two positions on the glass phase in SCF slag sample WS2092. The average (Ave) and standard deviation (s.d.) of all results over the detection limit are shown. Detection limits are quoted in section 6.7 – in this table four titanium determinations are below the limit.

	MgO	Al2O3	SiO2	CaO	SO3	Cr2O3	FeO	TiO2	CoO	NiO	Cu2O	Total
Ave	8.60	3.22	37.05	2.04	1.42	0.83	45.31	0.17	0.284	0.248	0.244	99.38
s.d.	0.16	0.07	0.56	0.08	0.17	0.40	0.41	0.03	0.023	0.108	0.078	0.54

Table A74: Results (in mass %) of electron microprobe analysis of twenty-two positions on the glass phase in SCF slag sample WS2095. The average (Ave) and standard deviation (s.d.) of all results over the detection limit are shown. Detection limits are quoted in section 6.7 – in this table eleven titanium determinations are below the limit.

	MgO	Al2O3	SiO2	CaO	SO3	Cr2O3	FeO	TiO2	CoO	NiO	Cu2O	Total
Ave	9.18	2.98	37.68	2.19	0.87	0.72	45.01	0.17	0.299	0.339	0.255	99.61
s.d.	0.38	0.11	0.81	0.13	0.14	0.36	0.82	0.02	0.023	0.136	0.109	0.80

Table A75: Results (in mass %) of electron microprobe analysis of twenty-three positions on the glass phase in SCF slag sample WS2096. The average (Ave) and standard deviation (s.d.) of all results over the detection limit are shown. Detection limits are quoted in section 6.7 – in this table fourteen titanium determinations are below the limit.

	MgO	Al2O3	SiO2	CaO	SO3	Cr2O3	FeO	TiO2	CoO	NiO	Cu2O	Total
Ave	9.01	2.98	37.31	1.96	1.26	0.80	45.20	0.17	0.317	0.349	0.260	99.51
s.d.	0.35	0.08	0.80	0.14	0.23	0.36	0.94	0.03	0.028	0.130	0.071	0.80

Table A76: Results (in mass %) of electron microprobe analysis of twenty-four positions on the glass phase in SCF slag sample WS2098. The average (Ave) and standard deviation (s.d.) of all results over the detection limit are shown. Detection limits are quoted in section 6.7 – in this table seven titanium determinations are below the limit.

	MgO	Al2O3	SiO2	CaO	SO3	Cr2O3	FeO	TiO2	CoO	NiO	Cu2O	Total
Ave	9.45	3.08	37.77	2.15	1.50	1.22	43.21	0.17	0.265	0.283	0.300	99.34
s.d.	0.22	0.06	0.71	0.06	0.23	0.50	0.51	0.03	0.022	0.100	0.070	0.83

Table A77: Results (in mass %) of electron microprobe analysis of ten spinel crystals in SCF slag sample WS2090. The average (Ave) and standard deviation (s.d.) of all results over the detection limit are shown. Detection limits are quoted in section 6.7 – in this table four titanium and four copper determinations are below the limit.

	MgO	Al2O3	SiO2	Cr2O3	FeO	TiO2	CoO	NiO	Cu2O	Total
Ave	3.54	2.27	0.11	61.41	30.63	0.21	0.438	0.391	0.036	98.93
s.d.	1.45	2.38	0.07	5.09	2.14	0.06	0.139	0.118	0.012	0.54

Table A78: Results (in mass %) of electron microprobe analysis of ten spinel crystals in SCF slag sample WS2091. The average (Ave) and standard deviation (s.d.) of all results over the detection limit are shown. Detection limits are quoted in section 6.7 – in this table four titanium and eight copper determinations are below the limit.

	MgO	Al2O3	SiO2	Cr2O3	FeO	TiO2	CoO	NiO	Cu2O	Total
Ave	4.32	3.84	0.15	57.96	32.18	0.21	0.357	0.453	0.045	99.40
s.d.	1.61	1.67	0.08	4.42	2.07	0.07	0.197	0.322	0.013	0.98

Table A79: Results (in mass %) of electron microprobe analysis of ten spinel crystals in SCF slag sample WS2092. The average (Ave) and standard deviation (s.d.) of all results over the detection limit are shown. Detection limits are quoted in section 6.7 – in this table two titanium and seven copper determinations are below the limit.

	MgO	Al2O3	SiO2	Cr2O3	FeO	TiO2	CoO	NiO	Cu2O	Total
Ave	4.77	4.46	0.18	58.03	30.86	0.21	0.287	0.300	0.115	99.08
s.d.	0.40	0.40	0.12	1.68	1.29	0.09	0.027	0.101	0.157	0.95

Table A80: Results (in mass %) of electron microprobe analysis of ten spinel crystals in SCF slag sample WS2095. The average (Ave) and standard deviation (s.d.) of all results over the detection limit are shown. Detection limits are quoted in section 6.7 – in this table two titanium and seven copper determinations are below the limit.

	MgO	Al2O3	SiO2	Cr2O3	FeO	TiO2	CoO	NiO	Cu2O	Total
Ave	4.91	4.08	0.15	59.80	29.69	0.18	0.270	0.224	0.027	99.27
s.d.	0.49	0.86	0.04	1.24	0.91	0.05	0.021	0.104	0.005	0.53

Table A81: Results (in mass %) of electron microprobe analysis of ten spinel crystals in SCF slag sample WS2096. The average (Ave) and standard deviation (s.d.) of all results over the detection limit are shown. Detection limits are quoted in section 6.7 – in this table six titanium and six copper determinations are below the limit.

WS2096	MgO	Al2O3	SiO2	Cr2O3	FeO	TiO2	CoO	NiO	Cu2O	Total
Ave	4.96	3.33	0.19	59.99	30.01	0.19	0.300	0.346	0.042	99.22
s.d.	0.41	1.43	0.14	2.11	0.93	0.09	0.029	0.125	0.024	0.74

Table A82: Results (in mass %) of electron microprobe analysis of ten spinel crystals in SCF slag sample WS2098. The average (Ave) and standard deviation (s.d.) of all results over the detection limit are shown. Detection limits are quoted in section 6.7 – in this table three titanium and seven copper determinations are below the limit.

	MgO	Al2O3	SiO2	Cr2O3	FeO	TiO2	CoO	NiO	Cu2O	Total
Ave	4.77	3.38	0.15	59.81	30.11	0.17	0.302	0.258	0.015	98.96
s.d.	0.90	1.81	0.08	2.85	1.11	0.08	0.067	0.043	0.016	0.91

Table A83: Results of averaged EDX analysis (in mass %), with standard deviations, for >7 µm entrained matte in the SCF slag sample MLA analyses. Size class compositions could not be established for these samples.

		S	Fe	Co	Ni	Cu
WS2091	Average	24.3	17.0	2.0	41.9	14.8
	s.d.	6.4	5.0	0.7	9.1	12.0
WS2098	Average	26.2	17.7	1.8	38.9	15.4
	s.d.	5.2	6.3	0.5	8.2	11.4

Table A84: Results of Mossbauer analysis of the 1999 slag samples, and the Fe^{3+}/Fe^{2+} ratios.

Sample	*Component*	IS mms^{-1} (±0.02)	QS mms^{-1} (±0.02)	Relative intensity (%)
FS1 slag	Doublet 1 Fe^{2+}	1.01	1.91	60±3
	Doublet 2 Fe^{2+}	1.22	2.28	25±4
	Doublet 3 Fe^{2+}	0.98	2.48	6±1
	Doublet 4 Fe^{3+}	0.16	-0.47	9±2
FS3 slag	Doublet 1 Fe^{2+}	1.01	1.87	83±3
	Doublet 2 Fe^{2+}	1.29	2.72	6±1
	Doublet 3 Fe^{3+}	0.15	-0.47	11±3
FS6 slag	Doublet 1 Fe^{2+}	0.97	1.85	50±3
	Doublet 2 Fe^{2+}	1.21	2.34	25±3
	Doublet 3 Fe^{2+}	0.98	2.48	15±3
	Doublet 4 Fe^{3+}	0.16	-0.47	10±2
FS8 slag	Doublet 1 Fe^{2+}	0.99	1.96	77±3
	Doublet 2 Fe^{2+}	1.20	2.32	12±3
	Doublet 3 Fe^{3+}	0.16	-0.47	11±3

Note: IS = Isomer shift relative to α-Fe, QS = Quadrupole splitting, H = Hyperfine magnetic field strength

Table A85: Results of Mossbauer analysis of the 2005 slag samples, and the Fe^{3+}/Fe^{2+} ratios.

Sample	*Component*	IS mms^{-1} (±0.02)	QS mms^{-1} (±0.02)	Relative intensity (%)
WS1989	Doublet 1 Fe^{2+}	1.12	1.98	57±3
	Doublet 2 Fe^{2+}	0.84	1.82	39±3
	Doublet 3 Fe^{3+}	0.11	-0.54	4±1
WS1990	Doublet 1 Fe^{2+}	1.07	2.22	40±2
	Doublet 2 Fe^{2+}	0.97	1.69	57±2
	Doublet 3 Fe^{3+}	0.05	-0.52	3±1
WS1999	Doublet 1 Fe^{2+}	1.12	2.03	41±2
	Doublet 2 Fe^{2+}	0.90	1.81	54±2
	Doublet 3 Fe^{3+}	0.11	-0.56	5±1
WS2007	Doublet 1 Fe^{2+}	1.09	1.99	63±3
	Doublet 2 Fe^{2+}	0.83	1.79	34±2
	Doublet 3 Fe^{3+}	0.06	-0.57	3±1
WS2008	Doublet 1 Fe^{2+}	1.12	1.98	52±3
	Doublet 2 Fe^{2+}	0.85	1.81	44±3
	Doublet 3 Fe^{3+}	0.09	-0.58	4±1
WS2015	Doublet 1 Fe^{2+}	1.13	2.04	48±4
	Doublet 2 Fe^{2+}	0.88	1.82	49±4
	Doublet 3 Fe^{3+}	0.06	-0.61	3±1
WS2020	Doublet 1 Fe^{2+}	1.11	1.99	61±4
	Doublet 2 Fe^{2+}	0.83	1.78	36±3
	Doublet 3 Fe^{3+}	0.05	-0.60	3±1
WS2025	Doublet 1 Fe^{2+}	1.14	2.00	50±4
	Doublet 2 Fe^{2+}	0.86	1.83	47±2
	Doublet 3 Fe^{3+}	0.07	-0.56	3±1

Note: IS = Isomer shift relative to α-Fe, QS = Quadrupole splitting
H = Hyperfine magnetic field strength

Table A86: Results of Mossbauer analysis of the 2005 SCF slag samples, and the Fe^{3+}/Fe^{2+} ratios.

Sample	*Component*	IS mms^{-1} (±0.02)	QS mms^{-1} (±0.02)	H Tesla (±0.3)	Relative intensity (%)
WS2100	Doublet 1 Fe^{2+}	1.13	2.75		67±1
WACS feed	Sextet 1	0.63	-0.27	43.6	12±1
	Sextet 2	0.28	0.07	47.3	21±2
WS2103	Doublet 1 Fe^{2+}	1.11	2.73		66±1
WACS feed	Sextet 1	1.14	-0.61	44.4	12±1
	Sextet 2	0.23	-0.15	46.9	22±2
WS2090	Doublet 1 Fe^{2+}	1.03	1.47		28±3
SCF slag	Doublet 2 Fe^{2+}	1.15	2.83		34±3
	Doublet 3 Fe^{2+}	1.09	2.12		36±4
	Doublet 4 Fe^{3+}	0.16	-0.47		2±1
WS2091	Doublet 1 Fe^{2+}	1.02	1.78		68±3
SCF slag	Doublet 2 Fe^{2+}	1.19	2.65		24±3
	Doublet 3 Fe^{2+}	0.94	2.53		6±3
	Doublet 4 Fe^{3+}	0.16	-0.47		2±1

Note: IS = Isomer shift relative to α-Fe, QS = Quadrupole splitting
H = Hyperfine magnetic field strength

Table A87: Base metal and sulphur distributions between matte and slag glass predicted on the 1999 six-in-line samples using FactSage, as compared to measured. L_{BM} = base metal in slag / base metal in matte.

Furnace 1	LCo actual	LCo predicted			Furnace 2	LCo actual	LCo predicted		
	Temperature °C	1550	1400	1300		Temperature °C	1550	1400	1300
FS1	0.1033	0.0281	0.0243	0.0219	FS6	0.1036	0.0329	0.0282	0.0253
FS2	0.1673	0.0254	0.0216	0.0193	FS7	0.1484	0.0285	0.0244	0.0219
FS3	0.1359	0.0244	0.0210	0.0189	FS8	0.1193	0.0250	0.0210	0.0186
Average	**0.1355**	**0.0260**	**0.0223**	**0.0200**	FS9	0.1054	0.0276	0.0237	0.0213
FS4	no matte analysis recorded				**Average**	**0.1192**	**0.0285**	**0.0243**	**0.0218**
FS5	no matte analysis recorded					LNi actual	LNi predicted		
	LNi actual	LNi predicted				Temperature °C	1550	1400	1300
	Temperature °C	1550	1400	1300	FS6	0.0063	0.0015	0.0011	0.0008
FS1	0.0059	0.0013	0.0009	0.0007	FS7	0.0073	0.0013	0.0009	0.0007
FS2	0.0065	0.0012	0.0008	0.0006	FS8	0.0057	0.0013	0.0009	0.0007
FS3	0.0078	0.0011	0.0008	0.0006	FS9	0.0077	0.0013	0.0009	0.0007
Average	**0.0068**	**0.0012**	**0.0008**	**0.0006**	**Average**	**0.0068**	**0.0013**	**0.0009**	**0.0007**
	LCu actual	LCu predicted				LCu actual	LCu predicted		
	Temperature °C	1550	1400	1300		Temperature °C	1550	1400	1300
FS1	0.0078	0.0045	0.0030	0.0022	FS6	0.0081	0.0050	0.0033	0.0024
FS2	0.0056	0.0043	0.0028	0.0020	FS7	0.0071	0.0047	0.0031	0.0022
FS3	0.0077	0.0039	0.0025	0.0018	FS8	0.0074	0.0044	0.0028	0.0020
Average	**0.0070**	**0.0042**	**0.0028**	**0.0020**	FS9	0.0079	0.0044	0.0029	0.0021
	LS actual	LS predicted			**Average**	**0.0076**	**0.0046**	**0.0030**	**0.0022**
	Temperature °C	1550	1400	1300		LS actual	LS predicted		
FS1	0.0127	0.0133	0.0097	0.0075		Temperature °C	1550	1400	1300
FS2	0.0133	0.0139	0.0100	0.0077	FS6	0.0152	0.0156	0.0116	0.0091
FS3	0.0107	0.0120	0.0087	0.0066	FS7	0.0143	0.0139	0.0102	0.0079
Average	**0.0122**	**0.0131**	**0.0095**	**0.0073**	FS8	0.0150	0.0163	0.0117	0.0090
					FS9	0.0152	0.0137	0.0100	0.0077
					Average	**0.0149**	**0.0149**	**0.0109**	**0.0084**

Table A88: Base metal and sulphur distributions between matte and slag glass predicted on the 2004 six-in-line samples using FactSage, as compared to measured. L_{BM} = base metal in slag / base metal in matte.

Furnace 1	LCo actual	LCo predicted			Furnace 1	LCu actual	LCu predicted		
Temperature °C		1550	1400	1300	Temperature °C		1550	1400	1300
WS1447	Nd	0.0283	0.0258	0.0244	WS1447	0.0052	0.0026	0.0017	0.0012
WS1451	Nd	0.0226	0.0206	0.0195	WS1451	0.0063	0.0025	0.0016	0.0012
WS1454	Nd	0.0208	0.0187	0.0176	WS1454	0.0051	0.0028	0.0018	0.0013
WS1459	Nd	0.0233	0.0212	0.0200	WS1459	0.0053	0.0026	0.0017	0.0012
WS1464	Nd	0.0224	0.0204	0.0192	WS1464	0.0063	0.0027	0.0018	0.0013
WS1465	Nd	0.0208	0.0188	0.0176	WS1465	0.0041	0.0028	0.0018	0.0013
WS1471	Nd	0.0260	0.0237	0.0225	WS1471	0.0052	0.0026	0.0017	0.0012
WS1478	Nd	0.0187	0.0166	0.0154	WS1478	0.0064	0.0027	0.0017	0.0012
WS1479	Nd	0.0271	0.0244	0.0228	WS1479	0.0053	0.0025	0.0015	0.0011
Average		**0.0233**	**0.0211**	**0.0199**	**Average**	**0.0055**	**0.0027**	**0.0017**	**0.0012**
	LNi actual	LNi predicted				LS actual	LS predicted		
Temperature °C		1550	1400	1300	Temperature °C		1550	1400	1300
WS1447	0.0041	0.0017	0.0013	0.0010	WS1447	0.0077	0.0083	0.0058	0.0043
WS1451	0.0035	0.0012	0.0009	0.0007	WS1451	0.0081	0.0082	0.0057	0.0042
WS1454	0.0039	0.0010	0.0007	0.0006	WS1454	0.0069	0.0087	0.0060	0.0045
WS1459	0.0040	0.0012	0.0009	0.0007	WS1459	0.0070	0.0085	0.0059	0.0044
WS1464	0.0038	0.0011	0.0008	0.0006	WS1464	0.0081	0.0083	0.0058	0.0043
WS1465	0.0038	0.0010	0.0007	0.0005	WS1465	0.0066	0.0085	0.0059	0.0044
WS1471	0.0038	0.0015	0.0011	0.0009	WS1471	0.0069	0.0082	0.0057	0.0042
WS1478	0.0044	0.0009	0.0007	0.0005	WS1478	0.0088	0.0095	0.0065	0.0048
WS1479	0.0038	0.0019	0.0014	0.0011	WS1479	0.0084	0.0088	0.0061	0.0045
Average	**0.0039**	**0.0013**	**0.0009**	**0.0007**	**Average**	**0.0076**	**0.0086**	**0.0059**	**0.0044**

Table A89: Base metal and sulphur distributions between matte and slag glass predicted on the 2005 six-in-line samples using FactSage, as compared to measured. L_{BM} = base metal in slag / base metal in matte.

Furnace 1	LCo actual	LCo predicted			Furnace 2	LCo actual	LCo predicted		
		1550	1400	1300			1550	1400	1300
WS 1995	0.0434	0.0221	0.0197	0.0183	WS 1996	0.0227	0.0196	0.0173	0.0160
WS 2003	0.0404	0.0191	0.0169	0.0155	WS 2000	0.0410	0.0190	0.0167	0.0154
WS 2012	0.0398	0.0227	0.0200	0.0184	WS 2009	0.0411	0.0206	0.0181	0.0166
WS 2016	0.0195	0.0212	0.0190	0.0177	WS 2018	0.0396	0.0206	0.0180	0.0166
Average	**0.0358**	**0.0213**	**0.0189**	**0.0175**	**Average**	**0.0361**	**0.0199**	**0.0175**	**0.0161**
	LNi actual	LNi predicted				LNi actual	LNi predicted		
Temperature °C		1550	1400	1300	Temperature °C		1550	1400	1300
WS 1995	0.0047	0.0010	0.0007	0.0006	WS 1996	0.0045	0.0010	0.0007	0.0005
WS 2003	0.0051	0.0008	0.0006	0.0004	WS 2000	0.0041	0.0008	0.0006	0.0004
WS 2012	0.0044	0.0011	0.0008	0.0006	WS 2009	0.0045	0.0010	0.0007	0.0005
WS 2016	0.0036	0.0010	0.0007	0.0005	WS 2018	0.0045	0.0010	0.0007	0.0006
Average	**0.0044**	**0.0010**	**0.0007**	**0.0005**	**Average**	**0.0044**	**0.0009**	**0.0007**	**0.0005**
	LCu actual	LCu predicted				LCu actual	LCu predicted		
Temperature °C		1550	1400	1300	Temperature °C		1550	1400	1300
WS 1995	0.0054	0.0031	0.0020	0.0014	WS 1996	0.0047	0.0029	0.0018	0.0013
WS 2003	0.0065	0.0003	0.0022	0.0016	WS 2000	0.0055	0.0032	0.0020	0.0015
WS 2012	0.0056	0.0032	0.0020	0.0015	WS 2009	0.0049	0.0032	0.0020	0.0015
WS 2016	0.0052	0.0029	0.0019	0.0013	WS 2018	0.0044	0.0031	0.0019	0.0014
Average	**0.0056**	**0.0024**	**0.0020**	**0.0015**	**Average**	**0.0049**	**0.0031**	**0.0020**	**0.0014**
	LS actual	LS predicted				LS actual	LS predicted		
Temperature °C		1550	1400	1300	Temperature °C		1550	1400	1300
WS 1995	0.0086	0.0088	0.0062	0.0046	WS 1996	0.0093	0.0096	0.0066	0.0049
WS 2003	0.0093	0.0090	0.0063	0.0048	WS 2000	0.0104	0.0094	0.0066	0.0049
WS 2012	0.0093	0.0094	0.0066	0.0049	WS 2009	0.0081	0.0096	0.0067	0.0050
WS 2016	0.0090	0.0084	0.0059	0.0044	WS 2018	0.0093	0.0102	0.0070	0.0052
Average	**0.0091**	**0.0089**	**0.0062**	**0.0047**	**Average**	**0.0093**	**0.0097**	**0.0067**	**0.0050**

Table A90: Base metal and sulphur distributions between matte and glass predicted on the 2005 SCF samples using FactSage, as compared to measured. L_{BM} = base metal in slag / base metal in matte.

Glass	LCo actual	LCo predicted				Glass	LCu actual	LCu predicted			
Temperature °C		1500	1400	1300	1200	Temperature °C		1500	1400	1300	1200
WS2098	0.1229	0.0605	0.0525	0.0452	0.0385	WS2098	0.0189	0.0121	0.0091	0.0068	0.0049
WS2096	0.1470	0.0591	0.0513	0.0443	0.0377	WS2096	0.0175	0.0126	0.0095	0.0071	0.0051
WS2090	0.1418	0.0511	0.0443	0.0381	0.0324	WS2090	0.0229	0.0132	0.0100	0.0075	0.0054
WS2092	0.1237	0.0566	0.0491	0.0424	0.0361	WS2092	0.0164	0.0130	0.0099	0.0074	0.0053
WS2091	0.1117	0.0532	0.0463	0.0400	0.0342	WS2091	0.0167	0.0124	0.0094	0.0070	0.0051
WS2095	0.1312	0.0552	0.0479	0.0413	0.0352	WS2095	0.0177	0.0125	0.0094	0.0070	0.0051
Average	**0.1297**	**0.0560**	**0.0486**	**0.0419**	**0.0357**	**Average**	**0.0184**	**0.0127**	**0.0096**	**0.0071**	**0.0051**
	LNi actual	LNi predicted					LS actual	LS predicted			
Temperature °C		1500	1400	1300	1200	Temperature °C		1500	1400	1300	1200
WS2098	0.0067	0.0027	0.0020	0.0015	0.0011	WS2098	0.0275	0.0394	0.0350	0.0304	0.0256
WS2096	0.0081	0.0026	0.0020	0.0015	0.0010	WS2096	0.0236	0.0409	0.0365	0.0319	0.0271
WS2090	0.0085	0.0023	0.0018	0.0013	0.0009	WS2090	0.0267	0.0551	0.0499	0.0442	0.0381
WS2092	0.0058	0.0025	0.0019	0.0014	0.0010	WS2092	0.0277	0.0435	0.0390	0.0342	0.0292
WS2091	0.0061	0.0023	0.0017	0.0013	0.0009	WS2091	0.0204	0.0359	0.0317	0.0273	0.0229
WS2095	0.0080	0.0025	0.0018	0.0014	0.0010	WS2095	0.0165	0.0387	0.0343	0.0297	0.0250
Average	**0.0072**	**0.0025**	**0.0019**	**0.0014**	**0.0010**	**Average**	**0.0237**	**0.0422**	**0.0377**	**0.0329**	**0.0280**

Table A91: Base metal and sulphur distributions between matte and spinel predicted on the 2005 SCF samples using FactSage, as compared to measured. L_{BM} = base metal in slag / base metal in matte.

Spinel	LCo actual	LCo predicted			
Temperature °C		1500	1400	1300	1200
WS2098	0.1424	0.0617	0.0595	0.0572	0.0548
WS2096	0.1382	0.0597	0.0575	0.0553	0.0531
WS2090	0.2088	0.0502	0.0484	0.0464	0.0444
WS2092	0.1285	0.0569	0.0548	0.0526	0.0504
WS2091	0.1547	0.0547	0.0529	0.0510	0.0491
WS2095	0.1185	0.0563	0.0544	0.0524	0.0503
Average	**0.1485**	**0.0566**	**0.0546**	**0.0525**	**0.0504**
	LNi actual	LNi predicted			
Temperature °C		1500	1400	1300	1200
WS2098	0.0063	0.0022	0.0020	0.0018	0.0017
WS2096	0.0082	0.0021	0.0019	0.0018	0.0017
WS2090	0.0100	0.0018	0.0016	0.0015	0.0014
WS2092	0.0070	0.0020	0.0018	0.0017	0.0016
WS2091	0.0106	0.0019	0.0017	0.0016	0.0015
WS2095	0.0052	0.0020	0.0018	0.0016	0.0015
Average	**0.0079**	**0.0020**	**0.0018**	**0.0017**	**0.0016**
	LCu actual	LCu predicted			
Temperature °C		1500	1400	1300	1200
WS2098	0.0006	No Cu predicted in spinel			
WS2096	0.0014				
WS2090	0.0015				
WS2092	0.0027				
WS2091	0.0014				
WS2095	0.0007				
Average	**0.0014**				

Table A92: Percentages of sulphidic dissolution in the silicate phase of the 1999 six-in-line slag samples.

Furnace 1	% Co as sulphide						% Ni as sulphide					
Temp °C	1300	1350	1400	1450	1500	1550	1300	1350	1400	1450	1500	1550
FS1	0.92	1.05	1.19	1.34	1.48	1.63	0.92	1.05	1.19	1.33	1.48	1.63
FS2	0.92	1.06	1.20	1.35	1.50	1.67	0.92	1.06	1.20	1.34	1.50	1.66
FS3	0.80	0.92	1.05	1.19	1.33	1.46	0.80	0.92	1.05	1.18	1.33	1.47
Average	**0.88**	**1.01**	**1.15**	**1.29**	**1.44**	**1.59**	**0.88**	**1.01**	**1.15**	**1.28**	**1.44**	**1.59**
Furnace 2	% Co as sulphide						% Ni as sulphide					
Temp °C	1300	1350	1400	1450	1500	1550	1300	1350	1400	1450	1500	1550
FS6	1.09	1.24	1.39	1.55	1.71	1.87	1.09	1.24	1.39	1.55	1.71	1.88
FS7	0.94	1.06	1.21	1.35	1.51	1.66	0.94	1.07	1.21	1.35	1.50	1.65
FS8	1.01	1.21	1.38	1.54	1.75	1.93	1.06	1.22	1.38	1.54	1.69	1.88
FS9	0.93	1.08	1.22	1.34	1.51	1.66	0.93	1.09	1.21	1.38	1.51	1.67
Average	**0.99**	**1.15**	**1.30**	**1.45**	**1.62**	**1.78**	**1.01**	**1.16**	**1.30**	**1.46**	**1.60**	**1.77**

Furnace 1	% Cu as sulphide					
Temp °C	1300	1350	1400	1450	1500	1550
FS1	0.84	0.96	1.09	1.22	1.35	1.49
FS2	0.84	0.97	1.10	1.23	1.37	1.52
FS3	0.74	0.85	0.96	1.08	1.21	1.34
Average	**0.81**	**0.93**	**1.05**	**1.18**	**1.31**	**1.45**
Furnace 2	% Cu as sulphide					
Temp °C	1300	1350	1400	1450	1500	1550
FS6	1.00	1.13	1.27	1.42	1.57	1.72
FS7	0.85	0.98	1.10	1.24	1.37	1.51
FS8	0.94	1.10	1.23	1.41	1.58	1.73
FS9	0.84	1.00	1.09	1.24	1.38	1.54
Average	**0.91**	**1.05**	**1.17**	**1.33**	**1.48**	**1.63**

Table A93: Percentages of sulphidic dissolution in the silicate phase of the 2004 six-in-line slag samples.

Furnace 1	% Co as sulphide					
Temp °C	1300	1350	1400	1450	1500	1550
WS1447	0.62	0.73	0.84	0.93	1.07	1.19
WS1454	0.61	0.71	0.82	0.93	1.06	1.18
WS1465	0.60	0.70	0.81	0.92	1.03	1.19
WS1478	0.65	0.75	0.86	0.99	1.12	1.28
Average	**0.62**	**0.72**	**0.83**	**0.94**	**1.07**	**1.21**
Furnace 1	% Ni as sulphide					
Temp °C	1300	1350	1400	1450	1500	1550
WS1447	0.64	0.70	0.83	0.94	1.08	1.20
WS1454	0.60	0.71	0.81	0.96	1.03	1.18
WS1465	0.60	0.70	0.80	0.91	1.03	1.18
WS1478	0.64	0.76	0.89	0.99	1.12	1.27
Average	**0.62**	**0.72**	**0.83**	**0.95**	**1.07**	**1.21**
Furnace 1	% Cu as sulphide					
Temp °C	1300	1350	1400	1450	1500	1550
WS1447	0.57	0.67	0.74	0.85	0.96	1.11
WS1454	0.56	0.65	0.74	0.84	0.98	1.07
WS1465	0.55	0.64	0.73	0.82	0.96	1.06
WS1478	0.59	0.69	0.81	0.90	1.05	1.14
Average	**0.57**	**0.66**	**0.76**	**0.85**	**0.99**	**1.10**

Table A94: Percentages of sulphidic dissolution in the silicate phase of the 2005 six-in-line slag samples.

Furnace 1	% Co as sulphide						% Ni as sulphide					
Temp °C	1300	1350	1400	1450	1500	1550	1300	1350	1400	1450	1500	1550
WS1995	0.59	0.70	0.79	0.90	1.02	1.18	0.60	0.69	0.76	0.90	1.01	1.14
WS2003	0.59	0.68	0.78	0.89	1.00	1.08	0.58	0.68	0.79	0.87	1.03	1.15
WS2012	0.63	0.73	0.83	0.95	1.05	1.18	0.63	0.71	0.86	0.96	1.09	1.17
WS2016	0.58	0.68	0.78	0.90	0.96	1.11	0.59	0.68	0.78	0.87	0.98	1.12
Average	**0.60**	**0.70**	**0.80**	**0.91**	**1.01**	**1.14**	**0.60**	**0.69**	**0.80**	**0.90**	**1.03**	**1.15**
Furnace 2	% Co as sulphide						% Ni as sulphide					
Temp °C	1300	1350	1400	1450	1500	1550	1300	1350	1400	1450	1500	1550
WS1996	0.63	0.73	0.85	0.97	1.09	1.17	0.63	0.73	0.86	0.95	1.09	1.22
WS2000	0.60	0.70	0.81	0.92	1.04	1.19	0.61	0.71	0.85	0.95	1.02	1.18
WS2009	0.63	0.73	0.84	0.96	1.04	1.20	0.63	0.73	0.86	0.93	1.09	1.20
WS2018	0.65	0.76	0.89	1.01	1.12	1.27	0.66	0.77	0.86	1.03	1.17	1.30
Average	**0.63**	**0.73**	**0.85**	**0.97**	**1.07**	**1.21**	**0.63**	**0.74**	**0.86**	**0.97**	**1.09**	**1.23**
Furnace 1	% Cu as sulphide											
Temp °C	1300	1350	1400	1450	1500	1550						
WS1995	0.53	0.63	0.72	0.82	0.93	1.03						
WS2003	0.56	0.60	0.70	0.79	0.91	1.03						
WS2012	0.89	0.68	0.78	0.87	0.98							
WS2016	0.54	0.65	0.74	0.83	0.92	1.04						
Average	**0.63**	**0.64**	**0.74**	**0.83**	**0.94**	**1.03**						
Furnace 2	% Cu as sulphide											
Temp °C	1300	1350	1400	1450	1500	1550						
WS1996	0.57	0.69	0.76	0.89	0.98	1.12						
WS2000	0.53	0.63	0.73	0.46	0.97	1.06						
WS2009	0.55	0.65	0.76	0.89	1.00	1.09						
WS2018	0.60	0.69	0.81	0.92	1.05	1.17						
Average	**0.56**	**0.67**	**0.77**	**0.79**	**1.00**	**1.11**						

Table A95: Percentages of sulphidic dissolution in the silicate phase of the 2005 SCF slag samples.

SCF	% Co as sulphide			
Temp °C	1200	1300	1400	1500
WS2096	2.29	2.83	3.21	3.64
WS2092	3.16	3.73	4.23	4.76
WS2095	1.94	2.45	2.82	3.22
Average	**2.46**	**3.00**	**3.42**	**3.87**
SCF	% Ni as sulphide			
Temp °C	1200	1300	1400	1500
WS2096	2.25	2.87	3.28	3.72
WS2092	3.13	3.80	4.24	4.71
WS2095	2.01	2.39	2.82	3.23
Average	**2.46**	**3.02**	**3.45**	**3.89**
SCF	% Cu as sulphide			
Temp °C	1200	1300	1400	1500
WS2096	2.20	2.52	2.98	3.35
WS2092	3.00	3.39	3.87	4.34
WS2095	1.79	2.20	2.53	2.93
Average	**2.33**	**2.70**	**3.13**	**3.54**

APPENDIX B – FIGURES

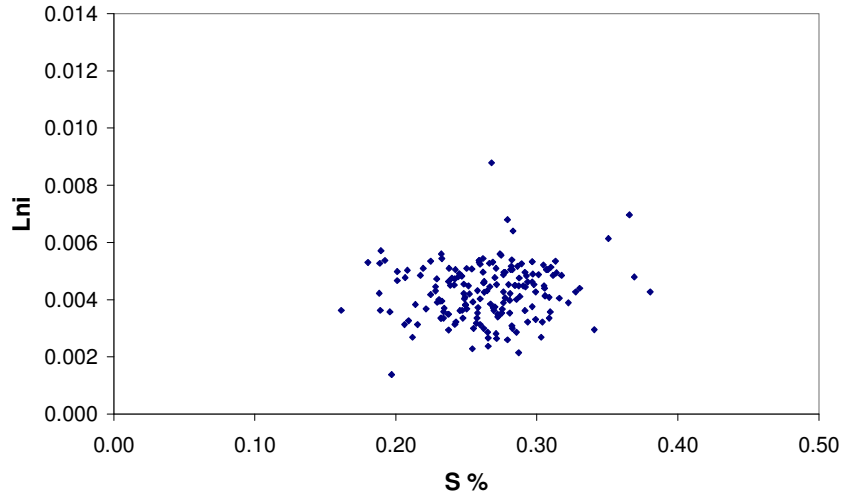

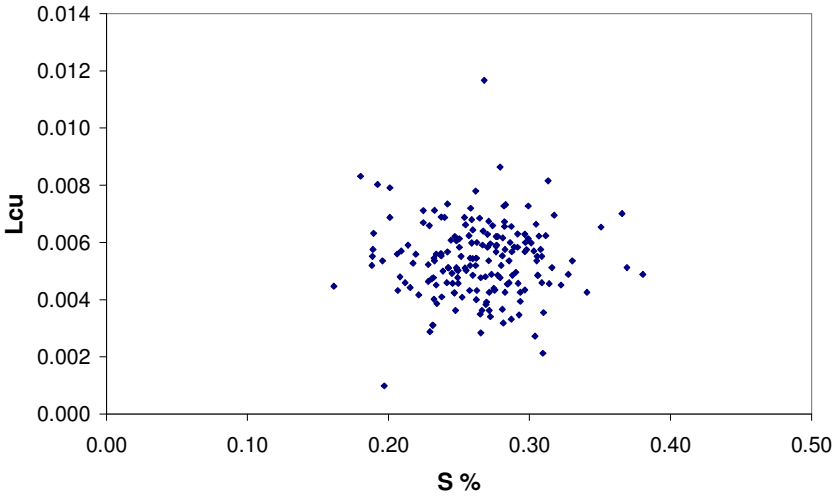

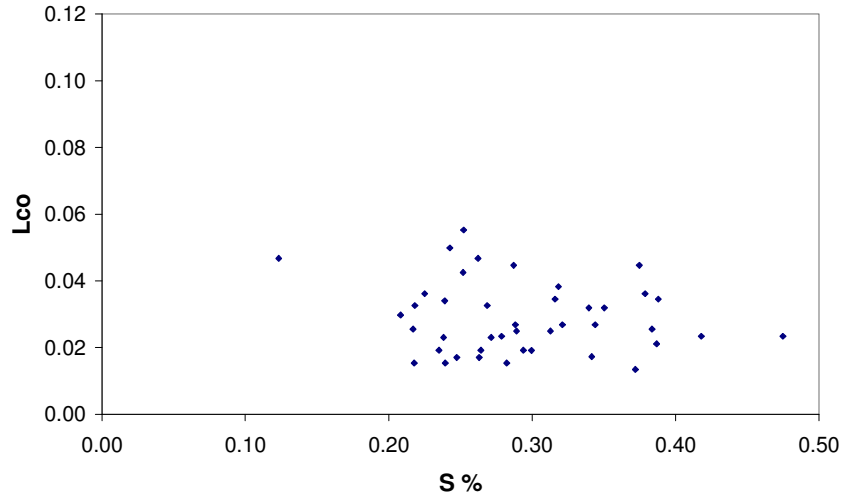

Figure B1: The relationship between L_{Ni}, L_{Cu} and L_{Co} and dissolved sulphur in Furnace 1slag (2005), where $L_{BM} = BM_{slag} / BM_{matte.}$ The plots are a composite of data from WS1989, 2007, 2015 and 2025.

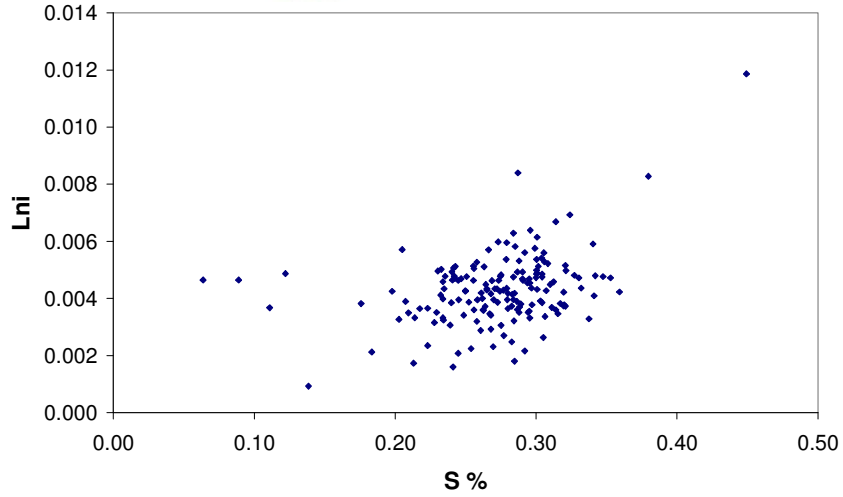

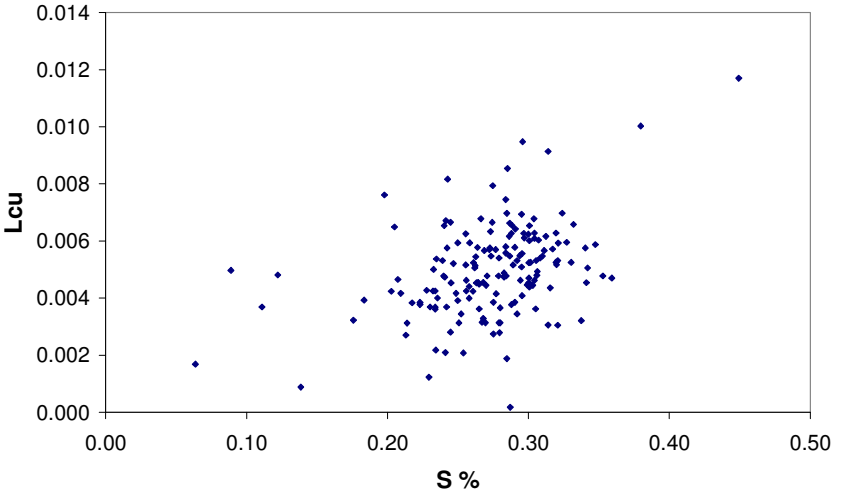

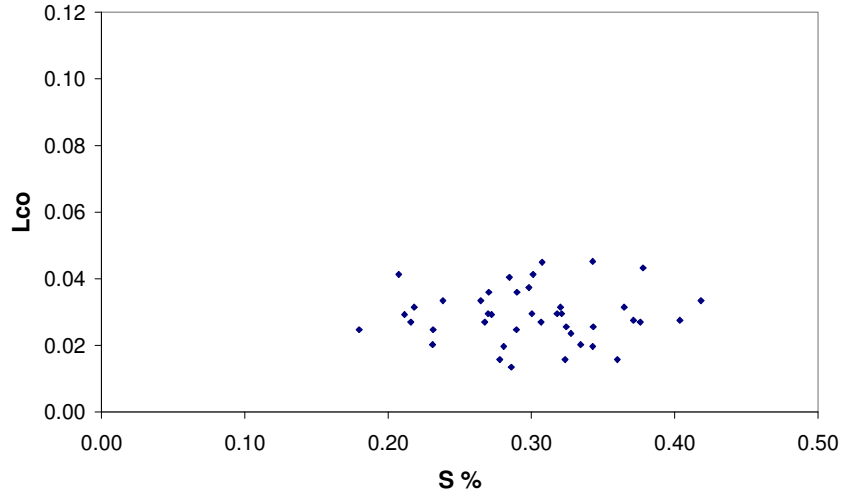

Figure B2: The relationship between L_{Ni}, L_{Cu} and L_{Co} and dissolved sulphur in Furnace 2 slag (2005), where $L_{BM} = BM_{slag} / BM_{matte.}$ The plots are a composite of data from WS1990, 1999, 2008 and 2020.

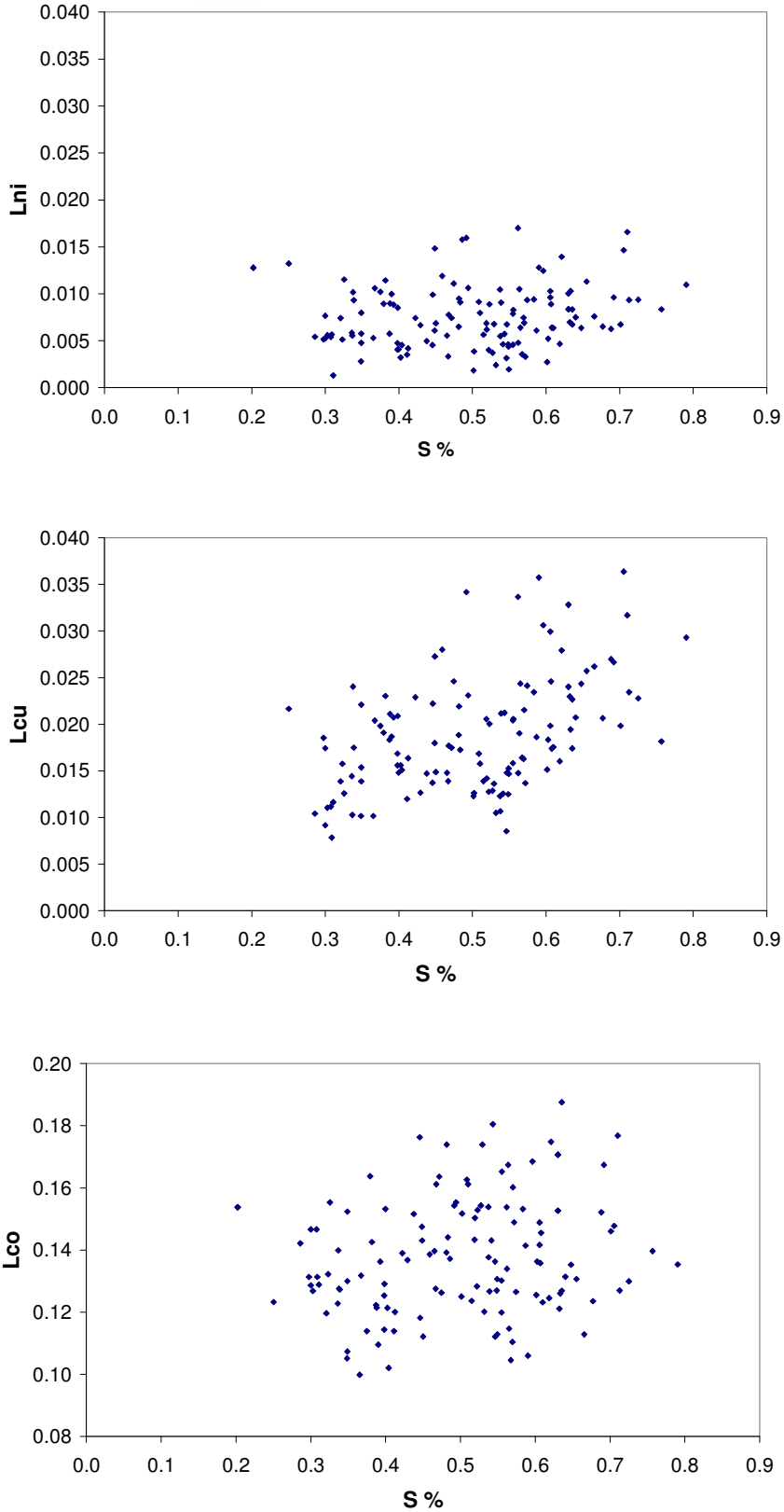

Figure B3: The relationship between L_{Ni}, L_{Cu} and L_{Co} and dissolved sulphur in SCF slag (2005), where $L_{BM} = BM_{slag} / BM_{matte.}$ The plots are a composite of data from WS2098, 2096, 2090, 2092, 2095 and 2091.

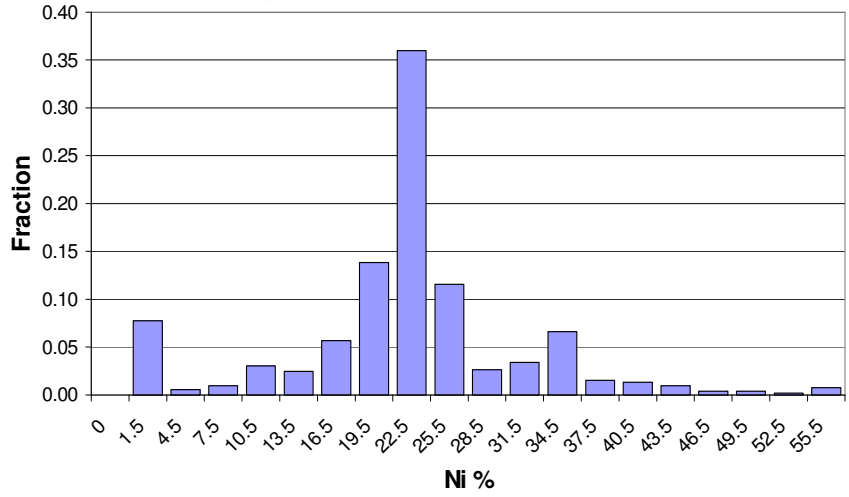

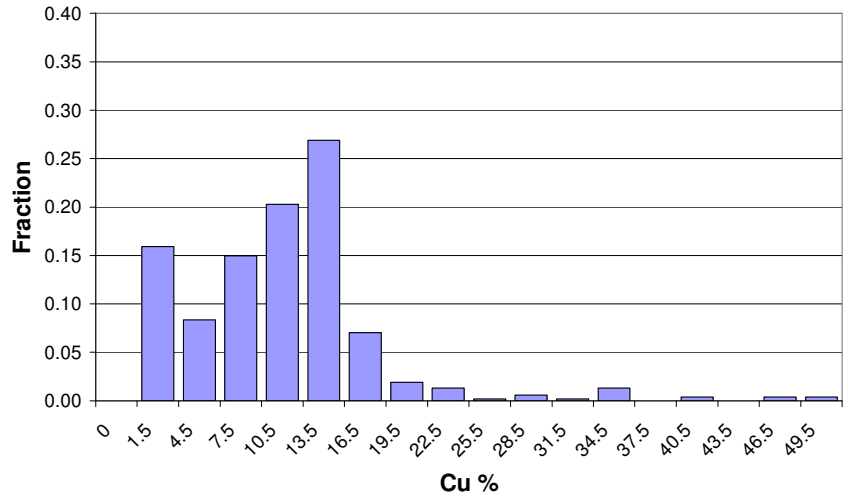

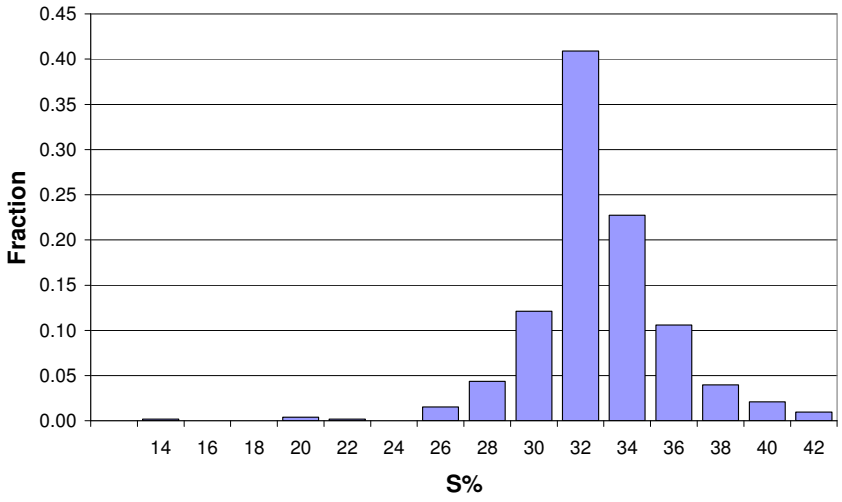

Figure B4: Compositional distribution plots for WS1989 slag (Furnace 1–2005). Note the bi- or multi-modal distributions of nickel and copper.

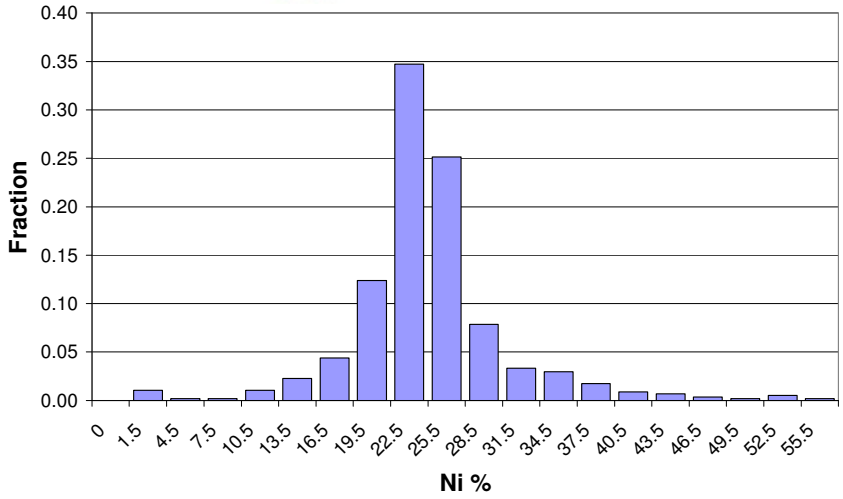

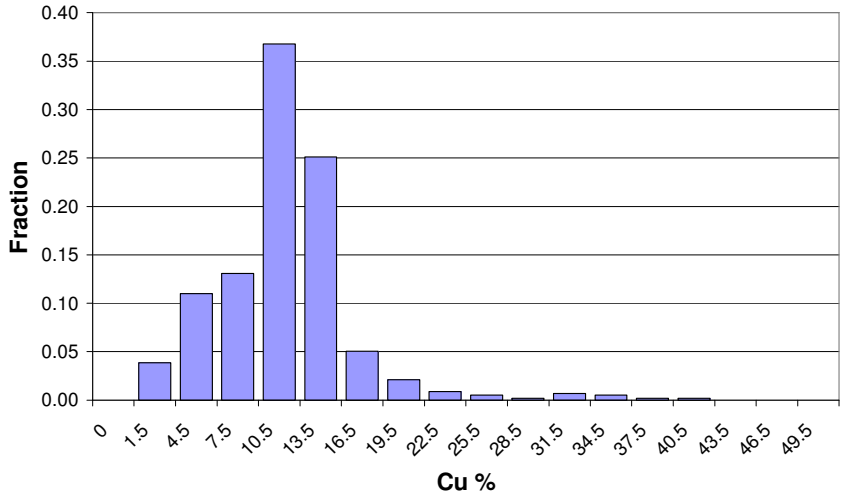

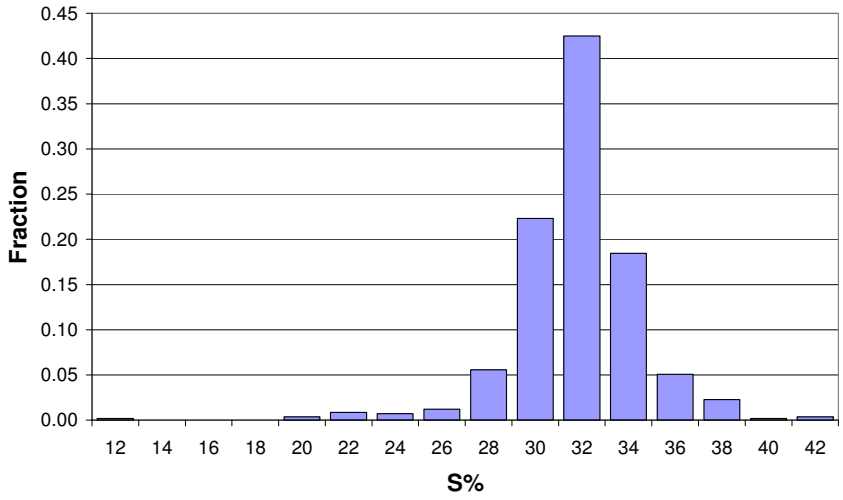

Figure B5: Compositional distribution plots for WS2008 slag (Furnace 1–2005). These distributions appear more homogenous than those of WS1989 slag.

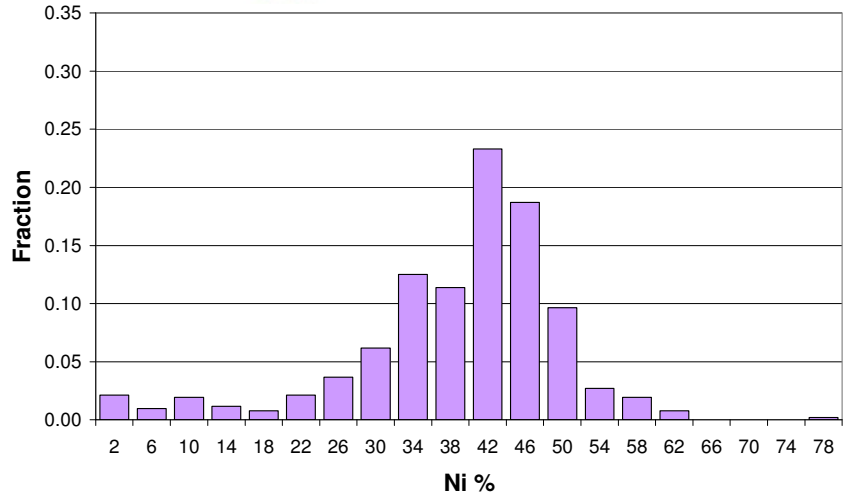

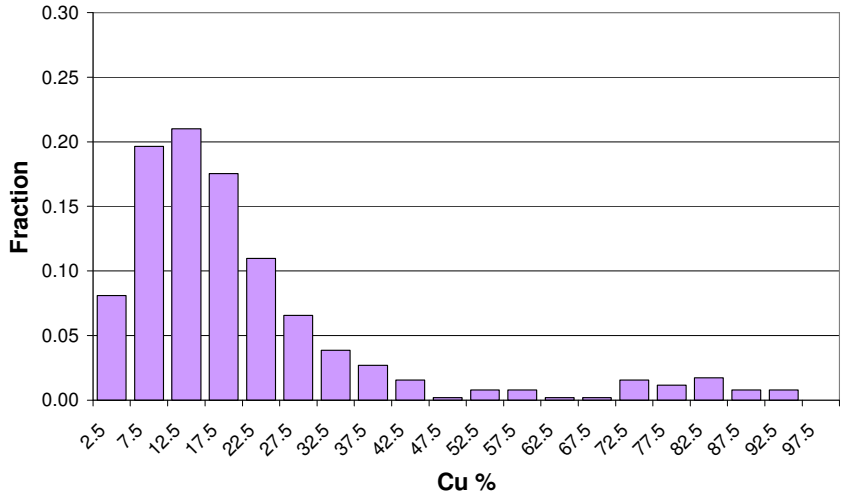

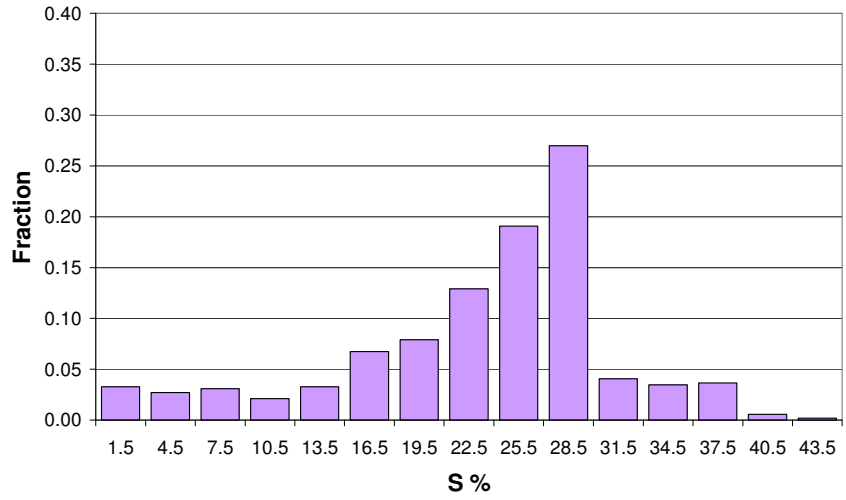

Figure B6: Compositional distribution plots for WS2091 slag (SCF–2005).

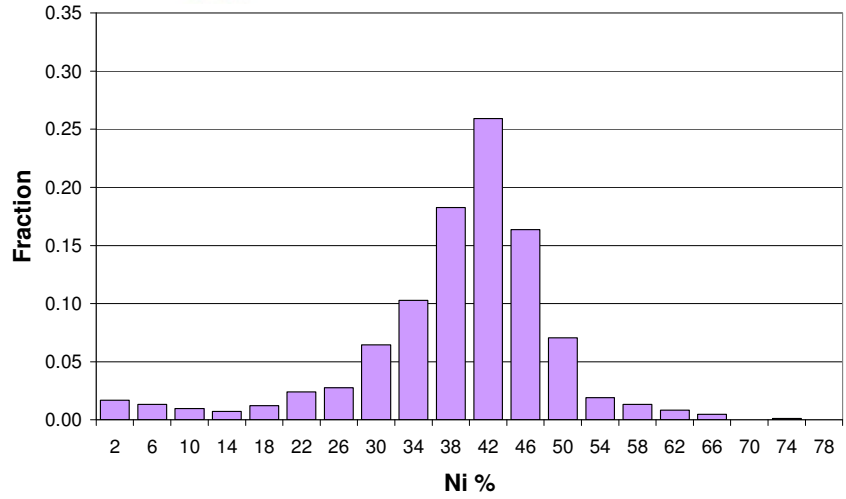

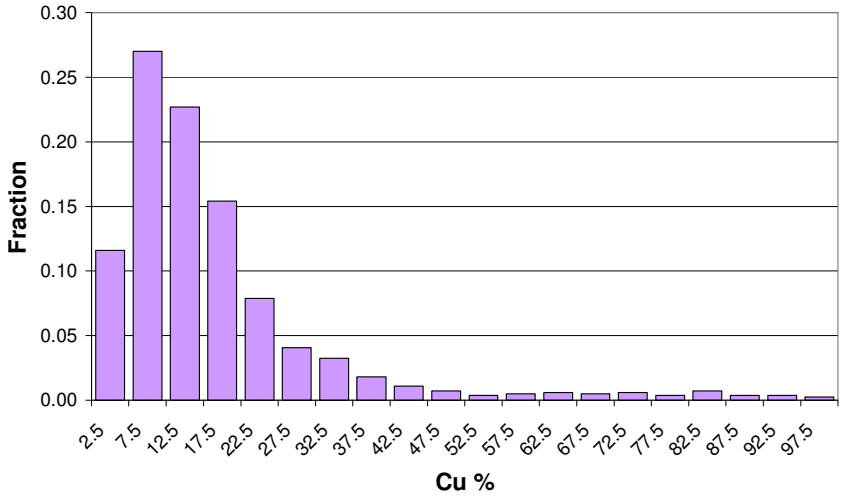

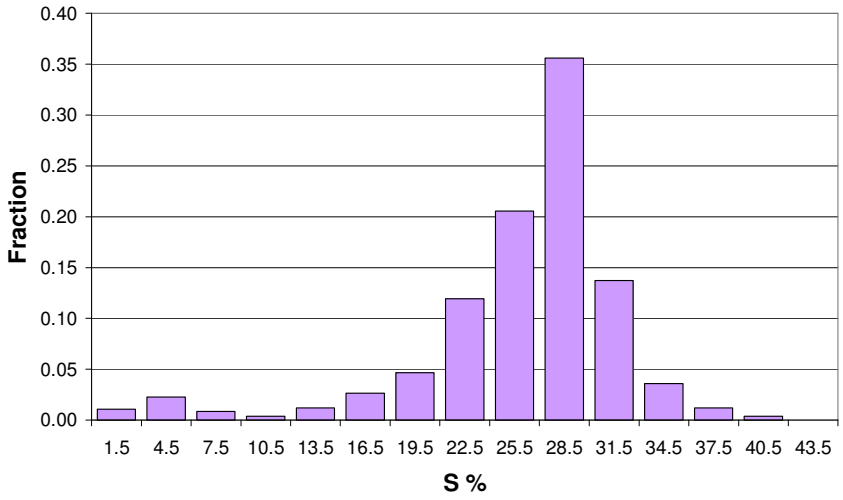

Figure B7: Compositional distribution plots for WS2098 slag (SCF–2005).

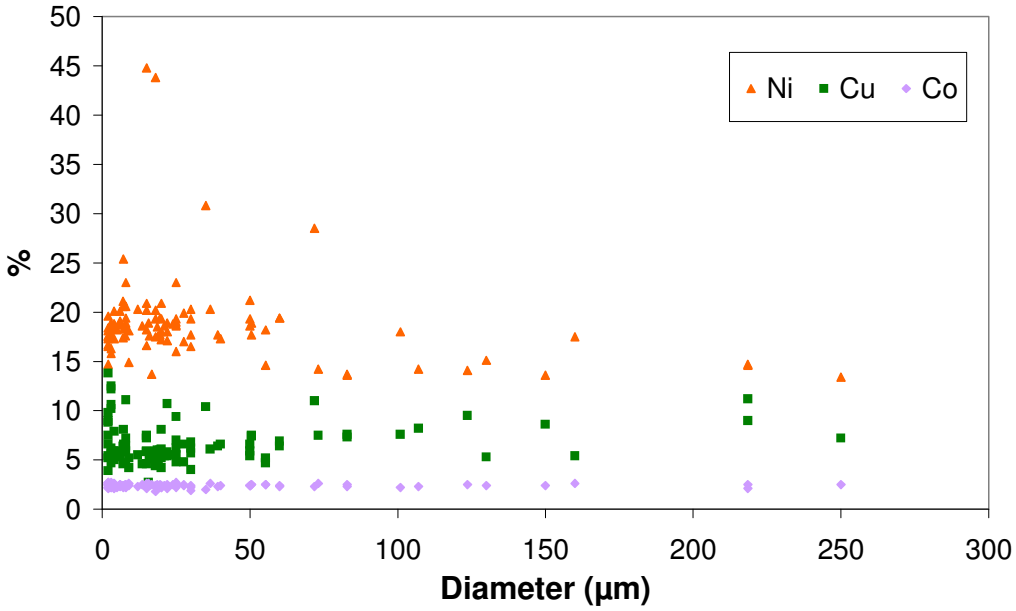

Figure B8: Entrained matte compositional variation with droplet diameter in FS1 (Furnace 1–1999) slag as determined manually on the SEM.

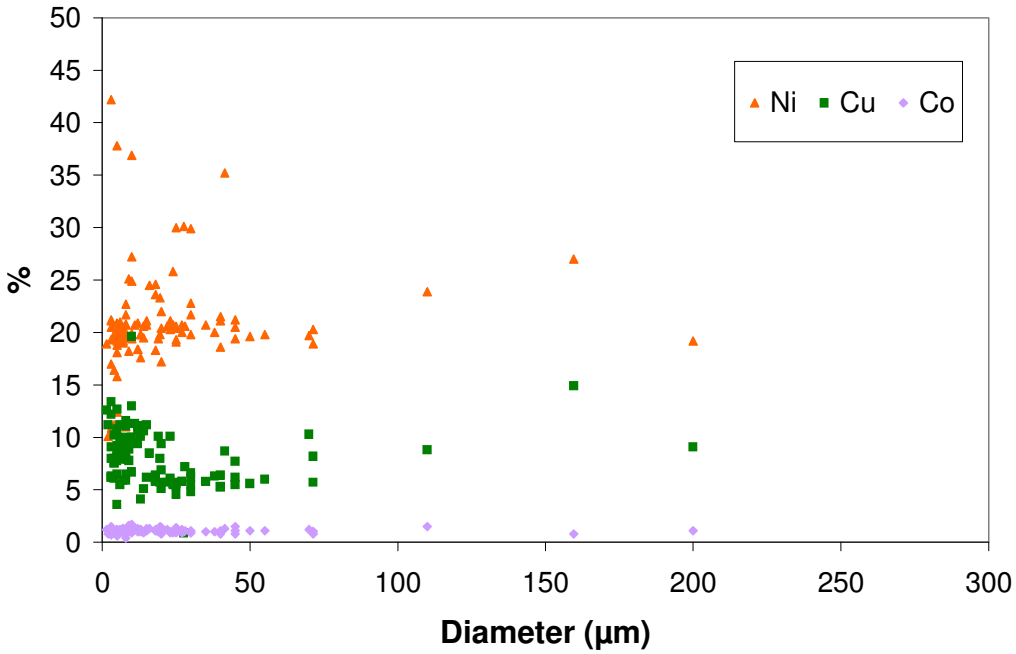

Figure B9: Entrained matte compositional variation with droplet diameter in FS6 (Furnace 2–1999) slag as determined manually on the SEM.

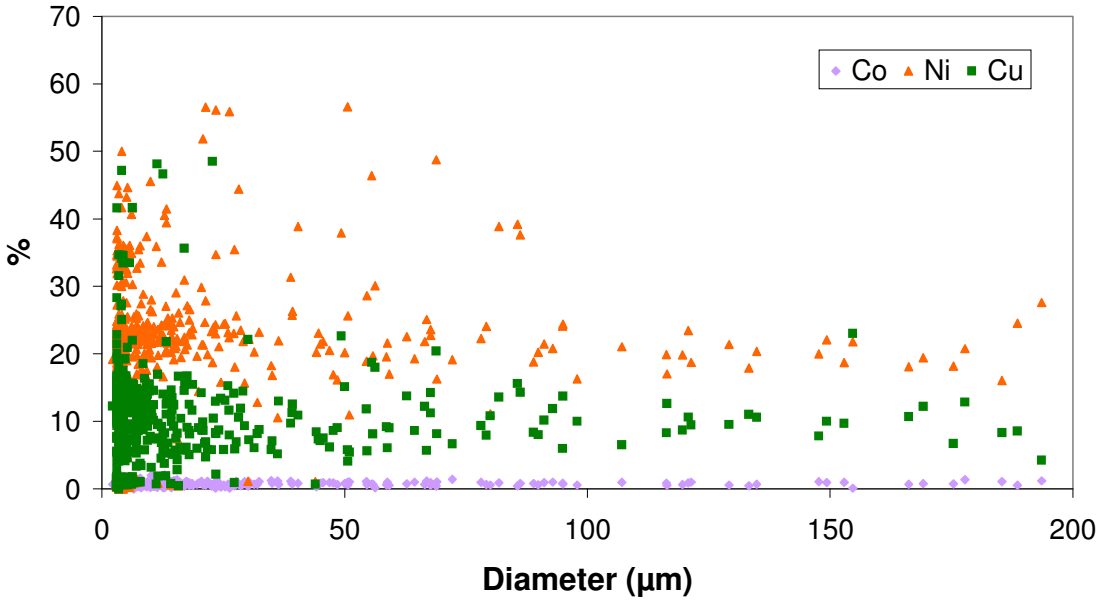

Figure B10: Entrained matte compositional variation with droplet diameter in WS1989 (Furnace 1–2005) slag as determined by MLA analysis.

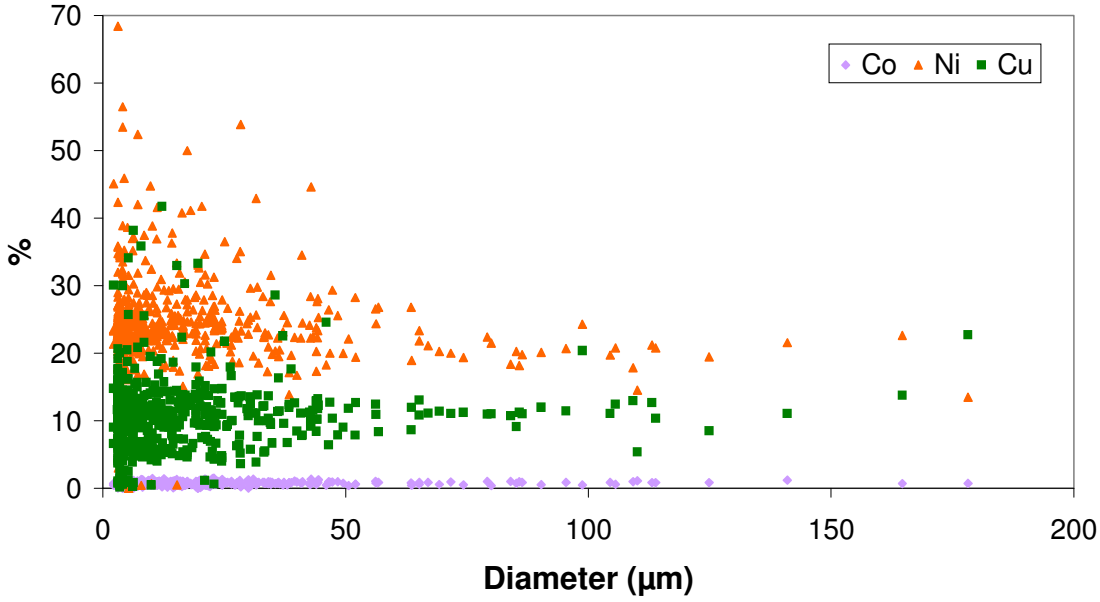

Figure B11: Entrained matte compositional variation with droplet diameter in WS2008 (Furnace 2–2005) slag as determined by MLA analysis.

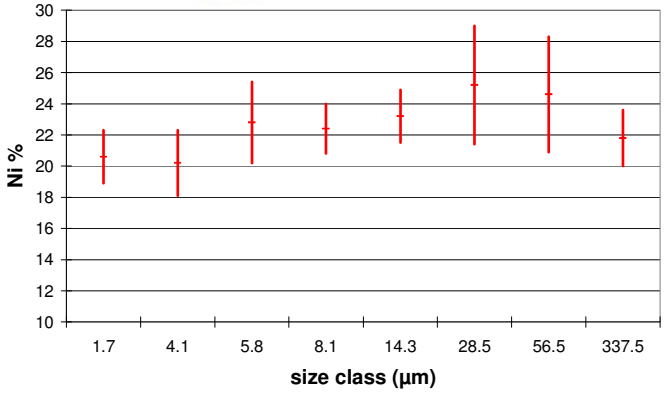

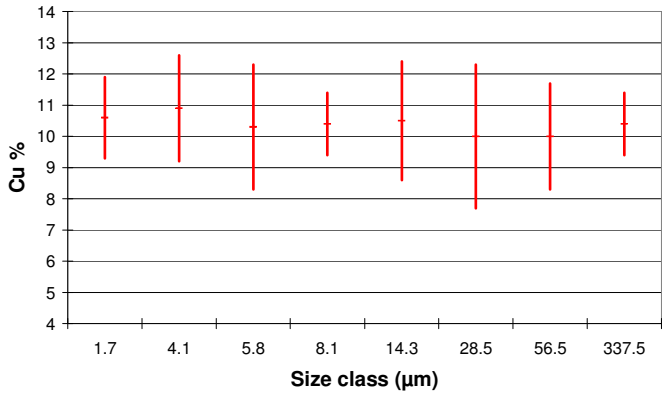

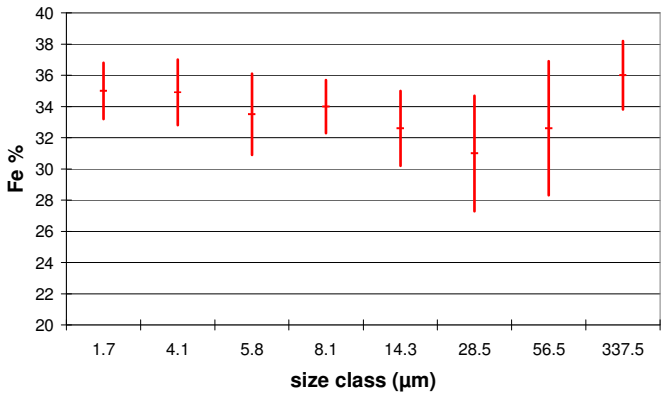

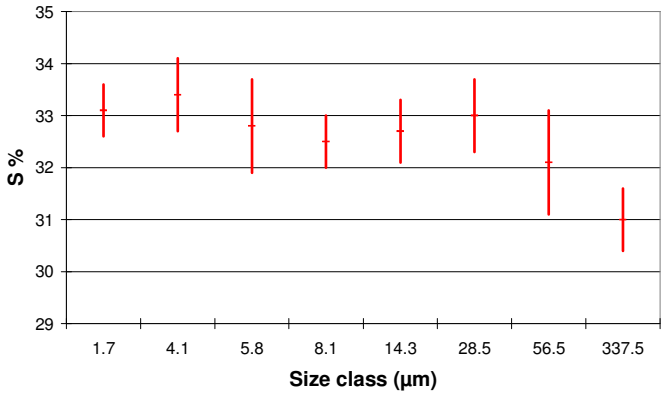

Figure B12: Confidence interval plots showing entrained matte composition variation with increasing droplet size class (from MLA data) for WS1989 slag (Furnace 1, 2005).

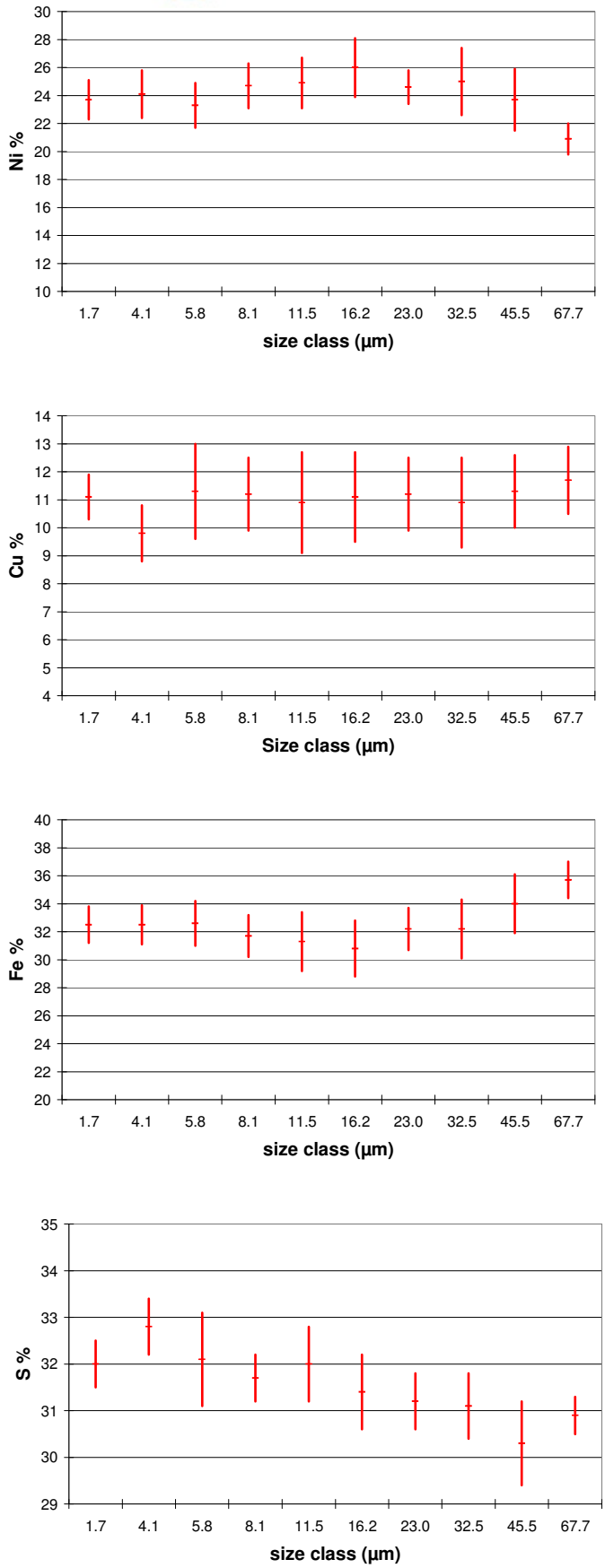

Figure B13: Confidence interval plots showing entrained matte composition variation with increasing droplet size class (from MLA data) for WS2008 slag (Furnace 2, 2005).

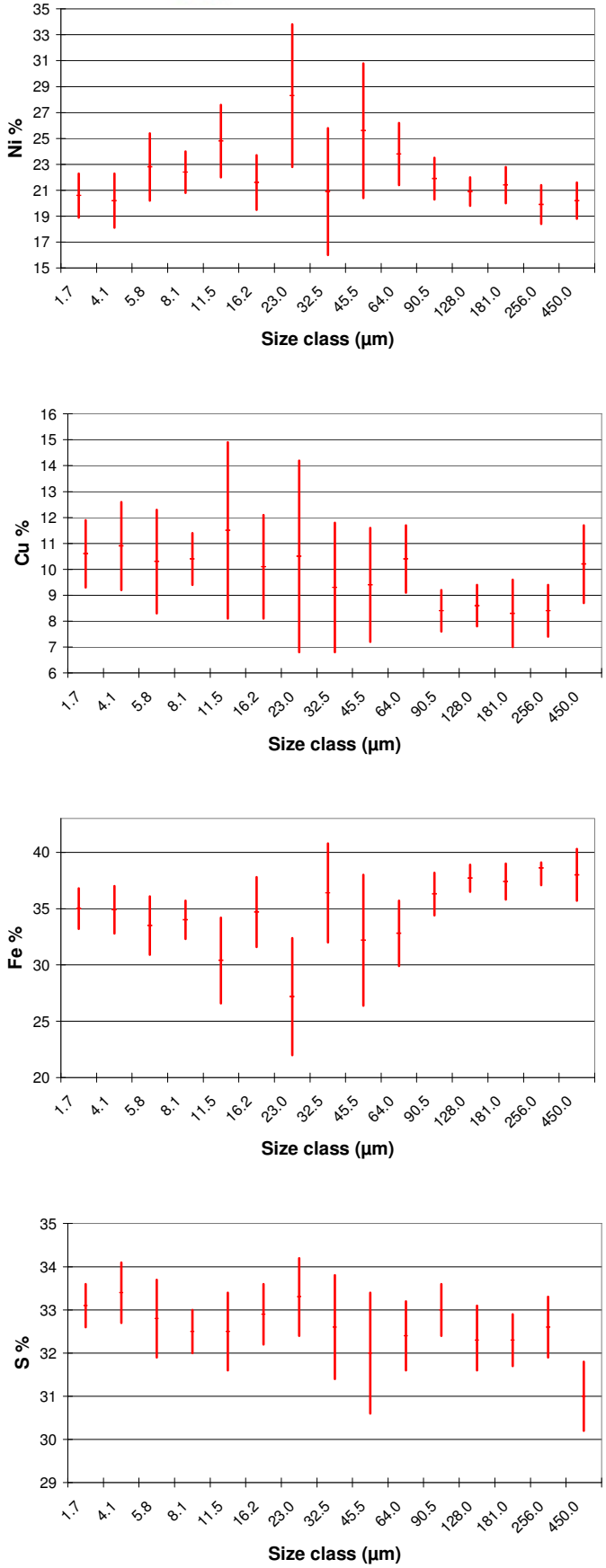

Figure B14: Confidence interval plots showing entrained matte composition variation with increasing droplet size class (from MLA and SEM data combined) for WS1989 slag (Furnace 1, 2005).

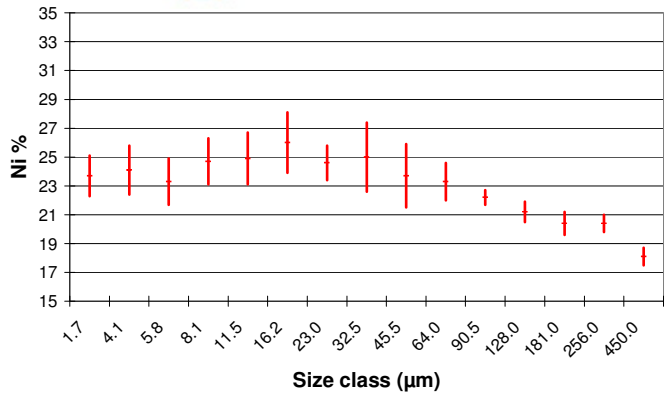

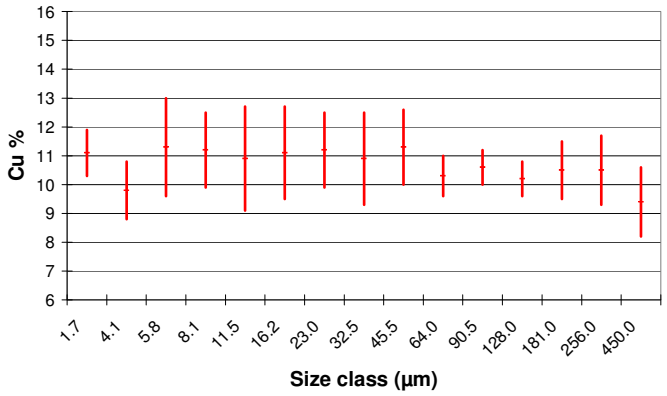

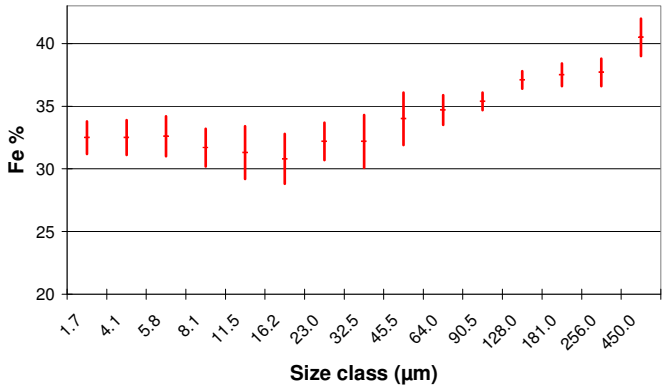

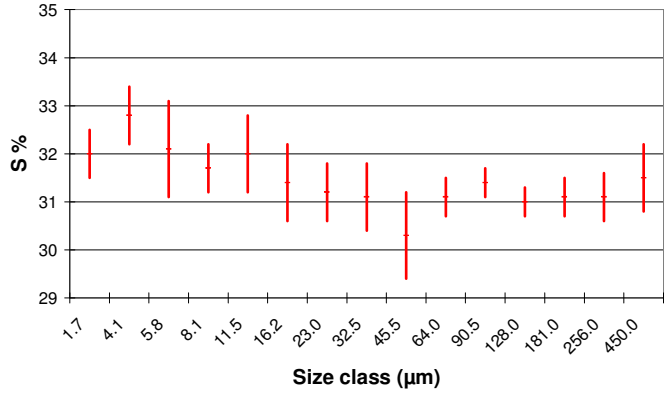

Figure B15: Confidence interval plots showing entrained matte composition variation with increasing droplet size class (from MLA and SEM data combined) for WS2008 slag (Furnace 2, 2005).

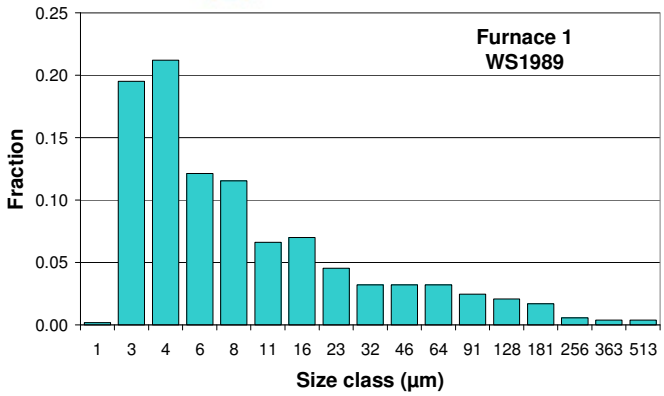

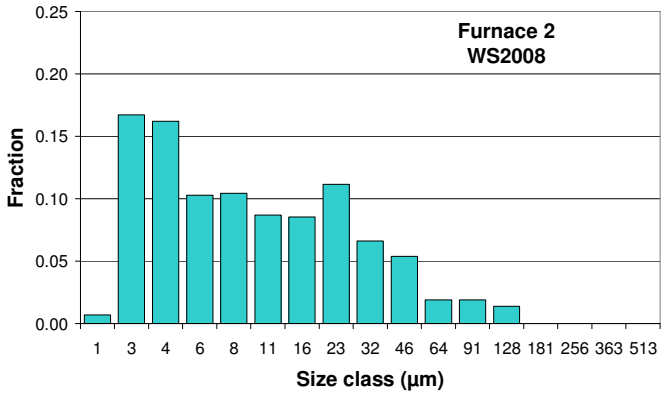

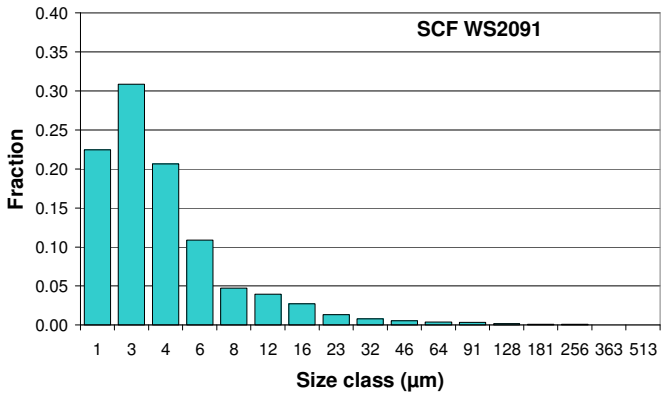

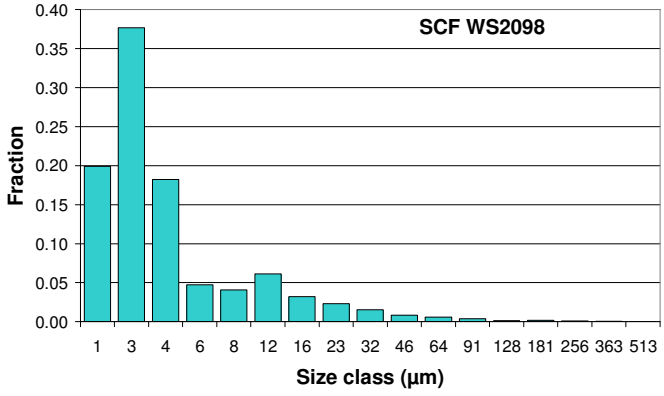

Figure B16: √2 size distributions of 2005 entrained matte droplets in six-in-line and SCF slag samples. Note the vertical scale difference between the two furnace types.

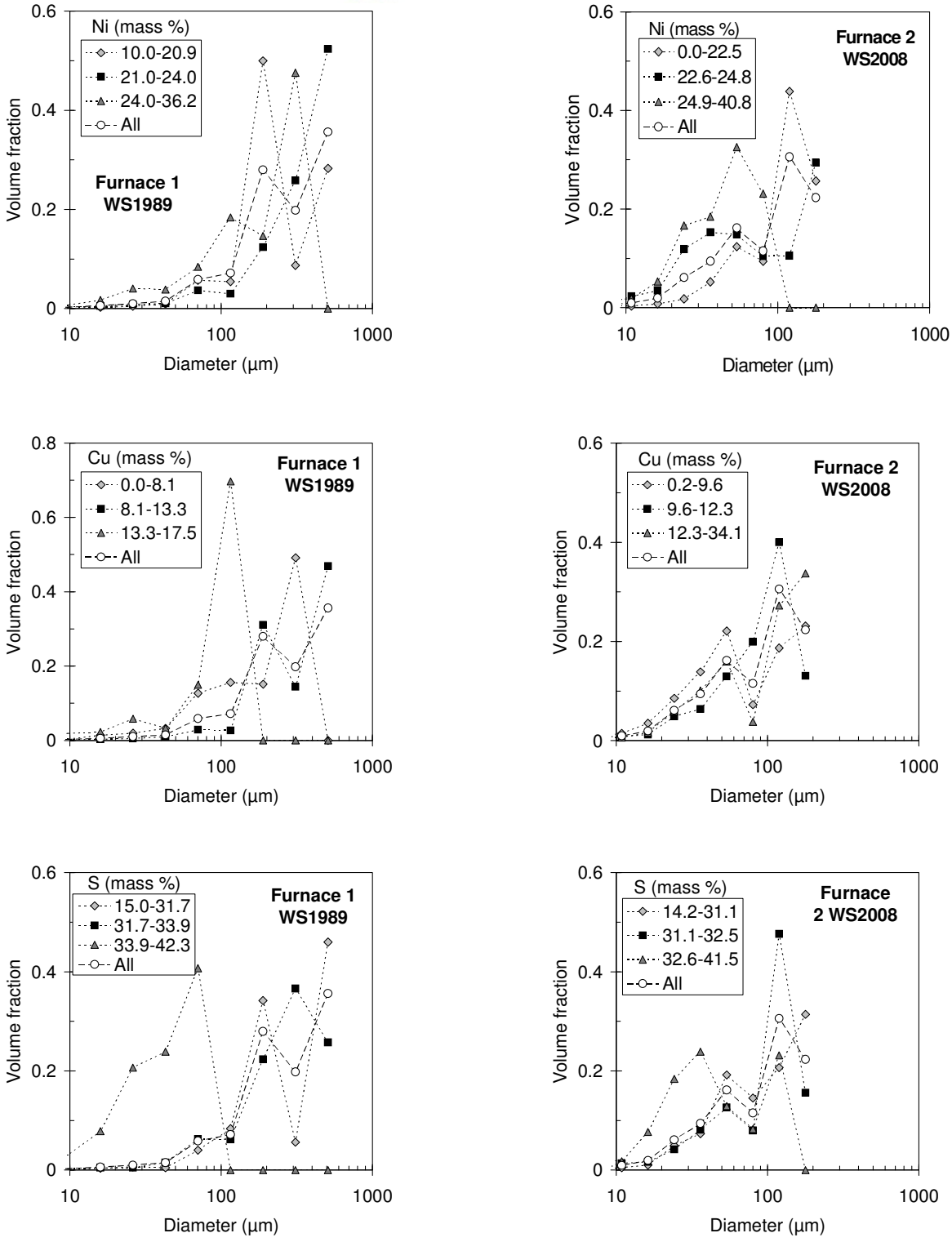

Figure B17: Corrected volume fraction comparisons for various mass % groups of nickel, copper and sulphur in the entrained matte of the 2005 six-in-line slag samples.

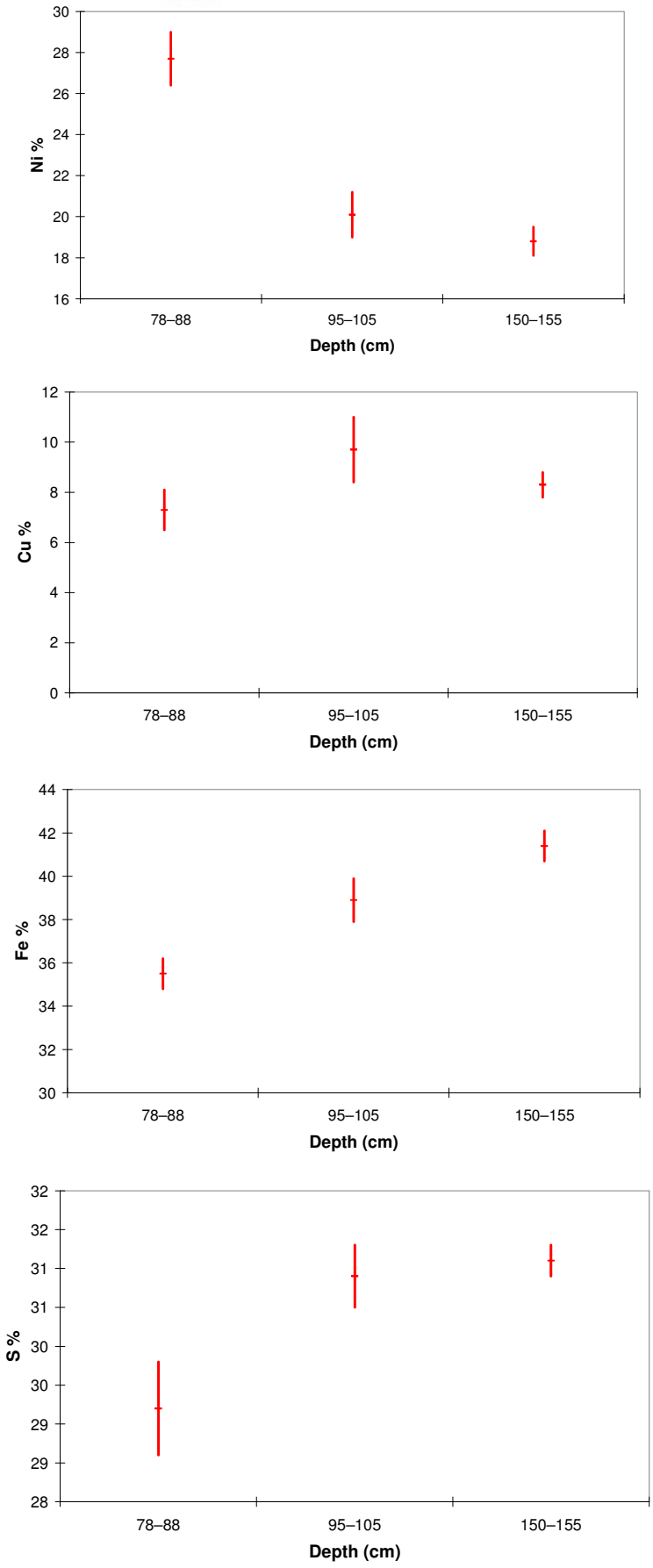

Figure B18: Confidence interval plots showing entrained matte composition variation with depth in the slag bath (from SEM data).

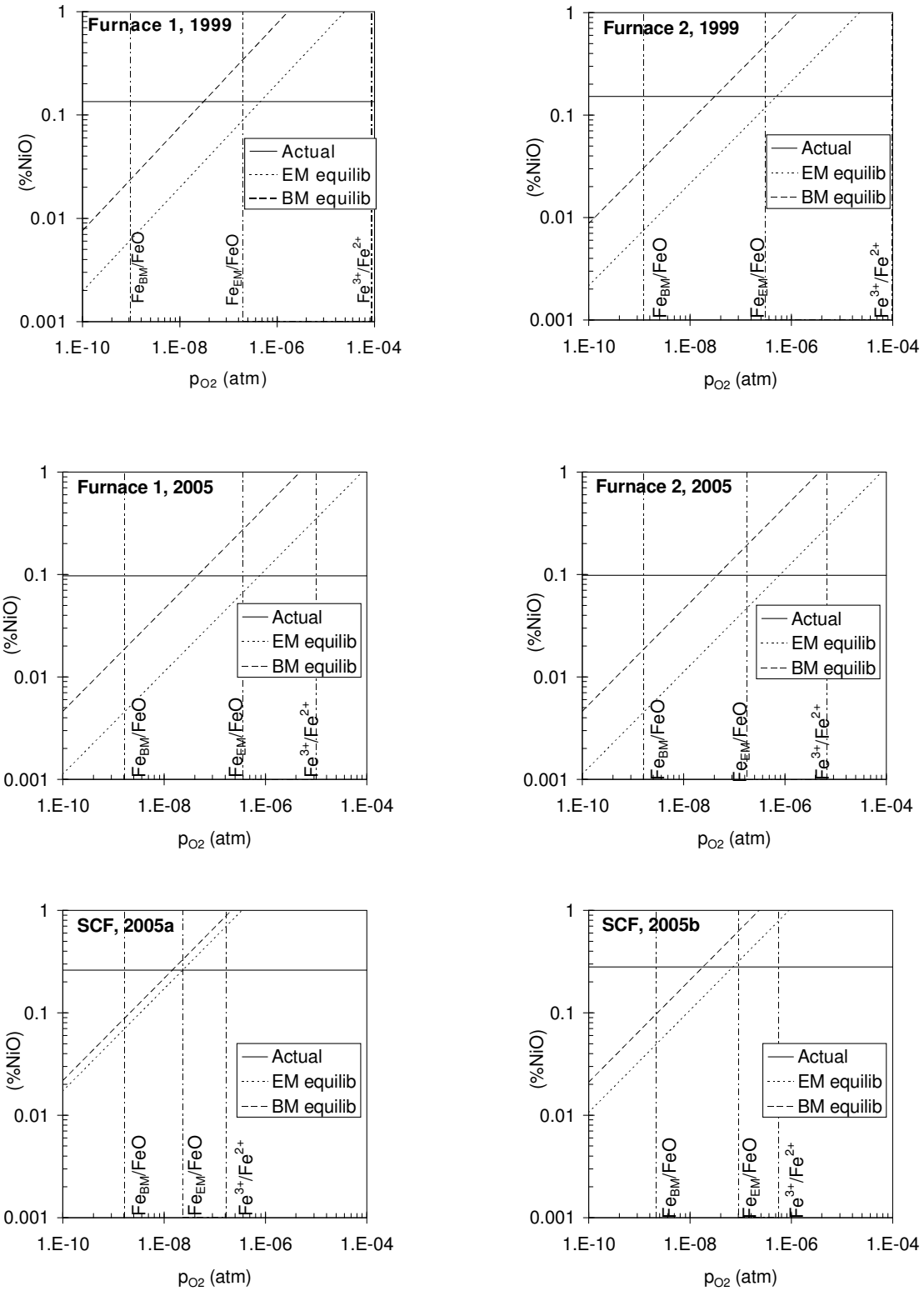

Figure B19: Base metal dissolution plots for nickel for the 1999 and 2005 furnaces and SCF. Dissolved NiO can be read off at the intersections of the Fe_{BM}/FeO and $Fe^{\#+}/Fe^{2+}$ buffers with the bulk matte equilibrium line or at the intersections of the Fe_{EM}/FeO and $Fe^{\#+}/Fe^{2+}$ buffers with the entrained matte equilibrium line. The levels so obtained can be compared with actual NiO measured on the microprobe.

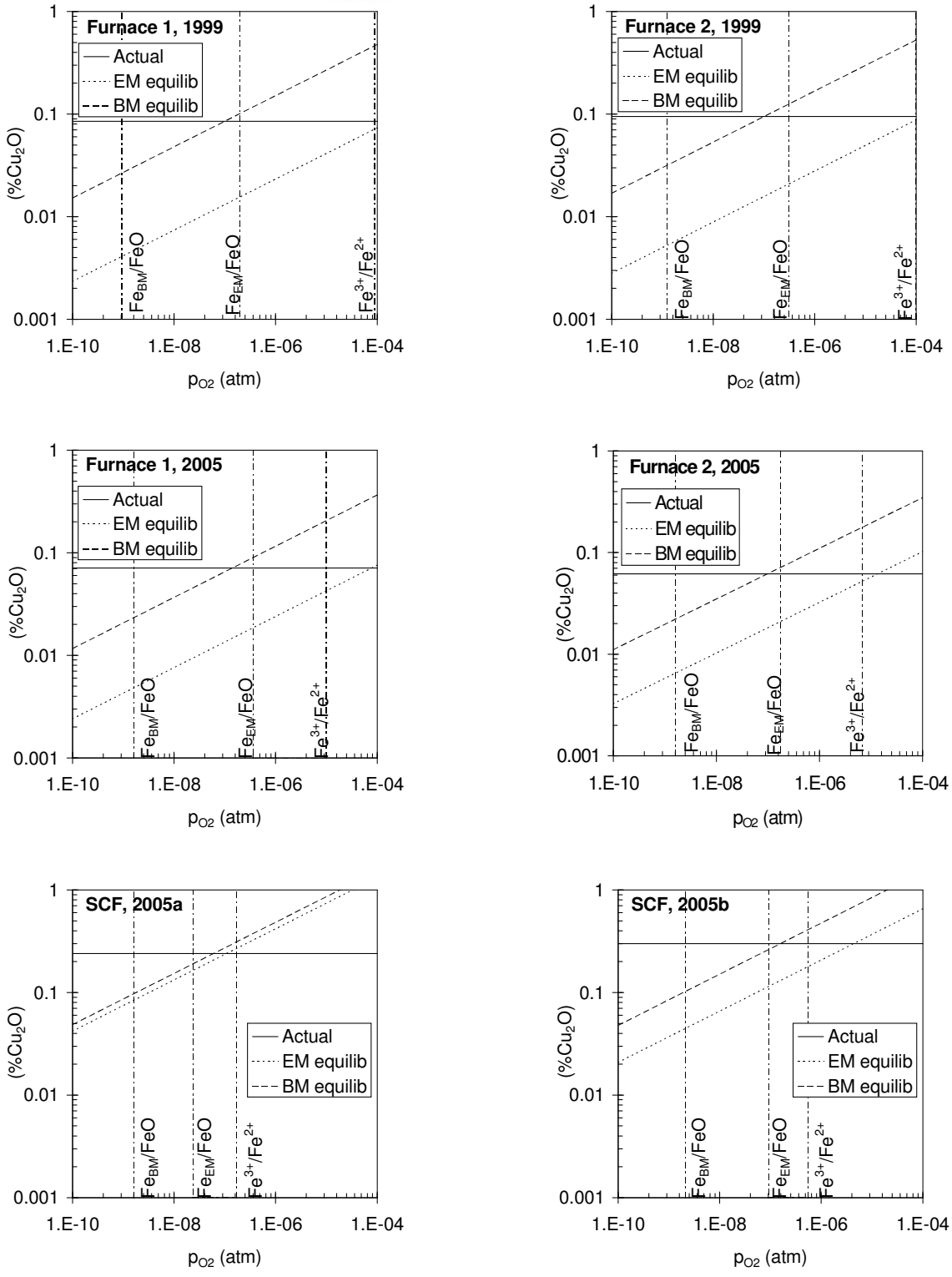

Figure B20: Base metal dissolution plots for copper for the 1999 and 2005 furnaces and SCF. Dissolved Cu_2O can be read off at the intersections of the Fe_{BM}/FeO and $Fe^{\#+}/Fe^{2+}$ buffers with the bulk matte equilibrium line or at the intersections of the Fe_{EM}/FeO and $Fe^{\#+}/Fe^{2+}$ buffers with the entrained matte equilibrium line. The levels so obtained can be compared with actual Cu_2O measured on the microprobe.

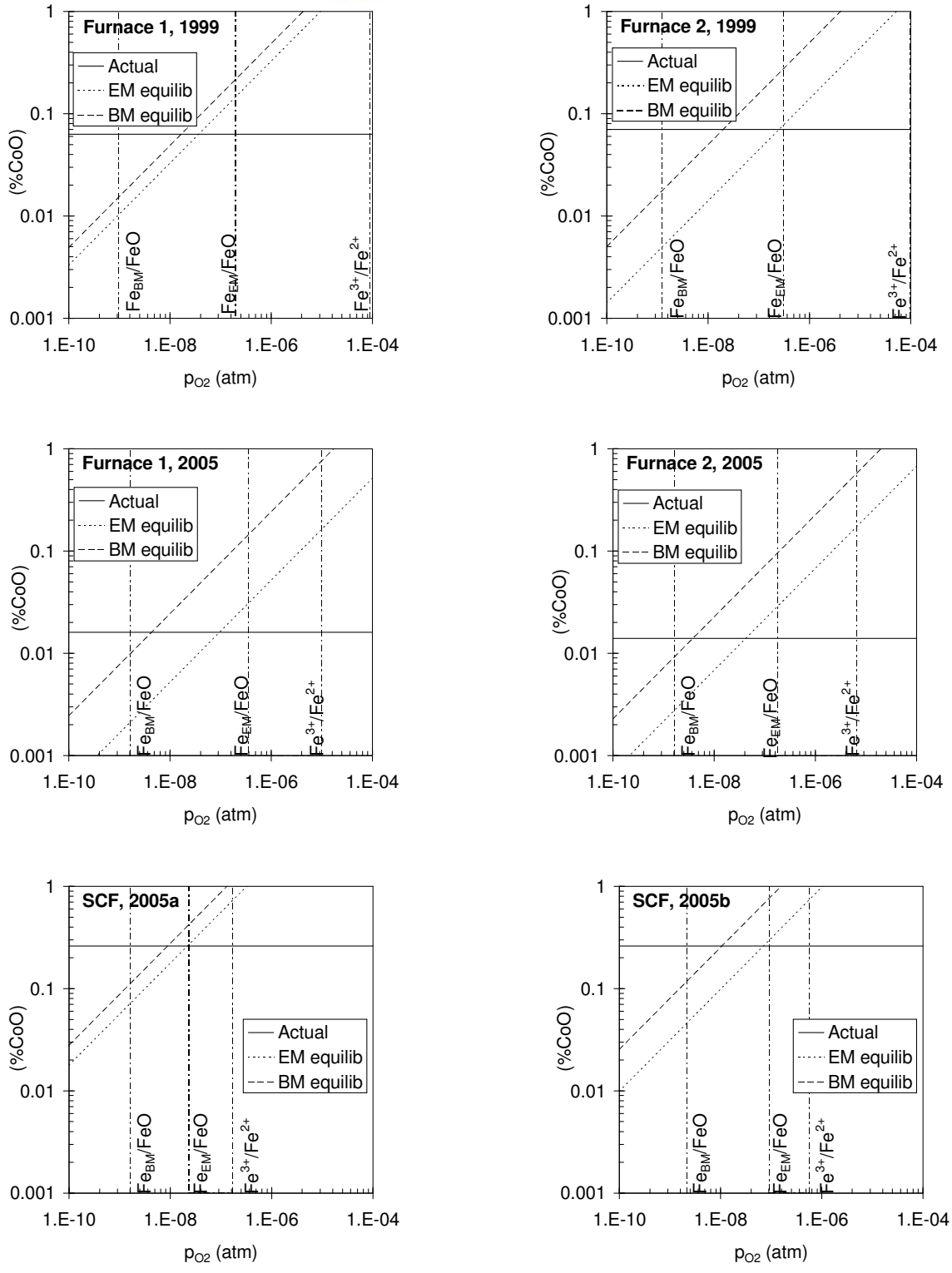

Figure B21: Base metal dissolution plots for cobalt for the 1999 and 2005 furnaces and SCF. Dissolved CoO can be read off at the intersections of the Fe_{BM}/FeO and $Fe^{\#+}/Fe^{2+}$ buffers with the bulk matte equilibrium line or at the intersections of the Fe_{EM}/FeO and $Fe^{\#+}/Fe^{2+}$ buffers with the entrained matte equilibrium line. The levels so obtained can be compared with actual CoO measured on the microprobe.

APPENDIX C – STATISTICAL FORMULAE AND CALCULATIONS

(N.B.: many of these assume normal distribution).

Average

The average, or arithmetic mean, ($\underline{x}$) = $\Sigma x/n$

where x = individual values, and n = the number of such values.

Standard deviation

The standard deviation, or root mean square deviation, (σ_x) = $\sqrt{(\Sigma(x-\underline{x})^2/n)}$

Confidence interval

The 95 % confidence interval for the mean (average) is $\mu_x \pm 2$ SE

where SE is the standard error of the mean ($\sigma_{\underline{x}}$) = $\sigma_x/\sqrt{n} = \sqrt{((\Sigma(x-\underline{x})^2/n(n-1))}$

Limit of Detection

The trace element detection limit (in mass %) as calculated in the electron microprobe software is

$$C_{DL} = C_S / \underline{N}_S - \underline{N}_{SB} \cdot \sqrt{2}(t_{n-1}{}^{1-\alpha})\sigma_c/\sqrt{n}$$

where C_S = element concentration (mass %) in the standard

$t_{n-1}{}^{1-\alpha}$ = Student t for $1-\alpha$ confidence and n-1 degrees of freedom

n = no. of data point acquired

σ_c = standard deviation of the measured values

$\underline{N}_S$ = average number of counts on the standard

$\underline{N}_{SB}$ = continuum background counts on the standard

References

DeHOFF (1968), GREGORY (1969), and KREMSER (1999).